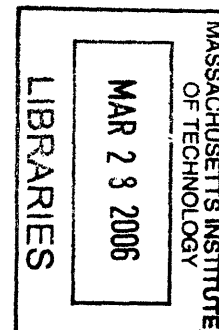


# Core Design and Reactor Physics of a Breed and Burn Gas-cooled Fast Reactor

By  
Peter Yarsky

B.S. Nuclear Engineering and Engineering Physics  
Rensselaer Polytechnic Institute, 2002

S.M. Nuclear Engineering  
Massachusetts Institute of Technology, 2004



SUBMITTED TO THE DEPARTMENT OF NUCLEAR ENGINEERING IN  
PARTIAL FULFILLMENT OF THE REQUIREMENTS FOR A DEGREE OF

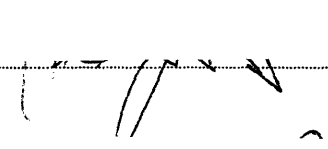
DOCTOR OF PHILOSOPHY IN NUCLEAR ENGINEERING  
AT THE  
MASSACHUSETTS INSTITUTE OF TECHNOLOGY

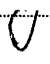
ARCHIVES

September 2005

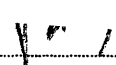
© Massachusetts Institute of Technology 2005. All rights reserved.

The author hereby grants to MIT permission to reproduce and to distribute publicly paper and electronic copies of this thesis document in whole or in part.

Author  Department of Nuclear Engineering

Certified by  Professor Emeritus Michael J. Driscoll  
Thesis Advisor

Certified by  Doctor Pavel Hejzlar  
Thesis Reader

Accepted by  Professor Jeffrey A. Coderre  
Chairman, Department Committee on Graduate Students



# Core Design and Reactor Physics of a Breed and Burn Gas-cooled Fast Reactor

By  
Peter Yarsky

SUBMITTED TO THE DEPARTMENT OF NUCLEAR ENGINEERING IN PARTIAL FULFILLMENT OF THE REQUIREMENTS FOR A DEGREE OF DOCTOR OF PHILOSOPHY IN NUCLEAR ENGINEERING AT THE MASSACHUSETTS INSTITUTE OF TECHNOLOGY

September 2005

## Abstract

In order to fulfill the goals set forth by the Generation IV International Forum, the current NERI funded research has focused on the design of a Gas-cooled Fast Reactor (GFR) operating in a Breed and Burn (B&B) fuel cycle mode. B&B refers to a once-through fuel cycle where low enriched uranium (less than 5 w/o  $^{235}\text{U}$  in U) subcritical assemblies are loaded into the core in equilibrium, yet in-situ plutonium breeding carries the fuel through a discharge burnup on the order of 150 MWD/kg<sub>HM</sub>. The B&B fuel cycle meets the GenIV goals of sustainability, economics, and proliferation resistance by increasing fuel burnup without the need for spent fuel reprocessing, recycle, or reuse of any kind.

The neutronic requirements for B&B are strict and require an ultra-hard neutron spectrum. Therefore, the GFR is ideally suited for this fuel cycle. In the present work the B&B GFR concept evolved into two practical reactor designs, both of which build on extensive previous gas-cooled reactor design experience.

The first version is the “demonstration” concept using highly neutronically reactive  $\text{U}^{15}\text{N}$  fuel in a hexagonal pin fuel array that is nearly 50 v/o fuel. The core is helium cooled, with an outlet temperature of 570 °C. The helium primary circuit is coupled to a steam Rankine power conversion system essentially identical to that for the British Advanced Gas-cooled Reactors. One advantage of the low coolant temperature compared to other GenIV GFR concepts is that it allows for the use of oxide dispersion strengthened stainless steels (ODS) in core. The fuel is manufactured using advanced vibration compaction techniques, clad in ODS, and vented in order to achieve the high burnup goal.

The second version, the “advanced” concept builds on the experience of the demonstration concept to develop a B&B GFR without the need for expensive  $\text{U}^{15}\text{N}$  fuel. In order to substitute the nitride fuel with carbide, significantly higher heavy metal loadings are required (60 v/o fuel for UC versus 50 v/o fuel for  $\text{U}^{15}\text{N}$ ) which are not practically achievable with a conventional pin fuel array. Therefore, an innovative tube-in-duct assembly design was proposed to achieve B&B operation with the less neutronically reactive carbide fuel. The advanced core offers significantly reduced natural uranium requirements and lower equilibrium fuel cycle costs (5 mills/kWhre) compared with conventional light water reactors (7 mills/kWhre), as the burnup is tripled for the same reload enrichment.

The B&B GFR designs, though requiring active decay heat removal, are semi-self-regulating from a reactivity feedback standpoint and are designed to withstand all plausible accident

scenarios, including loss of flow, loss of heat sink, and transient overpower all without scram. Reactor pressure vessel blowdown (LOCA) was investigated and while the B&B GFR has a low positive coolant void reactivity (less than 1\$), the added reactivity during blowdown is compensated through other strong negative reactivity feedback mechanisms, thereby allowing for the safe operation of the B&B GFR.

Thesis Advisor: Professor Emeritus Michael J. Driscoll  
Thesis Reader: Dr. Pavel Hejzlar



## Acknowledgements

I would like to thank the Department of Energy of the United States and the Nuclear Energy Research Initiative Program for sponsoring this research (Project Grant Number DE-FG07-02SF22608).

I would like to extend thanks to the following individuals for their various technical contributions to this research: Dr. Mitch Meyer, Dr. Kevan Weaver, Dan Wachs, Dr. Walt Kato, Professor Ron Ballinger, Professor Ken Czerwinski, Dr. Pradip Saha, Professor Mujid Kazimi, Kun Yu, Jonathan Plaue, and Dr. Vaclav Dostal.

Chris Handwerk, Mike Pope, Nate Carstens, and Dr. Zhiwen Xu also deserve my dearest thanks for their generosity, numerous contributions, and assistance for the duration of their project. These incredible individuals have been a joy to work with, and are responsible for the health, functionality, and versatility of the (completely indispensable) MIT Echelon Beowulf Computing Cluster and its codes.

I would like to extend my most grateful acknowledgements to my advisors Professor Emeritus Michael Driscoll and Dr. Pavel Hejzlar. Aside from their incredibly helpful guidance, know-how, feedback, and references; it takes considerable constitution to bear my incessant whining and flamboyant (at times) attitude. Extra thanks go to Professor Michael “Uncle Mike” Driscoll whose tireless efforts to make me the best nuclear engineer I could be have not been completely wasted (though possibly to a significant extent). He has been an excellent mentor, and I would not have been able to survive this project without his witticism and support.

Whitney Raas, Benjamin Parks, and Lisa Mullen are duly thanked for their efforts to keep me from completing my thesis. Without them there is no doubt that I would have suffered a severe nervous breakdown, and they will continue to be my friends forever.

Michael Stawicki, Dan Cavallari, Nathan Palmer, Susan Kane, Craig Gerardi, Matt Reinke, Bobby Middleton, Jane Diecker, and Dave Rigual are also thanked for being there for me through the rough spots, and helping to make my time here the best in my life.

I would also like to thank Tiffany Groode, Lucy Rodd, and Sara Hupp. Their support has been immeasurable and each and every one of them has helped me to change my life for the better. In living with them, I’ve realized how little I deserve friends as loyal and caring as them. They will continue to be the smart women that inspire me to be a better person. The first three spots in my speed dial are permanently reserved for them.

Lastly, no one deserves more thanks than my family. There have been no other people willing to give as much as they would (and have) for my health, happiness, and success. For them, no words of thanks exist that would be sufficient.



# Table of Contents

Abstract .....	3
Acknowledgements .....	5
Table of Contents .....	7
List of Figures .....	11
List of Tables.....	13
List of Tables.....	13
Nomenclature .....	15
Chapter 1. Introduction.....	17
1.1. Background .....	17
1.2. Objectives .....	18
1.3. Theory .....	18
1.4. Organization .....	26
Chapter 2. Methodology.....	27
2.1. Introduction .....	27
2.2. Neutronics .....	27
2.2.1. MCNP.....	27
2.2.2. Cladding Fluence.....	38
2.2.3. ORIGEN.....	39
2.2.4. MCODE.....	40
2.2.5. Quasi-Static Method.....	49
2.2.6. AIROX and CASMO-4 .....	53
2.3. Thermal Hydraulics .....	54
2.3.1. Pin Assemblies .....	55
2.3.2. Tube-in-Duct Assemblies.....	61
2.4. Fuel Cycle Economics.....	64
2.4.1. Once-Through-Then-Out Fuel Cycle Analysis .....	64
2.4.2. Alternative Fuel Cycle Analysis.....	68
2.5. Chapter 2 Summary .....	70
Chapter 3. Core Materials Selection.....	71
3.1. Introduction .....	71
3.2. Methodology .....	72
3.3. Ceramic Fuels.....	74
3.3.1. Reactivity.....	74
3.3.2. Ceramic Fuel Flux Spectra .....	77
3.3.3. Conversion Ratio .....	79
3.3.4. Conclusions .....	81
3.3.5. Chemical Concerns.....	82
3.4. Metallic Fuels.....	83
3.4.1. Flux Spectra.....	84
3.4.2. Conversion Ratio .....	86
3.4.3. Conclusions .....	87
3.4.4. Mechanical Concerns .....	87
3.5. Further Intercomparison of Metallic Alloys and Ceramic Fuels.....	88
3.5.1. Heavy Metal Density Dependence .....	88
3.5.2. Proliferation Resistance.....	91
3.5.3. Void Reactivity Worth .....	94
3.6. Cladding Selection.....	95
3.7. Gas Coolant Comparison.....	98

3.7.1.	Comparison with Liquid Lead Coolant .....	101
3.8.	Material Selections .....	102
3.9.	Temperature Limits .....	103
3.10.	VIPAC Fuel Conductivity .....	103
3.11.	Chapter 3 Summary .....	105
Chapter 4.	Demonstration Core Overview .....	107
4.1.	Introduction .....	107
4.2.	Fuel Assembly Design.....	107
4.3.	Balance of Plant.....	108
4.4.	Core Design Limitations and Strategies .....	109
4.4.1.	Primary Circuit Pressure.....	109
4.4.2.	Axial Power Shaping .....	111
4.4.3.	Fission Gas Venting .....	114
4.4.4.	Spent Fuel Characteristics .....	114
4.5.	Chapter 4 Summary .....	116
Chapter 5.	Demonstration Core Physics.....	117
5.1.	Introduction .....	117
5.2.	Preliminary Core Design .....	117
5.2.1.	Fuel Assembly Specifications .....	119
5.2.2.	Uncontrolled Reactivity History.....	119
5.2.3.	Assembly Power History in Equilibrium.....	121
5.2.4.	Delayed Neutron Fraction .....	122
5.2.5.	Control.....	124
5.3.	Final Design .....	127
5.3.1.	Poison Control and Fuel Assembly Design .....	129
5.3.2.	Quasi-Static Analysis .....	135
5.3.3.	Core Flooding.....	137
5.3.4.	Cladding Irradiation.....	140
5.4.	Chapter 5 Summary .....	142
Chapter 6.	Demonstration Core Thermal Hydraulics .....	143
6.1.	Introduction .....	143
6.2.	Steady State Operation .....	143
6.3.	Loss of Coolant and Blowdown Time.....	144
6.4.	Chapter 6 Summary .....	147
Chapter 7.	Demonstration Core Fuel Cycle Economics.....	149
7.1.	Introduction .....	149
7.2.	Cost of Generation.....	149
7.3.	Chapter 7 Summary .....	151
Chapter 8.	Advanced Core Overview.....	153
8.1.	Introduction .....	153
8.2.	Fuel Volume Fraction.....	154
8.3.	Advanced Core Primary Coolant Pressure .....	155
8.4.	Core Design Considerations and Lessons Learned .....	156
8.5.	Chapter 8 Summary .....	157
Chapter 9.	Advanced Core Physics .....	159
9.1.	Introduction .....	159
9.2.	Uncontrolled Reactivity History.....	160
9.3.	Reactivity Control .....	160
9.4.	Quasi-Static Analysis .....	161
9.5.	Cladding Irradiation.....	164
9.6.	Chapter 9 Summary .....	164

Chapter 10. Advanced Core Thermal Hydraulics .....	167
10.1. Introduction .....	167
10.2. The 2400 MW Base Case .....	167
10.3. The 3400 MW High Pressure & High Power Case .....	169
10.4. Chapter 10 Summary .....	171
Chapter 11. Advanced Core Fuel Cycle Economics .....	173
11.1. Introduction .....	173
11.2. Cost of Generation.....	173
11.3. Sustainability .....	174
11.4. Chapter 11 Summary .....	175
Chapter 12. Summary and Conclusions .....	177
12.1. Overview .....	177
12.2. Introduction .....	177
12.3. Theory and Methods.....	178
12.4. Demonstration Core: Fuel and Core Design.....	181
12.4.1. Safety .....	185
12.4.2. Economics .....	186
12.5. Advanced Core Fuel and Core Design .....	187
12.5.1. Safety .....	190
12.5.2. Economics .....	190
12.6. Conclusions .....	191
Chapter 13. Recommendations for Future Work.....	193
13.1. TID Fuel Assembly Fabrication, Systems, and Associated Costs.....	193
13.2. Verifying Temperature, Irradiation, and Velocity Limits .....	193
13.3. 3400 MW Advanced Core Design.....	194
13.4. Advanced Core Interassembly Control and Cooling.....	195
13.5. SiC as a Cladding Material.....	195
13.6. Improved VIPAC Conductivity Models.....	198
13.7. Increase Power Density by Power Shaping.....	198
Appendices .....	199
References .....	245



## List of Figures

Figure 1.1	The $^{239}\text{Pu}$ Microscopic Fission & Capture Cross Sections [46].	19
Figure 1.2	The $^{235}\text{U}$ & $^{239}\text{Pu}$ Ratio of Fission to Absorption Cross Sections [36].	20
Figure 1.3	The $^{235}\text{U}$ & $^{239}\text{Pu}$ Absorption Yields ( $\eta$ ) [36].	20
Figure 1.4	The $^{238}\text{U}$ Microscopic Fission Cross Section [46].	21
Figure 1.5	Reactivity Histories for a UC Pin Cell Using Different BOC Enrichments	25
Figure 2.1	FCA Homogenous Model Geometry	29
Figure 2.2	Neutron Spectra for Fuel Elements	30
Figure 2.3	Neutron Spectra for the Axial and Radial Blankets	31
Figure 2.4	Neutron Spectra for the Axial and Radial Reflectors	32
Figure 2.5	Heterogeneous One Quarter Symmetric Model Geometry	33
Figure 2.6	Central (first) Zone Matrix/Drawer Diagram	34
Figure 2.7	ENDFB6 and JEF2.2 $^{238}\text{U}$ Fission Cross Section Comparison	35
Figure 2.8	Representative Neutron Flux Spectra for B&B GFR Fuel Batches	36
Figure 2.9	MCODEv1 and MCODEv2 calculations for Full Core, Cycle 1.	42
Figure 2.10	Total Fluence Calculations for Three Cases (nvt in inverse barns)	43
Figure 2.11	Fast ( $E > 0.1\text{MeV}$ ) Fluence Calculations in Three Cases (nvt in inverse barns)	43
Figure 2.12	Effect of Plutonium Drift on Cell Eigenvalue	45
Figure 2.13	Peripheral Triangle Illustrating MCNP Fill Discrepancy (not-to-scale)	46
Figure 2.14	Compromise Approximation (not-to-scale)	47
Figure 2.15	Fill-Area-Discrepancy Calculation using MCODEv1	48
Figure 2.16	Equivalent Annulus Diagram	62
Figure 3.1	Unit Cell Geometry (not to scale)	73
Figure 3.2	Ceramic Fuel Reactivity Histories	75
Figure 3.3	Difference between Peak and Instantaneous Reactivity for Ceramic Fuels	76
Figure 3.4	Ceramic Fuel BOL Flux Spectra	77
Figure 3.5	Ceramic Fuel Conversion Ratio vs. Burnup	80
Figure 3.6	Microscopic $^{31}\text{P}$ Absorption Cross-section [46]	82
Figure 3.7	Alloy Fuel Reactivity Histories	83
Figure 3.8	Difference between Peak and Instantaneous Reactivity for Metallic Fuels	84
Figure 3.9	Metallic Alloy Fuel BOL Flux Spectra	85
Figure 3.10	Alloy Fuel Conversion Ratio vs. Burnup	86
Figure 3.11	Reactivity Dependence on Heavy Metal Density	89
Figure 3.12	Peak vs. BOL Reactivity for Every Fuel Type Considered	91
Figure 3.13	Number Density of Fissile Species in UC and U-10Zr fuel	94
Figure 3.14	Cladding Effect on Reactivity	96
Figure 3.15	Reactivity History Comparison for Different Cladding Materials	97
Figure 3.16	Gas Coolant Flux Comparisons	99
Figure 3.17	Reactivity Histories for Different Coolant Cases	100
Figure 3.18	Conversion Ratio History for US fuel with different coolants.	101
Figure 3.19	Lead vs. Helium Coolant Burnup Comparison	102
Figure 4.1	Horizontal Cross-sectional View of a Fuel Assembly	108
Figure 4.2	AGR Plant Layout [22]	108
Figure 4.3	Axial Power Shape History for Uniform Fuel	111
Figure 4.4	Axial Power Shape History for Enrichment-Zoned BOL Fuel	112
Figure 4.5	$k_{inf}$ as a Function of Burnup for Different PWR Cases	115
Figure 5.1	Preliminary Core Design 1/6 <sup>th</sup> Symmetric Model	118
Figure 5.2	Preliminary Design Demonstration Core Reactivity History	120
Figure 5.3	Demonstration Core Assembly Power History	122
Figure 5.4	B&B GFR Neutron Flux Spectra	123

Figure 5.5	The Buildup of <sup>149</sup> Sm and <sup>101</sup> Ru During GFR Irradiation .....	125
Figure 5.6	Spectral Shift for Some Control Materials .....	127
Figure 5.7	Demonstration Core Final Design Layout.....	128
Figure 5.8	Final Fuel Assembly Design with a Control Cluster.....	129
Figure 5.9	Final Design Demonstration Core Reactivity History.....	131
Figure 5.10	Power History Comparison .....	133
Figure 5.11	Power History versus Burnup.....	134
Figure 5.12	Effect of Core Flooding on EOEC Core Eigenvalue (Poison Withdrawn) .....	138
Figure 5.13	Effect of Core Flooding on EOEC Core Eigenvalue (Poison Inserted) .....	139
Figure 8.1	TID Conceptual Diagram .....	153
Figure 8.2	BOC Infinite Medium Reactivity Assessment for TID Fuel.....	154
Figure 8.3	Burnup Histories for Various Fuel Volume Fractions.....	155
Figure 9.1	Advanced Core Layout.....	159
Figure 9.2	Advanced Core Uncontrolled Reactivity History.....	160
Figure 10.1	Advanced Core Hot Channel Temperature Profile.....	168
Figure 10.2	Advanced Core Average Channel (orificed) Temperature Profile .....	168
Figure 12.1	Comparison of Fuels' Reactivity History.....	179
Figure 12.2	Relationship between Reactivity and Heavy Metal Density .....	180
Figure 12.3	Impact of Enrichment on High Burnup Reactivity.....	181
Figure 12.4	Demonstration Core Fuel Assembly.....	182
Figure 12.5	Demonstration Core Layout .....	183
Figure 12.6	Demonstration Core Uncontrolled Reactivity History .....	184
Figure 12.7	Tube-in-Duct Fuel Assembly Schematic.....	188
Figure 12.8	Advanced Core Layout.....	189
Figure 12.9	Advanced Core Uncontrolled Reactivity History.....	189
Figure 13.1	ODS and SiC Cladding Comparison .....	196
Figure 13.2	SiC at Double Thickness Reactivity History .....	197



## List of Tables

Table 2-1	Core Eigenvalues using Prebroadened Cross Section Libraries.....	36
Table 2-2	Comparison of Core and Pin Cell Models and Doppler Coefficient.....	37
Table 2-3	Multi-group Displacement Cross Sections.....	39
Table 2-4	Fission Products and Their AIROX Removal Fractions [48,52].....	54
Table 2-5	Global Parameters for the Pin Assembly Calculations.....	56
Table 2-6	Cell-wise Properties of the Coolant.....	57
Table 2-7	Cell-wise Heat Transfer Parameters.....	58
Table 2-8	Cell-wise Pressure Drop Parameters.....	59
Table 2-9	Key GCFR Comparison Model Input Parameters.....	60
Table 2-10	Output Comparison to GCFR.....	61
Table 2-11	Modified Parameters for the TID Finite volume Model.....	62
Table 2-12	Input Parameters to Flow-Split and the FVM for the Comparison Study.....	63
Table 2-13	Comparison Study Results.....	64
Table 2-14	Economic Parameters for OTTO Analyses.....	65
Table 2-15	LWR Reference Values for OTTO Analysis.....	68
Table 3-1	Fuel Properties [32,31,68,4].....	72
Table 3-2	Zone Identification.....	73
Table 3-3	Comparison of Lattice Geometry for UC fuel.....	74
Table 3-4	Reactivity Parameters for Fuel Ceramics.....	75
Table 3-5	Average Epithermal Flux Energy for Fuel Ceramics.....	79
Table 3-6	Burnup Behavior of <sup>239</sup> Pu Cross Sections for UC fuel.....	79
Table 3-7	U <sup>15</sup> N peak values vs. UO <sub>2</sub> peak values.....	81
Table 3-8	Reactivity Parameters for Alloy Fuels.....	83
Table 3-9	Average Epithermal Flux Energy for Fuel Alloys.....	85
Table 3-10	Burnup Behavior of <sup>239</sup> Pu Cross Sections for U-10Zr fuel.....	86
Table 3-11	Microscopic Absorption Cross Sections from Diluent Study [74].....	90
Table 3-12	One Group <sup>239</sup> Pu Microscopic Cross-sections.....	92
Table 3-13	Plutonium Number Densities at 160 MWD/kg <sub>HM</sub> .....	92
Table 3-14	Plutonium Discharge Vector at 160 MWD/kg <sub>HM</sub> .....	93
Table 3-15	Steel Clad Compositions (by weight percentage).....	97
Table 3-16	Slowing Down Power Comparison [21].....	99
Table 3-17	Cladding Temperature Limits (Hot Channel).....	103
Table 4-1	Systematic Comparison for a 2400 MW <sub>th</sub> B&B GFR Core (pin-type).....	110
Table 4-2	Power Peaking History for Uniform BOL Enrichment.....	112
Table 4-3	Power Peaking History for Zoned Enrichment.....	113
Table 4-4	Spent Fuel Fissile Content.....	114
Table 5-1	Preliminary Design Demonstration Core Geometry.....	119
Table 5-2	Startup and Reload Sequence.....	120
Table 5-3	Delayed Neutron Fraction.....	124
Table 5-4	Core Eigenvalues for Various Control Materials.....	126
Table 5-5	Final Design Demonstration Core Geometry.....	130
Table 5-6	Neutron Economy Performance with Poison Control.....	132
Table 5-7	Impact of Control Clusters on Radial Power Peaking.....	133
Table 5-8	Calculated Reactivity Feedback Parameters and Uncertainty.....	136
Table 5-9	Reactivity Feedback Parameters for Several Fast Reactor Designs.....	137
Table 5-10	Reactivity Consequences of Core Flooding.....	139
Table 5-11	Samarium Diluent and Startup Flooding.....	140
Table 5-12	U <sup>15</sup> N Pin Model Fluence and DPA Calculation.....	141
Table 6-1	Input into the Demonstration Core FVM.....	143

Table 6-2	Demonstration Core Hot Channel FVM Output.....	144
Table 6-3	GFR Loss of Coolant Blowdown Times .....	147
Table 7-1	Infinite Assembly Reactivity at BOL for Direct Fuel Reuse in the GFR.....	149
Table 7-2	Alternative Fuel Cycle Economic Assessment.....	150
Table 7-3	Breakeven HEN Unit Cost .....	150
Table 8-1	Parametric Comparison for the TID Assembly .....	156
Table 8-2	Advanced Core Geometry .....	157
Table 9-1	Neutron Economy Performance of Advanced B&B Concept .....	161
Table 9-2	Calculated Reactivity Feedback Parameters and Uncertainty .....	162
Table 9-3	Demonstration and Advanced Core Reactivity Feedback .....	163
Table 9-4	UC TID Model Fluence and DPA Calculation.....	164
Table 10-1	Advanced Core FVM Input Parameters .....	167
Table 10-2	Advanced Core FVM Output .....	169
Table 10-3	High Pressure & Power Advanced Core FVM Input Parameters.....	170
Table 10-4	High Pressure & Power Advanced Core FVM Output.....	171
Table 11-1	Advanced B&B GFR Fuel Cycle Cost Assessment .....	173
Table 11-2	Startup Fuel Cycle Costs With LWR Reuse .....	174
Table 12-1	Demonstration Core Geometry.....	183
Table 12-2	Startup Core and Fuel Shuffle Sequence .....	184
Table 12-3	Quasi-Static Analysis of the Demonstration Core.....	186
Table 12-4	Demonstration Core Cost of Generation and Alternative Fuel Cycles.....	187
Table 12-5	Advanced Core Geometry .....	188
Table 12-6	Quasi-Static Analysis of the Advanced Core .....	190
Table 12-7	Advanced Core Cost of Generation.....	191
Table 12-8	Summary of B&B GFR Core Attributes .....	192
Table 13-1	SiC Effect on Neutron Economy .....	198

## Nomenclature

ABR	Actinide Burner Reactor
AGR	British Advanced Gas-cooled Reactor
AIROX	Atomics International Reduction Oxidation Process
ANL	Argonne National Laboratory
APPF	Axial Power Peaking Factor
B&B	Breed and Burn
BAD	Burnup Accrual Discrepancy
BOC	Beginning of Cycle
BOEC	Beginning of Equilibrium Cycle
BOL	Beginning of Life
BWR	Boiling Water Reactor
CANDU	Canada Deuterium Uranium Reactor
CARBOX	Carbothermic Oxidation Reduction Process
CARDIO	Carbon Dioxide Oxidation Process
CEA	Commissariat a l'Energie Atomique (Atomic Energy Commission of France)
CF	Capacity Factor
CR	Conversion Ratio
CRA	Control Rod Assembly
DPA	Displacements per Atom
DUPIC	Direct Use of PWR Spent Fuel in CANDU Reactors
ENDF	Evaluated Nuclear Data File
EOEC	End of Equilibrium Cycle
FAD	Fill Area Discrepancy
FCA	Fast Critical Assembly
FVM	Finite Volume Model
FFF	Fertile Fission Fraction
FTF	Flat to Flat Distance
GA GCFR	General Atomics Gas-Cooled Fast Reactor
GenIV	Generation IV
GFR	Gas-cooled Fast Reactor
HEN	Highly Enriched Nitrogen
HM	Heavy Metal
HMD	Heavy Metal Density
IFR	Integral Fast Reactor
IHX	Intermediate Heat Exchanger
JAERI	Japan Atomic Energy Research Institute
JEF	Joint Evaluated File
JENDL	Japanese Evaluated Nuclear Data Library
KAERI	Korea Atomic Energy Research Institute
LEU	Low Enriched Uranium
LMFBR	Liquid Metal Fast Breeder Reactor
LWR	Light Water Reactor
MCNP	Monte Carlo N-Particle Transport Core
MCODE	MCNP ORIGEN Depletion Program
ODS	Oxide Dispersion Strengthened Stainless Steel

OREOX	Oxidation and Reduction of Oxide Fuel Process
ORIGEN	Oak Ridge Isotope Generation and Depletion Code
OTTO	Once-Through-Then-Out Fuel Cycle
PCS	Power Conversion System
PWR	Pressurized Water Reactor
RERTR	Reduced Enrichment for Research and Test Reactors
RPPF	Radial Power Peaking Factor
S-CO <sub>2</sub>	Supercritical Carbon Dioxide
TID	Tube-in-Duct
U <sup>15</sup> N	Uranium Nitride Fuel, Highly Enriched (>99%) in the isotope <sup>15</sup> N
USD	United States Dollars
VIPAC	Vibration Compaction Process
ZPR	Zero Power Reactor

# Chapter 1. Introduction

## 1.1. Background

The Nuclear Energy Research Initiative funded work described here is focused on a next generation Gas-cooled Fast Reactor (GFR). In particular, the ultra-hard neutron spectrum associated with the GFR enables the design of next generation reactors with advanced fuel cycles, such as the Breed and Burn (B&B) concept of present interest. The GFR was studied extensively between 1960 and 1980 in the US and Europe [20]. The GFR is now receiving renewed attention after being selected as a potential candidate for deployment in the 2025 time frame by the Generation IV International Forum (GIF) [28]. At MIT, several research projects have been completed that examine the neutronic characteristics of different GFR concepts [74], [49] exploring the impact of core diluents, reflectors, and coolants on neutronic parameters of the core. The current work however is more application driven, and strives to develop a working concept that characterizes the benefits of a GFR with a B&B fuel cycle.

The B&B concept refers to a nuclear fuel cycle where the equilibrium reload fuel is low enriched uranium (LEU) (up to 5 w/o  $^{235}\text{U}$ ). Plutonium is aggressively bred in-situ and reactivity sharing among fresh and partially burnt fuel assemblies carries the fuel through discharge burnup on the order of 150 MWD/kg<sub>HM</sub>. A hard neutron spectrum is conducive to fulfilling the stringent neutronic requirements of a B&B reactor, thus making the GFR an ideal candidate for the B&B fuel cycle.

The B&B fuel cycle dramatically increases the utilization of LEU fuel, even without spent fuel reprocessing and recycle. This would permit early introduction of reactors with breeding capability before the deployment of commercial reprocessing facilities.

B&B is not a new concept. B&B was first mentioned in 1958 by Feinberg [23], studied in 1970 by Fischer, et al. [24] with collaborators at MIT [39], [3], and a lead cooled alloy version has been recently explored by Toshinsky, et al. in the 1990s [64]. Though research has been conducted that indicates that B&B may be possible with natural uranium, such proposed fuel cycles are complicated and require extremely long residency times and complex fuel shuffling sequences. Ryu and Sekimoto have recently described a pebble bed approach with online refueling, yet still requiring extra-long fuel residency times [56].

Several recent developments have motivated examining the GFR for B&B service. While the reactor physics design of the GFR is a major challenge, it cannot be done in the absence of several other concerns. The high burnup of the fuel will require the use of a robust creep and fluence-damage resistant cladding. Additionally, fuel, and especially cladding, temperature limits must not be exceeded, even under accident scenarios, which is a particularly difficult challenge for gas-cooled reactors.

With regards to advances in nuclear fuels, advanced Vibration-Compaction (VIPAC) fuel manufacturing processes developed and tested for  $\text{UO}_2$  in Russia can achieve very high smear density (90-91% of the theoretical density); and post irradiation examination of experimental fuel assemblies tested in Russian fast reactors indicate that concerns over both chemical and thermochemical fuel-cladding interactions are practically eliminated and burnup is effectively limited by the choice of cladding material [8,41]. VIPAC is thus an ideal fuel manufacturing process for meeting strict neutron economy requirements while maintaining acceptable fuel performance for extended periods of irradiation.

The higher burnup of the B&B GFR will result in longer cycle lengths and longer fuel residency times than conventional fast reactors; this becomes a factor in the economic viability of the concept. While improved uranium utilization may completely offset the higher carrying costs incurred, the economic value of the spent fuel offers some attractive end-use options. With the advent of simple, proliferation resistant fuel reuse technology such as AIROX [48], the B&B fuel cycle can likely be improved by implementing a similar technique. AIROX refers to a process where repeated oxidation and reduction reactions are used to release the volatile fission products from the fuel without separating any transuranics. The B&B GFR discharge fuel can likely be treated and used in LWRs as  $UO_2$ , or potentially recycled directly into the GFR after reconversion to UC or UN.

## 1.2. Objectives

The goal of the current work is to design and evaluate a GFR concept that addresses many of the practical concerns with operating a B&B fuel cycle. Namely concerns regarding material limitations, safety, and economics are addressed in arriving at a final design.

The reactor physics presents the over-arching design challenge. In other words, the goal of the work will be to design a GFR that operates on the B&B fuel cycle in equilibrium without any need for spent fuel reprocessing of any kind. The potential approaches for meeting this fuel cycle are only acceptable when thermal hydraulic and material limits can be acceptably met.

In addition to the limits imposed by the basic physical phenomena, a realistic and practical B&B GFR design must meet the goals set forth by the GIF. While the fuel cycle itself is instrumental in meeting several GIF objectives, an integral approach is used to accommodate these goals (in addition to physical limitations) to complete the design. Specifically, GenIV reactors are intended to improve: sustainability, economics, safety and reliability, and proliferation resistance.

The B&B GFR implicitly strives to improve economics and sustainability by increasing uranium utilization without spent fuel reprocessing. Additionally, since the reload fuel is LEU and the spent fuel requires no reprocessing treatment, the cycle is considered to be proliferation resistant compared with other fast reactor concepts that require spent fuel reprocessing. Thus, safety and reliability move to the forefront as key design goals in the current work.

Shutdown cooling and transient response are the purview of other investigators involved in the overall B&B program and are not considered in detail in the present work.

## 1.3. Theory

The B&B GFR uses LEU fresh assemblies; in a hard spectrum reactor the infinite medium multiplication factor for the fresh assemblies is less than unity. During irradiation,  $^{239}\text{Pu}$  is bred in such that the partially burnt assemblies have excess reactivity to share with the fresh assemblies. This is quite different from LWR fuel cycles where fresh assemblies tend to have excess reactivity to share with partially burnt assemblies. The first step in understanding the reactor physics behavior of the B&B GFR is to examine and understand the reactivity history of the fuel.

The fuel neutronic performance cannot be completely evaluated based solely on the beginning of cycle (BOC) characteristics. For a constant enrichment and weakly absorbing fuel constituent (for example carbon in UC), the fissile loading, and therefore the heavy metal density of the fuel, determines the BOC reactivity. However, this is by no means a complete picture of the history of

the fuel during irradiation. Though heavy metal density appears to be the prime determinant of BOC reactivity and a key factor in overall fuel performance, the burnup characteristics depend on more than the BOC reactivity, specifically the hardness of the flux spectrum.

The hardness of the flux spectrum determines the trend in reactivity as a function of burnup via two major components. The first is the worth of the bred Plutonium and the second, the conversion ratio. Figure 1.1 shows the  $^{239}\text{Pu}$  microscopic fission and capture cross sections. In the energy range above 10 keV, the capture cross section falls off with energy compared to the fission cross section, which is roughly constant above 1 keV. Therefore, if the flux spectrum is exceptionally hard the fission to absorption ratio for  $^{239}\text{Pu}$  will be large.

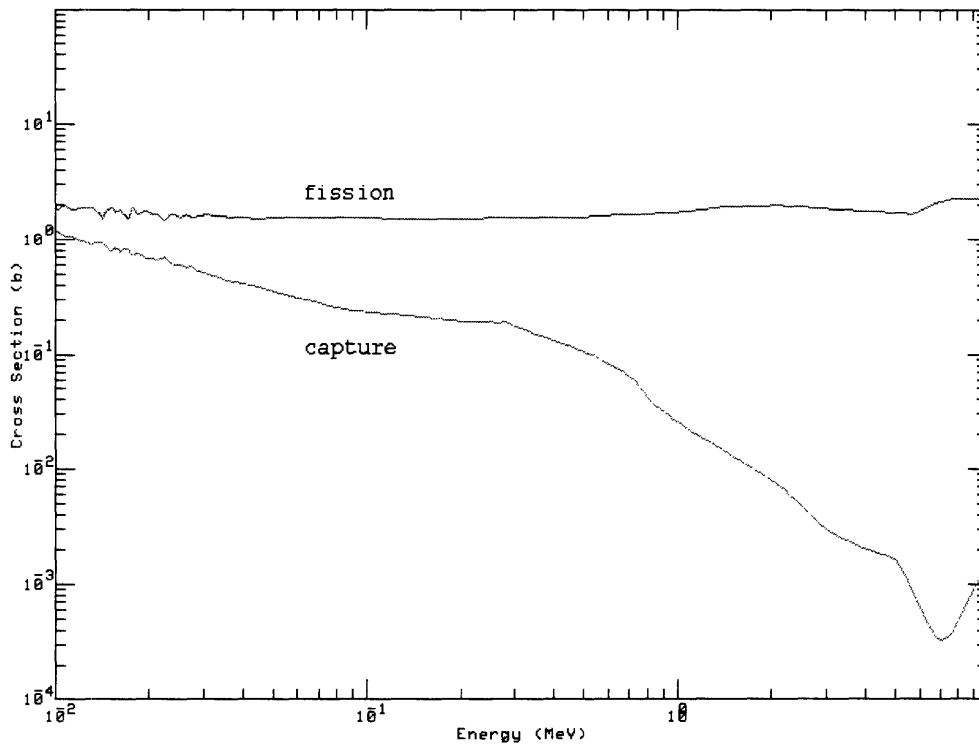


Figure 1.1 The  $^{239}\text{Pu}$  Microscopic Fission & Capture Cross Sections [46].

For comparison the ratio of fission to absorption is plotted for  $^{235}\text{U}$  and  $^{239}\text{Pu}$  in Figure 1.2. Though the  $^{235}\text{U}$  ratio is gradually increasing from 0.75 to unity between neutron energies of 1 keV to 1 MeV, the  $^{239}\text{Pu}$  ratio increases dramatically from 0.6 to unity. Figure 1.3 shows a related plot of the ratio of absorption yield for  $^{235}\text{U}$  and  $^{239}\text{Pu}$ ; the combination of these figures indicate that the neutron yield from absorption of  $^{239}\text{Pu}$  in the core is heavily dependent on the energy distribution of the neutron flux. It also indicates that each  $^{239}\text{Pu}$  nucleus will contribute more to the core reactivity than a single  $^{235}\text{U}$  nucleus.

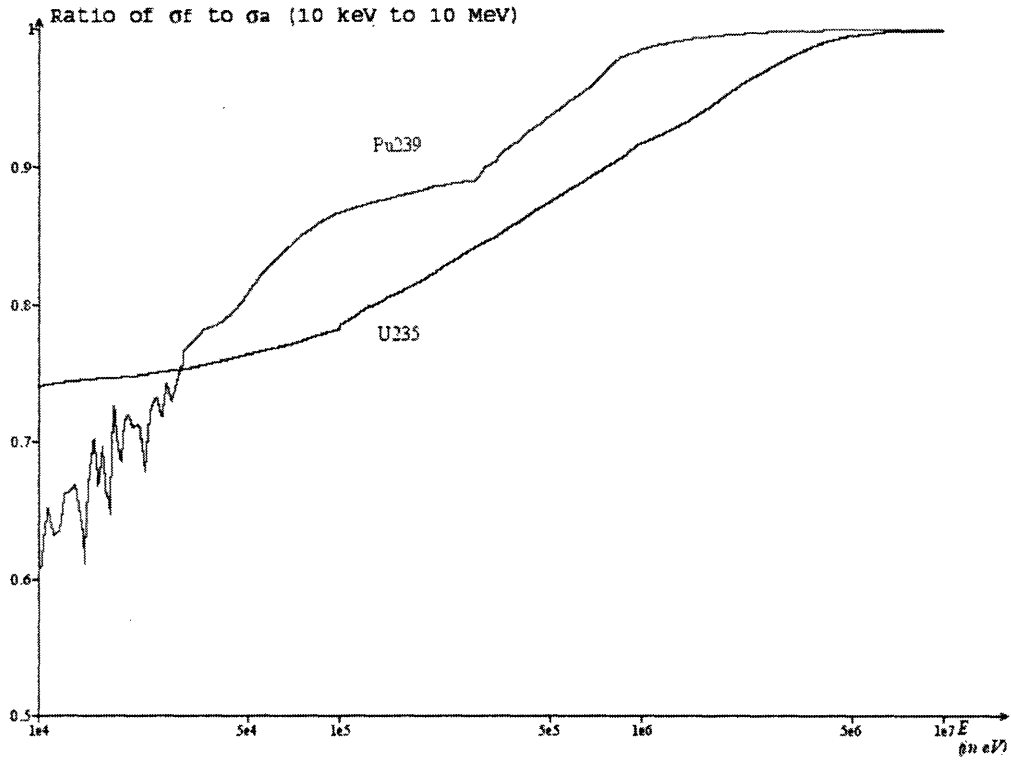


Figure 1.2 The  $^{235}\text{U}$  &  $^{239}\text{Pu}$  Ratio of Fission to Absorption Cross Sections [36].

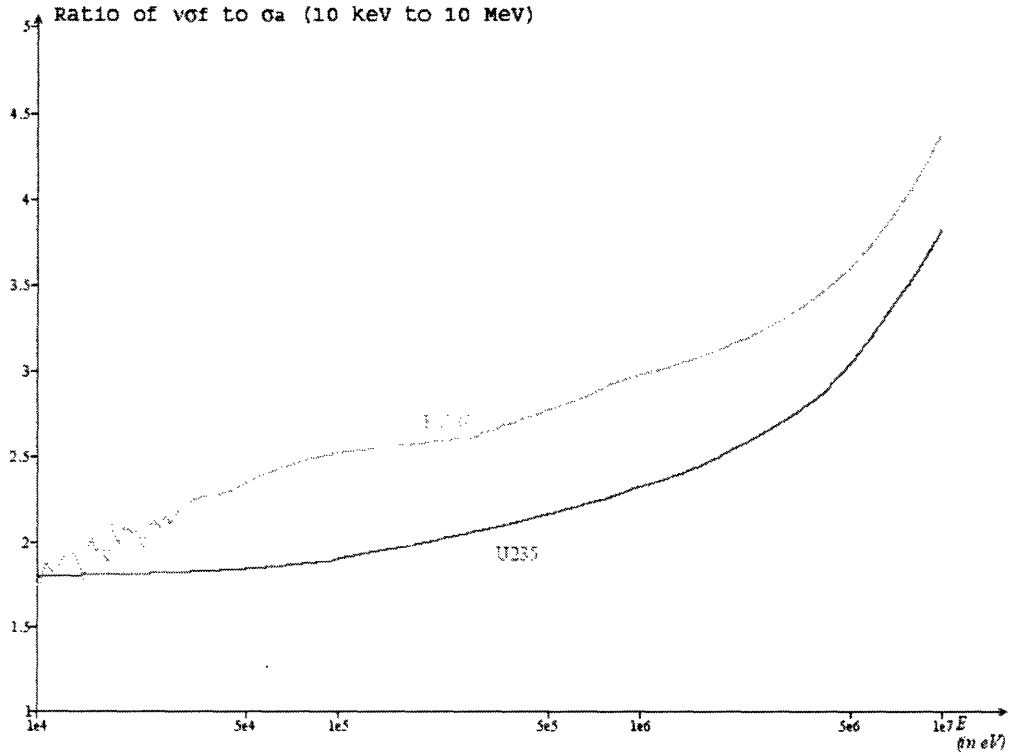


Figure 1.3 The  $^{235}\text{U}$  &  $^{239}\text{Pu}$  Absorption Yields ( $\eta$ ) [36].



Before the  $^{239}\text{Pu}$  fissions it is bred into the fuel by neutron capture in  $^{238}\text{U}$ . However, the GFR neutron spectrum is exceptionally hard, and thus a significant portion of the flux is above 0.1 MeV. Figure 1.4 shows a plot of the  $^{238}\text{U}$  fission cross section between 10 keV and 10 MeV. While threshold fission is of little concern in LWRs it is critically important in the operation of a B&B GFR, especially when one considers metrics used to indicate neutronic performance.

The conversion ratio is basically a measure of the production of  $^{239}\text{Pu}$  in the fuel during irradiation. The conversion ratio is simply the ratio of the production rate of fissile material divided by the destruction rate of fissile material. An approximate representation for the conversion ratio is expressed symbolically in Equation (1.1). The expression does not consider potential transmutation of the intermediate nuclides during decay from the excited nucleus to the fissile daughter.

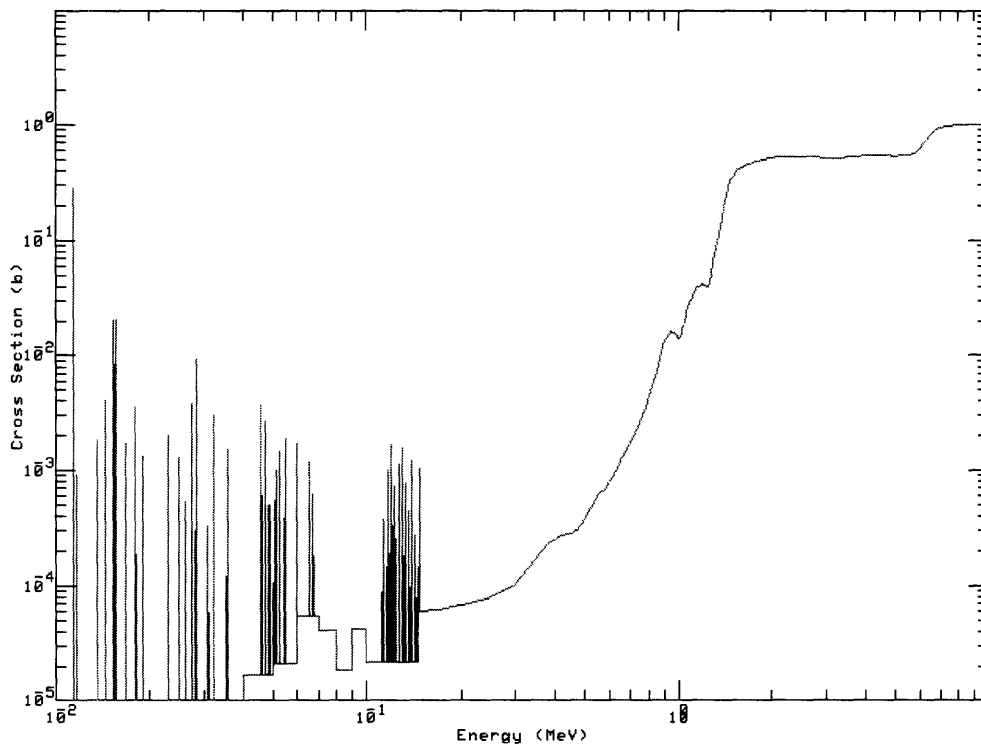


Figure 1.4 The  $^{238}\text{U}$  Microscopic Fission Cross Section [46].

$$CR \approx \frac{\sum_e \Sigma_\gamma^e}{\sum_i \Sigma_a^i} \tag{1.1}$$

Where CR is the conversion ratio,  
 $\Sigma$  is the macroscopic cross section,  
e denotes fertile,  
i denotes fissile,  
 $\gamma$  denotes capture, and  
a denotes absorption (capture and fission).

Here, the cross sections are spectrum averaged. The summation over “e” is over all fertile nuclides. At BOC the only fertile nuclide is  $^{238}\text{U}$ , but with burnup  $^{240}\text{Pu}$  and other nuclides become an increasingly important component of the fissile production rate. The summation over “i” is over all fissile nuclides. In the hard GFR spectrum, fertile fission is significant, and can account for as much as 20% of fissions.

However, the conversion ratio for the B&B GFR is an inadequate metric for evaluating the neutron economy. There is a trade off between conversion ratio and the neutron absorption yield in  $^{239}\text{Pu}$ . Let us take an example reactor where all of the neutrons are above 0.1 MeV. To maintain the same reactivity in a very hard neutron spectrum core less  $^{239}\text{Pu}$  would be required than  $^{235}\text{U}$  because of the higher fission to absorption ratio and prompt yield, therefore with conversion ratios less than unity the reactivity may be constant or even increasing during irradiation as  $^{235}\text{U}$  is being burnt and  $^{239}\text{Pu}$  bred. Secondly, there will be a substantial component of the fission rate coming from direct  $^{238}\text{U}$  fission.

If  $^{239}\text{Pu}$  undergoes fission it would, over time, require two neutrons. The first neutron converts the  $^{238}\text{U}$  to  $^{239}\text{Pu}$  and the second induces fission. Therefore, while the prompt yield from  $^{238}\text{U}$  fission may be somewhat lower than that for  $^{239}\text{Pu}$  it is beneficial from a long-term neutron economic standpoint to design a reactor that makes fullest use of  $^{238}\text{U}$  direct fission.

In the example reactor discussed above there will be a large contribution to the instantaneous reactivity from direct  $^{238}\text{U}$  fission, however, a softer spectrum reactor would have a larger portion of the flux below the  $^{238}\text{U}$  fission threshold and thus a higher  $^{238}\text{U}$  capture cross section. The larger capture cross section in a softer spectrum would thus yield a higher conversion ratio. However, the reactivity would be lower (because there is a smaller contribution from  $^{238}\text{U}$ ) and more  $^{239}\text{Pu}$  would be needed to sustain criticality as the  $^{239}\text{Pu}$  neutron absorption yield increases with energy. Therefore, the B&B GFR strives for a very hard neutron flux; this is somewhat contrary to earlier approaches that would use limited addition of moderator to improve conversion ratio [3].

In general, as the neutron spectrum becomes harder the neutron economy improves because it will require fewer neutrons to induce eventual fissions and reactivity is supplemented by fertile fission. Therefore a new metric for assessing the neutron economic potential for the reactor must be used. Establishing this metric will prove very useful later when evaluating control schemes for the reactor. Any approach for developing this metric must examine more than the ratio of two instantaneous rates such that the long-term potential of the reactor to sustain criticality, i.e. breed in more reactivity, can be captured in a single quantity.

All fission neutrons are eventually lost, but they are lost in both productive and unproductive mechanisms. The productive mechanisms would lead to either fission (ideally) or fissile production. The unproductive mechanisms would include leakage or absorption in non-fertile species. It costs one neutron to fission  $^{238}\text{U}$  directly, and two neutrons to fission  $^{239}\text{Pu}$  in the B&B reactor. Here a metric of neutron economy (Y) is derived such that it will give a measure of a reactor’s capability to breed reactivity using spectrum averaged quantities.

Imagine that the cost of fission in the current generation is borne entirely by the fission neutrons in the current generation. If that is the case, then the long-term ability of the reactor to breed reactivity will be related to the excess of fission neutrons available for breeding, as well as the worth of the bred material (namely  $^{239}\text{Pu}$ ). The inverse of Y is the fraction of fission neutrons that must be dedicated to inducing fission to produce the next generation. Therefore, Y becomes a

measure of the neutrons that are available for breeding new fissile material, and thus a measure of the potential for the reactor to breed additional reactivity.

The metric of neutron economy (Y) is shown symbolically as follows in Equation (1.2). It is approximated for the current purpose. The major approximations are that the primary species of interest are  $^{238}\text{U}$  and  $^{239}\text{Pu}$ , the yield from fertile capture to fissile production is unity, and both  $^{238}\text{U}$  and  $^{239}\text{Pu}$  have approximately the same prompt neutron yield.

$$\frac{1}{Y} \equiv \left( \frac{\sigma_f^{28}}{\sigma_a^{28}} + 2 \frac{\sigma_\gamma^{28}}{\sigma_a^{28}} \frac{1}{y(29,49)} \frac{\sigma_a^{49}}{\sigma_f^{49}} \right) \frac{\Sigma_a^{28}}{\Sigma_L} \approx \left( \frac{\sigma_f^{28}}{\sigma_a^{28}} + 2 \frac{\sigma_\gamma^{28}}{\sigma_a^{28}} \frac{\sigma_a^{49}}{\sigma_f^{49}} \right) \frac{\Sigma_a^{28}}{\frac{\bar{\nu}}{k} (\Sigma_f^{28} + \Sigma_f^{49})}$$

$$\frac{1}{Y} \approx \frac{k}{\bar{\nu}} \left( \frac{\sigma_f^{28} + 2 \sigma_\gamma^{28} \frac{\sigma_a^{49}}{\sigma_f^{49}}}{X \sigma_f^{49} + \sigma_f^{28}} \right) \quad (1.2)$$

Where Y is the proposed metric,  
 $\sigma$  is the microscopic cross section,  
k is the multiplication factor,  
 $\bar{\nu}$  is the average prompt neutron yield,  
X is the ratio of the number density of  $^{239}\text{Pu}$  to the number density of  $^{238}\text{U}$ ,  
49 denotes  $^{239}\text{Pu}$ ,  
28 denotes  $^{238}\text{U}$ ,  
29 denotes  $^{239}\text{U}$ ,  
 $y(29,49)$  is the probability that  $^{239}\text{U}$  will become  $^{239}\text{Pu}$ ,  
f denotes fission,  
L denotes loss.

The total loss rate is characterized above by a neutron loss cross section. It is the same as approximating a leakage cross section using buckling and adding that to the absorption cross section; however, the multiplication factor is the ratio of the production to loss, and the loss rate is represented using these quantities instead.

The inverse of Y is shown in Equation (1.2) to more clearly illustrate the physical meaning. Y takes into account several of the phenomena discussed above, namely that fertile fission must be taken into account, first because it is a significant fraction of the total fission rate, and secondly it takes fewer neutrons to induce direct fission than to breed and then fission  $^{239}\text{Pu}$ . While not being fully time-integral, the approach here attempts to take into account the past behavior of the fuel during irradiation by lumping the history of the fuel into an instantaneous rate.

The factor of two on the  $^{239}\text{Pu}$  cross section is meant to take this into account, and thus bring to light in some approximate sense the effectiveness of the reactor in utilizing neutrons over time. Additionally, spectral effects are accounted for in the  $^{239}\text{Pu}$  as the absorption to fission ratio is present. This factor takes into account that some neutrons absorbed in  $^{239}\text{Pu}$  do not induce fission, and as this ratio increases the cost to induce fission in  $^{239}\text{Pu}$  is higher.

It can be shown that Y is related to a reactor's ability to breed reactivity. Imagine that a reactor is modeled without control rods. In the uncontrolled reactor, the reactivity would increase with

irradiation time as additional  $^{239}\text{Pu}$  is bred. It would continue to increase until reaching an asymptotic trend where the conversion ratio becomes unity. Fissile buildup has been studied for blankets in fast reactors and similar trends have been observed for several systems [57]. The maximum fissile inventory achievable, which is directly related to the asymptotic reactivity after long irradiation times, is directly related to the spectrum averaged cross sections, particularly those used in the expression for Y. Equation (1.3) shows that Y can be rewritten in terms of spectral indices as follows. The capture to fission ratio for a very hard spectrum reactor will be somewhat small for  $^{239}\text{Pu}$  and is neglected in the denominator in the following approximation.

$$\begin{aligned} \frac{1}{Y} &\approx \frac{k}{\bar{\nu}} \left( \frac{\sigma_f^{28} + 2\sigma_\gamma^{28} \frac{\sigma_a^{49}}{\sigma_f^{49}}}{X\sigma_f^{49} + \sigma_f^{28}} \right) = k \left( \frac{\frac{\Sigma_f^{28}}{\Sigma_a^{49}} + 2 \frac{\Sigma_\gamma^{28}}{\Sigma_a^{49}} \frac{1}{(1+\alpha^{49})}}{\eta^{49} (1+\delta)} \right) \\ \frac{1}{Y} &\approx k \left( \frac{\frac{\delta}{1+\alpha^{49}} + \frac{2}{(1+\alpha^{49})}}{\eta^{49} (1+\delta)} \right) \approx k \left( \frac{2 + \frac{\delta}{(1+\alpha^{49})}}{\eta^{49} (1+\delta)} \right) \end{aligned} \quad (1.3)$$

Where  $\alpha$  is the capture to fission ratio,  
 $\eta$  is the absorption yield, and  
 $\delta$  is the fertile to fissile fission ratio.

When the conversion ratio is unity, one can write an expression for the peak asymptotic reactivity. If all species besides  $^{238}\text{U}$  and  $^{239}\text{Pu}$  are neglected and spectrum averaged cross sections are assumed constant during irradiation, then Equation (1.4) shows that Y is related to the peak asymptotic reactivity, further reinforcing its usefulness as a metric to show the capability of a reactor to breed reactivity. It also illustrates the relationship between these two values: as the achievable reactivity (or peak asymptotic reactivity) increases so does Y. Yet, while Equation (1.4) is simpler than Equation (1.2), one cannot know the peak asymptotic reactivity a priori, and therefore, it is easier to calculate Y based on the instantaneous spectrum averaged cross sections using Equation (1.2).

$$\begin{aligned} \rho_{asy} &= 1 - \frac{\Sigma_a}{\nu\Sigma_f} = 1 - \frac{2 + \frac{\delta}{(1+\alpha^{49})}}{\eta^{49} (1+\delta)} \\ \therefore \frac{1}{Y} &\approx k(1 - \rho_{asy}) \\ Y &\approx \frac{1}{k(1 - \rho_{asy})} \end{aligned} \quad (1.4)$$

By using Y instead of CR it will be clear why a harder neutron spectrum is preferred during operation of the reactor at all stages of burnup. The  $^{235}\text{U}$  is left out of the metric, namely because

it will not dictate the long-term physics behavior of the fuel. Since the enrichment at the BOC is only 5% and the fuel reaches atomic burnup on the order of 15%, the long-term, high burnup trends in reactivity will be dictated purely by the  $^{238}\text{U}$  content and the spectrum. Also, while changing the enrichment from 5% to 10% may represent a 100% change in the  $^{235}\text{U}$  content, it is only ~5% change in the  $^{238}\text{U}$  content; in essence, the long-term trend in fuel reactivity will be nearly completely independent of the initial enrichment. Figure 1.5 illustrates the asymptotic behavior using a simple unit cell fuel pin model (which is in agreement with the general trends displayed in reference [57]); thus motivating the investigation of natural uranium fueled B&B concepts. Yet, it is the long-term trends the metric is aimed at assessing, while the integral of the reactivity is what determines the limitations on discharge burnup, and thus fuel residency.

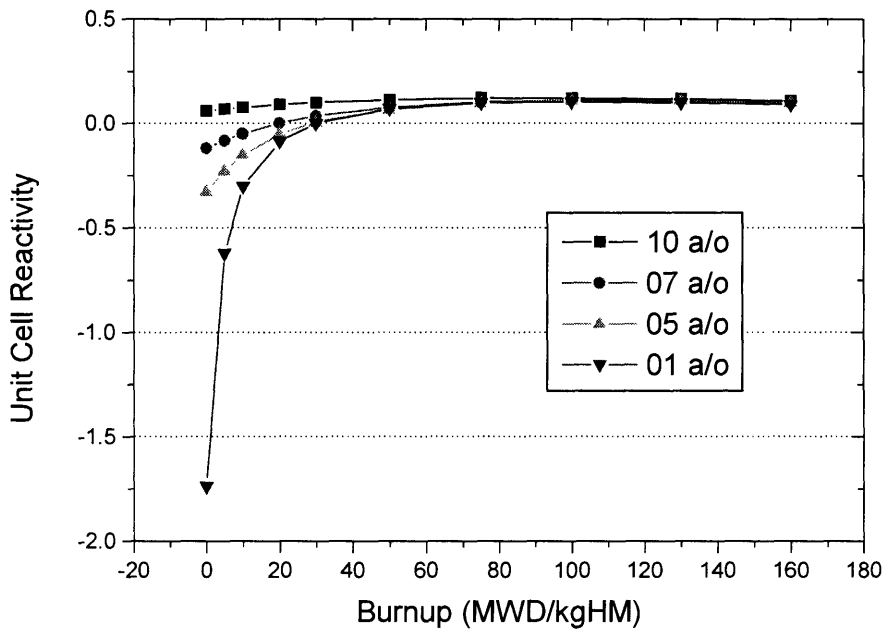


Figure 1.5 Reactivity Histories for a UC Pin Cell Using Different BOC Enrichments<sup>1</sup>

The benefit to using LEU for reload fuel is that the reactivity integrated over burnup will be higher and thus the reactivity limited burnup is reduced. Unlike a LWR the reactivity limited burnup for the B&B GFR is a minimum burnup that the fuel must attain in order to sustain criticality through subsequent cycles. This is implicit to the B&B cycle because the partially burnt and discharge assemblies have excess reactivity while the fresh assemblies require reactivity sharing in order to breed sufficient plutonium. Therefore, choosing LEU fuel for reload instead of natural uranium will reduce the reactivity limited burnup and fuel residency time to reasonable levels suitable for a practical reactor design.

On the same note, the nature of the cycle presents a challenge when designing a control scheme. The discharged assemblies during operation have much higher fissile content than fresh

<sup>1</sup> Figure 1.5 only shows results for UC cases, Chapter 3 will describe the impacts of other factors, particularly fuel density, on the reactivity histories more fully.

assemblies, and therefore, the partially burnt assemblies must breed in enough plutonium during a given cycle to overcome the difference in reactivity between the discharged (high plutonium content) and fresh assemblies (negative reactivity, LEU). Thus the reactivity swing for a cycle will be necessarily large and positive (the opposite of thermal spectrum converter reactors such as LWRs).

For initial studies comparing core materials, it will be sufficient to use the asymptotic reactivity (which is a direct result of calculations), however, when direct calculations are prohibitive as in the case for critical burnup given limited resources,  $\lambda$  becomes increasingly useful. Schemes that control the buildup of reactivity over the cycle must be sensitive to how the control devices impact the future neutron economy and this is a prime example of a case where  $\lambda$  is a useful metric.

## **1.4. Organization**

This thesis is organized into three sections, each containing several chapters. The first section covers the methodology and the simple models used to make initial design decisions regarding core materials. Chapter 2 covers the codes and methods used to calculate neutronic and thermal hydraulic characteristics. Chapter 3 shows how the methods, once applied to simplified models allow for the selection of candidates for core materials. The second section begins with a brief overview of a demonstration B&B GFR core concept in Chapter 4. The demonstration core is in many ways easier to design and construct, however, at a penalty to the fuel cycle economics. Chapter 5 covers the neutronics of the demonstration core, Chapter 6 the thermal hydraulic analysis, and finally Chapter 7 describes the fuel cycle economics. Chapter 8 begins the third section of the thesis by describing the advanced core. The advanced core, while requiring an additional stretch from current design practices will improve the economics of the fuel cycle given some technology development. Chapter 9 deals with the neutronics of the advanced core, Chapter 10 the thermal hydraulics, and lastly Chapter 11 covers the economics. Final conclusions about the B&B GFR are made in Chapter 12 and recommendations for further investigation are made in Chapter 13.

## Chapter 2. Methodology

### 2.1. Introduction

This chapter describes the methods used during the course of this project to evaluate the performance of various core concepts. The nature of the calculations can be broken into three categories, the first of which is neutronics. The second category is the assessment of the thermal hydraulic performance of the core, and the last category deals with the fuel cycle economics. In many cases the methodologies, when applicable, were compared with other calculations or experiments to lend credence to the results.

### 2.2. Neutronics

#### 2.2.1. MCNP

MCNP stands for Monte Carlo N-Particle Code. The code is a general purpose transport code developed at Los Alamos National Laboratory and is useful in calculating not only neutron transport problems, but is capable of coupled neutron, photon, and electron problems. The code uses interaction data, such as neutron cross sections from ENDF. The code simulates particle trajectories through a model geometry and is capable of predicting eigenvalues for reactor systems and performing “tallies” in order to perform spectrum averaging of cross sections, calculate power shapes, and calculate neutron spectra [40].

MCNP is a Monte Carlo type code, which means that random numbers are used to simulate the trajectory, or history, of many individual particles. Therefore, while the results are subject to errors introduced by the cross section evaluations themselves, there is additional statistical uncertainty arising from the method itself. However, with the MIT Echelon Beowulf computing cluster, several computers are run in parallel to complete MCNP calculations, thus reducing the real-time necessary to perform sufficient trajectory calculations for a given error tolerance.

Several types of MCNP models are used to conduct analyses in the current project. Simplified studies are done using unit cell (or pin cell) models. These types of models reflect single fuel pins with radially reflective boundary conditions, hence effectively modeling an infinite array of fuel pins of one type. These types of models are excellent for predicting some neutronic parameters as well as for comparison studies when general trends are of particular interest. Pin cell models are sometimes modeled with both radially and axially reflective boundary conditions; this would in effect, model an infinite array of infinitely long, identical fuel elements. These types of models are particularly useful for calculating cladding fluence, or comparing calculations that require many neutron histories, such as calculations of the Doppler coefficient. Another set of pin cell models were used; these models retained the radially reflective boundary conditions, but allowed neutron leakage axially; these models are particularly useful for investigating axial power shapes and axial reflector comparisons.

Aside from pin cell models, infinite assembly calculations were also done. An infinite assembly is much like a pin cell model in that the radial, and perhaps axial, boundary conditions are reflective, except that instead of representing an infinite array of fuel pins, the model represents an infinite array of fuel assemblies.

Lastly, full core models were created. These are the most complex and truest to life models. They represent, as fully as possible, the heterogeneity of a reactor core with axial and radial

leakage. While called a full core model, several do contain reflecting boundary conditions where symmetry is present. Since the statistical uncertainty associated with an MCNP model is related to the number of histories traveling through the model geometry, it is advantageous to model as little volume as possible and make the fullest use of symmetry in the modeling.

Our MCNP modeling approach was tested using information published on a fast critical assembly experiment to validate the code as well as the cross sections used for physics calculations, as discussed in greater detail in section 2.2.1.1.

In the full core models, aside from limitations imposed by the computer runtime necessary to run enough neutron histories for acceptable statistical error, there are limitations imposed by the available computer memory. The full core models used in the current work are approximate in several senses because there is insufficient memory on the current computers to carry out very high fidelity calculations. The fuel assemblies in the models are created using a repeating lattice method, as are the fuel batches comprised of these assemblies. Thus, the fuel in any batch is represented by a single materials card. It would be impossible to define in the model each and every fuel pin distinctly. Yet, while for a startup core there is high confidence in the MCNP results using the repeating lattice approach; during depletion analyses, the composition of the fuel is smeared throughout the entire batch.

Aside from employing a repeating lattice approach in the core geometry, there is not enough memory on the Echelon Beowulf computing cluster nodes to store enough geometry specification for full core models to allow for separate axial nodes in the fuel, and the radial reflector is modeled without heterogeneous coolant channels. Where possible simpler models, such as pin cell or infinite assembly models are used to quantify inaccuracies that arise from these methods. As these approximations are most relevant for burnup calculations, the assessment of the errors introduced as a result of these limitations are discussed at further length in sections 2.2.4.3 and 2.2.4.4.

#### 2.2.1.1. **ZPR-9 Benchmark**

MCNP4c along with Evaluated Nuclear Data Files (ENDF) versions B5, B6, and B6vII cross sections were used for the neutronic calculations of the B&B GFR.<sup>2</sup> The code and data were evaluated by performing a benchmark calculation against one of the ZPR-9 Gas-cooled Fast Reactor critical assemblies. The 28<sup>th</sup>, 29<sup>th</sup>, and 30<sup>th</sup> assemblies of ZPR-9 were built to support the evaluation and design of Gas-cooled Fast Reactors [37]. The critical assembly modeled was constructed between June 1975 and September of 1976. To perform the benchmark, a series of MCNP calculations were performed using a model constructed of the phase III critical assembly (the 30<sup>th</sup> ZPR-9 assembly). Both homogenous and heterogeneous reactor models were developed using specifications in Argonne National Laboratory reports on the ZPR-9 experiment [44].

##### 2.2.1.1.1. *Homogenous Model*

A homogenous approximation to the ZPR 9 GCFR Phase III experiment was created for MCNP4c2. The assembly is modeled with quarter-assembly symmetry, that is, only one fourth of the assembly was input in the model and reflecting boundary conditions were specified for the x-z and y-z planes. The cell-averaged homogenous number densities were calculated by ANL and used directly in the model [44]. Appendix A contains the MCNP deck used for the homogenous assembly calculations. The fast critical assembly (FCA) geometry is depicted in Figure 2.1.

---

<sup>2</sup> ENDFB6vII cross sections were used when available, and in cases where not available were replaced with ENDFB6; if those were not available then ENDF5 was used. All nuclides of interest were available among these sets with ENDFB6 representing most of the nuclides.



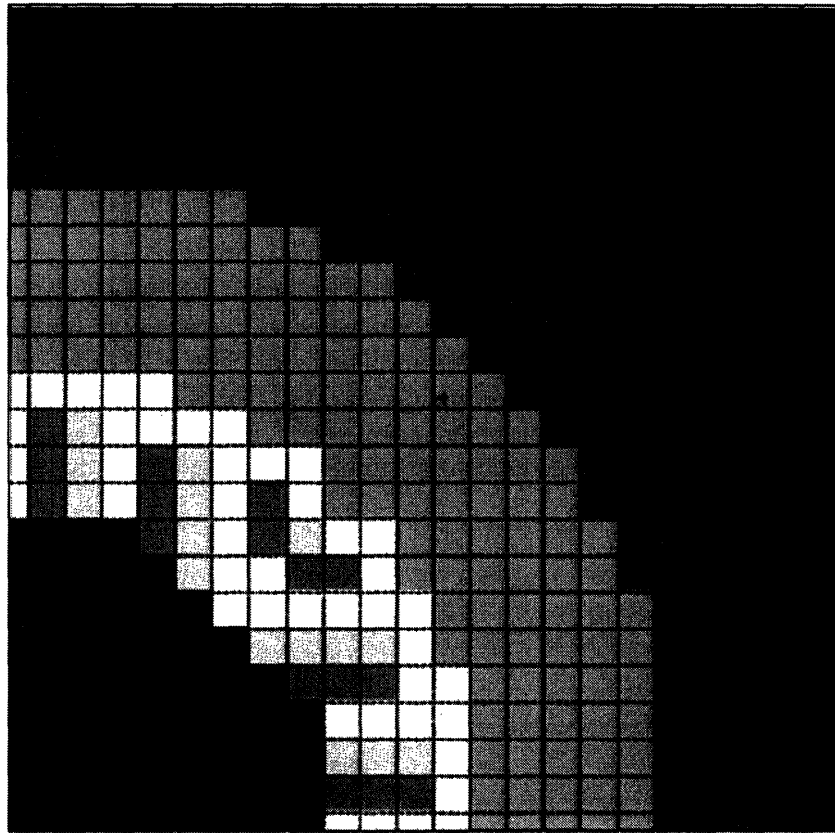


Figure 2.1 FCA Homogenous Model Geometry

The assembly is divided into three zones. The amount of plutonium in each zone is adjusted such that the equivalent enrichment of the fuel in zones 1, 2, and 3 is 13.1%, 17.3%, and 25.5% respectively. The equivalent enrichment is merely the ratio of fissile plutonium to total heavy metal in each zone. Each zone has a separate axial blanket, and the assembly is reflected by stainless steel blocks. Each zone is comprised of stacks of plates in drawers. Each drawer is approximately 5 cm x 5 cm and the total assembly height, including axial reflectors is approximately 214 cm.

While the homogenous model does not include reactivity effects from neutron streaming or heterogeneous self shielding, it is used to roughly determine the ability of MCNP4c to predict the multiplication factor as well as plot a flux spectrum to determine if the FCA results are applicable to a B&B GFR flux spectrum. The neutron streaming in the radial direction is purposefully “interrupted.” In the FCA; samples are arranged in the various regions to avert “line of sight” streaming paths between the zones, thus reducing radial neutron streaming. Axial neutron streaming is still present, but the upper and lower axial reflectors are solid, thus improving the axial neutron reflection relative to power producing cores where coolant channels would most likely be present.

For the purposes of the benchmark, the model was run on both the Echelon Beowulf computing cluster as well as the MightyAlpha computer at MIT. MCNP4c2 was used on both computers. Only one computer (node 13) of the 30 parallel computers of the Echelon cluster was used. The

result for the MightyAlpha calculation was 0.9698 with a standard deviation of 0.0003. For node 13, the eigenvalue was calculated to be 0.9694 with a standard deviation of 0.0004.

While these quantities are lower than unity, it is expected that the underestimated self-shielding of the fuel would contribute to an under-predicted reactivity value. While the homogenization eliminates direct streaming paths (and would increase reactivity), the FCA was designed to reduce radial streaming, and therefore it is likely that the reduction in reactivity arising from loss of self-shielding due to homogenization would be greater than the increase in reactivity arising from the reduction in axial neutron streaming.

Figure 2.2 shows the neutron flux spectra for the fuel elements. The flux spectrum is of interest in establishing if MCNP4c results are applicable for fast spectrum reactors. There are five types of fuel elements in the FCA; the first (inner) and third (outer) radial assembly regions are each comprised of one distinct type of fuel cell for that region. The second (middle) radial region, however, is comprised of three distinct types of fuel cells.<sup>3</sup> While there are subtle differences, each of the regions experiences essentially the same neutron spectrum as predicted by the homogenous MCNP model.

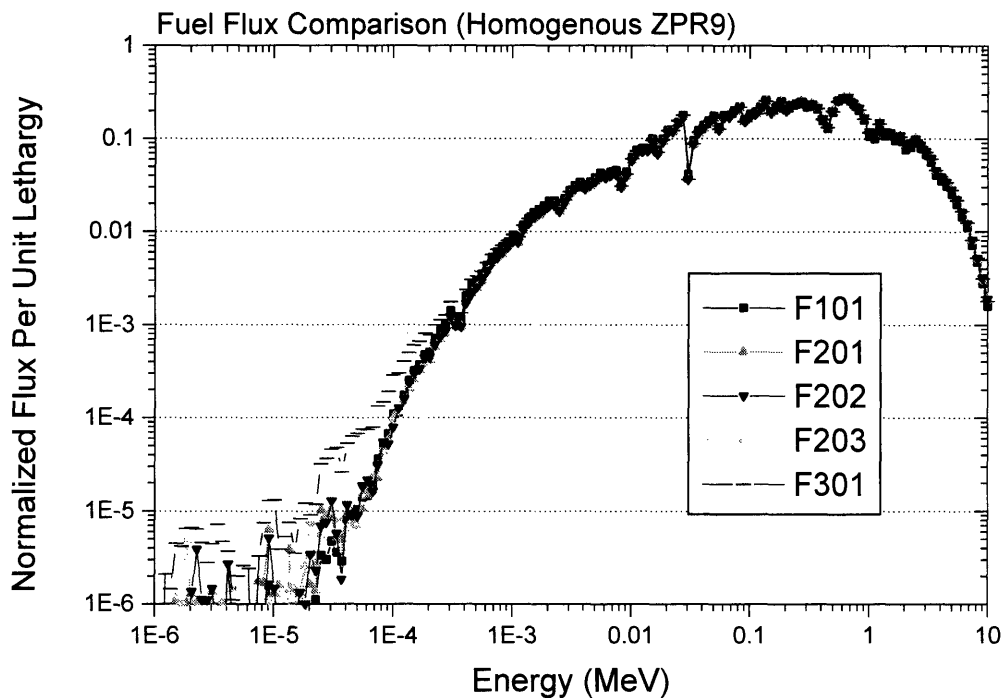


Figure 2.2 Neutron Spectra for Fuel Elements

<sup>3</sup> Tally F101 refers to the flux spectrum in the first zone of the first fuel type. F201 refers to the flux spectrum in the second zone of the first fuel type, and F202 to the second zone of the second fuel type, and so on.

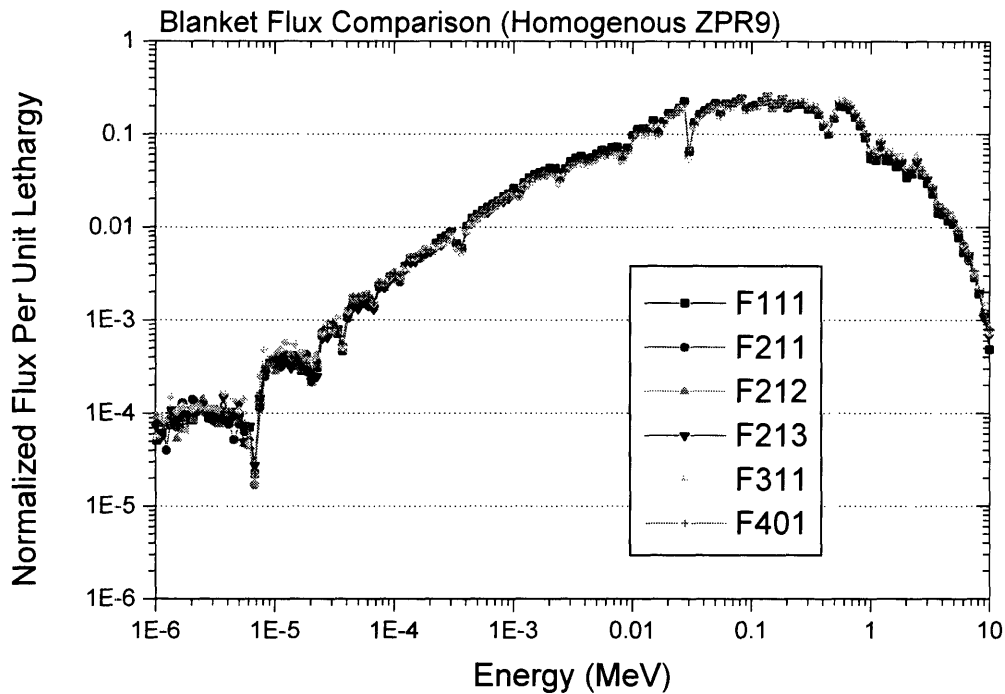


Figure 2.3 Neutron Spectra for the Axial and Radial Blankets

Figure 2.3 shows the neutron spectra in the axial and radial blankets. Again, there are only subtle differences in the spectra among the different radial zones. There are six tallies here because there are distinctive blanket cells for each of the fuel assemblies to preserve axial streaming channels. There is a sixth tally to represent the radial blanket.

Figure 2.4 is a plot of the neutron flux spectra in the radial and axial reflectors.<sup>4</sup> The results are fairly consistent and agree with the neutron spectra in the blanket and fuel cells of the FCA. The purpose of calculating the flux is to show that in hard neutron spectra that MCNP4c is adequate for calculating assembly eigenvalues. As shown in these plots significant portions of the flux resides above 10 keV and the flux peaks near 0.1 MeV, much like the B&B GFR neutron spectrum.<sup>5</sup>

<sup>4</sup> F601 refers to the axial reflector and F501 to the radial reflector.

<sup>5</sup>Figure 2.8 shows a plot of representative B&B GFR neutron flux spectra for comparison.

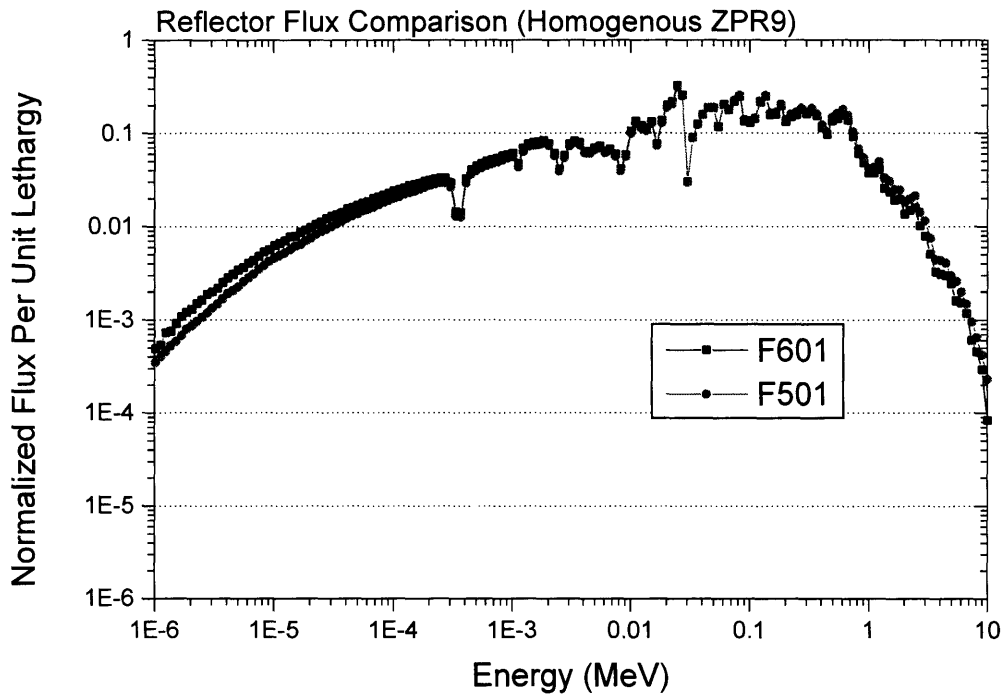


Figure 2.4 Neutron Spectra for the Axial and Radial Reflectors

#### 2.2.1.1.2. *Heterogeneous Model*

A heterogeneous reactor MCNP model, still one quarter symmetric, was built. The material compositions for the samples were taken from the table of hot constants included in [44]. There are several assumptions made to enable the development of this model. The mass of the samples was used to generate the mass densities, and the isotopic compositions were developed based on the relative masses of the isotopes in the sample.

The plutonium was modeled throughout the assembly with a single composition. For each plutonium sample, the plutonium core (meat of the sample) and can (clad of the sample) were smeared together. While this introduces some error because the plutonium isotopics in different zones are slightly different, the divergence from the average composition is very small in all cases. Additionally, the hot constants table was somewhat inaccurate in that significant quantities of  $^{241}\text{Pu}$  had decayed to  $^{241}\text{Am}$  between when the material compositions were measured and the time of the actual experiment. The  $^{241}\text{Pu}$  and  $^{241}\text{Am}$  content of the plutonium elements was adjusted to reflect an equivalent enrichment of 25.5% in the third zone.

An intermediate model was created that took into account the heterogeneity of the small sample plates in the drawers without including the stainless steel in the matrix and drawers. The results showed that the model predicted a slightly higher than unity assembly eigenvalue. Based on the results of the preliminary analysis, additional model complexity was required to include the significant neutronic impact of the matrix and drawers.

Figure 2.5 shows the heterogeneous, one-quarter symmetric model geometry, which clearly illustrates the high degree of heterogeneity of the samples in the drawers. The matrix tubes and

drawers are also explicitly included, however, these are modeled with a single stainless steel region surrounding every 5 cm x 5 cm drawer location in the model. While the actual matrix and drawers include some void, the size of the matrix/drawer region in the current model is adjusted so that the mass of stainless steel in each cell is the same as the experiment, while the dimensions are reduced for the given density of the uniform stainless steel material. This approximation slightly increases the size of the small sample plates in the drawers; however, the density is reduced such that the mass is also consistent.

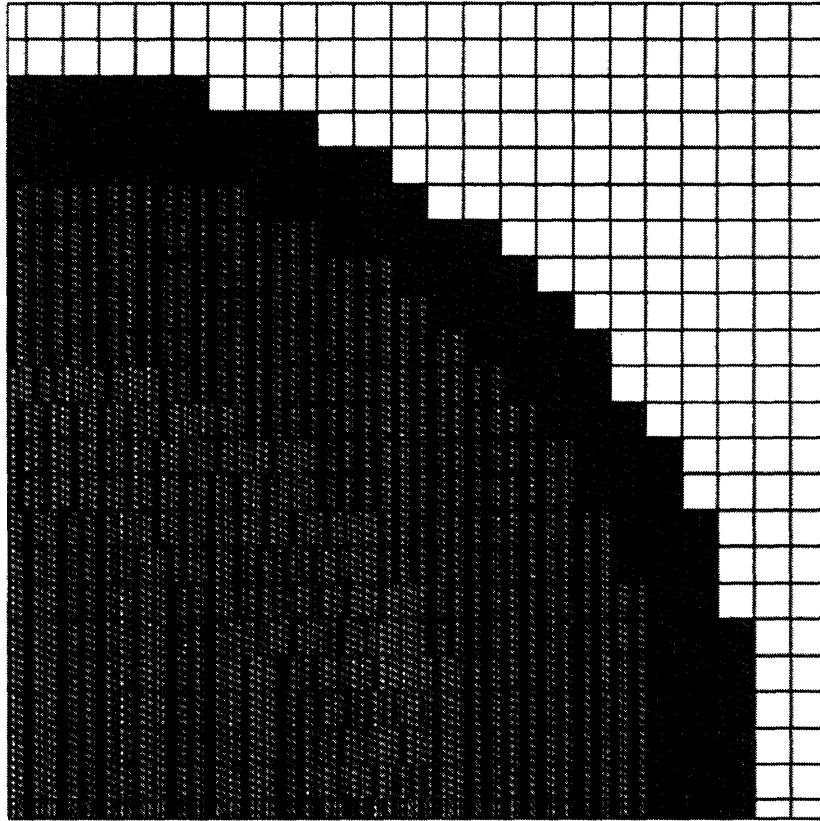


Figure 2.5 Heterogeneous One Quarter Symmetric Model Geometry

Figure 2.6 is a picture of a horizontal cross section of a matrix/drawer cell in the first (inner) zone of the FCA. The MCNP4c input (used in both MCNP4c2 and MCNP4c3) is shown in Appendix B.

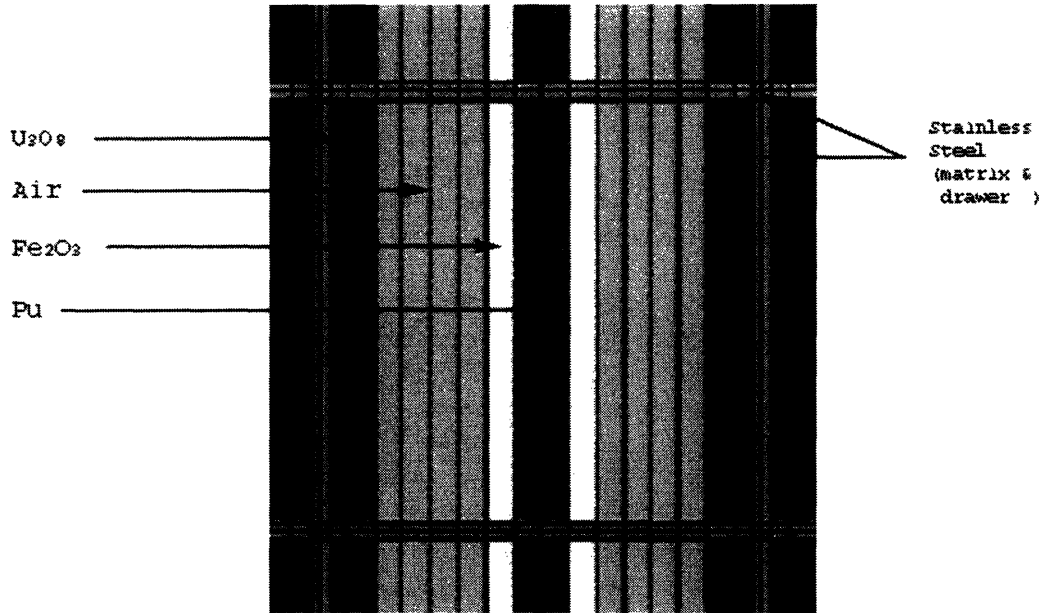


Figure 2.6 Central (first) Zone Matrix/Drawer Diagram

Calculation of the assembly effective eigenvalue clearly indicates that the errors associated with these approximations are very small. The model was run using MCNP4c3 on node 13 of the Echelon Beowulf cluster and MCNP4c2 on the MightyAlpha computer. The Beowulf result for assembly eigenvalue was 1.0003 with a standard deviation of 0.001 and the MightyAlpha result for assembly eigenvalue was 0.99993 with a standard deviation of 0.001. The results not only indicate that MCNP can accurately model fast spectrum systems using ENDFB6 cross section libraries, but that MCNP4c2 and MCNP4c3 yield consistent results across different computing platforms.

#### 2.2.1.2. Cross Section Comparison and Doppler Coefficient

As a basis for comparison between different cross section libraries, the Doppler reactivity coefficient was evaluated for a representative full core MCNP model of the end of cycle GFR equilibrium configuration without control devices (described in Chapter 5 and Appendix E). The calculation was carried out using pre-broadened libraries for the actinides. A complete set of ENDFB6 libraries for the actinides at temperatures of 900 K and 300 K were used to evaluate the reactivity difference. A second analysis was carried out with JEF2.2 pre-broadened libraries at temperatures of 1000 K and 300 K to verify the result. A major difference between the two sets is shown in Figure 2.7 for the  $^{238}U$  fission cross section at 300 K.

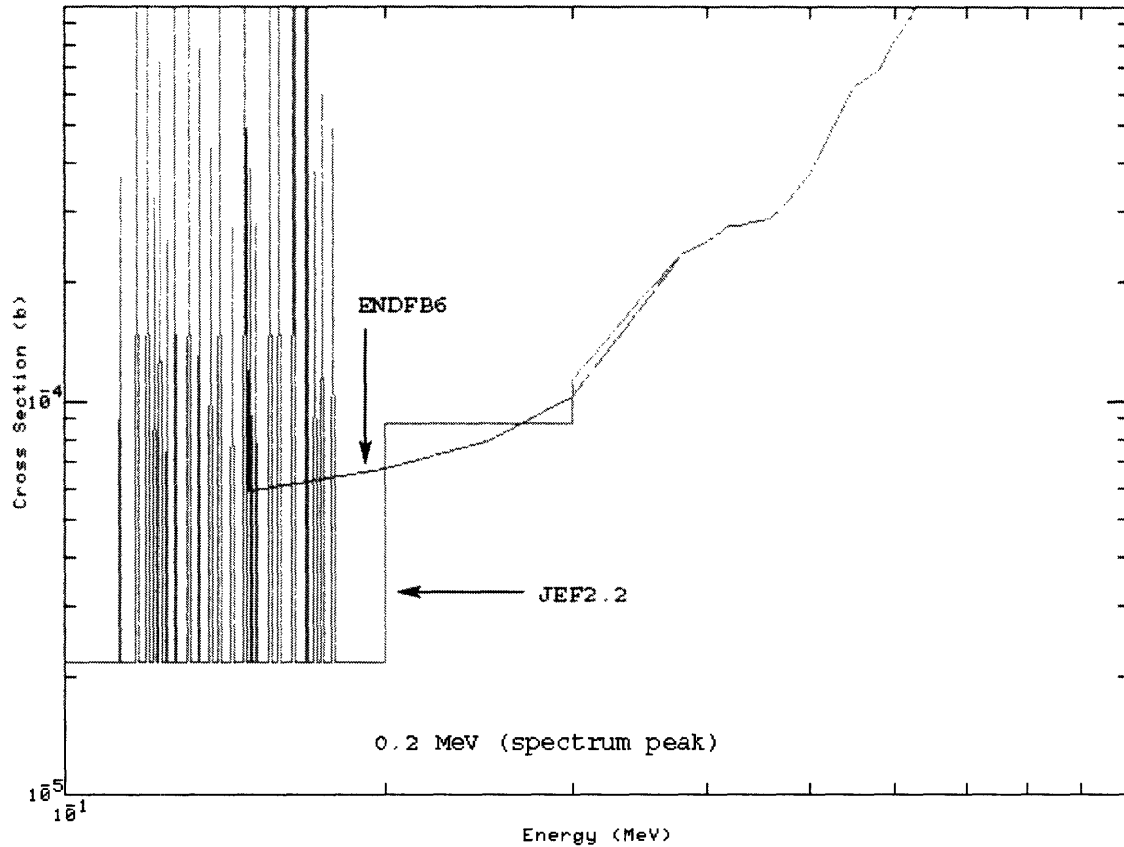


Figure 2.7 ENDFB6 and JEF2.2  $^{238}\text{U}$  Fission Cross Section Comparison

It was found that subtle differences in the  $^{238}\text{U}$  sub-threshold fission cross section led to notable differences in the reactivity at any temperature. The JEF2.2  $^{238}\text{U}$  microscopic fission cross section in the energy range between 150 keV and 200 keV at 300 K is approximately one order of magnitude lower than in the ENDFB6 library. While this may not initially seem like a large discrepancy, the GFR neutron flux spectrum peaks in this energy range. Figure 2.8 is a plot of representative B&B GFR neutron spectra. The plot illustrates that the peak in the neutron flux spectrum is essentially at the transition energy between the resolved resonance regime and the continuum for  $^{238}\text{U}$ , thereby making subtle differences in the cross section representation at these energies important.

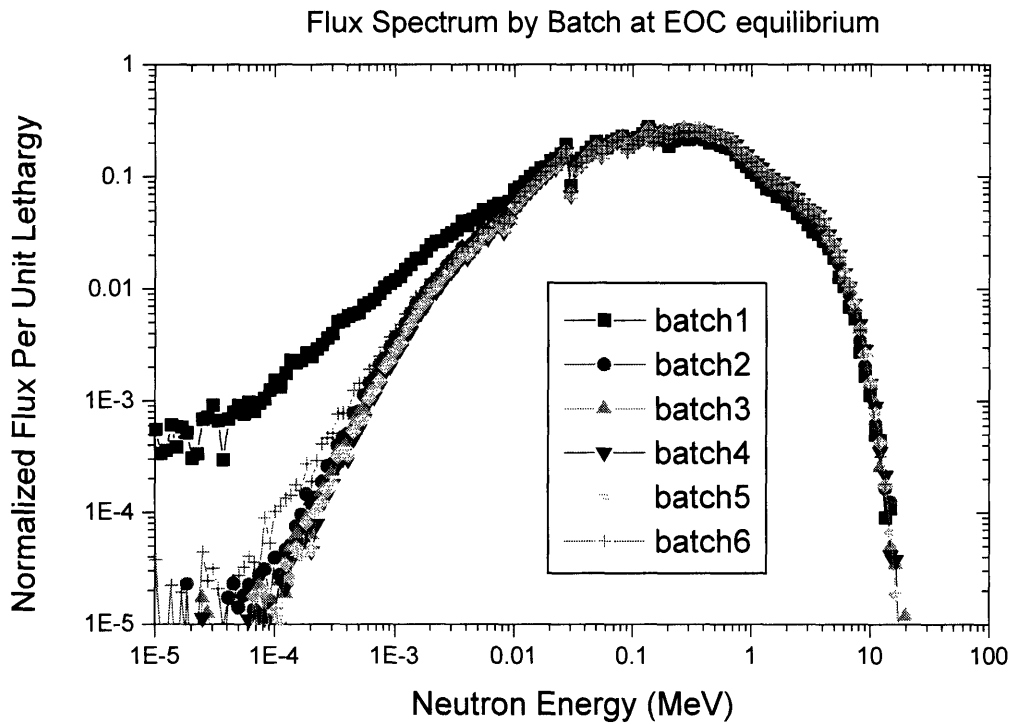


Figure 2.8 Representative Neutron Flux Spectra for B&B GFR Fuel Batches

Table 2-1 summarizes the results for the core eigenvalues calculated for all of the cases, including these four.

Table 2-1 Core Eigenvalues using Prebroadened Cross Section Libraries

Description	keff	std-dev
Full Core EOC equilibrium ENDFB6 libraries T=900K	1.06312	0.00030
Full Core EOC equilibrium ENDFB6 libraries T=300K	1.07034	0.00049
Full Core EOC equilibrium JEF2.2 libraries T=1000K	1.05128	0.00030
Full Core EOC equilibrium JEF2.2 libraries T=300K	1.05407	0.00030
Representative Pin Cell Coarse Case ENDFB6 libraries T=900K	1.00567	0.00183
Representative Pin Cell Coarse Case ENDFB6 libraries T=300K	1.01284	0.00173
Representative Pin Cell Coarse Case JEF2.2 libraries T=1000K	0.99565	0.00127
Representative Pin Cell Coarse Case JEF2.2 libraries T=300K	1.00038	0.0016
Representative Pin Cell Fine Case ENDFB6 libraries T=900K	1.00538	0.00005
Representative Pin Cell Fine Case ENDFB6 libraries T=300K	1.01203	0.00005
Representative Pin Cell Fine Case JEF2.2 libraries T=1000K	0.99336	0.00005
Representative Pin Cell Fine Case JEF2.2 libraries T=300K	1.00113	0.00005

The standard deviation of the eigenvalues is relatively large compared to the difference in the core eigenvalues, but the results seem to indicate that the ENDFB6 libraries yield a larger estimation of the Doppler reactivity coefficient than do the JEF2.2 libraries. To test the libraries a representative pin cell model was created. The purpose for using a representative pin cell is to



reduce statistical uncertainty in the calculations without requiring prohibitively long computer run time.

The pin cell model is an axial and radial reflected model of a single fuel pin. The pin is the same dimension and pitch as those in the B&B GFR. The fuel material is modeled as a homogenous mixture of 50 a/o  $^{15}\text{N}$ , 47 a/o  $^{238}\text{U}$ , and 3 a/o  $^{239}\text{Pu}$ . The infinite cell reactivity was calculated for the pin cell using ENDFB6 libraries at 900 K and 300 K, as well as for JEF2.2 libraries at 1000 K and 300 K. The eigenvalues are shown in Table 2-1. Two cases were examined, a coarse case and a fine case. In the coarse case there were roughly 60,000 active neutron histories per cc of model volume, and roughly 60,000,000 active histories per cc of model volume for the fine case.

The Doppler reactivity coefficient is assumed to have a  $T^{-1/2}$  dependence, and the difference in reactivity between the two temperature points was used to predict the Doppler reactivity coefficient in each case at 900 K as shown in Equation (2.1).

$$\alpha_D(900\text{K}) = \frac{\rho(T_{hot}) - \rho(T_{cold})}{2(\sqrt{T_{hot}} - \sqrt{T_{cold}})} \left( \frac{1}{\sqrt{900\text{K}}} \right) \quad (2.1)$$

Where  $\alpha_D$  is the Doppler coefficient in  $\text{K}^{-1}$ ,  
 T is the temperature in K,  
 Hot refers to the high temperature (900 or 1000 K), and  
 Cold refers to the low temperature (300 K).

Furthermore, the convergence of the Doppler coefficient was observed as the number of neutron histories was increased in the MCNP model (from the coarse case to the fine case). The results of the pin cell model study are shown in Table 2-2. The results indicate that for a small number of neutron histories the JEF2.2 libraries under-predict the Doppler reactivity coefficient. However, as the number of neutron histories is increased the two sets begin to converge.

Table 2-2 Comparison of Core and Pin Cell Models and Doppler Coefficient

	$\alpha_D$ (900K)	std-dev	$\alpha_D$ (900K)
	pem $^{\circ}\text{C}$	pem $^{\circ}\text{C}$	$\epsilon/^{\circ}\text{C}$
Full Core			
ENDFB6	-0.83	0.07	-0.15
JEF2.2	-0.29	0.04	-0.05
Coarse Pin			
ENDFB6	-0.93	0.33	-0.17
JEF2.2	-0.55	0.24	-0.10
Fine Pin			
ENDFB6	-0.86	0.01	-0.16
JEF2.2	-0.91	0.01	-0.17

It is expected, since the JEF2.2 fertile fission cross section is somewhat smaller than that for the ENDFB6 libraries, that the core eigenvalue would be smaller for the JEF2.2 case and that the spectrum would be somewhat softer as well. Since the JEF2.2 spectrum is slightly softer than the spectrum predicted by the ENDFB6 libraries, the Doppler coefficient predicted by the JEF2.2 libraries should be slightly larger (as a larger portion of the flux spectrum is in the resonance

range as opposed to the continuum regime). This is the observed trend, but only after a very large number of neutron histories are run (60,000 active histories in the coarse case and 60,000,000 active histories in the fine case). The results are dependent on the convergence of the spectrum in energy space, which for the JEF2.2 libraries only occurs after many histories due to the step function representation of the  $^{238}\text{U}$  fission cross section.

For comparison JENDL3.3 was also used in the study, however, pre-broadened libraries were not available. NJOY was used to broaden JENDL3.3 libraries for the actinides to 900 K. MCNP4c3 was used to calculate the eigenvalues for the pin cell using 300 K JENDL3.3 libraries (0.99252 standard deviation of 0.00005) and 900 K JENDL3.3 libraries (0.98537 standard deviation of 0.00004). The calculated Doppler coefficient is  $-0.96$  pcm/K, which is in general agreement with the result calculated using the ENDFB6 libraries. Additionally, since ENDFB6 libraries were used for the ZPR-9 benchmark analysis, they are used for all further analysis in the current work.

Furthermore, the constraint on the core geometry due to limited computer memory on the MIT Echelon Beowulf computing cluster nodes leads to one major simplifying approximation, that is, the fuel throughout the core is modeled using cross sections at a single temperature, representing the average temperature for a hot full power condition.

### 2.2.2. Cladding Fluence

Aside from neutronic parameters concerning the fuel and overall core multiplication factor, the effects of neutron irradiation on the cladding and structural material must be considered in a design evaluation. Therefore, methods were used to evaluate several of the irradiation damage mechanisms for the cladding material. MCNP4c models were easily modified to perform tallies of the neutron flux in the cladding for a few energy groups. However, the neutron fluence alone is not enough to evaluate the material damage arising from irradiation. The number of atomic displacements as well as the buildup of inert gases, such as helium, are also critically important for a final assessment.

Both full core and pin cell calculations were used to calculate the neutron flux in the cladding during irradiation. These MCNP4c models merely included a tally for the neutron flux in the cladding cells. As discussed in section 2.2.4.2 pin cell and full core models predict essentially the same neutron flux in the cladding, and therefore, the simpler models are used for the calculations of cladding irradiation effects.

The atomic displacements arising from irradiation in a hard neutron spectrum was assessed using MCNP4c and tabulated data on displacement cross sections. Two models of atomic displacement were used, the first is the Lindhard Model for stainless steel and the second is the Half-Nelson model for Iron, both summarized in [16] in 1975. As noted in the Addendum of the same reference, the cross sections were adjusted by a factor of  $2/3$  in the analyses. The energy dependent displacement cross sections with the noted adjustment are shown in Table 2-3.

Table 2-3 Multi-group Displacement Cross Sections

Group Lower Bound (MeV)	Lindhard (stainless) (barn)	Half-Nelson (iron) (barn)
1.00E+01	2093	955
6.07E+00	1893	955
3.68E+00	1633	955
2.23E+00	1333	827
1.35E+00	913	588
8.21E-01	574	433
4.98E-01	423	385
3.02E-01	353	303
1.83E-01	198	173
1.11E-01	167	132
6.74E-02	137	118
4.09E-02	74	60.6
2.48E-02	123	156
1.50E-02	23.6	6.3
9.12E-02	22.9	12.1
5.53E-03	27.5	24.5
3.36E-03	13.9	7.1
2.03E-03	6.25	4.9
1.23E-03	3.64	0
7.49E-04	4.02	0
4.54E-04	1.45	0
2.75E-04	0.08	0
1.67E-04	0.15	0
1.01E-04	0.19	0

The cross sections were input into the MCNP4c model using the EMN card, which allows the neutron tallies within a certain energy band to be multiplied by a specific factor for each energy band. The results of the tally were totaled and normalized to get the displacement per atom (dpa) for the cladding material. An example MCNP4c input deck using the EMN card is shown in Appendix C.

The helium production was also of interest. An MCNP tally was used to calculate the one-group (n,α) cross section for the cladding. The cross section was then multiplied by the fluence in order to calculate the helium concentration assuming no escape by diffusion.

### 2.2.3. ORIGEN

ORIGEN2.2 is used in the current project for depletion analysis. ORIGEN stands for Oak Ridge Isotope Generation and Depletion Code and was developed at Oak Ridge National Laboratory [70]. ORIGEN is a one-group depletion code that solves the combined radioactive decay and fission production of various nuclides in materials based on the half-lives of those materials, the neutron flux, and the one-group, spectrum-averaged cross sections for the nuclides. It is primarily used for calculating the nuclide compositions of fuel during and post- irradiation.

The code itself is generalized such that properties of the nuclides must be input to the code via several data libraries. The first of these libraries is the radioactive decay library. This library holds all of the data related to the various decay chains for every nuclide as well as information about the half lives for various modes of decay. The second library is the cross section and fission product yield data. This library houses the spectrum-averaged cross sections for all of the nuclides as well as the fission product yield; this information is critically important for calculating the composition during irradiation, particularly because the spectrum-averaged cross sections are unique, not only for each core concept, but also depend on location within a particular core. Lastly, ORIGEN must be supplied with a photon library. The photon library tells ORIGEN the number of photons released per decay in an 18-energy group structure. ORIGEN uses these data to calculate the photon energy emission rate, and thereby calculate the largest contributor to photon dose (for instance) [70].

In the current work, a great deal of attention is paid particularly to the second library (cross section and fission yield data). As noted above MCNP has the capability to calculate spectrum-averaged cross sections, however, the computing power necessary to calculate the cross-sections for each and every isotope with an acceptable statistical uncertainty would be prohibitive.

ORIGEN is packaged with a variety of libraries that were created based on experience with a variety of reactors. In the present work, in cases where MCNP is not used to explicitly calculate one-group cross sections for nuclides, the data are imported from a library developed for the Fast Flux Test Facility (FFTF).

#### 2.2.4. **MCODE**

MCODE was developed at MIT by Dr. Zhiwen Xu, and stands for MCNP-ORIGEN Depletion Program. MCODE is a linkage program written in C that couples MCNP and ORIGEN. The purpose of the code is to do depletion calculations for arbitrary core models. The code works by conducting a static MCNP calculation. The result of that calculation yields core eigenvalue, spectrum averaged cross sections, and region averaged fluxes. Based on user input (such as power density) the material composition, one group cross sections, and neutron flux are input into ORIGEN. ORIGEN is then used to compute the material composition after some user specified period of irradiation. After the ORIGEN run, MCODE takes the material compositions and creates an MCNP input deck for another static calculation. This process would constitute one burnup step in the calculation. Several burnup steps are needed to simulate the irradiation of fuel over several cycles in a core model [72].

##### 2.2.4.1. **Version 1**

MCODE version 1 (MCODEv1) requires two input files. The first is the MCNP input file, and the second is a MCODE input file (a sample is shown in Appendix F). One of the strengths, and weaknesses, of MCODEv1 is that the user must input in the materials card of the MCNP input each and every fission product and actinide that will be tracked over the course of the burnup calculation. These are labeled on the MCNP materials card with comment lines denoting the start and end of MCODE materials to be tracked.

The separate MCODEv1 input file contains information that MCODE needs to perform the burnup calculations, namely the volume of the cells in the MCNP model. It is particularly important to input these values for the whole core, as MCNP models tend to take advantage of symmetry or repeating lattices, and as a result MCNP calculated volumes may be incorrect. Secondly, the heavy metal mass must be input as well. Again, this is very important because in

subsequent cycles the initial heavy metal mass of the fuel is the same during each cycle, however, the heavy metal mass at the start of the cycle for partially burnt assemblies will not be the same as the initial heavy metal mass. The MCODEv1 input file also contains the reference ORIGEN libraries for decay constants, photon emission constants, and neutron cross sections that are not explicitly calculated by MCNP.

Lastly, MCODEv1 needs the power density and a list of the burnup steps (either in effective full power days (EFPD) or burnup intervals (MWD/kg<sub>HM</sub>)). While MCODEv1 has been updated, the ability to track any user specified nuclide, as well as the ability to input the initial heavy metal mass that is different from the heavy metal mass at the start of the burnup calculation are both invaluable and thus this version is used throughout the current work.

#### 2.2.4.2. **Version 2**

The update in MCODE from MCODEv1 to MCODEv2 involved a major simplification for the user. Namely, instead of specifying a list of fission products and actinides to track at the onset of the calculation, MCODEv2 includes fission products and actinides in the fuel materials card as they are produced during irradiation. Only nuclides that contribute to the reactivity more than a specified threshold are included in the material card and subsequently in tallies, thus improving the performance, as fewer tallies are required at the onset of the calculation, and removing the burden on the user to predict a complete list of important nuclides to track. Appendix C contains an example of MCODEv2 input at the end of the MCNP input file; the inputs are contained in the same file for MCODEv2.

Comparisons began with a representative advanced core model for the first cycle. That is the core model that begins without fission products. The results are shown in Figure 2.9. The MCODEv2 run was made with a reduced number of neutron histories. As one can see there is greater uncertainty for the MCODEv2 run, and the behavior is not as smooth, but at all points during irradiation the MCODEv1 and MCODEv2 runs agree nicely.

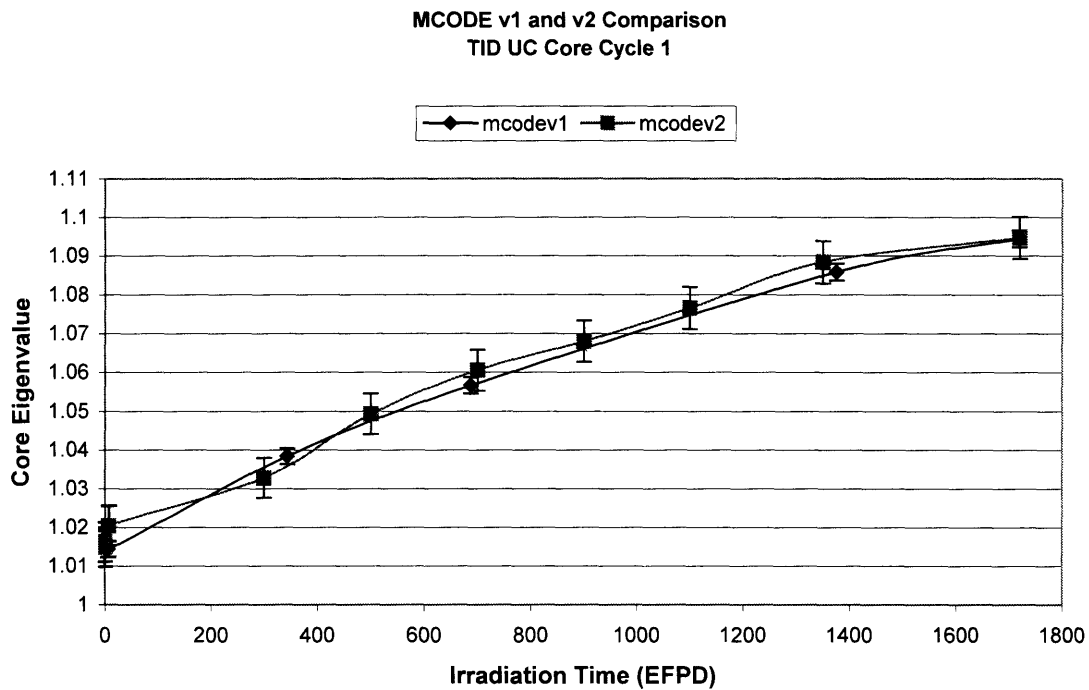


Figure 2.9 MCODEv1 and MCODEv2 calculations for Full Core, Cycle 1.

Another case was also selected for the comparison study: a cladding fluence calculation (described in further detail in 2.2.2). The purpose of this study was two-fold. The first is to confirm that pin-cell and full core models adequately predict the same cladding fluence, and secondly to form a basis of comparison between MCODEv1 and MCODEv2. Figure 2.10 and Figure 2.11 show plots of the cladding fluence calculations using the demonstration equilibrium cycle MCODEv1 runs as well as a pin-cell model for the demonstration and advanced core concepts.

The results clearly illustrate that the data mined from the full core models in the equilibrium cycle for the demonstration core and the pin-cell model of a representative fuel pin in the demonstration core predict essentially the same total and fast fluence. Not only is the reactivity history for the demonstration and advanced cores quite similar, but one can also see that the fluence trends are essentially similar as well.

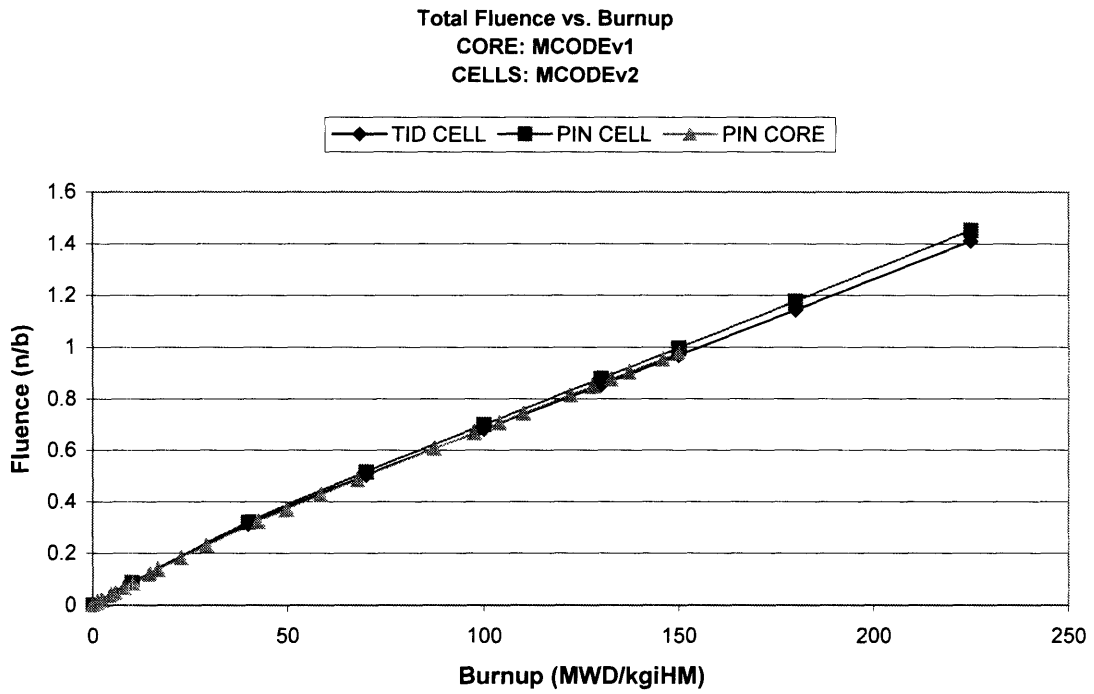


Figure 2.10 Total Fluence Calculations for Three Cases (nvt in inverse barns)

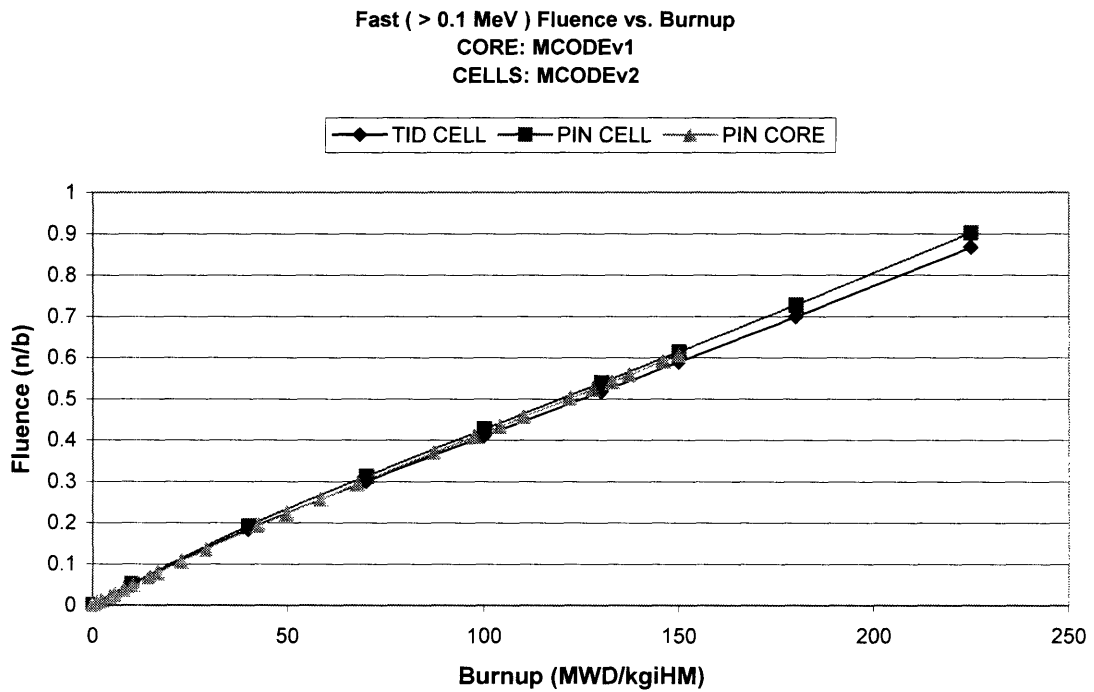


Figure 2.11 Fast ( $E > 0.1\text{MeV}$ ) Fluence Calculations in Three Cases (nvt in inverse barns)

The comparisons just shown lead to two conclusions. The first is that MCODEv2 offers significant benefits in terms of computer run time: MCODEv2 runs more than twice as fast as MCODEv1. MCODEv2 also reduces the burden on the user in terms of identifying key nuclides, and does so with adequate similarity in simulation to MCODEv1, therefore, further investigation was conducted using MCODEv2. Furthermore, the comparison between the pin-cell and full core models of the demonstration core indicate that pin-cell models adequately predict average cladding fluence, and therefore, use of the MCODEv2 full core models of the advanced core to predict cladding fluence were not pursued, as the pin-cell model will be adequate for the assessment. The peak fluence was calculated by multiplying the discharge burnup by the axial power peaking factor and using the fluence versus burnup curves to determine the fluence for that level of burnup.

#### 2.2.4.3. **Plutonium Drift Reactivity**

The full core model reactivity calculations as a function of burnup are conservative due to “plutonium drift.” The full core model does not axially zone the fuel, because the number of regions necessary to define the geometry is currently prohibitive to run on the Echelon Beowulf cluster. Therefore the fuel pins are modeled with one axial region. Hence, during burnup, the plutonium bred in the center of the fuel pin is smeared through the entire length of the pin after each burnup step (ORIGEN calculation) in MCODE. Since the plutonium, which would otherwise be in the center of the core is pushed to the axial periphery, there is an increase in the axial leakage, and as a result, the plutonium drift phenomenon in the full core model leads to an under-prediction of the core reactivity.

A cell model was used to observe the reactivity effect of plutonium drift. The cell model accounts for axial leakage with radial reflective boundary conditions. Figure 2.12 shows a plot of the cell eigenvalue as a function of burnup for a case with axial slices to prevent plutonium drift (SLICE) and for a case with no axial slices where the fuel composition after each burnup step is smeared across the entire pin length (FLAT).



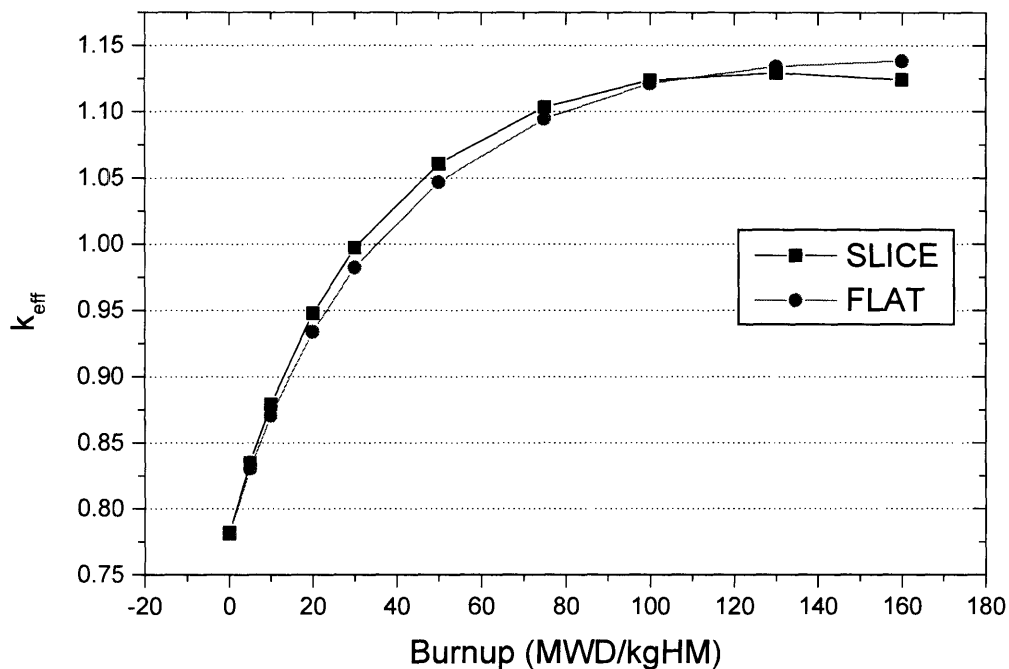


Figure 2.12 Effect of Plutonium Drift on Cell Eigenvalue<sup>6</sup>

At the beginning of irradiation, the SLICE and FLAT models predict the exact same eigenvalue for the semi-infinite cell. At long burnup (120 MWD/kgHM) the center region of the fuel begins to burn plutonium faster than it is bred locally. For the predominance of the irradiation, the FLAT model underestimates the reactivity. The error is not entirely negligible. However, the unit cell can be used as a surrogate to estimate its order of magnitude in the full core calculations, and in any case, the results from full core modeling will be conservative.

#### 2.2.4.4. Fill Area Discrepancy

The Fill-Area-Discrepancy (FAD) arises from the manner of defining repeating lattice geometry in the case of matrix block or Tube-In-Duct fuel assemblies for burnup calculations. The repeating lattices in triangular pitch assemblies (hexagonal unit cells) leave small triangles along the periphery of the hexagonal fuel assembly duct outside of the lattice cells. Figure 2.13 is a blown-up diagram of the edge of a fuel assembly model. The model was created by filling an entire hexagonal assembly with coolant channel lattice cells. At the edge of the assembly, there is a discrepancy because some of the cladding and coolant from the lattice cells is present in the peripheral triangle, leading to a discrepancy in the material composition of the fuel assembly at the very edge. An option in MCNP is to fill the peripheral triangles with a material that has the same composition as the fuel (i.e. has the same material card), however, MCODE is not able to update the number density associated with these small triangular regions.

<sup>6</sup> Standard deviation of all data points is < 0.0005

The repeating lattice elements are inserted into a hexagonal cell in the model with a given composition and number density. After each burnup step MCODE updates the material composition on the material card and the number density in the repeating lattice cell card; however, in the triangular cells at the periphery of the assembly, the number density cannot be updated unless these peripheral triangles are filled with the lattice cells themselves. The number density in the fill region will not be updated at each burnup step otherwise. Figure 2.13 shows a blown-up picture of an assembly where the lattice cell elements are used to fill the peripheral triangles. As the figure illustrates, additional error would be introduced if the lattice cells were also used to fill in the small triangular regions at the edge of the hexagonal assembly.

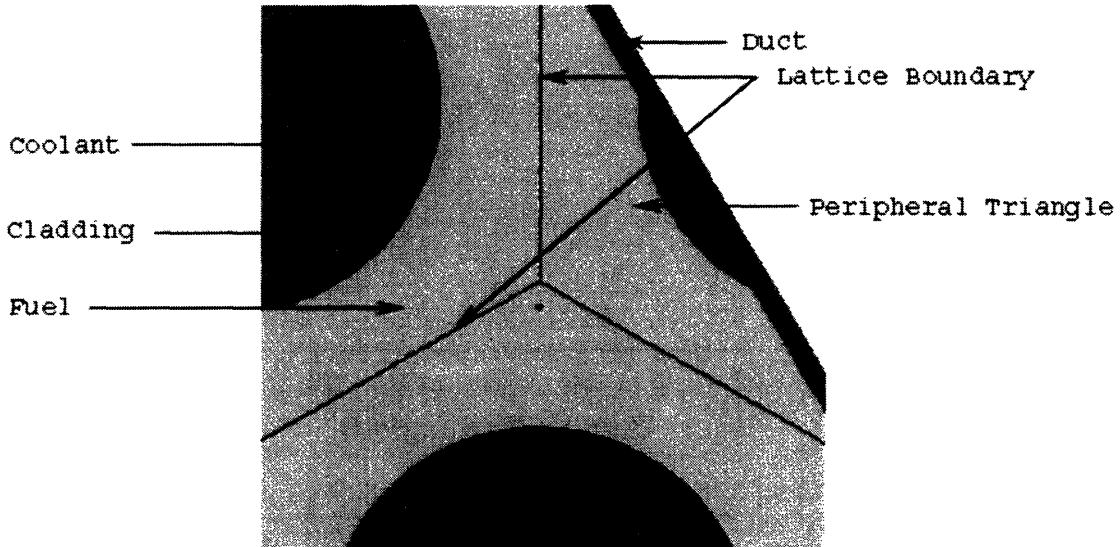


Figure 2.13 Peripheral Triangle Illustrating MCNP Fill Discrepancy (not-to-scale)

There are several approaches to solving the FAD. The first is to adjust the number density of the fuel, slightly increasing the number density so as to have the same mass of fuel in the assembly to account for the reduced fuel volume, as there is a small volume in the periphery occupied by additional clad and coolant, which would not actually be in the peripheral triangle regions. The cladding and coolant density could likewise be reduced to preserve mass. Since the partial coolant channels in the peripheral triangles are small, this would likely have only a small impact on the neutronic calculations, however, MCODE will not keep an exact record of the true fuel density, and therefore, calculations for the composition would have to be corrected.

Another approach is to define a second lattice cell for each fuel composition and add a second material card for each assembly type, such that MCODE can distinguish between the interior fuel and the fuel in the peripheral triangles at the edge of the assembly. This approach is very cumbersome because it would double the number of materials to track and dramatically increase the complexity of the core models.

Therefore an approximate correction was applied to an infinite assembly model. The purpose was to see if the fuel could still be modeled with a single material and single lattice cell card yet accurately predict the physics behavior of the fuel while at the same time keep a precise inventory of the nuclides in the fuel and their number density. The compromise correction is to fold the duct material into the peripheral triangles and eliminate the duct in the model. The fuel is then represented purely within the repeating lattice cells and the duct is represented by the peripheral triangles.

At the same volume fractions, this “compromise correction” should accurately predict neutronic parameters while maintaining the correct inventory of nuclides in the core. This can be accomplished without doubling the number of tallies performed or creating an overly complex geometry. Figure 2.14 shows a diagram similar to Figure 2.13 illustrating the nature of the compromise correction.

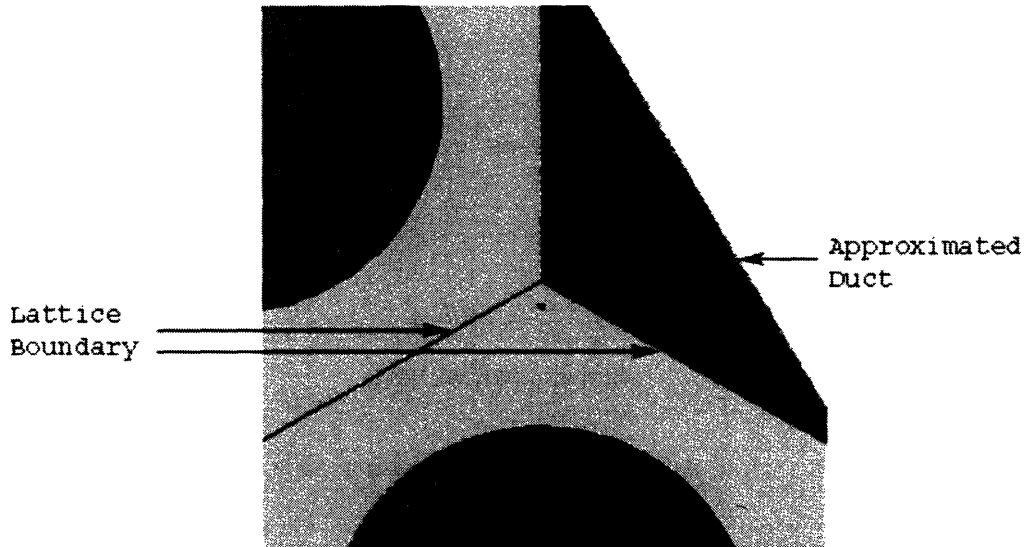


Figure 2.14 Compromise Approximation (not-to-scale)

The correct volume can be input on the cell card, and the duct material is for the most part neutronically inert, so the loading and composition will be correct. In general, if the volume of the peripheral cells exceeds the duct volume, then the density of the duct material can be adjusted in the MCNP fill definition for the assembly.

Calculations were carried out with MCODEv1 using a TID infinite assembly model. Three models were created, the first used the MCNP fill option to put fuel in the peripheral triangles; however, the number density of the material in the triangles was not updated after each burnup step (“nominal”) and the fuel density was decreased slightly. The second model used two separate lattice cells to fully account for the peripheral triangle cells (“peripheral”) and the fuel density was decreased slightly, though more than the nominal case, and a third used the compromise approach to correctly predict the nuclide inventories and loading (“compromise”) and the fuel density was the nominal value. The density changes were input such that the mass of heavy metal is the same in each model. The results of the reactivity history calculations are shown in Figure 2.15.

## MCODE Fill Burnup Comparison

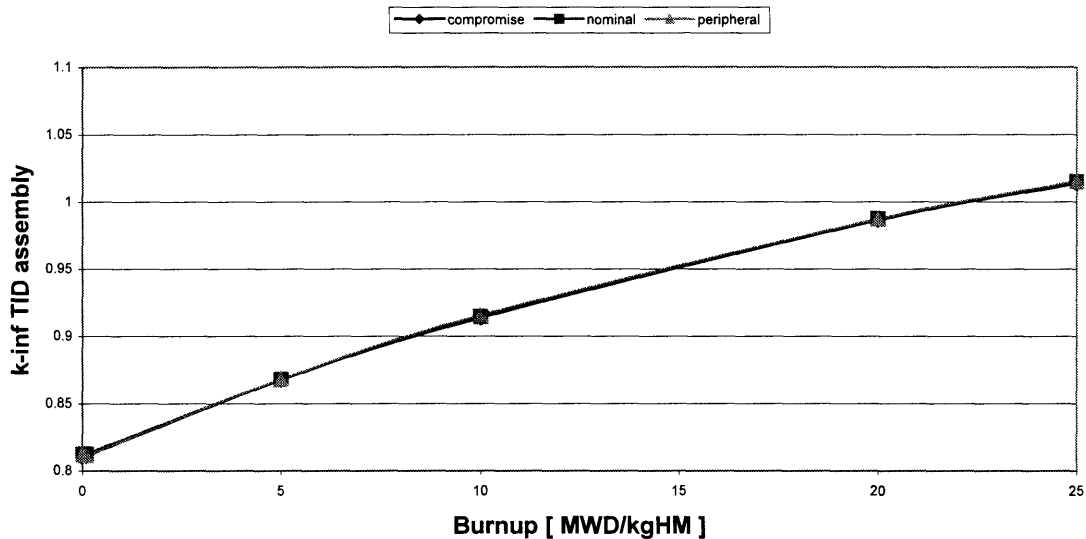


Figure 2.15 Fill-Area-Discrepancy Calculation using MCODEv1

The results confirm expectations that discrepancies of such small magnitude will not affect the analyses in a meaningful way. Therefore, in calculations the compromise approach is used to simplify modeling while maintaining the correct composition and loading of fuel.

### 2.2.4.5. Burnup Accrual Discrepancy

While MCODEv2 offers significant advantages over MCODEv1, there are several areas where one must exercise caution in using MCODEv2, particularly in the simulation of burnup over multiple cycles. MCODEv1 requires the user to specify both the volume of fuel as well as the initial mass of heavy metal and the density of the fuel (in the MCNP input). While this appears to be redundant, it is a useful way to calculate the burnup accrued by fuel in future cycles.

MCODEv1 was used to calculate the reactivity history of the core over several cycles. Each cycle represented one MCODEv1 run, and thus a number of MCNP runs equivalent to the number of burnup steps in a given cycle. In the MCODEv1 input file, the burnup steps in units of MWD/kg<sub>HM</sub> was supplied, as well as the power density, volume of the fuel, and mass of the initial heavy metal. After the first cycle, the MCODEv1 generated MCNP input file at the end of the first cycle was used to generate the input file for the beginning of the second cycle. The material card for the 6<sup>th</sup> batch was deleted, and each composition and fuel density was advanced into the next batch location. The 1<sup>st</sup> batch material card and density was then input into the MCNP input file after all of the other batches had been advanced. The tallies were removed from the input file and a new MCODEv1 input file was created.

The MCODEv1 input file for the first cycle was updated to be used as the input file for the second and subsequent cycles, however, the initial heavy metal masses were unchanged in the MCODEv1 input file. The initial heavy metal mass is what is used to calculate the burnup accrued by the fuel in each batch. In the second cycle, and all subsequent cycles, the mass of the heavy metal at the beginning of the MCODEv1 run is less than the mass of heavy metal specified as the “initial heavy metal mass” because five of the six batches are partially burnt.

MCODEv2 actually requires only the fuel volume for the input file, and uses the fuel density and volume to calculate the heavy metal mass, however, during irradiation the calculated burnup will actually be higher than the true burnup accrued by the fuel because when MCODEv2 divides the energy in MWD by the heavy metal mass, it is dividing by the mass of heavy metal at the start of the MCODEv2 run and not the heavy metal mass of the fuel at the beginning of irradiation, which was several MCODEv2 runs in the past. The method for calculating the burnup accrued by fuel in subsequent cycles leads to an error dubbed the Burnup Accrual Discrepancy (BAD). Therefore, when using MCODEv2 to do burnup calculations, it is essential to disregard the burnup calculated except for the very first cycle and to specify the burnup steps in units of effective full power time (in effective full power days) in order to avoid the BAD.

### 2.2.5. Quasi-Static Method

The Quasi-Static Method is used to calculate the steady state trends in fuel and cladding temperatures under a variety of accident scenarios. The method was first developed by Wade, et al. to form the basis for the design rationale behind the Integral Fast Reactor (IFR) [66]. The method uses a reactivity balance to determine the steady state fuel and coolant temperatures during a variety of postulated accidents. In particular, loss of flow, loss of ultimate heat sink, and control rod ejection are considered to establish an envelope [66]. The GFR is somewhat less constrained than liquid metal cooled reactors previously analyzed using this method in that coolant freezing is not a concern [55]. The B&B GFR depends on active cooling systems; therefore, the Quasi-Static assessment will only verify semi-passive self-regulation. Additionally, as coolant depressurization may occur rapidly (as discussed in section 6.3), the results of these analyses may not be fully applicable to large break loss of coolant accidents.

The balance equation lumps several reactivity feedback parameters into three coefficients. These coefficients are related to the normalized power, flow and coolant inlet temperature of the reactor. These individual contributors are lumped into macroscopic coefficients: A, B, and C. These are the net reactivity decrement due to core power perturbation, power/flow coefficient of reactivity, and the inlet temperature reactivity coefficient respectively. They are calculated as follows in Equation (2.2).

$$\begin{aligned}
 A &= (\alpha_D + \alpha_e)\Delta T_f \\
 B &= (\alpha_D + \alpha_e + \alpha_{Co} + 2\alpha_{RD} + 2\alpha_R) \frac{\Delta T_c}{2} \\
 C &= \alpha_D + \alpha_e + \alpha_{Co} + \alpha_R
 \end{aligned}
 \tag{2.2}$$

Where  $\Delta T_f$  is the difference in temperature between the fuel and coolant in K,  
 $\Delta T_c$  is the temperature rise across the core at steady state conditions [K],  
 $\alpha_D$  is the Doppler coefficient in  $\text{¢/K}$ ,  
 $\alpha_e$  is the fuel thermal expansion reactivity coefficient [ $\text{¢/K}$ ],  
 $\alpha_{Co}$  is the coolant temperature coefficient [ $\text{¢/K}$ ],  
 $\alpha_{RD}$  is the control rod drive line coefficient [ $\text{¢/K}$ ], and  
 $\alpha_R$  is the radial thermal expansion coefficient (core flowering) [ $\text{¢/K}$ ].

Individual reactivity feedback parameters were calculated using MCNP by altering the intermediate MCNP input files generated by the MCODE calculations. The parameters are the

Doppler coefficient, the fuel thermal expansion reactivity coefficient (assuming clad-fuel bonding for VIPAC), the coolant temperature coefficient (derived as a coolant density coefficient and adjusted using the ideal gas relationship for the GFR helium coolant), the control rod driveline expansion reactivity coefficient, and lastly, the core radial thermal expansion coefficient (or flowering coefficient).

The reactivity balance is given by a simple summation given the lumped coefficients (A, B, and C) simply as illustrated in Equation (2.3) [66].

$$0 = \Delta\rho_{ext} + \delta T_{in} C + \left(\frac{P}{F} - 1\right)B + (P - 1)A \quad (2.3)$$

Where  $\Delta\rho_{ext}$  is the change in reactivity from external sources (i.e. control rods),  
P is the normalized power (at nominal power P is unity),  
F is the normalized flow (at nominal flow rate F is unity), and  
 $\delta T_{in}$  is the change from nominal coolant inlet temperature.

Limits can be established for the lumped coefficients based on an enveloping set of accident scenarios. The steady state trends in temperature based on these accidents are related to the reactivity feedback coefficients of the core, and therefore, upon calculating the coefficients, the limits can be compared to particular ratios of the lumped coefficients and design changes can be made as necessary to ensure that the reactor will remain safe. A margin factor ( $\gamma$ ) of 2/3 was applied to the maximum allowable temperature perturbations to add conservatism.

The three accidents as stated above are loss of flow (LOF), loss of heat sink (LOHS), and control-rod-run out overpower (TOP); all without scram. Each of these accidents impose a limit based on the maximum coolant temperature at the outlet of the core. The limit based on the LOF accident is shown in Equation (2.4); Equation (2.5) is the limit based on LOHS, and Equation (2.6) is the limit based on TOP.

$$\frac{A}{B} \leq \gamma \frac{\delta \hat{T}_{out}}{\Delta T_c} \quad (2.4)$$

Where  $\gamma$  is the margin factor (applied for conservatism), and  
 $\delta T_{out}$  is the maximum tolerable increase in coolant outlet temperature.

$$\frac{1 + \frac{A}{B}}{\frac{C\Delta T_c}{B}} - 1 \leq \gamma \frac{\delta \hat{T}_{out}}{\Delta T_c} \quad (2.5)$$

$$\frac{-\Delta\rho_{TOP}}{C} \leq \gamma \delta \hat{T}_{out} \quad (2.6)$$

By combining Equation (2.4) and Equation (2.5) the LOHS limit can be rewritten as shown in Equation (2.7).

$$\frac{C\Delta T_c}{B} \geq \frac{1 + \frac{A}{B_{\max}}}{\gamma \frac{\widehat{\delta T}_{out}}{\Delta T_c} + 1} = 1 \quad (2.7)$$

Similarly, by combining the result of Equation (2.7) and Equation (2.6) the TOP limit can be rewritten as shown in Equation (2.8).

$$\frac{-\Delta\rho_{TOP}}{|B|} \leq \left( \frac{C}{B} \Delta T_c \right)_{\min} \gamma \frac{\widehat{\delta T}_{out}}{\Delta T_c} = \gamma \frac{\widehat{\delta T}_{out}}{\Delta T_c} \quad (2.8)$$

For the B&B GFR the maximum temperature increase is between 585 °C and 660 °C. With a core temperature rise of 385 °C and a margin factor of 2/3, the LOF and TOP limits are between 1.01 (advanced core) and 1.14 (demonstration core).

These limits, as derived, are less constrained than those derived for the Integral Fast Reactor because coolant freezing does not impose any lower limit on the reactor coolant inlet temperature. As a result, negative reactivity from control rod driveline thermal expansion in the middle of a cycle for the B&B GFR, though contributing negative reactivity, will always benefit safety, and is therefore excluded from the current analysis for conservatism.

As complex transient thermal hydraulic models are not used in the current work, the maximum allowable temperature perturbation in the reactor coolant outlet temperature is taken to be approximately the same as the maximum allowable temperature perturbation in the cladding material. While this is only approximate, a margin factor has been included in the analysis.

The different individual reactivity feedback coefficients were calculated using MCNP at the beginning of life (BOL), beginning of the equilibrium cycle (BOEC), and the end of the equilibrium cycle (EOEC). To calculate all of the coefficients for each point in core life, seven MCNP runs were required. The first calculates the nominal core eigenvalue with very low statistical error. The second is used to calculate the delayed neutron fraction; this is done by using the TOTNU card in MCNP to remove the delayed neutron yield from the fission neutron yields. The delayed neutron fraction is then calculated according to Equation (2.9).

$$\beta_{eff} = \frac{k - k_p}{k} \quad (2.9)$$

Where  $\beta_{eff}$  is the effective delayed neutron fraction,  
 $k$  is the nominal eigenvalue, and  
 $k_p$  is the eigenvalue in the model when only prompt neutrons are included.

The third is used to calculate the Doppler coefficient, in much the same way as discussed above in section 2.2.1.2. The cross sections for the actinides were replaced with 300 K libraries and a  $T^{-1/2}$  dependence was assumed.

The fourth calculation is used to calculate the reactivity from TOP; in this case the highest worth control rod is withdrawn from the core model and replaced with coolant; the reactivity is merely based on the difference in reactivity between the TOP and nominal cases. In cases where the entire bank is inserted only somewhat, as would be the case for the BOL or BOEC where there is only a small amount of excess reactivity, a MCNP calculation was not performed. The reactivity associated with TOP was estimated based on the flux profile and the number of control elements (either control pins or control rod assemblies). The nominal condition quoted for BOL and BOEC is often somewhat supercritical by at most a few dollars. This is because the BOL and BOEC are assumed to always be uncontrolled in the modeling. In practice the excess reactivity would be suppressed by slightly inserting the bank of control elements. However, in the interest of rapid calculation, the approximation shown in Equation (2.10) is used [21].

$$\Delta\rho_{TOP} = \left(1 - \frac{1}{k}\right) \left(\frac{\phi_{peak}}{\phi_{avg}}\right)^2 \left(\frac{N_{out}}{N_{tot}}\right) \quad (2.10)$$

Where  $\Delta\rho_{TOP}$  is the reactivity from a control element ejection,  
 $k$  is the eigenvalue at the BOC condition,<sup>7</sup>  
 $\phi$  is the neutron flux,  
 $N$  is the total number of control elements,  
 $out$  denotes control elements ejected (i.e. the number of control rods in a CRA),  
 $tot$  denotes the total number of control elements (i.e. the total number of control rods),  
 $peak$  denotes the maximum value, and  
 $avg$  denotes the average value.

The remaining coefficients deal with thermal expansion. The fifth calculation is used to calculate the coolant thermal expansion reactivity coefficient. However, the purpose of this calculation is dual purpose, in that MCNP is used to calculate the void reactivity by reducing the coolant density to that at atmospheric pressure in the core while keeping the temperature the same. This calculation is somewhat conservative in that the coolant temperature during blowdown will decrease and the final pressure will likely be several atmospheres; therefore the prescribed method under-predicts the helium density after blowdown. This assumption is deemed appropriate because the operating pressure is two orders of magnitude greater than atmospheric pressure. The voided condition helium density at a temperature lower than the operating temperature and pressure higher than atmospheric would be perhaps a factor of 3 – 5 higher, representing only a very small change in the difference in the densities between the nominal and voided case.

The coolant void reactivity worth is then used to estimate the coolant thermal expansion coefficient based on the following assumptions. First, the reactivity is assumed to scale linearly with temperature. Second, since the void calculation is based on the reactivity difference for two

---

<sup>7</sup> The BOC condition refers to the slightly supercritical uncontrolled reactor configuration. The core was designed so that the uncontrolled configuration at the BOC would be approximately critical, though often in these calculations the value is slightly over reactive, and control rods were not inserted in the model at this stage to compensate for the slight difference.



different coolant pressures, the ideal gas law is used to derive a pseudo coolant temperature (at operating pressure) that corresponds to the post-blowdown helium density. The coolant thermal expansion reactivity coefficient based on the void reactivity is calculated using the formula shown in Equation (2.11) where the ratio of the nominal condition and voided condition pressures is used to calculate the pseudo coolant temperature.

$$\alpha_{Co} = \frac{\Delta\rho_{void}}{T_V - T_N} = \frac{\Delta\rho_{void}}{\frac{P_N}{P_V} T_N - T_N} = \frac{\Delta\rho_{void}}{T_N \left( \frac{P_N}{P_V} - 1 \right)} \approx \frac{\Delta\rho_{void}}{\left( T_m + \frac{\Delta T_c}{2} \right) \left( \frac{P_N}{P_V} \right)} \quad (2.11)$$

Where T is the average coolant temperature,  
P is the coolant pressure,  
N denotes nominal, and  
V denotes void.

The sixth and seventh calculations deal with the thermal expansion of solid materials. The sixth is the fuel thermal expansion reactivity coefficient; this is calculated by increasing the dimensions of the fuel by 1% and preserving the mass by reducing the density in the model. The fuel temperature is held constant to differentiate the effect of thermal expansion from the Doppler coefficient. The difference in the reactivity is then used to calculate the coefficient assuming that the reactivity changes linearly with temperature. As the fuel is VIPAC, it is assumed to expand with the cladding material (i.e. bonded), and therefore, the fuel thermal expansion reactivity coefficient is based on the temperature change associated with a 1% increase in dimension based upon the thermal expansion coefficient of the cladding material. As VIPAC fuel may sinter during irradiation, this assumption may not be valid under all circumstances.

In calculating the radial expansion coefficient it was assumed that the fuel element supports were constructed to allow for thermal expansion. The radial expansion coefficient is calculated by increasing the pitch between the fuel elements by 1% in both axial and radial directions. For the pin assemblies this is done by increasing the pin pitch as well as the assembly pitch. For the tube-in-duct assemblies only the fuel assembly pitch is changed. These dimensional changes, again, are translated into a temperature change using the thermal expansion coefficient of the structural material. The reactivity is assumed to change linearly with temperature here as well. The difference in reactivity between the adjusted and nominal model, however, is halved in order to reflect the fact that radial expansion occurs primarily at the top of the core, and not so much at the inlet where the coolant temperature is much cooler.

#### 2.2.6. AIROX and CASMO-4

Atomics International Reduction/Oxidation (AIROX) processing of spent fuel was investigated on several levels. This section deals primarily with the neutronic evaluation of the potential reuse of B&B GFR spent fuel in LWRs. While AIROX is currently applicable to spent fuel in oxide form, proposed AIROX-like processes could be easily adapted to alternative spent fuel forms, such as carbide. Carbon Dioxide Oxidation (CARDIO) is a proposed one-step treatment process applicable to UC spent fuel and builds on the experience developed for the Oxidation Carbothermic Reduction process (CARBOX) [48]. While several processes exist to date, such as those mentioned in addition to the Oxidation and Reduction of Oxide Fuel (OREOX), the general techniques remain strikingly similar in that the spent fuel is repeatedly chemically oxidized and

reduced as to release volatile fission products from the spent fuel. The treated fuel is then refabricated for further irradiation.

AIROX fuel processing was investigated to enhance the B&B GFR fuel cycle economics by potentially allowing spent fuel reuse without increased proliferation risk. The methodologies employed for the study of the economic costs and benefits of such a fuel cycle are discussed in section 2.4.2 and results discussed in Chapter 7 and Chapter 11.

The first alternative fuel cycle proposed is to treat the B&B GFR spent fuel with an AIROX-like treatment and convert the fuel form to UO<sub>2</sub>. The fuel would resemble mixed oxide fuel, except that there would be no separation of the transuranics and there would also be residual nonvolatile fission products. Removal fractions for a variety of volatile fission products have been studied [48,33]. The following fission products were tracked using MCODEv1 and the removal fractions were assumed as shown in Table 2-4. Regardless of the B&B GFR fuel form, these removal fractions were applied in the simulation of hypothetical spent fuel treatment.

Table 2-4 Fission Products and Their AIROX Removal Fractions [48,52]

Fission Product	Removal Fraction
Technetium	75%
Iodine	100%
Xenon	100%
Cesium	90%

MCODEv1 was used to simulate the burnup of a B&B GFR UC fuel pin to 130 MWD/kg<sub>HM</sub> of burnup. MCODEv1 is used because it is essential to track strong thermal absorbers, such as xenon and samarium; MCODEv2 would not include these fission products as their contribution to the reactivity in a hard neutron spectrum is minimal.

At the end of the burnup calculation, ORIGEN was used to simulate the cool-down of the fuel for 5 years. The composition was taken from ORIGEN and the concentrations of the fission products in Table 2-4 were adjusted by the removal fraction.

The composition was then used in a CASMO-4 model of an infinite PWR fuel assembly [69]. CASMO-4 is a multi-group, two-dimensional neutronic code developed by Studsvik. CASMO-4 is used for burnup calculations of LWR assemblies or pin cell models. The code is capable of using the multi-group neutron libraries and geometry input to calculate the infinite medium eigenvalue and perform burnup calculations. CASMO-4 is able to update the material composition and recalculate the infinite medium eigenvalue. The neutron libraries are based on JEF2.2 and ENDFB6 [69]. CASMO-4 is used for this particular purpose instead of MCODE for the LWR burnup calculations because CASMO-4 is a deterministic code, and runs much faster than MCNP. It is also specifically tailored and benchmarked for LWR applications. A CASMO-4 input deck is included as a reference in Appendix D.

### 2.3. Thermal Hydraulics

Thermal Hydraulics analyses were limited to steady state calculations. For the purpose of rapid assessment, a simple finite volume model for the fuel assembly was created using Microsoft Excel. Several spreadsheets are included in the model to accept geometric and coolant parameters, as well as correlations for specific quantities. Two models were created for two types

of fuel assemblies; the fundamental difference between the two is simply in the geometry specifications.

The first is for a basic pin-type assembly, and the second for a tube-in-duct (TID) type assembly. TID assemblies are similar to block type assemblies in that instead of coolant flowing around fuel pins, the TID assemblies allows coolant to flow through coolant channels surrounded by interstitial fuel. The pin assembly model is described in section 2.3.1, and the TID assembly model in section 2.3.2.

Each model preassumes a secondary power conversion cycle, which is based on the Advanced Gas-cooled Reactor (AGR) Rankine cycle steam plant. While the power levels for the B&B GFR core differ from the AGR, the inherent assumption is that, given the same inlet and outlet temperatures for the intermediate heat exchanger (IHX), which is a steam generator, that the same secondary cycle efficiency can be achieved.

### 2.3.1. **Pin Assemblies**

The basic inputs for the pin model are the fuel assembly geometry, axial power shape, radial power peaking factor, correlations for coolant and fuel properties, core inlet temperature, core temperature rise, the number of pin spacers and their drag coefficient. Based on these parameters, an iterative method is used to calculate the coolant properties, pressure, and associated temperatures for the coolant, clad, and fuel in 1 cm tall cells along the axial length of the fuel.

Several assumptions were made during the modeling process. First, only two isolated channels were modeled, thus no cross flow or azimuthal asymmetries were taken into account. The fluid is assumed to be an ideal gas with a constant specific heat at constant pressure. The fuel-clad contact thermal resistance was neglected. Lastly, fluid properties, such as conductivity and viscosity were assumed to only vary with temperature (and not pressure).

The calculation is based on the hot and average coolant channels. The calculation begins by calculating the pressure drop in the average channel, and uses this as input to the hot channel calculation. This process is necessary, as the mass flow rate through the hot channel is not known a priori. The calculation will be discussed in several stages. Table 2-5 shows many of the input parameters, and shows the calculation for the hydraulic diameter and average linear heat rate. Since the method used a finite volumes approach, in subsequent formulae, the subscript “i” will denote the value in the *i*th cell, each 1 cm tall in the axial direction.

The term “equivalent core temperature rise” is used because the core will employ an orificing strategy to reduce the pump work [53]. In so doing, the coolant temperature rise, with a perfect orificing scheme, will be the same as the temperature rise across the hot channel. The actual core temperature rise is given by the product of the radial power peaking factor and the equivalent core temperature rise.

Table 2-5 Global Parameters for the Pin Assembly Calculations

Core/Global Parameters	Symbol	Formula
Pin Locations per Assembly	n	Input
Fuel Pins per Assembly	n'	Input
Core Height	L	Input
Axial Reflector Length	R	Input
Assembly Flat-to-Flat Length	FTF	Input
Pin Pitch	p	Input
Pin Diameter	d	Input
Fuel Diameter	d <sub>in</sub>	Input
Number of Assemblies	N	Input
Equivalent Core Temperature Rise	ΔT <sub>eq</sub>	Input
Operating Pressure	P <sub>op</sub>	Input
Thermal Power	P <sub>th</sub>	Input
Axial Power Peaking Factor	APPF	Input
Radial Power Peaking Factor	RPPF	Input
Spacer Drag Coefficient	K <sub>sp</sub>	Input
Primary Circulator Inlet Temperature (or Helium IHX Outlet Temperature)	T <sub>i</sub>	Input
Hydraulic Diameter	D	$4 \left( \frac{\frac{\sqrt{3}}{2} FTF^2 - \frac{\pi}{4} nd^2}{\pi nd + \frac{6}{\sqrt{3}} FTF} \right)$
Average Linear Heat Rate	q' <sub>0</sub>	$\frac{P_{th}}{Ln'N}$

The next set of parameters predominantly refer to the fluid properties in the *i*th cell. The calculation is iterative, as the core inlet temperature depends on the helium temperature at the outlet of the primary circulator, and the circulator power depends on the pressure drop. The pressure drop calculation will be discussed subsequently. Two formulae appear for the Helium Temperature in the *i*th cell, the first is to denote the temperature in the first cell at the base of the bottom axial reflector and the second for the temperature in the following cells. Table 2-6 summarizes the formulae used to calculate the fluid properties of interest.

Table 2-6 Cell-wise Properties of the Coolant

Fluid Properties	Symbol	Formula
Helium Temperature	T	$T_1 = T_i + \Delta T_{pump}$ $T_i = T_{i-1} + \delta T_{i-1}$
Helium Density <sup>8</sup>	$\rho$	$\rho_i = \frac{P_i}{P_{op}} \frac{4.76}{T_i + 273}$ [g/cc]
Helium Viscosity [42] <sup>9</sup>	$\mu$	$\mu_i = 1.89 \times 10^{-4} + 4.01 \times 10^{-7} T_i$ [g/cm-sec]
Helium Conductivity [42]	k	$k_i = 0.00144 + 3.277 \times 10^{-6} T_i$ [W/cm-°C]
Helium Specific Heat (constant Pressure) [42]	$C_p$	5.19 J/g-K (assumed constant)
Temperature Rise Across Cell	$\delta T$	$\delta T_i = \frac{q_i}{C_p w}$
Helium Velocity	v	$v_i = \frac{w}{\rho_i} \left( \frac{n}{\frac{\sqrt{3}}{2} FTF^2 - \frac{\pi}{4} nd^2} \right)$
Helium Channel Mass Flow Rate <sup>10</sup>	w	$w_{avg} = \frac{P_{th}}{C_p \Delta T_{eq} n' N}$
Helium Circulator Temperature Rise	$\Delta T_{pump}$	$\Delta T_{pump} = \frac{\Delta P}{C_p \rho_1}$

The remaining variables for the finite volume calculation deal with the calculation of the temperature profile for the cladding and fuel (heat transfer parameters) and the calculation of the core pressure drop (pressure parameters). The heat transfer parameters and formulae are shown in Table 2-7. The Gnielinski heat transfer and friction factor correlations are used in the current analyses as suggested by Dostal, et al. [17].

<sup>8</sup> Helium is taken as an ideal gas here.

<sup>9</sup> A linear fit was used for the viscosity and conductivity to simplify the calculation.

<sup>10</sup> The average mass flow rate is calculated here; the mass flow rate in the hot channel is calculated by adjusting the mass flow rate until the pressure drop in the hot channel is the same as the pressure drop in the average channel

Table 2-7 Cell-wise Heat Transfer Parameters

Heat Transfer Parameters	Symbol	Formula
Prandtl Number	Pr	$Pr_i = \frac{\mu_i C_p}{k_i}$
Reynolds Number	Re	$Re_i = \frac{\rho_i v_i D}{\mu_i}$
Cladding Thermal Conductivity [34]	$k_C$	0.25 W/cm <sup>2</sup> °C (assumed constant)
Fuel Thermal Conductivity <sup>11</sup>	$k_F$	$k_{F_i} = k_F(T_{F_{i-1}})$ (see section 3.10)
Heat Transfer Coefficient [29]	h	$h_i = \frac{k_i}{D} \left( \frac{\frac{f_i}{8} (Re_i - 100) Pr_i}{1 + 12.7 (Pr_i^{2/3} - 1) \sqrt{\frac{f_i}{8}}} \right)$
Coolant Thermal Resistance [63]	$R_{co}$	$R_{co_i} = \frac{1}{\pi d_m h_i}$
Cladding Thermal Resistance [63]	$R_{cl}$	$R_{cl} = \frac{\ln\left(\frac{d}{d_m}\right)}{2\pi k_C}$
Fuel Thermal Resistance [63]	$R_F$	$R_{F_i} = \frac{1}{4\pi k_{F_i}}$
Film Temperature Difference	$\delta T_{film}$	$\delta T_{film_i} = q_i R_{co_i}$
Cladding Temperature	$T_{cl}$	$T_{cl_i} = T_i + \delta T_{film_i} + q_i R_{cl_i}$
Fuel Temperature	$T_F$	$T_{F_i} = T_{cl_i} + q_i R_{F_i}$
Extrapolated Core Height [21] <sup>12</sup>	$L_{ex}$	$APPF = \frac{\frac{\pi L}{2L_{ex}}}{\sin\left(\frac{\pi L}{2L_{ex}}\right)}$
Heat Deposition in the Cell <sup>13</sup>	q	$q_i = APPF(RPPF)q'_0 \cos\left(\pi \frac{z}{L_{ex}}\right) (1cm)$

The last component of the finite volume calculations are the variables dealing with the coolant pressure, which are used to determine the coolant density, core pressure drop, and subsequently,

<sup>11</sup> Note that the fuel conductivity in the ith cell is approximated using an expression for the fuel conductivity but using the temperature in the i-1th cell. This is to avoid a second iteration loop.

<sup>12</sup> The extrapolated core height is found by iteratively solving the shown transcendental equation.

<sup>13</sup> z refers to the axial height in the core; in the reflector region this quantity is set to 0 and z ranges between -100 and 100 for a 200 cm tall core. The height of each cell is 1 cm, that is why it appears in the calculation. In the average channel (as opposed to hot) the RPPF is set to unity for this quantity.

the core inlet temperature. These following set of formulae in Table 2-8 close the system of equations and allow the iterative calculation to determine the axial profile for all of the variables of interest.

Table 2-8 Cell-wise Pressure Drop Parameters

Pressure Parameters	Symbol	Formula
Friction Factor [29]	f	$f_i = \left( \frac{1}{1.8 \log(\text{Re}_i) - 1.5} \right)^2$
Cell Friction Pressure Drop	$\delta p_{fr}$	$\delta p_{fr_i} = \frac{f_i \rho_i v_i^2}{D} (1cm)$
Cell Acceleration Pressure Drop	$\delta p_{ac}$	$\delta p_{ac_i} = \rho_i v_i^2 - \rho_{i-1} v_{i-1}^2$
Cell Gravity Pressure Drop	$\delta p_{gr}$	$\delta p_{gr_i} = \rho_i g (1cm)$
Cell Spacer Pressure Drop <sup>14</sup>	$\delta p_{sp}$	$\delta p_{sp_i} = K_{sp} \frac{\rho_i v_i^2}{2}$
Total Cell Pressure Drop	$\delta p$	$\delta p_i = \delta p_{fr_i} + \delta p_{ac_i} + \delta p_{gr_i} + \delta p_{sp_i}$
Cell Pressure	P	$P_i = P_{op} - \sum_{j=1}^{i-1} \delta p_j$
Core Pressure Drop	$\Delta P$	$\Delta P = \sum_{j=1}^{150} \delta p_j$

The cycle efficiency is estimated from the thermal power, given figures for AGR-type steam plants, and the core pressure drop. The AGR power conversion system (PCS) is a Rankine steam plant. The calculation for the core thermal hydraulics assumes the same inlet and outlet temperatures on the secondary side of the steam generator (the IHX). The AGR plant efficiency is 40% [63]. The net efficiency is calculated for the B&B GFR by multiplying the thermal reactor power by 40%, and then subtracting the necessary pump work from the gross electric generation. The pump work is calculated according to Equation (2.12). It is worth noting that the current analysis is conservative because it neglects the AGR primary circulator power, which would indicate that the AGR PCS efficiency is actually higher than 40%. However, pressure drop in the IHX and system piping are neglected, as they are assumed small compared to the pressure drop for a core with a very high fuel volume fraction.

$$W = \frac{\Delta P w n N}{(RPPF) \eta \rho_1} \quad (2.12)$$

Where W is the pump work, and  
 $\eta$  is the circulator efficiency.

The circulator is assumed to be 90% efficient (a detailed circulator design was not considered). Additionally, it is assumed that ideal orificing can be used for the coolant flow. The net power

<sup>14</sup> Only included at axial heights where a spacer is specified.

generation and net efficiency are calculated according to Equation (2.13) and Equation (2.14) respectively.

$$P_{net} = 0.40P_{th} - W \tag{2.13}$$

Where  $P_{net}$  is the net electric power generation.

$$\eta_{net} = \frac{P_{net}}{P_{th}} \tag{2.14}$$

Where  $\eta_{net}$  is the net efficiency for converting thermal power to electric generation.

### 2.3.1.1. Comparison with the GA GCFR

The finite volume model was compared with results for the General Atomics GCFR. Data from reference [15] was input into the model to check that the model produced roughly the same results for key thermal hydraulic parameters given by the same reference. The model was updated only slightly to remove flow channel orificing (thus equating the equivalent core temperature rise and the actual core temperature rise). Table 2-9 summarizes key input parameters into the comparison model.

Table 2-9 Key GCFR Comparison Model Input Parameters

Number of Fuel Assemblies	91	
Fuel Pins Per Assembly	270	
Fuel Assembly FTF	18.67	cm
Core Thermal Power	830	MW
Operating Pressure	9	MPa
Core Temperature Rise	228	°C
Axial PPF	1.21	
Radial PPF	1.25	
Helium Temperature at Core Inlet	322	°C

The results for the Average and Hot Channel are shown below as well as how they compare with the quoted values from [15]. As is clear from the calculation summarized in Table 2-10, the average channel results are in excellent agreement with the GCFR results. The key results, maximum clad temperature and pressure drop, are in very close agreement. Therefore, the method, while simple, was judged to be adequate for carrying out steady state calculations for the B&B GFR Core.



Table 2-10 Output Comparison to GCFR

	Average Channel Calculation	Hot Channel Calculation	Average Channel Quoted in [15]	
q' peak over pin	408.48	510.60	410	W/cm
Core Mass Flow Rate	701.42	701.42	702	kg/sec
core $\Delta P$	<b>307.84</b>	325.79 <sup>15</sup>	<b>290</b>	kPa
Pump Work	27.00	28.57	24.5	MW
Helium Outlet Velocity	119.03	127.54		m/sec
Peak Clad Temperature	<b>693.26</b>	784.02	<b>700</b>	oC

Additionally, as a result of the comparison study, the helium outlet velocity was calculated, though not quoted in the reference. The outlet velocity is on the order of 120 m/sec, and this quantity has been adopted as a limit for the velocity during the design optimization for the B&B GFR Core.

### 2.3.2. Tube-in-Duct Assemblies

For the tube-in-duct arrangement, the fundamental methodology is the same. There are a few changes that are required to reflect the difference in the geometries. These differences arise in the treatment of the hydraulic diameter, helium velocity, the fuel thermal resistance, and the spacer pressure drop. In particular, the spacer pressure drop is completely eliminated.

Instead of inputting the number of fuel pins per assembly ( $n$ ), the number of coolant channels is entered. The pin pitch ( $p$ ) is replaced by the coolant channel pitch; and the pin diameter ( $d$ ) and fuel diameter ( $d_{in}$ ) are replaced by the cladding outer ( $D_{c,o}$ ) and inner ( $D_{c,i}$ ) diameter respectively. Table 2-11 shows the modifications to the parameters.

In these calculations to the cladding-fuel contact resistance was neglected, therefore, the fuel temperature is somewhat underestimated. However, the fuel temperature margin is significant because ceramic fuels are used and the coolant outlet temperature is less than 600 °C.

---

<sup>15</sup> The pressure drop iteration was set to a relatively high tolerance because the average parameters were the ones of interest here. The results are shown to illustrate that the calculation ended up with reasonable results.

Table 2-11 Modified Parameters for the TID Finite volume Model

Modified Parameters	Symbol	Formula
number of coolant channels per assembly	n	Input
Cladding Inner Diameter	$D_{c,i}$	Input
Cladding Outer Diameter	$D_{c,o}$	Input
Channel Pitch	p	Input
Equivalent Annulus Diameter	$D_{EA}$	$D_{EA} = p \sqrt{\frac{2\sqrt{3}}{\pi}}$
hydraulic diameter	D	$D = D_{c,i}$
helium velocity	v	$v_i = \frac{4w}{\rho_i \pi D_{c,i}^2}$
fuel thermal resistance	$R_F$	$R_F = \frac{\ln\left(\frac{D_{EA}}{D_{c,o}}\right)}{2\pi k_F (T_{i-1})}$

The geometry input was used to calculate the equivalent diameter of an annular unit cell ( $D_{EA}$ ). The channels are arranged in a hexagonal array; however, the peak fuel temperature is calculated using an approximate method where the fuel surrounding each channel is modeled as a cylindrical sleeve surrounding the channel so that a simple heat transfer resistance method can be used to calculate the fuel temperature. The equivalent diameter is calculated such that the volume of the fuel is the same in the approximate annular scheme as in the actual model geometry. A diagram is shown in Figure 2.16.

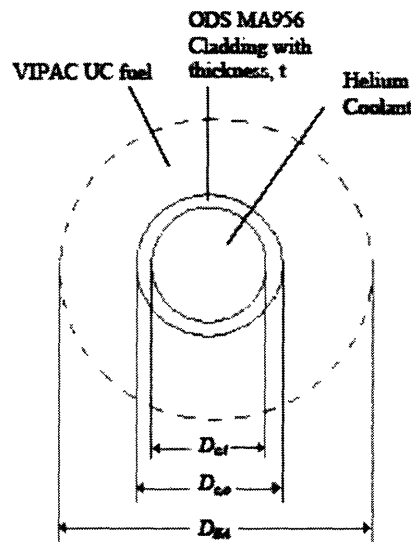


Figure 2.16 Equivalent Annulus Diagram<sup>16</sup>

<sup>16</sup> Provided by Michael Pope

2.3.2.1. **TID Calculation Comparison to Flow-Split**

For the purposes of validating the updated version of the finite volumes model, a comparison study was done with Michael Pope. Pope employed the Flow-Split code, developed at MIT by Dr. Pavel Hejzlar in 1993 for steady state thermal hydraulic calculations. The input parameters were agreed upon and listed in Table 2-12.

Table 2-12 Input Parameters to Flow-Split and the FVM for the Comparison Study

Core Thermal Power	2400 MW
Average Power Density	128 kW/l
Axial Peaking Factor	1.4
Radial Peaking Factor	1.77
Number of Channels	59683
Unit Cell Pitch	1.3468 cm
Coolant Channel Diameter	1 cm
Cladding Thickness	0.8 mm
Volume Fraction Coolant	0.5
Volume Fraction Cladding	0.1728
Volume Fraction Fuel	0.3272
Diameter of Equivalent Fuel Annulus	1.414 cm
Channel Height	280 cm
Fueled Height	200 cm
Helium Coolant Inlet Pressure	10 MPa
Helium Coolant Inlet Temperature	420 °C
Helium Coolant Mass Flow Rate	3183 kg/sec
Fuel Form	UC VIPAC 91% TD
Equivalent Core Diameter	345 cm
Average Heat Flux	$6.4 \times 10^5 \text{ W/m}^2$
Max Heat Flux (average channel)	$9.1 \times 10^5 \text{ W/m}^2$
Max Heat Flux (hot channel)	$1.6 \times 10^6 \text{ W/m}^2$

The two methods were applied independently and the results are tabulated in Table 2-13. Aside from some difference in the average Reynolds number (~20%), the results show excellent agreement. While, the comparison here is by no means a full benchmark study, the agreement between outputs with the same inputs, given two different numerical approaches gives some credibility to the finite volume model.

Table 2-13 Comparison Study Results

Parameters for comparison	Hot channel	
	(Yarsky / FVM)	(Pope / Flow-Split)
peak clad temperature	821	844
average heat transfer coefficient	0.84	0.89
total pressure drop	266	232
average Reynolds number	173600	140090
form pressure losses	61	56.2
outlet temperature	683	694
inlet velocity	102	92.7
total mass flow rate	3083	3180
outlet density	4.85	4.83

The total mass flow rates are slightly (~3%) different. As the finite volume model calculates the mass flow rate given the power, specific heat, and core temperature rise, specifying the mass flow rate would over-specify the problem.

## 2.4. Fuel Cycle Economics

The B&B GFR core is designed to sustain criticality to a discharge burnup of 150 MWD/kg<sub>HM</sub> for the fuel without any requirement for spent fuel reprocessing or recycle of any kind. The fuel cycle costs for the once-through-then-out fuel cycle (OTTO) are thus compared with a typical LWR to determine the economic advantages of the B&B GFR. However, further consideration is given to alternative fuel cycles as the spent fuel tends to have large concentrations of plutonium, and therefore value that can further supplement the economic advantages of the B&B GFR. This chapter will describe the methodology for evaluating the OTTO mode as well as the methods used to treat the costs and revenues associated with alternative fuel cycles.

### 2.4.1. Once-Through-Then-Out Fuel Cycle Analysis

The once-through-then-out fuel cycle (OTTO) is comprised of many processes and steps that must occur prior to fuel irradiation. Uranium must be mined, milled, converted, enriched, and fabricated into fuel assemblies. These stages are common to both conventional thermal reactors and the B&B GFR. A simple methodology is proposed here to compute the levelized fuel cycle costs on a consistent basis between the B&B GFR and a conventional LWR. The strategy in performing this assessment is to compute the current costs at the time for each stage that occurs before irradiation, then apply a future worth factor in order to present value all of the process costs to the time at the beginning of irradiation. A capital recovery factor is then applied to the period of irradiation to compute the levelized fuel cycle costs.

To perform this assessment several cost variables are required, and many are common to both the B&B GFR as well as a LWR. Table 2-14 Summarizes the relevant unit costs for the front end fuel cycle stages, as well as the lead times prior to irradiation when these steps take place, Table 2-14 also contains macroscopic economic parameters, process variables, and core specific variables to be input into the calculations. The costs, lead times, process variables, and macroeconomic parameters are taken from reference [71] and the costs are in constant 1994 USD. All further assessments were done using 1994 USD without including any price escalation, and therefore the analyses are meant only to show the relative economic performance of the B&B GFR in comparison with LWRs.

Table 2-14 Economic Parameters for OTTO Analyses

<b>Process Costs</b>	<b>Unit Cost</b>	<b>Units</b>	<b>Lead Time</b>
Mining and Milling	50	\$/kg <sub>U</sub>	2
Conversion	8	\$/kg <sub>U</sub>	1.5
Enrichment	110	\$/kg <sub>SWU</sub>	1
Fabrication	275	\$/kg <sub>U</sub>	0.5
Spent Fuel Storage	120	\$/kg <sub>U</sub>	discharge
<b>Process Variables</b>	<b>Units</b>	<b>Symbol</b>	<b>Value</b>
Conversion Losses	%	l <sub>C</sub>	0.5
Enrichment Tails Assay	w/o	x <sub>W</sub>	0.3
Uranium Feed Enrichment	w/o	x <sub>F</sub>	0.711
Fabrication Losses	%	l <sub>F</sub>	1.0
<b>Macroeconomic Parameters</b>	<b>Units</b>	<b>Symbol</b>	<b>Value</b>
Carrying Charge per Annum	%/yr	i <sub>d</sub>	10
Federal Waste Disposal Fee	mills/kWhre	e <sub>DISP</sub>	1
<b>Input Variables</b>	<b>Units</b>	<b>Symbol</b>	
Discharge Burnup	MWD/kg <sub>HM</sub>	B <sub>d</sub>	
Net Efficiency	%	η	
Cycle Length	EFPY	T	
Number of Batches		n	
Capacity Factor		CF	
Enrichment	w/o	x <sub>P</sub>	

The unit costs are known; however, the mass flow through each process step is needed to calculate the direct cost of that step. The mass flow is not constant through each step as much of the material mined is discarded during the enrichment phase and there are process losses during conversion and fabrication. The fuel cycle costs are calculated based on a single kilogram of heavy metal being irradiated, such that the costs computed represent the fuel cycle cost per kilogram of heavy metal to be irradiated.

The formulae for calculating the mass flow through each step are shown in Equation (2.15) [71].

$$\begin{aligned}
M_{sto} &= 1 \\
M_{fab} &= 1 \\
P &= \frac{1}{1-l_F} M_{fab} \\
F &= \frac{x_P - x_W}{x_F - x_W} P \\
M_{con} &= F \\
M_{ore} &= \frac{1}{1-l_C} M_{con}
\end{aligned}
\tag{2.15}$$

Where, M is the mass in kg<sub>HM</sub>,  
P is the mass of enriched product at the end of the enrichment stage [kg<sub>HM</sub>],  
F is the feed of material to the enrichment stage [kg<sub>HM</sub>],  
sto denotes the storage stage,  
fab denotes the fabrication stage,  
con denotes the conversion stage, and  
ore denotes the mining and milling stage.

While Equation (2.15) gives the mass flow through each stage, the unit cost of enrichment is measured in units of separative work units and is not directly proportional to the feed or product mass. The separative work units (SWU) for the enrichment stage are calculated according to the formulae shown in Equation (2.16) [30].

$$\begin{aligned}
SWU &= P \left( V(x_P) - V(x_W) - \frac{x_P - x_W}{x_F - x_W} (V(x_F) - V(x_W)) \right) \\
V(x) &= (1 - 2x) \ln \left( \frac{1-x}{x} \right)
\end{aligned}
\tag{2.16}$$

With the unit costs in Table 2-14 and the formulae in Equation (2.15) and Equation (2.16) it is possible to solve for the direct costs associated at each stage of the OTTO scenario by multiplying the unit cost by the mass flow at each stage. However, these direct costs must be multiplied by the future worth factor to determine their present value at the beginning of irradiation. In order to do this the carrying charge per annum must be converted to an equivalent continuously compounding rate as shown in Equation (2.17).

$$i_c = \ln(1 + i_d)
\tag{2.17}$$

Where  $i_c$  is the equivalent continuously compounding rate in yr<sup>-1</sup>

The direct costs and future worth factors for each stage are all shown in Equation (2.18) [71,30]. The fuel cycle cost is then the sum of these five costs present valued to the start of irradiation.

$$\begin{aligned}
C_{ore} &= UC_{ore} M_{ore} e^{i_c Le_{ore}} \\
C_{con} &= UC_{con} M_{con} e^{i_c Le_{con}} \\
C_{enr} &= UC_{enr} SWU e^{i_c Le_{enr}} \\
C_{fab} &= UC_{fab} M_{fab} e^{i_c Le_{fab}} \\
C_{sto} &= UC_{sto} M_{fab} \exp\left(\frac{-i_c nT}{CF}\right)
\end{aligned}
\tag{2.18}$$

Where  $C$  is the contribution to the fuel cycle cost in  $\$/\text{kg}_{\text{IHM}}$ ,  
 $UC$  is the unit cost,  
 $Le$  is the lead time, and  
 $enr$  denotes the enrichment stage.

When exotic fuel forms, such as  $\text{U}^{15}\text{N}$  are employed, the additional cost of the highly enriched nitrogen must be factored into the cost of fabricating the fuel. For  $\text{U}^{15}\text{N}$  fueled B&B GFR cores the fabrication cost is adjusted as shown in Equation (2.19).

$$C_{fab} = \left( UC_{fab} + UC_{hen} \frac{15}{238} \right) M_{fab} e^{i_c Le_{fab}}
\tag{2.19}$$

Where  $UC_{hen}$  is the cost of highly enriched nitrogen in  $\$/\text{kg}_{\text{HEN}}$ .

The federal waste disposal fee must also be included, however, this fee is extracted continuously over the period of fuel irradiation, and is also in the units of mills/kWhre. Therefore, the annuity factor must be applied to the present value of the fuel cycle costs at the beginning of irradiation and all units must be converted to mills/kWhre. The conversion and appropriate continuous capital recovery factor are shown in Equation (2.20) [71,30]. The capacity factor is present to convert the cycle length from units of effective full power time to calendar time.

$$e_{OTTO} = e_{DISP} + (C_{ore} + C_{con} + C_{enr} + C_{fab} + C_{sto}) \left( \frac{\frac{i_c nT}{CF}}{1 - \exp\left(\frac{-i_c nT}{CF}\right)} \right) \left( \frac{1}{24\eta B_d} \right)
\tag{2.20}$$

Where  $e_{OTTO}$  is the total levelized fuel cycle cost in mills/kWhre,  
 $\eta$  is the efficiency (in order to convert from thermal to electrical energy),  
 $B_d$  is the discharge burnup in  $\text{MWD}/\text{kg}_{\text{IHM}}$ ,  
 $CF$  is the capacity factor,  
 $C$  is the fuel cycle cost in units of  $\$/\text{kg}_{\text{IHM}}$ , and  
the factor of 24 is present to convert the MWD into MWhr.

The current formalism was used for a typical LWR. The input parameters are the discharge burnup, thermal efficiency, cycle length, number of batches, capacity factor, and enrichment. A

set of reference parameters was taken to represent a standard LWR. These reference parameters are shown in Table 2-15.

Table 2-15 LWR Reference Values for OTTO Analysis

<b>Input Variables</b>	<b>Units</b>	<b>Symbol</b>	<b>LWR Reference Value</b>
Discharge Burnup	MWD/kg <sub>HM</sub>	B <sub>d</sub>	50
Net Efficiency	%	η	33
Cycle Length	EFPY	T	1.5
Number of Batches		n	2.68
Capacity Factor		CF	0.90
Enrichment	w/o	x <sub>p</sub>	4.5

Based on these input parameters a fuel cycle cost of 6.72 mills/kWhre was calculated (in 1994 mills). This is in basic agreement with the results of reference [71] which predicts a fuel cycle cost of ~6.8 mills/kWhre (also in 1994 mills) for a slightly different set of input parameters (namely a slightly larger number of batches, slightly higher efficiency and slightly smaller capacity factor).

#### 2.4.2. Alternative Fuel Cycle Analysis

Alternative fuel cycles were also considered. All of the alternative fuel cycles considered involve back end fuel cycle stages, and therefore, require the present valuing of costs and revenues that occur post-irradiation to the beginning of irradiation and combining them with the front end costs to determine the levelized cost. In order to perform the calculation, the lag times instead of lead times are incorporated into the cash flows that occur post-irradiation.

The first alternative considered is the AIROX treatment of the GFR spent fuel and disposition in LWRs, and while several variations on this general theme are considered at greater length in section 4.4.3, Chapter 7 and Chapter 11, this section discusses the methods for incorporating the costs and revenues associated with AIROX treatment at the back end of the nuclear fuel cycle.

For the purposes of conducting an economic analysis, the costs for B&B GFR spent fuel treatment are based on research conducted for AIROX processes for LWRs. An AIROX-like process, OREOX, is the proposed method for the disposition of PWR fuel in CANDU reactors. The direct use of PWR spent fuel in CANDU reactors (DUPIC) was investigated by the Korea Atomic Energy Research Institute (KAERI) jointly with the Atomic Energy of Canada Limited and the US Department of State beginning in the 1990's[11].

The research conducted by KAERI in this time frame focused on developing a conceptual design for a DUPIC plant and calculating the cost of DUPIC fuel fabrication, handling, transportation, and disposal [11,12,10,9]. The unit costs were assumed to be the same for a hypothetical B&B GFR spent fuel treatment facility and transportation scheme. Of key interest in the current assessment is the DUPIC fuel manufacturing unit cost and associated transportation costs. The results of references [11] and [9] list unit cost estimates for DUPIC fuel with maximum, minimum, and most likely values in 1999 USD. The fabrication costs were estimated between ~450 1999 USD/kg<sub>HM</sub> to ~830 1999 USD/kg<sub>HM</sub>. The transportation costs range between ~12 1999 USD/kg<sub>HM</sub> and ~55 1999 USD/kg<sub>HM</sub>.



In the current assessment, it is assumed that in a single post-irradiation treatment stage the GFR spent fuel is transported twice, with no process losses, and fabricated all at the same point in time. While only approximate, the approach is judged acceptable given the large range of the cost estimates and the hypothetical nature of the calculation. The prices are also given in 1999 USD while the analysis is done in 1994 USD. Inflation data could be used to escalate the 1994 USD to 1999 USD equivalent values, but instead the 1999 USD price estimates are held constant (assuming the same numerical value for the costs in 1994 USD), thus adding some conservatism to the economic analysis.

Therefore the AIROX treatment unit cost is estimated according to Equation (2.21).

$$UC_{AIROX} = (2UC_{trans} + UC_{fab}) \quad (2.21)$$

Where  $UC_{AIROX}$  is the approximated unit cost of the stage in 1994 USD/kg<sub>HM</sub>,  
 $UC_{trans}$  is the most likely unit cost of transportation in 1999 USD/kg<sub>HM</sub> from [9], and  
 $UC_{fab}$  is the most likely unit cost of fabrication [1999 USD/kg<sub>HM</sub>] from [9].

The most likely transportation and fabrication unit costs are 43.9 and 616 in 1999 USD/kg<sub>HM</sub> respectively, thus yielding an approximate AIROX unit cost of 704 1994 USD/kg<sub>HM</sub>.

The AIROX treatment of spent fuel is assumed to occur after four years of cooling post-irradiation in order to be irradiated in a LWR after five years of total cooling. The AIROX treatment costs are then present valued to the beginning of GFR irradiation and included in the fuel cycle cost. The treated fuel would then be sold to a LWR four and a half years post GFR irradiation. The value (sale price) of the treated fuel is taken as the equivalent of fabricated (though unirradiated) fuel assemblies for a standard PWR as calculated according to the reference model discussed in section 2.4.1.

Given the lag times of four years and four and a half years for the AIROX treatment and subsequent sale, the present values of these transactions are calculated according to Equation (2.22) and incorporated into the fuel cycle cost assessment.

$$C_{AIROX} \approx M_{fab} (1 - AB) UC_{AIROX} \exp \left[ -i_c \left( \frac{nT}{CF} + La_{AIROX} \right) \right]$$

$$C_{LWR} \approx M_{fab} (1 - AB) UR_{LWR} \exp \left[ -i_c \left( \frac{nT}{CF} + La_{LWR} \right) \right] \quad (2.22)$$

Where C is the contribution to the fuel cycle cost,  
AB is the atom-fraction burnup at discharge (0.15),  
La is the lag time (4 or 4.5 years),  
UR is the unit revenue from the sale, and will have a negative value,  
AIROX denotes the treatment stage, and  
LWR denotes the sale of the treated fuel to a LWR.

The unit revenue is assumed to be the same as the worth of LWR fuel at the front end of a fuel cycle at the end of the fabrication stage. This quantity is calculated by present valuing the cost of

all front-end fuel cycle stages for the LWR OTTO to the end of the fabrication stage. It is calculated by adjusting the present value formulae in Equation (2.18) to subtract the fabrication lead time from each future worth factor as shown in Equation (2.23).

$$\begin{aligned}
 C_{ore}' &= UC_{ore} M_{ore} \exp(i_C (Le_{ore} - Le_{fab})) \\
 C_{con}' &= UC_{con} M_{con} \exp(i_C (Le_{con} - Le_{fab})) \\
 C_{enr}' &= UC_{enr} SWU \exp(i_C (Le_{enr} - Le_{fab})) \\
 C_{fab}' &= UC_{fab} M_{fab} \\
 UR_{LWR} &= C_{ore}' + C_{con}' + C_{enr}' + C_{fab}'
 \end{aligned}
 \tag{2.23}$$

Aside from the sale of treated fuel to a LWR, other alternative fuel cycle concepts were considered. Direct recycle into the GFR was also considered; in this case, the method for evaluating the unit revenue is directly akin to the LWR option, except GFR costs are used instead. Additionally, when exotic fuel forms, such as  $U^{15}N$  are employed, the option of recovering the nitrogen was explored. It was optimistically assumed that, without an increase in the unit cost of AIROX processing, the nitrogen could be recovered and sold with no loss. The unit revenue from this sale is included at the point where the treated fuel is sold to either a LWR or back to the GFR.

## 2.5. Chapter 2 Summary

This chapter has described the codes and equations used throughout this work to design and evaluate the B&B GFR core. In each area, codes and methods were compared to comparable experiments, assessments, or experience to verify their validity for their application. The ZPR-9 FCA experiment was not only used to verify MCNP, but also aid in selecting the appropriate cross section sets. Comparison of the thermal hydraulics model to the reference values for the GA GCFR verified the applicability of the finite volume approach. Lastly, using the methodology for assessing fuel cycle economics and arriving at the appropriate LWR fuel cycle cost confirms this final methodology.

## Chapter 3. Core Materials Selection

### 3.1. Introduction

Before design work began, an exhaustive study of potential candidate fuels and other core materials was conducted to identify those materials with the highest B&B potential. The fuel must have a sufficiently large breeding gain and neutron yield to support subcritical reload fuel assemblies until the reload fuel builds up a critical concentration of  $^{239}\text{Pu}$ . Therefore the design of a B&B GFR will be driven by neutronics considerations.

A list of potential B&B fuels was developed based on a variety of sources. Ceramics and metallic alloys were chosen for candidates; some of these materials were exotic and evaluated primarily to gain insight into neutronic phenomena.

$\text{UO}_2$  was studied as a potential fuel based on its widespread use in conventional reactors. UN fuel was considered based on its high heavy metal density [32].  $\text{U}_3\text{N}_2$  was also considered, but at low temperature ( $< 900\text{ }^\circ\text{C}$ ) the fuel restructures to UN [31]. UC, US, UP, and  $\text{U}_3\text{Si}$  are all ceramics that have been suggested as potential fast reactor fuel [67].  $\text{U}_3\text{Si}$  was not considered based on its low melting temperature of  $930\text{ }^\circ\text{C}$  [32].

Several ceramics were selected based on commonalities with the already chosen candidates. USe and UTe were selected as exotic candidates because of the chemical similarity to US, however, selenium and tellurium are heavier than sulfur, hence they do not significantly contribute to neutron moderation in the fuel. UCO was selected as a candidate because of its similarity to  $\text{UO}_2$  and UC and recent interest in its use as an HTGR fuel.  $\text{U}^{15}\text{N}$  was also analyzed because it offers some neutronic advantages over UN and is under serious consideration by Japanese researchers [35].

A set of metallic alloy fuel candidates was developed based on earlier LMFBR program experience and on the work of the ANL Reduced Enrichment for Research Test Reactors (RERTR) program. ANL, within the scope of the RERTR program, has evaluated several high heavy metal density fuels for potential use in high flux research reactors. Based on that selection, several alloys were identified for potential use in a GFR. These include U-2Mo, U-5Mo, U-9Mo, U-10Zr, and U-4Zr-2Nb [32]. Each of these metals is employed as the uranium stabilized gamma phase. Table 3-1 summarizes some of the properties of the fuel forms that were investigated.

Table 3-1 Fuel Properties [32,31,67,4]

Fuels	Metallic Alloy	Density	Melting Point	U density
	Compound		(*or max temp)	
		[g/cc]	[°C]	[gU/cc]
U-10Zr	Metallic Alloy	16.00	1160	14.40
U-2Mo	Metallic Alloy	18.50	1135	18.10
U <sub>3</sub> Si	Compound	15.40	930*	14.80
U <sub>3</sub> Si <sub>2</sub>	Compound	12.20	1650	11.30
U-4Zr-2Nb	Metallic Alloy	17.30	1135	15.90
U-5Mo	Metallic Alloy	17.90	1135	17.00
U-6.5Mo	Metallic Alloy	17.50	1135	16.40
U <sub>6</sub> Fe	Compound	17.70	815*	17.00
U <sub>6</sub> Mn	Compound	17.80	725*	17.00
U <sub>6</sub> Ni	Compound	17.60	790*	16.90
U-7Nb	Metallic Alloy	17.00	1160	15.00
U-8Mo	Metallic Alloy	17.30	1135	15.90
U-9Mo	Metallic Alloy	17.00	1135	15.50
UAl <sub>2</sub>	Compound	8.10	1590	6.60*
UC	Compound	13.60	2400	13.00
UN	Compound	14.30	2650	13.50
UO <sub>2</sub>	Compound	10.90	2750	9.70
UP	Compound	10.20	2600	8.99
US	Compound	10.90	2475	9.58
USe	Compound	11.30	--	8.48
UTe	Compound	10.43	1740	6.79
U <sub>3</sub> N <sub>2</sub>	Compound	--	900*	--
UCO	Compound	12.25	2400	10.96

### 3.2. Methodology

Unit cell analyses were used to compare the neutronic behavior of each candidate fuel over a burnup of 160 MWD/kg<sub>HM</sub>. The fuels were compared on the basis of consistent geometry, as the volume fraction of structure and coolant was the same in each case.

The ceramic fuels were taken at 85% of their theoretical density (assumed to accommodate high burnup). The metallic fuels were modeled at 75% theoretical density [45] and a liquid lead metallic bond was added to the fuel region of the cell. Since fuel swelling is commonly much higher in metallic fuel than in ceramics, this approach was taken to more accurately account for fuel designed to reach high burnup.

A unit cell was chosen to analyze the different fuels because it takes into account the basic and heterogeneous nature of the reactor core. The unit cell sacrifices the precision of a full core calculation in the interest of speed of computation. In the current work, the analysis was being used predominantly for the indication of neutronics trends, and the analysis of a unit cell is well suited for this purpose.

The fuel dimensions were based on LMFBR and earlier GCFR fuel parameters [63]. The fuel zone is 1 meter tall and 0.7 cm diameter. A 10 cm BaS axial reflector is added to the top and bottom of the model. The cladding thickness was 0.055 cm, based on an average of the LMFBR (0.07 cm) and AGR (0.038 cm) clad thickness [63,1]. The outer cell boundary was cylinderized to facilitate the alteration of the volume fraction of coolant. The volume fraction of coolant was specified to be ~ 35%. Figure 3.1 and Table 3-2 illustrate the unit cell geometry.

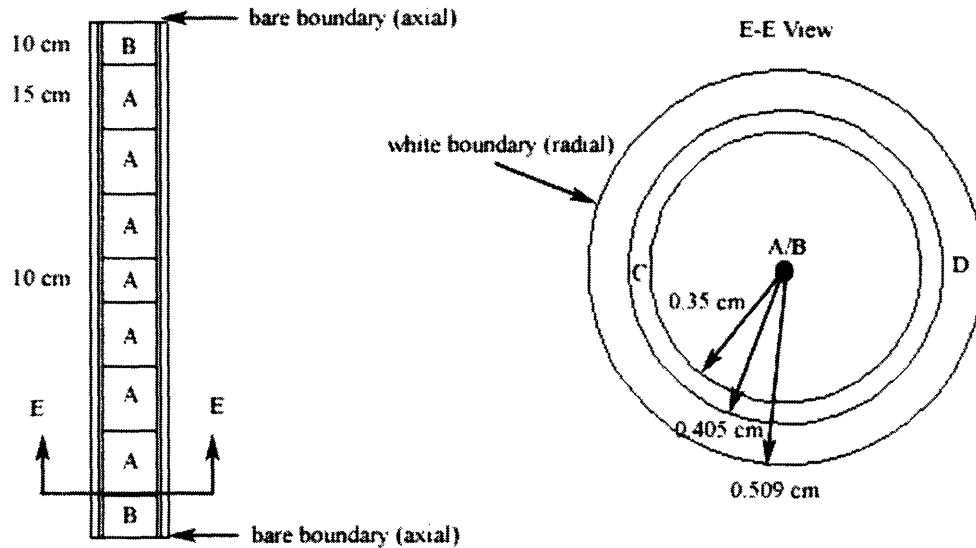


Figure 3.1 Unit Cell Geometry (not to scale)

The model is a tall cylinder. The figure is not to scale and the dimensions are quoted in centimeters. The different materials are denoted with letters. Table 3-2 gives the materials for each letter.

Table 3-2 Zone Identification

Zone Label	Region	Density	Temperature
A	Fuel Region	--	$1.200 \times 10^{-7}$ MeV (1120 °C)
B	BaS Axial Reflector	4.25 g/cc	$0.900 \times 10^{-7}$ MeV (770 °C)
C	HT-9 Stainless Steel	7.81 g/cc	$0.900 \times 10^{-7}$ MeV (770 °C)
D	Helium Coolant	$5.30 \times 10^{-3}$ g/cc	$0.623 \times 10^{-7}$ MeV (450 °C)

Only the fuel material in the pin was changed based on the case to be studied. The cladding material was taken to be HT-9 stainless steel at 7.81 g/cc. The coolant was helium gas at 450 °C and 8 MPa of pressure. Axially, the fuel was divided into seven regions. At BOL these regions had the same material composition.

A MCNP4c2 model of the unit cell was constructed based on the parameters given. The unit cell is annular with a white reflecting outer cylindrical boundary. The entire model is 120 cm tall from bottom to top. The top and bottom, axially, are terminated by bare boundary conditions.

A constant enrichment was assumed for the BOL fuel. Each fuel type was assumed to be 10 % enriched in  $^{235}\text{U}$  by atomic fraction. The enrichment was selected so that the  $\text{UO}_2$  fuel case would

have a  $k_{\text{eff}}$  slightly larger than unity at BOL. The choice to maintain consistent enrichment for all fuels was made so that the ratio of fissile to fertile material in each fuel would be identical at BOL. However, as discussed in section 1.3, the initial enrichment has little impact on the long-term reactivity trends, and the current scoping analysis is meant to examine the differences in long-term trends.

The annular unit cell (concentric cylinder) model was compared with hexagonal (triangular pitch) as well as square lattice models for UC fuel. The other models were made by changing the outer surfaces of the cylinderized model whilst maintaining the same volume fraction of coolant. This comparison was carried out to confirm that the eigenvalue calculation is not heavily dependent on the lattice geometry. Table 3-3 summarizes the results of the calculations.

Table 3-3 Comparison of Lattice Geometry for UC fuel

Lattice Geometry	$k_{\text{eff}}$ at BOL	$\sigma$ standard deviation
Annular	1.06548	0.00062
Square	1.06579	0.00058
Triangular	1.06594	0.00060

The eigenvalues differ by less than a standard deviation. The close agreement in  $k_{\text{eff}}$  shows that the volume fraction, and not the lattice geometry, is the leading determinant of the unit cell criticality. Therefore, the unit cell conclusions can be translated directly between different lattice geometries for a pin-type core.

The pin-cell model results are, therefore, representative of a wide range of lattice geometries and BOL enrichments; thus making this mode of comparison suitable for fuel screening.

### 3.3. Ceramic Fuels

To characterize a fuel, the peak reactivity and reactivity gain were computed for the reactivity histories associated with each fuel. The conversion ratio was also computed, and the trend in the conversion ratio during fuel burnup was also examined.

Lastly, to explain the reactivity behavior of the fuels, the flux spectra at BOL for each of the fuel types were calculated. For a single case the one group cross sections for  $^{239}\text{Pu}$  were computed at each burnup step to evaluate the effect of burnup on the spectrum and  $^{239}\text{Pu}$  worth.

#### 3.3.1. Reactivity

The B&B GFR fuel must not only attain high reactivity in a fast spectrum at low uranium enrichment, but it must also have an affinity for substantial breeding to sustain reactivity in a short irradiation time as to allow for practical reactor design. Since the reactivity is heavily spectrum dependent, the best neutronics performance is not necessarily associated with those fuel types with the largest breeding ratios.

The MCODE results for the unit cell reactivity over burnup was tabulated for each burnup step between 0 MWD/kgHM and 160 MWD/kgHM. The peak reactivity, and rate of reactivity gain and burnout can be viewed directly from the plot in Figure 3.2.

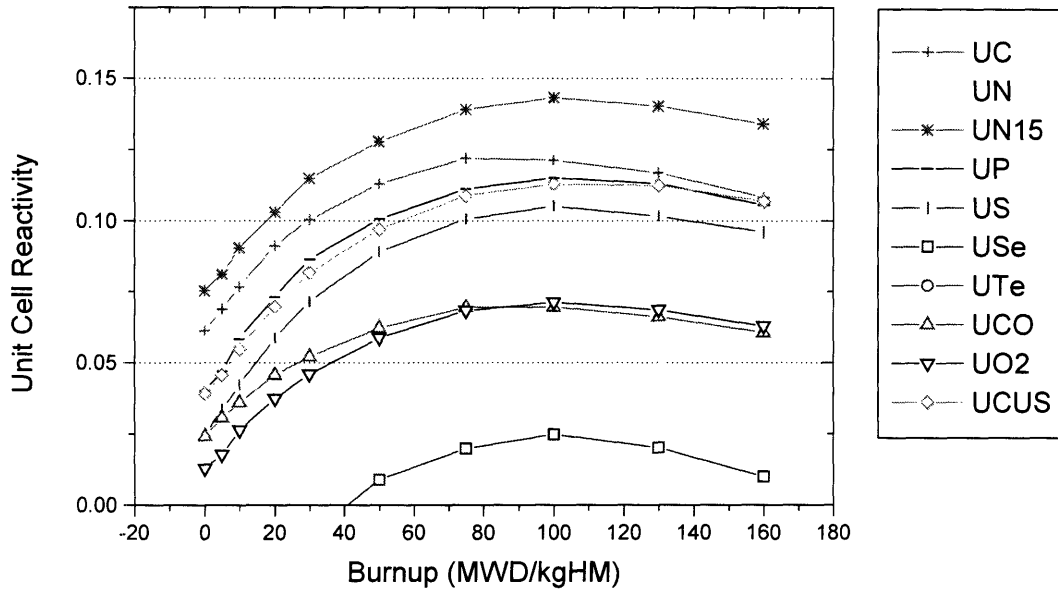


Figure 3.2 Ceramic Fuel Reactivity Histories

Quantitatively, the peak reactivity and gain were calculated for each fuel type. Qualitatively, the slope of the reactivity post peak is observed from the graph. The peak reactivity is the highest unit cell reactivity attained as a function of burnup. The gain is the difference between the peak and BOL reactivity. For the most part the reactivity histories are parallel with subtle differences in slope.

Table 3-4 summarizes the peak reactivity and gain for each of the ceramic fuel types analyzed. An ideal B&B fuel would attain large peak reactivity and maintain the high reactivity through burnup. The gain is computed here as well to characterize a fuel's affinity for breeding reactivity. The results show, however, that there is no one fuel which has the largest values for both of these parameters simultaneously.

Table 3-4 Reactivity Parameters for Fuel Ceramics

Reactivity	UC	UN	U <sup>15</sup> N	UP	US	USe	UTe	UCO	UO <sub>2</sub>	UC/US
Gain	0.060	0.051	0.068	0.075	<b>0.080</b>	0.083	0.086	0.046	0.058	0.074
Peak	0.122	0.090	<b>0.143</b>	0.115	0.105	0.025	0.027	0.070	0.071	0.113

Enough neutron histories were run in MCNP such that the standard deviation of the reactivity figures is approximately 0.0006 in all cases. Fuels with large peak reactivity (such as U<sup>15</sup>N) have mediocre gains (0.068). US, on the other hand has a strong gain (0.080), but a low peak reactivity (0.105). UC has the second highest peak reactivity (0.122). When UC and US are mixed in a solid state solution (50% / 50% by volume), the resultant solution has a peak reactivity between that of UC and US. The solid solution gain is slightly lower than the pure US fuel.

Interestingly, though the peak reactivity differs dramatically for each fuel type, the gains are similar among every species.

After the peak several of the fuel types burn out quickly. UC has a relatively steep slope post peak reactivity, whereas the UC/US solid state solution has a relatively shallow slope post peak reactivity, and  $U^{15}N$  similarly has a shallow slope post peak reactivity.

USe and UTe are subcritical at BOL, and the UTe reactivity remains negative throughout burnup. USe eventually gains enough reactivity to attain a peak of 0.025. These two fuels contain strongly absorbing, high Z constituents. After USe and UTe,  $UO_2$  and UCO attain the next lowest peak reactivities. These two fuels, however, have very little parasitic absorption in the low Z constituents.

US and  $UO_2$  have similar heavy metal densities [32]. Therefore the difference in reactivity through burnup is attributable to the differences in the flux spectrum. The flux spectrum influences the burnup characteristics for these two fuels in such a way that  $UO_2$  attains lower peak reactivity with a smaller gain than US.

In Figure 3.3 a plot of the difference between the peak reactivity and the reactivity, as a function of burnup, is shown. The graph illustrates the gain clearly; the fuels with the greatest values at BOL have the largest gains. Additionally, the fuels with the smallest values at 160 MWD/kg<sub>HM</sub> have the smallest post peak reactivity swings.

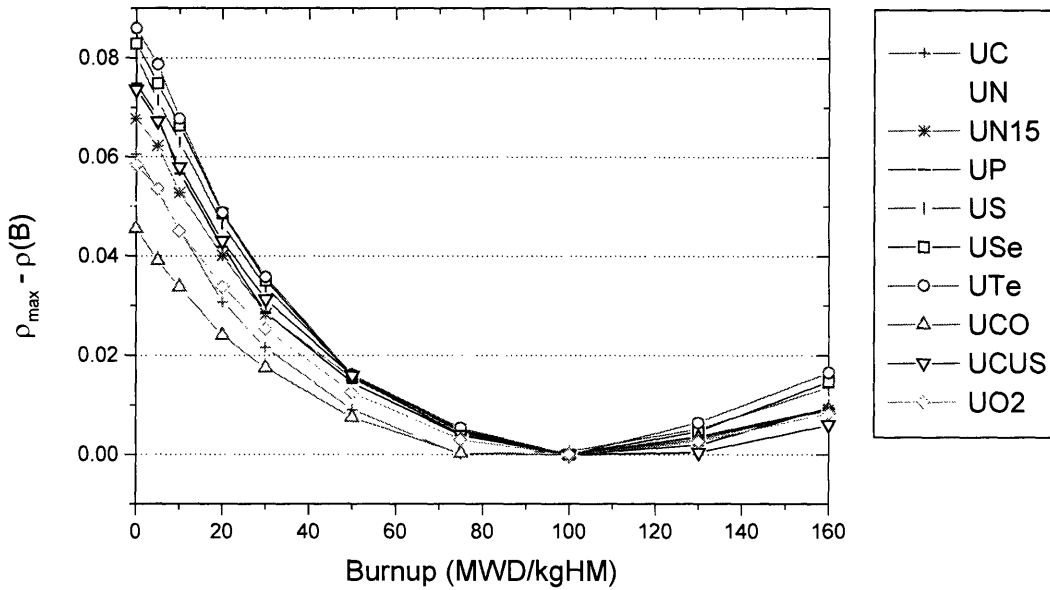


Figure 3.3 Difference between Peak and Instantaneous Reactivity for Ceramic Fuels

The UC/US solid state solution has one of the strongest gains as well as the shallowest post peak decline in reactivity.  $U^{15}N$  has a gain and post peak slope near the average. Since every curve is shifted to the peak reactivity for that fuel, Figure 3.3 only identifies the trend in reactivity and not



the absolute reactivity. Overall, most of the fuels have the same behavior. Subcritical fuels (such as USe and UTe), and highly moderating fuels (such as UCO) can be ignored because of insufficient reactivity. The remainder of the fuels have mostly similar shapes, and hence the most important measure of fuel performance is peak reactivity.

Fuels approach an asymptotic reactivity trend at high burnup, as discussed in section 1.3. The gain, which is meant to characterize a fuel's affinity to breed  $^{239}\text{Pu}$  quickly, is not a very good metric for fuel neutronic performance. In actual B&B operation, the reload fuel will have low enrichment, and will be subcritical at the BOL. The level of burnup where enough  $^{239}\text{Pu}$  is bred to reach criticality is not dictated by the fuel's gain, as for each fuel type the trend in reactivity is essentially the same, while large differences in peak reactivity are apparent.

### 3.3.2. Ceramic Fuel Flux Spectra

The reactivity trends as a function of burnup, though similar in shape, are heavily dependent on the one group  $^{239}\text{Pu}$  cross sections. As was discussed in section 1.3, the ratio of the fission to absorption microscopic cross section for  $^{239}\text{Pu}$  increases with the hardness of the flux spectrum. The BOL flux spectra were computed for the different ceramic fuel types and are plotted in Figure 3.4.

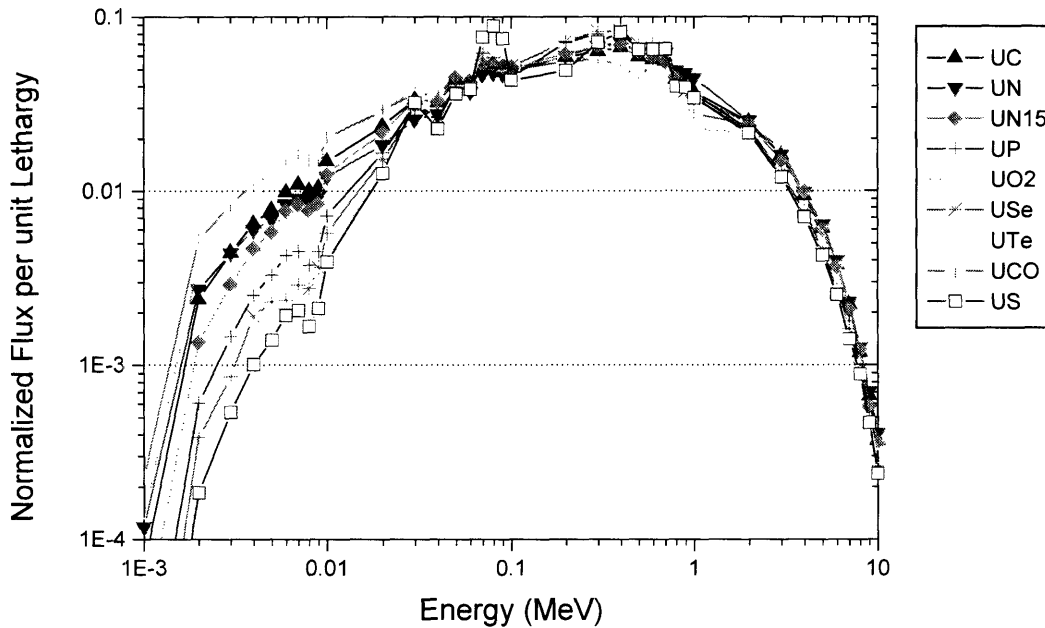


Figure 3.4 Ceramic Fuel BOL Flux Spectra

On the log scale it is hard to distinguish the flux spectrum hardness at energies above 1 MeV, however, in the epithermal energy range above 1 keV, the differences in the spectra are clearer. The flux is normalized to unity, and therefore, by observing the fuel types that exhibit large normalized flux per unit lethargy values at low energy, one can infer which of the fuels are associated with softer spectra.

UCO, UO<sub>2</sub>, and UC have the softest spectra. These fuels contain strong moderating (low Z) constituents. The hardest flux spectra are associated with US, USe, and UP.

A metric used for quantifying the spectrum hardness is the flux-per-unit-lethargy-weighted average epithermal energy. This is an artificial metric that roughly predicts how far shifted to the right on the energy axis the flux per unit lethargy curve is. Alone this metric does not have a significant physical interpretation. Equation (3.1) shows the approximate formula for calculating the average epithermal energy.

$$\langle E \rangle = \frac{\int_{0.05eV}^{1MeV} Ef(E)dE}{\int_{0.05eV}^{1MeV} f(E)dE} \approx \frac{\sum_{E=1e-3MeV}^{1MeV} Ef(E)}{\sum_{E=1e-3MeV}^{1MeV} f(E)} \quad (3.1)$$

Where  $\langle E \rangle$  is the weighted energy, and  $f$  is the normalized flux per unit lethargy.

The weighting function is calculated by taking the flux tally for each energy bin and dividing the tally by the lethargy width of the bin; then the value of the normalized flux per unit lethargy is assigned to the upper energy of the bin.

The higher the average epithermal energy, the more the flux curve is shifted to the right on the energy axis, and thus the harder the spectrum. This is not necessarily a very good metric for fuels with large fast absorption. Some of the fuel types have constituents with low absorption cross sections, UC for example. The scattering from the carbon nuclei in the fuel will scatter the fast neutrons to lower energy and shift the curve towards lower energies. In fuels with large fast parasitic absorption cross sections, UN for example, the flux at very high energy (above several hundred keV) is depressed without a corresponding increase in the low energy flux (around several keV). Large fast absorption does not shift the curve, but rather, squeezes the flux shape and creates a peak at intermediate energies.

For the fuel types analyzed, this fast absorption effect is small, and for the most part, the flux-weighted energy gives an approximate ordering for the flux hardness. Table 3-5 summarizes the spectrum hardness using the average epithermal energies for all of the evaluated ceramic fuels.

Table 3-5 Average Epithermal Flux Energy for Fuel Ceramics

Fuel	<E> [MeV]
UP	0.351
UN	0.348
UTe	0.343
Use	0.334
US	0.329
U <sup>15</sup> N	0.317
UC	0.312
UCO	0.283
UO <sub>2</sub>	0.281
Average	0.322
std-dev	0.0262

The table shows that UP has the hardest spectrum, followed by UTe, Use, and US. This is visible on the plot in Figure 3.4. UO<sub>2</sub>, UCO and UC have the softest spectra.

Only BOL spectra are compared here. For the case of UC fuel the flux averaged one group <sup>239</sup>Pu microscopic cross sections were tabulated. The results are shown in Table 3-6.

Table 3-6 Burnup Behavior of <sup>239</sup>Pu Cross Sections for UC fuel

UC										
B[MWD/kg <sub>HM</sub> ]	0	5	10	20	30	50	75	100	130	160
$\sigma_f^{49}$ [b]	1.682	1.686	1.684	1.684	1.684	1.682	1.684	1.683	1.685	1.684
$\sigma_a^{49}$ [b]	0.372	0.375	0.374	0.374	0.374	0.371	0.374	0.372	0.377	0.378
$\sigma_f^{49} / \sigma_a^{49}$	0.819	0.818	0.818	0.818	0.818	0.819	0.818	0.819	0.817	0.817

The ratio of fission to absorption microscopic cross section for <sup>239</sup>Pu is quite constant through irradiation, which indicates that the fission product buildup does not have a large impact on the fuel region flux spectrum. Therefore the BOL spectra may be used to predict the value for <sup>239</sup>Pu worth during burnup.

### 3.3.3. Conversion Ratio

The flux spectrum itself does not explain the burnup trends for the fuels, but a combination of the spectrum hardness and conversion ratio explain the peak reactivity and gain for each case. The conversion ratio was computed for each fuel type at every burnup step. Figure 3.5 illustrates the trend in the conversion ratio during burnup. The conversion ratio ranges between 1.02 and 0.91. In all cases the conversion ratio decreases as a function of burnup.

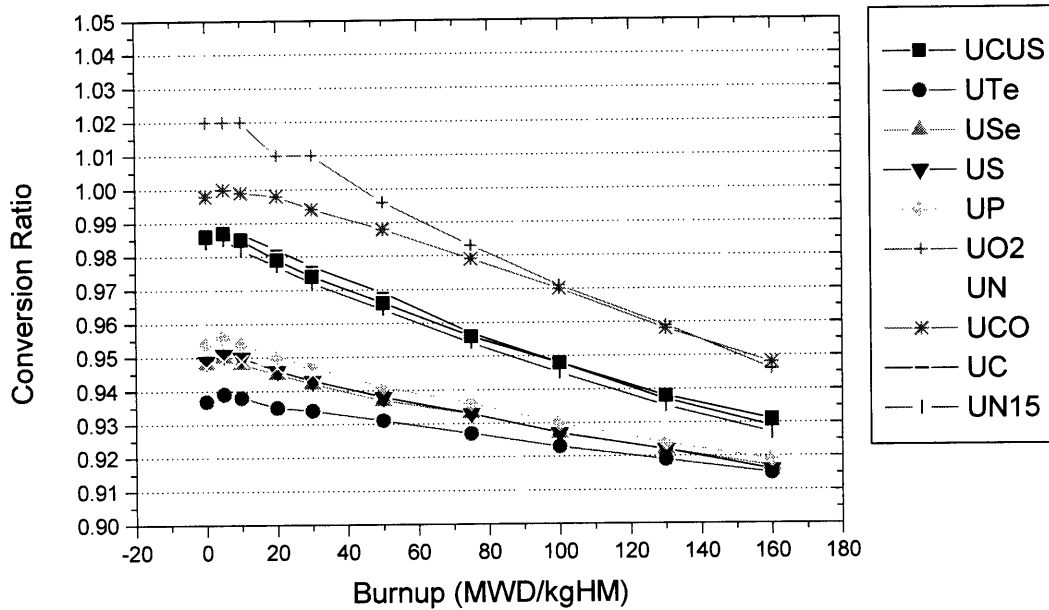


Figure 3.5 Ceramic Fuel Conversion Ratio vs. Burnup

UO<sub>2</sub> and UCO have the highest conversion ratios. US has one of the lowest conversion ratios. UC and U<sup>15</sup>N have midrange conversion ratios.

It may appear counterintuitive that the fuels with the highest conversion ratio exhibit the lowest peak reactivity and relatively weak reactivity gain. UO<sub>2</sub> is an excellent example of a fuel that has very high conversion ratio (1.02 at BOL), with low peak reactivity and weak gain.

The explanation of the seemingly counterintuitive disconnection between reactivity and conversion is inherent in the nature of  $\eta^{49}$  (the ratio of the neutron production from <sup>239</sup>Pu fission to the loss of neutrons to <sup>239</sup>Pu absorption) and the fission cross section for fertile <sup>238</sup>U.

UO<sub>2</sub> contains two oxygen atoms for each atom of heavy metal. The oxygen slows neutrons down to epithermal energies inside the fuel. Thus, the probability of resonance capture in fertile <sup>238</sup>U is much higher than in the fuel cases where fewer low Z atoms are present. The resonance capture advantage of UO<sub>2</sub> increases the conversion ratio.

The subsequent spectrum softening from the oxygen in UO<sub>2</sub> has a two-pronged effect that impacts the total fission cross section. Spectrum softening reduces the value of  $\eta^{49}$  and also reduces the fertile fission fraction, because a smaller fraction of the neutron flux is above the 1 MeV <sup>238</sup>U fission threshold. Since there is no plutonium in the fuel at BOL, the fertile fission fraction (FFF) at BOL is given by the ratio given in Equation (3.2).

$$FFF = \frac{\Sigma_f^{28}}{\Sigma_f^{28} + \Sigma_f^{25}} = \frac{1}{1 + \frac{\Sigma_f^{25}}{\Sigma_f^{28}}} = \frac{1}{1 + \frac{N^{25} \sigma_f^{25}}{N^{28} \sigma_f^{28}}} = \frac{1}{1 + \frac{X \sigma_f^{25}}{(1-X) \sigma_f^{28}}} \quad (3.2)$$

Where X is the enrichment (10 a/o in each case).

For UO<sub>2</sub> the fertile fission fraction is 0.164 and for U<sup>15</sup>N this fraction is 0.181. This represents a slight increase in fertile fission for the harder spectrum fuel. U<sup>15</sup>N has a harder spectrum than UO<sub>2</sub> and a higher heavy metal density. Though it is clear from the reactivity history that the U<sup>15</sup>N fuel achieves a substantially larger peak reactivity, a comparison between these two fuels was made to contrast the ratio of peak <sup>239</sup>Pu content to the initial fertile inventory and the peak reactivity as shown in Table 3-7.

Table 3-7 U<sup>15</sup>N peak values vs. UO<sub>2</sub> peak values

	N28(0) atoms/b-cm	N49(peak) atoms/b-cm	<u>N49(peak)</u> N28(0)	ρHM(TD) gU/cc	$\frac{\sigma^{49f}}{\sigma^{49a}}$	ρ peak
U <sup>15</sup> N	0.02613	0.00202	0.077	13.5	0.84	0.143
UO <sub>2</sub>	0.0186	0.00155	0.083	9.70	0.79	0.0713

UO<sub>2</sub> achieves a larger percentage of <sup>239</sup>Pu content, however, the U<sup>15</sup>N peak reactivity is more than double that for UO<sub>2</sub>. The spectral effects on η<sup>49</sup> and heavy metal density clearly outweigh the benefits of improved conversion ratio by this comparison.

### 3.3.4. Conclusions

Therefore, for a B&B reactor, designing to maximize the conversion ratio is not the best approach. Instead, the B&B GFR fuel must be chosen so that the production rate of reactivity, and not fissile mass, is maximized. Therefore, peak reactivity is a much better measure of overall fuel performance than conversion ratio as discussed in section 1.3, but now clearly illustrated.

Peak reactivity is tightly coupled with the heavy metal density, parasitic absorption, and η<sup>49</sup>. The two former parameters dictate the initial reactivity whereas the latter parameter influences the trend in the reactivity. In general harder spectra, high heavy metal density fuels with weakly absorbing constituents have the best performance. U<sup>15</sup>N has a strong mix of these three characteristics. U<sup>15</sup>N has the highest heavy metal density of any of the ceramic fuels (13.5 gU/cc Theoretical Density) and the flux weighted average energy is only slightly lower than that for US (0.317 MeV for U<sup>15</sup>N and 0.329 MeV for US). From a purely neutronic standpoint U<sup>15</sup>N appears to be an excellent potential nuclear fuel for B&B operation.

As an alternative, UC is proposed. UC has very low parasitic absorption and relatively large heavy metal density (13.0 gU/cc TD). UC has a relatively soft spectrum, but the improvement in conversion ratio partially offsets the <sup>239</sup>Pu worth disadvantage so that a significant peak reactivity of 0.122 is achieved. UC has only one moderating atom per heavy metal atom so the spectrum is harder than in the case of UO<sub>2</sub> or UCO.

UP was also considered. The reactivity history illustrated in Figure 3.2 is deceptive. The ENDFB6 cross section library used for the UP calculation lacks any resonance structure. A plot of the microscopic  $^{31}\text{P}$  cross section is included in Figure 3.6.

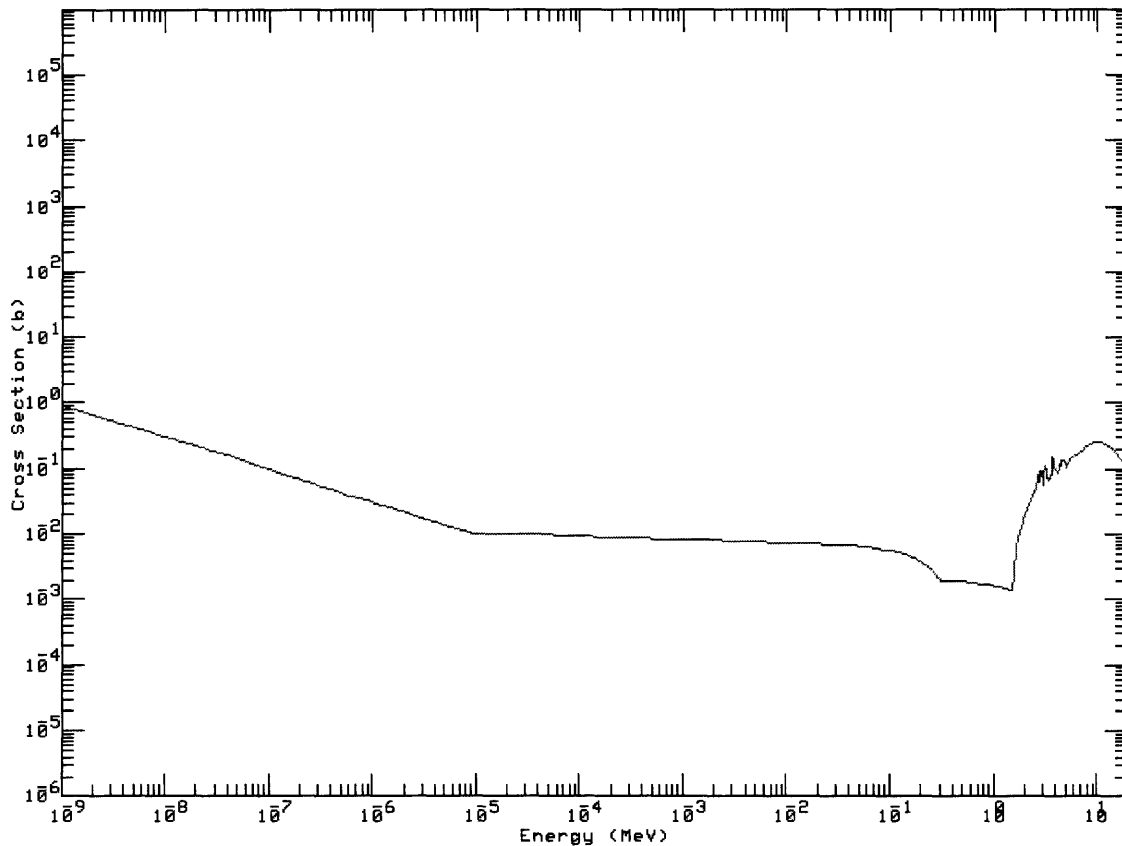


Figure 3.6 Microscopic  $^{31}\text{P}$  Absorption Cross-section [46]

As can be seen, there are no resonances. At high fuel temperature and high average neutron energy, the resonance absorption in the fuel region by the light constituent has a significant impact on the overall performance. UP has a slightly lower peak reactivity than UC, and is therefore not a leading candidate compared to  $\text{U}^{15}\text{N}$  or UC. It is also likely that given more accurate cross section values its performance would be poorer than shown by the present calculations. Therefore, UP is not recommended for B&B service.

### 3.3.5. Chemical Concerns

Supercritical  $\text{CO}_2$  has also been proposed as an alternative to Helium for a GFR coolant. The S- $\text{CO}_2$  in core is at 20 MPa and 450 °C. The cycle efficiency for a direct cycle promises to outperform helium at the same temperature [18]. Helium Brayton cycles are not competitive except at significantly higher temperatures. By utilizing the S- $\text{CO}_2$  cycle, and the lower coolant temperatures, it will be feasible to use core materials (cladding and structural materials) that have relatively low melting temperatures compared with those used in high temperature reactors.

Most of the ceramic fuel types proposed have interactions with  $\text{CO}_2$  at the temperatures of interest. Thermo-chemical calculations of free energy show that UC, US, and UN will react with  $\text{CO}_2$  [62]. Whereas US oxidizes at the same density, UC and UN will oxidize at a significant

decrease in density [62]. Therefore UC or UN may not be employable in a CO<sub>2</sub> cooled reactor because of the threat of fuel damage should the cladding be breached.

### 3.4. Metallic Fuels

Similar to the investigation of ceramic fuel types, analyses were done for the metallic alloy fuels. Figure 3.7 shows the reactivity histories for the fuel alloys. The important characteristics of the plot are again, the peak reactivity, the gain, and the character of the reactivity behavior after the peak. As can be seen from the figure, the low molybdenum alloys and U-10Zr exhibit similar reactivity histories. The U-4Zr-2Nb alloy has the steepest drop in reactivity after the peak, and one of the lowest peak reactivities.

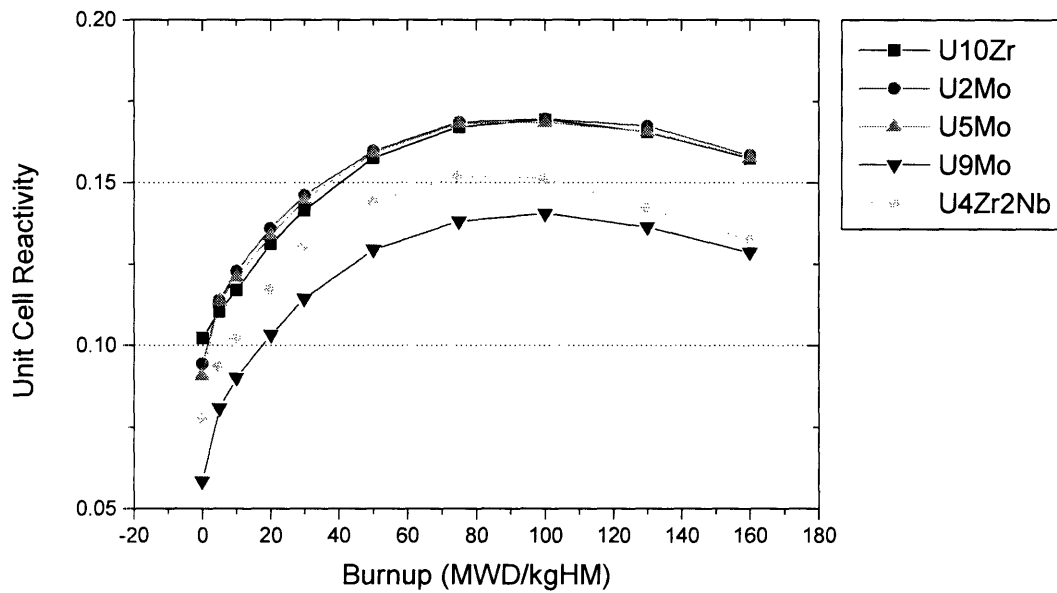


Figure 3.7 Alloy Fuel Reactivity Histories

The theoretical heavy metal density of the metallic alloys is consistently greater than that for the ceramics. The peak reactivities of the alloys are greater than the peak reactivities attainable in the ceramic fuels (the ceramic fuel reactivities are shown in Table 3-8).

Table 3-8 Reactivity Parameters for Alloy Fuels

Reactivity	U-10Zr	U-2Mo	U-5Mo	U-9Mo	U-4Zr-2Nb
Gain	0.067	0.075	0.078	<b>0.082</b>	0.074
Peak	<b>0.169</b>	0.170	0.168	0.140	0.152

Of the fuel alloy constituents, zirconium is the weakest fast neutron absorber. Of the metals analyzed in this study U-10Zr has the lowest heavy metal density (14.40 gU/cc TD). The remaining candidates have heavy metal densities in excess of 15.50 gU/cc, where U-9Mo has the second lowest heavy metal density of the alloys.

U-9Mo has the strongest reactivity gain. The lower weight fraction molybdenum alloys are comparable to U-10Zr. The post peak reactivity slopes are comparable among the molybdenum alloys.

To more clearly illustrate the burnup behavior in reactivity, the difference between peak and instantaneous reactivity is plotted in Figure 3.8. The graph is analogous to the plot for ceramic fuels shown in Figure 3.3.

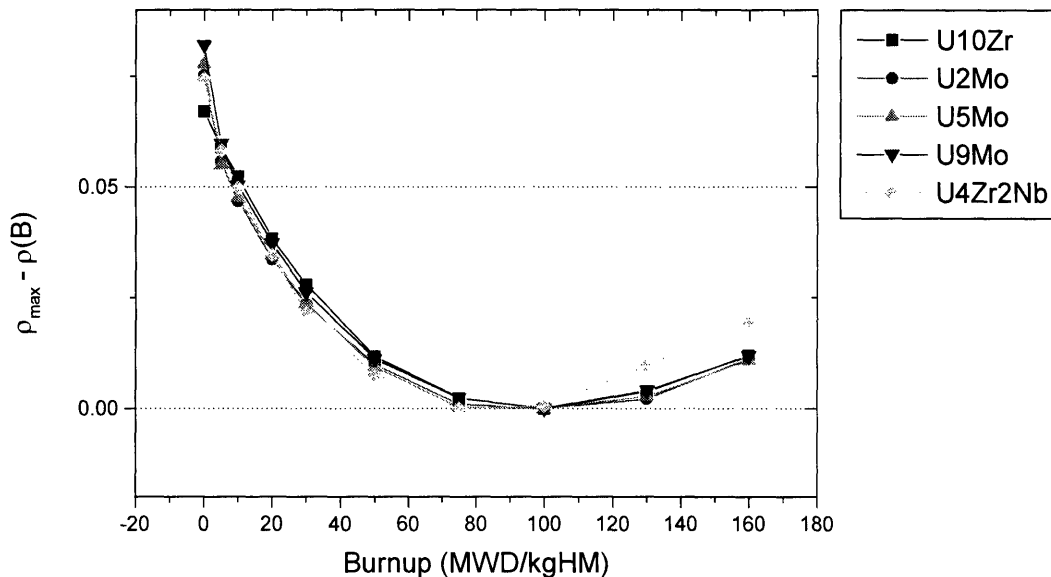


Figure 3.8 Difference between Peak and Instantaneous Reactivity for Metallic Fuels

This graph clearly illustrates the importance of peak reactivity. Each fuel type has very similar gain; U-9Mo has the largest gain, but the trend as a function of burnup is almost identical to that of the other metallic alloy fuels. The only clear difference between the fuels is for U-4Zr-2Nb, which has the largest reactivity decline after the peak reactivity is attained.

### 3.4.1. Flux Spectra

The flux spectra were compared for the metallic alloys. In each case the fuel is predominantly heavy metal and the liquid metal bond. The constituents in the fuel, such as zirconium in U-10Zr, are typically heavier than the constituents of the ceramic fuels. The high Z materials do not significantly contribute to spectrum softening in the fuel.

In each of the cases the flux spectrum is very similar. There are some advantages for the low molybdenum content alloys. Figure 3.9 shows plots of the flux spectra for the metallic alloy fuels analyzed.



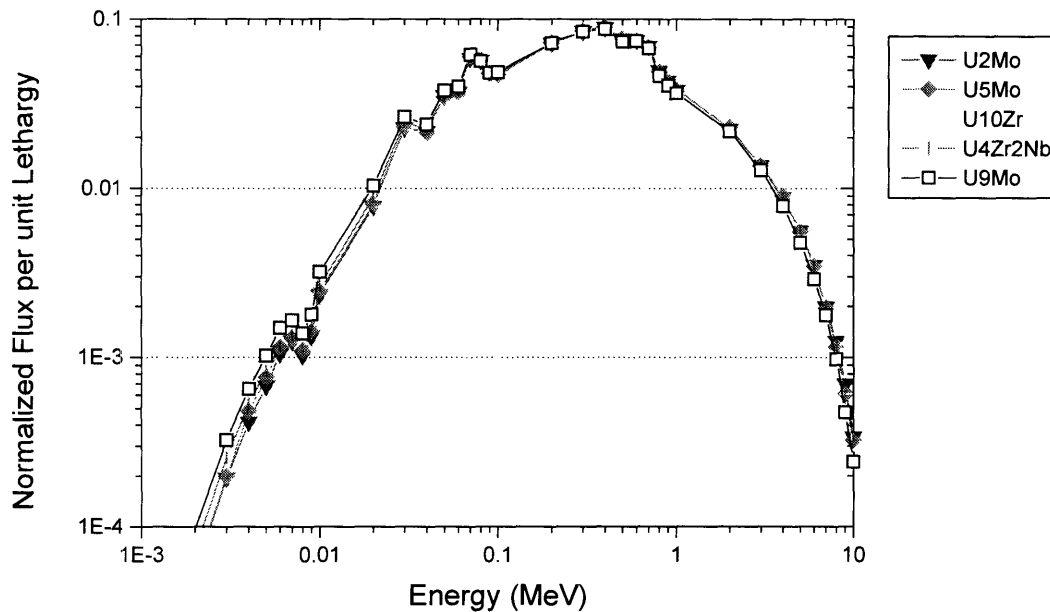


Figure 3.9 Metallic Alloy Fuel BOL Flux Spectra

It is difficult by inspection to distinguish which of the spectra is the hardest. The average epithermal energy (the normalized flux per unit lethargy weighted average energy) was computed using the same technique as described for the ceramic fuels. It is meant to give a measure of the spectrum hardness. Table 3-9 below summarizes the flux-weighted average energies. U-9Mo has the softest spectrum of these species, but its average epithermal flux energy is only slightly different from the average, and they are all approximately 0.36 – 0.37 MeV.

Table 3-9 Average Epithermal Flux Energy for Fuel Alloys

Fuel	<E> [MeV]
U-2Mo	0.369
U-5Mo	0.368
U-9Mo	0.356
U-10Zr	0.362
U-4Zr-2Nb	0.366
Average	0.3642
std-dev	0.0053

Based on this comparison, the differences in fuel neutronic behavior cannot be attributed to large differences in the flux spectrum (the standard deviation is only 0.005 MeV). The differences observed for the Zr/Nb alloy are related to the strong absorption at epithermal and fast energies in niobium. The high molybdenum content alloy (U-9Mo), though it has the strongest gain, has reactivity as a function of burnup roughly parallel with the low molybdenum content alloys, and

is less reactive at all points in burnup. Molybdenum is a stronger fast neutron absorber than zirconium.

To confirm a static neutron flux energy distribution, U-10Zr fuel was examined to show that the  $^{239}\text{Pu}$  cross sections are quite constant as a function of burnup. The cross sections for U-10Zr fuel were found in the same way as the cross sections for UC fuel. Table 3-10 summarizes the changes in one group cross sections as a function of the unit cell burnup.

Table 3-10 Burnup Behavior of  $^{239}\text{Pu}$  Cross Sections for U-10Zr fuel

U-10Zr										
B[MWD/kg <sub>HM</sub> ]	0	5	10	20	30	50	75	100	130	160
$\sigma_f^{49}$ [b]	1.592	1.592	1.592	1.593	1.593	1.594	1.594	1.594	1.594	1.594
$\sigma_a^{49}$ [b]	0.224	0.223	0.224	0.226	0.226	0.228	0.228	0.228	0.231	0.235
$\sigma_f^{49} / \sigma_a^{49}$	0.877	0.877	0.877	0.876	0.876	0.875	0.875	0.875	0.873	0.872

The approximately constant values of the cross sections indicate that the buildup of fission products does not shift the spectrum significantly.

### 3.4.2. Conversion Ratio

In each of the metallic alloy fuel cases examined the heavy metal densities were similar, more so than for the ceramic fuel types. The flux spectra are all also more similar, especially compared to the variance in spectra observed for the ceramic fuels. The conversion ratio<sup>17</sup> is also similar amongst the metallic alloy fuel types. Figure 3.10 shows a plot of the conversion ratio for each of the alloy fuels as a function of burnup.

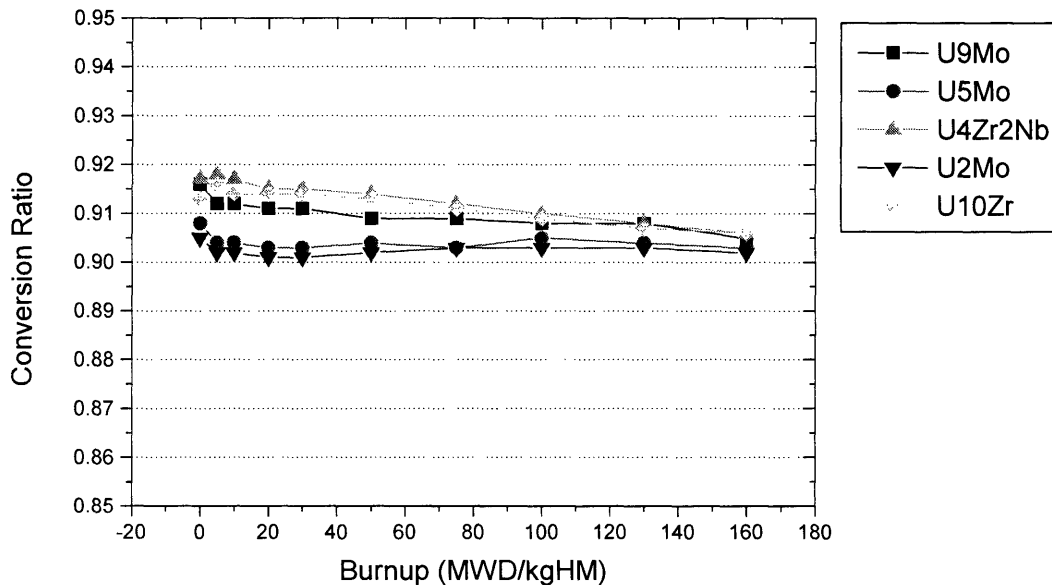


Figure 3.10 Alloy Fuel Conversion Ratio vs. Burnup

<sup>17</sup> As defined in section 1.3.

For all of the types analyzed, the conversion ratio is roughly constant throughout burnup and ranges between 0.90 and 0.92. These conversion ratios are relatively low compared to the ceramic fuels because of the internal moderation effect in the latter. The flux spectrum in the fuel region for metallic fuels is harder than the flux for ceramic fuels as the metallic fuels do not have low Z light constituents.

#### 3.4.3. **Conclusions**

For the extended burnup of 150 MWD/kgHM or more, higher alloy content will probably be necessary to help stabilize the uranium gamma phase and suppress swelling. The low molybdenum content alloys are not recommended for this reason, and since the U-10Zr achieves comparable physics performance, U-10Zr is recommended for use in a B&B GFR.

Though U-10Zr is the most highly recommended fuel from a physics standpoint, if other criteria rule out the use of U-10Zr fuel, U-9Mo is recommended as a backup fuel. U-9Mo has been used as fast reactor fuel previously in the Fermi I and Dounreay reactors, and is much more likely to withstand the mechanical strains induced by high burnup than lower molybdenum content alloys. Additionally, the post peak reactivity decline is shallower than the decline for the Zr/Nb alloy.

#### 3.4.4. **Mechanical Concerns**

High heavy metal density nuclear reactor fuels have not been used extensively in commercial power reactors. However, based on extensive experience in EBR II, the IFR concept is based on the use of U-10Zr fuel [61]. The Russian SFPR fuel is also proposed to be U-10Zr [65]. Both of these designs, however, make use of different liquid metal coolants (sodium in the former, lead or LBE in the latter). Liquid metals have significantly different heat removal capability compared to gas coolants. Since metallic alloy fuels have low melting temperature, adopting U-10Zr fuel for a GFR may prove to be difficult.

U-9Mo has not been widely used. Fermi I, an early 60 MWe fast sodium-cooled reactor in Monroe, Michigan, used metallic sodium bonded - uranium-molybdenum alloy fuel. Fermi I, however, was shut down in 1972 [51]. U-9Mo alloy fuel is under current evaluation for research reactors at burnup up to 80% [5].

For GFR applicability, the metallic alloy must not operate above its melting point. The melting point of the metallic alloys, on average, is lower than the melting temperature for the ceramic fuels by several hundred degrees Celsius. As noted earlier, the fuel density was taken to be 75% to allow for swelling. For U-10Zr fuel, steady state operating temperatures of up to 1000 °C are manageable [5].

### 3.5. Further Intercomparison of Metallic Alloys and Ceramic Fuels.

This section takes the results and conclusions of the previous two sections and compares the ceramic fuel types to the metallic alloy fuel types. Some general results are discussed and specific parallels are made for the leading fuel candidates. In section 3.5.1 the average trends in neutronic behavior are compared for the ceramic and alloy fuels, and simple schemes for anticipating reactivity trends are developed. In the subsequent sections additional physics concerns are described and the metals and fuels are compared both qualitatively and quantitatively.

#### 3.5.1. Heavy Metal Density Dependence

By considering both the metallic alloys and the ceramics, fuels with a wide range of heavy metal densities were compared. The importance of heavy metal density is key in reactivity performance because of the competition between heavy metal absorption and diluent absorption.

In this case the core diluent is comprised of the cladding material (HT-9) and the axial reflector (BaS). Since the diluent is constant in each of the fuel cases examined, the absorption cross section for the diluent is roughly constant. The BOL reactivity for different fuels can be predicted based on the heavy metal density if the light fuel constituent is weakly absorbing. Equation (3.3) illustrates the relationship between reactivity and material cross sections.

$$\rho_{\infty} \equiv \frac{k-1}{k} = 1 - \frac{1}{\frac{\eta \Sigma_a^F}{\Sigma_a}} = 1 - \frac{\Sigma_a^F + \Sigma_a^N}{\eta \Sigma_a^F} = 1 - \frac{1}{\eta} - \frac{1}{\eta \frac{\Sigma_a^F}{\Sigma_a^N}} \quad (3.3)$$

Where N denotes the non-fuel materials.

Recall that  $\eta^X$  is the ratio of fission to absorption multiplied by the prompt yield for isotope "X". The prompt neutron yield,  $\nu$  is weakly dependent on the incident neutron energy (the slope is  $0.127 \text{ MeV}^{-1}$  for  $^{239}\text{Pu}$  and similar for  $^{235}\text{U}$  [58]), therefore  $\eta^X$  varies predominantly due to the differences in the fission and absorption cross sections. The  $^{235}\text{U}$  cross sections are fairly similar for fast energies.  $^{239}\text{Pu}$  cross sections, however, have been shown to change significantly for different neutron energies above 1 keV. If we make the assumption that the spectra are similar and  $\eta^{25}$  is roughly the same in each case, then one can rewrite Equation (3.3) for the BOL reactivity in Equation (3.4).

$$\rho_{\infty} = 1 - \frac{1}{\eta} \left(1 + \frac{\Sigma_a^N}{\Sigma_a^F}\right) = 1 - \frac{1}{\eta} - \frac{1}{\eta} \left(\frac{M \Sigma_a^N}{d_{HM} N_{av} \sigma_a^F}\right) = A - B \frac{1}{d_{HM}} \quad (3.4)$$

Where  $d_{HM}$  is the heavy metal density.

The infinite medium reactivity is assumed to be approximately the same as the unit cell reactivity. It is possible to treat the neutron leakage as a component of the absorption cross section. Since a

unit cell model is employed, only axial leakage is calculated. Since an axial BaS reflector is present, the contribution from leakage is assumed to be relatively small, and similar in all cases.<sup>18</sup>

From the data for each fuel the BOL unit cell reactivity and the heavy metal density were tabulated. A plot of the data is shown in Figure 3.11. Though this is a simplistic approach, the approximately linear trend verifies that the heavy metal density is a leading determinant of reactivity, but secondary effects must still be considered. The heavy metal density in this plot is the reduced fuel region smear density used in the model, i.e. the theoretical density multiplied by 0.75 for metals or 0.85 for ceramics.

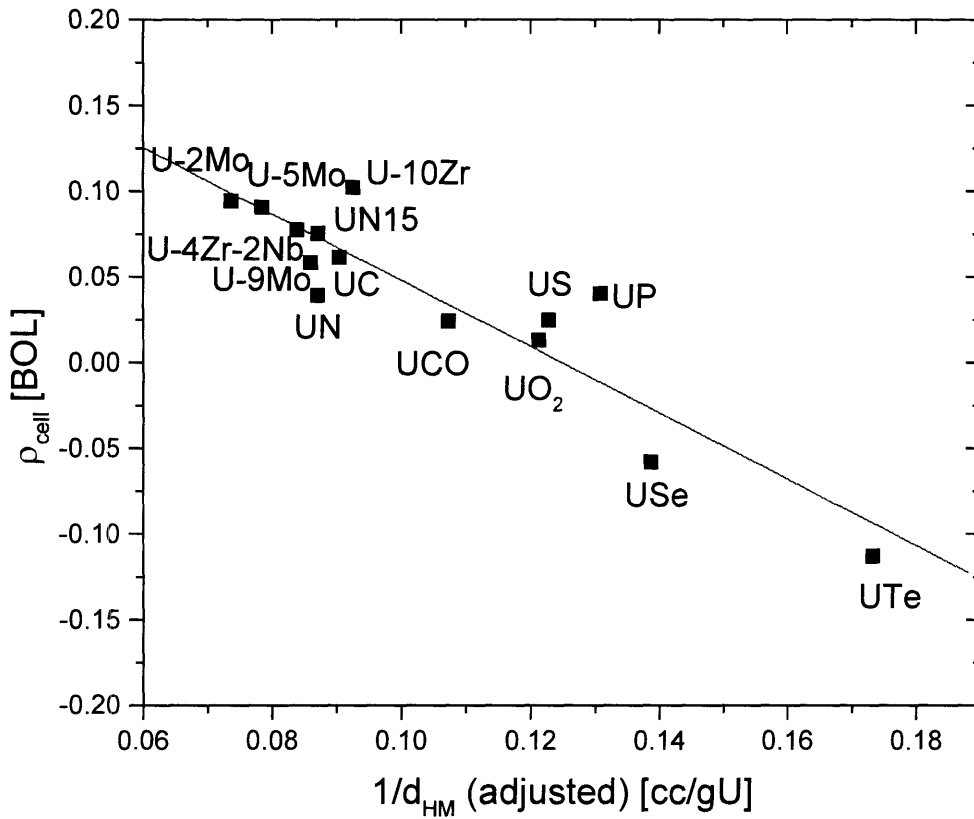


Figure 3.11 Reactivity Dependence on Heavy Metal Density

<sup>18</sup> Capping the unit cell model with reflecting boundary conditions at the top and bottom and rerunning the UC fuel pin was done to assess the relative importance of the leakage. At the BOL with axial leakage the calculated eigenvalue is 1.06(5), whereas with reflecting axial boundary conditions, the calculated eigenvalue is 1.07(8). The same fuel pin was then modeled with zero cladding thickness. The BOL eigenvalue for the no-cladding UC fuel pin was increased from 1.06(5) to 1.13(2). The  $-\Delta\rho$  contributed by leakage is therefore 0.0113 and the  $-\Delta\rho$  contributed by cladding absorption is 0.0556 (almost 5 times as great as leakage). Therefore the leakage, though significant, is a smaller contribution to parasitic neutron loss than absorption in structural materials.

As can be seen from the figure, there are several more effects that must be taken into account. Since the parasitic absorption in the fuel light constituents cannot be ignored, the assumption of a constant macroscopic absorption cross section is a crude approximation, and as one can see, cases where the parasitic absorption is low have points well above the trend line, as is the case for  $U^{15}N$ , UP, and U-10Zr; while stronger absorbers such as natural nitrogen, selenium, tellurium and molybdenum cause fuels with these constituents to fall below the trend line. Table 3-11 shows representative spectrum averaged cross sections for the four strong absorbers mentioned above as well as several of the weak absorbers.

Table 3-11 Microscopic Absorption Cross Sections from Diluent Study [74].

<b>Nuclide</b>	<b><math>\sigma_a(\text{tot})</math></b>	<b>Nuclide</b>	<b><math>\sigma_a(\text{tot})</math></b>
<b>(strong)</b>	<b>[mb]</b>	<b>(weak)</b>	<b>[mb]</b>
Nnat	22.6	$^{15}N$	0.02
Se	> 200	C	0.064
Te	84.9	O	0.725
Mo	110.8	P	7.2

Recall that the number density of zirconium in the U-10Zr is small compared to the heavy metal density (the atom ratio of zirconium to heavy metal is less than 1/3), and the microscopic cross section must be multiplied by the number density to calculate reaction rates.  $U^{15}N$ , UC, US, and  $UO_2$  fit nicely into the model that peak reactivity is driven primarily by heavy metal density. The ceramic fuels that fit well into the model have internal moderation that softens the spectrum; yet, the aforementioned ceramic fuels have low parasitic absorption. However, when large parasitic absorption comes into play, as is the case for USe, UTe, and UN, the peak reactivity is reduced by the absorption in the constituent.

In general, the metallic alloys have higher heavy metal density, and therefore greater reactivity than the ceramic fuels. For some fuels this is not the case, however. For example, UC has a heavy metal density (adjusted) of 11.1 g/cc and U-10Zr has a heavy metal density of 10.8 g/cc. The metallic alloys do not have as considerable an atom fraction of constituent as do the ceramics. The U-XMo and U-10Zr are almost purely uranium (2/3 of the nuclei or more are heavy metal), whereas half of all nuclei in UN, UC, UP, etc are light constituents. The combination of higher heavy metal density (in general), and weaker slowing down power in the fuel region yield better reactivity performance as a function of burnup for the metallic alloy fuel types.

To test the impact of internal moderation on fuel performance at the BOL, the UC fuel sample was run with the heavy metal density held fixed, but the carbon number density in the fuel was artificially set equal to zero. The resultant eigenvalue at BOL is 1.14(5) for the unmoderated fuel. The nominal UC case yielded an eigenvalue of 1.06(5) at BOL. The reactivity is much closer to that of U-10Zr (1.11(3)) because they have approximately the same heavy metal density. There is some internal slowing down power present in the U-10Zr from the zirconium as well as inelastic scattering from the liquid lead bond (which is homogenized throughout the fuel region), and zirconium isotopes (namely those other than  $^{90}Zr$ ) contribute to neutron absorption. The combined effect of the alloying material and the liquid metal bond, and slightly lower heavy metal density explain the relatively small difference between the U-10Zr fuel and the unmoderated UC (without C) fuel.

The BOL and Peak reactivity are plotted in Figure 3.12. The trend is approximately linear. Of interest for B&B applications are fuels that lie above the trend line and to the right. These represent highly reactive fuel types with gains above the average value.

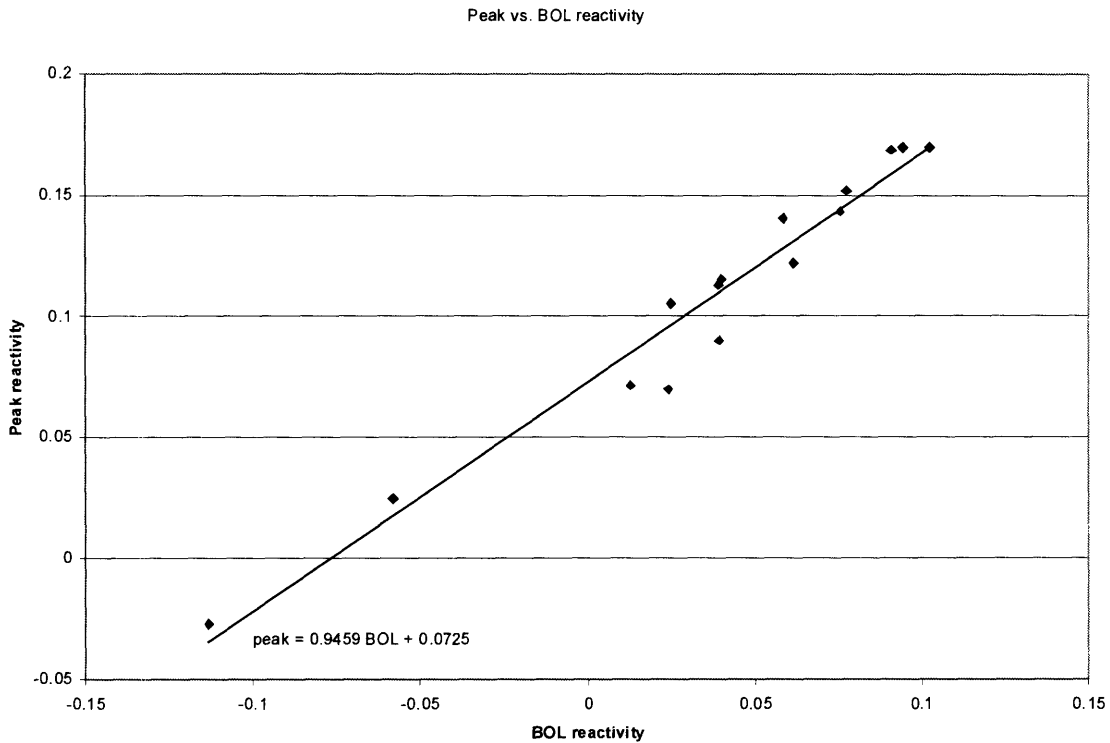


Figure 3.12 Peak vs. BOL Reactivity for Every Fuel Type Considered

The data were fit with a linear trend line. The slope of the fit is almost unity ( $\sim 0.95$ ). The results of the fit indicate that all of the fuels are exhibiting parallel reactivity histories and that an average gain of 0.07 is almost universal for every fuel type. This further substantiates the claim that gain is not an important indicator of fuel performance. Since the reactivity histories are mostly parallel, the peak reactivity is the best indicator of fuel performance. The only other indicator of interest is the slope in reactivity post peak. Conversion ratio and gain are used only to understand the fuel neutronic behavior.

The good correspondence between peak and BOL reactivity indicates that preliminary screening of additional fuel types could be done based on the BOL reactivity. Any additional fuels of interest could be selected based on high heavy metal density, weak absorption in the constituent, and low internal moderating power.

### 3.5.2. Proliferation Resistance

As a consequence of having more internal neutron moderation, the ceramic fuels have higher conversion ratios than the metallic fuels in general. The light constituents contribute to slowing down in the fuel region, and thereby increase resonant fertile capture. The ceramic fuel types have conversion ratios, on average, that are 5-10% higher than the conversion ratio for metallic fuel types.

A comparison was made between two ceramic and two metallic alloy fuels to show the differences in  $^{239}\text{Pu}$  cross sections. At the BOL there is no plutonium 239 in the core, but MCNP calculates the one group microscopic cross sections based on the flux spectrum. The MCODE output gives a table for these cross sections. Again, the basis for comparison is the axial central fuel region. The one group capture and fission cross sections are shown in Table 3-12. The metallic alloys typically have harder flux spectra; the implication in terms of  $^{239}\text{Pu}$  worth is made clear by the one group cross sections.

Table 3-12 One Group  $^{239}\text{Pu}$  Microscopic Cross-sections

	UC/US	U <sup>15</sup> N	U-10Zr	U-9Mo
$\sigma_f^{49}$ [b]	1.64	1.65	1.59	1.59
$\sigma_\gamma^{49}$ [b]	0.313	0.326	0.224	0.224
$\sigma_f / \sigma_a$	0.84	0.84	0.88	0.88

The ratio of the fission to absorption cross section is an estimator for the relative value of  $\eta^{49}$  (the number of neutrons released per absorption). Even though the prompt fission yield is dependent on the incident neutron energy, the slope for  $^{239}\text{Pu}$  is small - roughly  $0.127 \text{ MeV}^{-1}$ . It is clear that in the harder flux spectrum the value of  $\sigma_f / \sigma_a$  increases and that the metallic alloys have a significant advantage. This table quantifies the advantage of hard spectrum  $^{239}\text{Pu}$  reactivity worth. The fission cross sections are roughly comparable in the materials of interest but the capture cross section is much smaller in the hard spectrum, and this gives the metallic alloys an advantage.

For the same fuel types, the discharge plutonium vectors were calculated. Table 3-13 gives the number density of the plutonium isotopes in the central expanse of the fuel for each of the proposed fuel types. From the number densities it is possible to calculate the atom fraction of each isotope present in the discharged fuel at 160 MWD/kg<sub>HM</sub>.

Table 3-13 Plutonium Number Densities at 160 MWD/kg<sub>HM</sub>

	UC/US	U <sup>15</sup> N	U-10Zr	U-9Mo
$^{238}\text{Pu}$	$2.42 \times 10^{-5}$	$3.45 \times 10^{-5}$	$2.55 \times 10^{-5}$	$2.72 \times 10^{-5}$
$^{239}\text{Pu}$	$1.77 \times 10^{-3}$	$2.18 \times 10^{-3}$	$1.86 \times 10^{-3}$	$2.00 \times 10^{-3}$
$^{240}\text{Pu}$	$3.38 \times 10^{-4}$	$4.59 \times 10^{-4}$	$3.11 \times 10^{-4}$	$3.54 \times 10^{-4}$
$^{241}\text{Pu}$	$3.12 \times 10^{-5}$	$4.47 \times 10^{-5}$	$2.62 \times 10^{-5}$	$2.88 \times 10^{-5}$
$^{242}\text{Pu}$	$3.12 \times 10^{-6}$	$4.86 \times 10^{-6}$	$2.65 \times 10^{-6}$	$2.88 \times 10^{-6}$

The number densities are measured in atoms / b-cm. The  $^{237}\text{Pu}$  concentration in each case is lower than  $10^{-7}$  atoms / b-cm and is therefore neglected in the vector. It should be noted that the number density of the plutonium isotopes is greater in the discharged ceramic fuels than in the discharged metallic fuels. Table 3-14 converts the number densities to atom fractions.



Table 3-14 Plutonium Discharge Vector at 160 MWD/kg<sub>HM</sub>

	UC/US [%]	U <sup>15</sup> N [%]	U-10Zr [%]	U-9Mo [%]
<sup>238</sup> Pu	1.12	1.26	1.15	1.13
<sup>239</sup> Pu	81.7	80.1	83.6	82.9
<sup>240</sup> Pu	15.6	16.8	14.0	14.7
<sup>241</sup> Pu	1.44	1.64	1.18	1.19
<sup>242</sup> Pu	0.14	0.18	0.12	0.12

The <sup>239</sup>Pu percentage in the metallic alloy fuels is consistently greater, though similar to the <sup>239</sup>Pu percentage in the ceramic discharge fuel. The discharge plutonium is clean (~80% <sup>239</sup>Pu) compared to LWR spent fuel (~60% <sup>239</sup>Pu) [59]. Due to the clean discharge plutonium isotopics the B&B GFR is potentially a proliferation concern without the use of a fuel reuse technique (such as AIROX or pyroprocessing) to reduce the <sup>239</sup>Pu percentage in the spent fuel; however, proliferation risks are difficult to assess, particularly since fuel reuse after discharge is not essential.

In the harder flux spectra of the metallic alloys the <sup>239</sup>Pu percentage is higher. This is due to the increase in the ratio of the microscopic fission to absorption cross sections for <sup>239</sup>Pu at energies exceeding 1 keV. In the harder spectra of U-10Zr and U-9Mo the likelihood of <sup>239</sup>Pu fission is greater than the likelihood of <sup>239</sup>Pu capture, and the fraction of higher Pu isotopes in the metallic fuels is smaller.

Though the plutonium vector for the metallic fuels has a higher fraction of <sup>239</sup>Pu than the ceramic fuels, the number density of the plutonium in the ceramic fuels is greater. This is a result, primarily, of the internal moderation effect. The light constituents slow down neutrons internally in the ceramic fuel. In the metallic fuels the neutrons are slowed down almost solely by the small amount of cladding. The ceramic fuels have stronger internal slowing down power, and thus higher conversion ratios and higher plutonium number density at discharge.

Ceramic fuels have slightly better plutonium isotopics, but generate more plutonium than the metallic alloys because of a slightly higher conversion ratio. Yet, the percentage of <sup>239</sup>Pu in the discharge plutonium, overall, is very similar among all of the fuel types and no one of these fuels is extremely promising from the standpoint of proliferation resistance.

The number densities of <sup>235</sup>U and <sup>239</sup>Pu have been plotted a function of burnup for UC and U-10Zr fuel in Figure 3.13. UC at a smear density of 0.85 has a heavy metal density of 11.1 gU/cc. U-10Zr has a similar heavy metal density. At a smear density of 0.75, the heavy metal density in the U-10Zr fuel is 10.8 gU/cc. Figure 3.13 illustrates that the BOL <sup>235</sup>U number density is about the same for each fuel type.

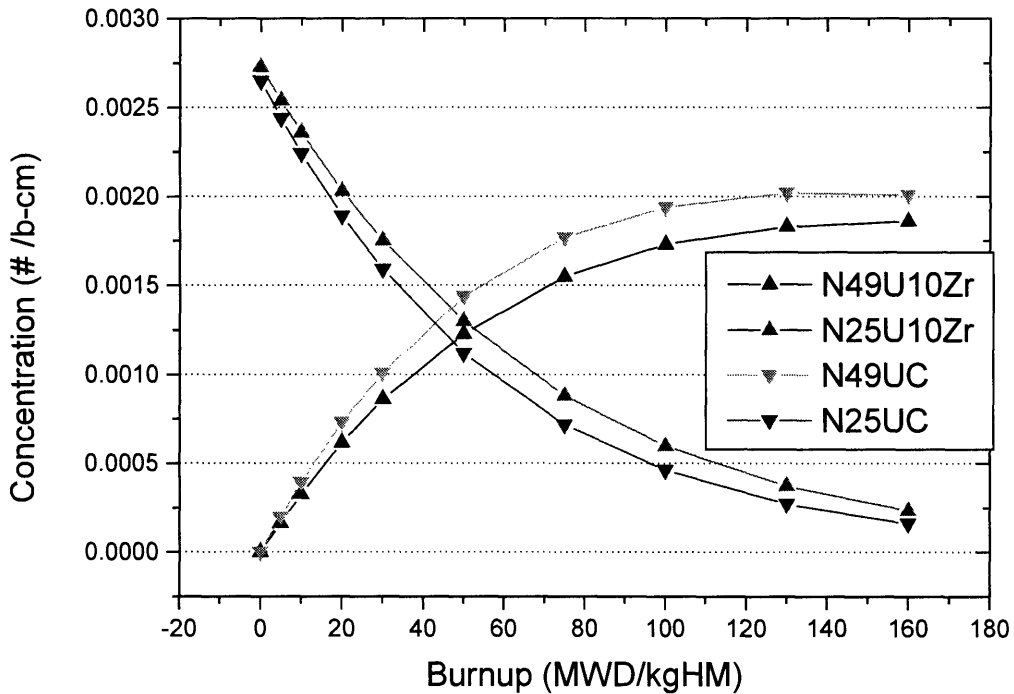


Figure 3.13 Number Density of Fissile Species in UC and U-10Zr fuel

As a function of burnup, the burnout of  $^{235}\text{U}$  is accompanied by a buildup of  $^{239}\text{Pu}$ , and overall, the reactivity is maintained above zero for both fuel types. It can be seen from the graph that the UC fuel breeds a larger amount of  $^{239}\text{Pu}$  than the U-10Zr, even though the two fuels have a comparable heavy metal density. U-10Zr has a harder spectrum than UC and the  $^{239}\text{Pu}$  fission to capture ratio is higher.

Though there are distinct differences discernable in the plutonium vectors and quantities, neither of these potential fuels offers a significant proliferation resistance advantage. Therefore, there is no basis to use inherent proliferation resistance as a selection criterion for the B&B GFR fuel.

### 3.5.3. Void Reactivity Worth

The  $^{239}\text{Pu}$  worth is tightly coupled with the neutron flux spectrum. It has been shown that spectrum hardening increases both fertile fission and  $^{239}\text{Pu}$  worth. Therefore, for any point in burnup, an effect that hardens the spectrum will increase the instantaneous reactivity.

The coolant, be it helium or S-CO<sub>2</sub>, contributes to neutron slowing down. If the coolant is voided then the reactivity of the core will increase for both the ceramic and the alloy fuel types. Since the actual value of the void reactivity worth is a function of the leakage (including neutron streaming) as well as spectral effects, a full core model is needed to correctly evaluate it. Qualitatively, however, the metals and ceramics can be compared.

It has also been shown that the light constituents of the ceramic fuels contribute to neutron slowing down inside the fuel region. Therefore, in the event of a LOCA where all of the moderating coolant is removed from the core, the light materials in the fuel will still contribute to neutron slowing down, and therefore the spectrum hardening associated with a LOCA is mitigated by the light elements in the fuel.

If the coolant is removed from an alloy-fueled core, however, there is no residual moderating material remaining in the core to slow neutrons down. The spectral hardening in the case of the metal fuel is more acute, and therefore, it is expected that the void reactivity worth will be greater in the case of metallic alloy fuels than in the case of ceramic fuels because there is less residual moderation. Coolant void reactivity worth is discussed at greater lengths in Chapter 5 and Chapter 9.

### 3.6. Cladding Selection

For the initial fuel materials screening, HT-9 stainless steel was the assumed cladding material. However, a variety of other cladding materials may meet or exceed the chemical and mechanical limitations for the fuel design whilst increasing the neutronic performance of the reactor. In the B&B operation mode, every neutron is valuable, and the strong limitations on the neutronic performance motivate a screening of potential cladding materials as well as quantifying the reactivity worth of the cladding.

The UC fuel, HT-9 clad unit cell was adjusted to have several cladding thicknesses. The cell was run in MCNP at BOL to calculate the effective eigenvalue (with a standard deviation of 0.0006). The thicknesses selected range from 0 mm to 0.7 mm. A linear fit was added to show the approximate linear change in reactivity with additional cladding thickness (the mass and volume increase nearly linearly for a thin cylinder as thickness is increased). As noted earlier, effects due to leakage, and hence changes in leakage, are small.

The data predict that the k-eff at BOL for the unit cell is given by Equation (3.5).

$$k = 1.13023 - 0.00132x \tag{3.5}$$

Where x is the cladding thickness in  $10^{-5}$  meters.

A run was made with HT-9 cladding artificially set to double the nominal density of the reference clad thickness of 0.055 cm. The resultant unit cell multiplication factor was found to be 1.012(5). Taking the result in Equation (3.5) and evaluating for a thickness of 0.11 cm, the k is 0.98503. The results are different for two reasons. First, the trend in the reactivity curve is not perfectly linear, and the model will under-predict the reactivity for large clad thickness. Second, as the clad thickness increases, the axial leakage is reduced because the volume fraction of coolant is decreased and axial neutron streaming is reduced.

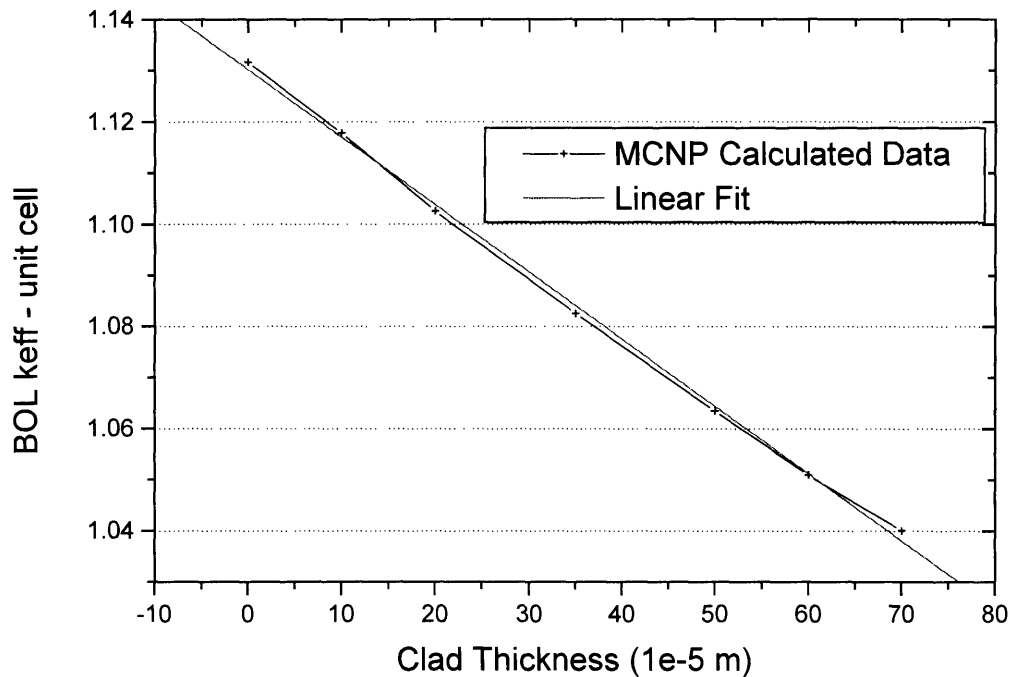


Figure 3.14 Cladding Effect on Reactivity

The curve is not perfectly linear because mass is not directly proportional to thickness. The reactivity depends on the volume fraction of cladding that is being added with each increase in thickness. The cladding is very thin compared to the outer radius of the fuel pin, and therefore increasing the thickness by a small amount (at a relatively large radius) for a hollow cylinder will increase the volume approximately linearly with the increase in thickness.

As can be seen from the plot in Figure 3.14, the cladding volume should be minimized because it has a significant impact on the unit cell reactivity.

Fuel materials, specifically, US, contain constituents which undergo (n,p) or (n, $\alpha$ ) reactions at high neutron energy. Some studies have looked into the helium gas release from (n, $\alpha$ ) reactions in US, and have concluded that it is a small fraction compared to the total release of fission gases. If sulfur is used in a matrix, diluent, or internal reflector the gas buildup will be more important [74].

Going to extremely long burnup not only puts a strain on the fuel cladding materials from irradiation, and creep, but the buildup of gases in the fuel pin will contribute to the probability of fuel failure. If CO<sub>2</sub> coolant is used, corrosion and oxidation are also potential concerns.

A robust cladding scheme is necessary for such prolonged burnup as envisioned with the B&B GFR. Fuel materials that have better fission product retention capabilities will reduce the burden on cladding performance requirements. Therefore, in situations where fission gas, or helium gas release is significant, the reactivity penalty from the use of thicker cladding may outweigh the

relative performance of another fuel with better fission product retention or fuels with smaller (n,p) and (n, $\alpha$ ) reaction cross sections. As noted subsequently in section 4.4.3, vented fuel has been adopted to reduce cladding strain; the lower clad thickness is also beneficial neutronically.

A variety of cladding options were analyzed to find which yields the highest reactivity for the unit cell. A neutronically transparent clad material may be employed at greater thicknesses than HT-9 with a smaller overall impact on neutronics performance. The clad materials analyzed include: V-20Ti alloy, titanium, AGR cladding (SS-310), HT-9, and MA956 ODS steel [7, 74,34]. Table 3-15 shows the composition for each of the steel cladding alternatives.

Table 3-15 Steel Clad Compositions (by weight percentage)

	Fe	Cr	Al	Ti	C	Y <sub>2</sub> O <sub>3</sub>	Ni	Mo	Si	W	V	Mn	P	S
<b>SS 310</b>	51.3	25.0	0	0	0.08	0	20.0	0	1.50	0	0	2.00	0.05	0.03
<b>MA956</b>	74.5	20.0	4.50	0.50	0.05	0.50	0	0	0	0	0	0	0	0
<b>HT-9</b>	85.8	11.5	0	0	0.20	0	0	1.00	0.25	0.50	0.30	0.50	0	0

Each of these cladding materials is expected to meet the materials demands of either a helium or S-CO<sub>2</sub> cycle. In some cases, such as AGR cladding or MA956 ODS steel, the industrial experience indicates excellent oxidation resistance in a CO<sub>2</sub> atmosphere. For the purposes of the comparison a constant cladding thickness of 0.55 mm was assumed and a unit cell burnup analysis was done for each of the proposed cladding materials. Figure 3.15 shows the reactivity histories for the five clad alloys with UC fuel.

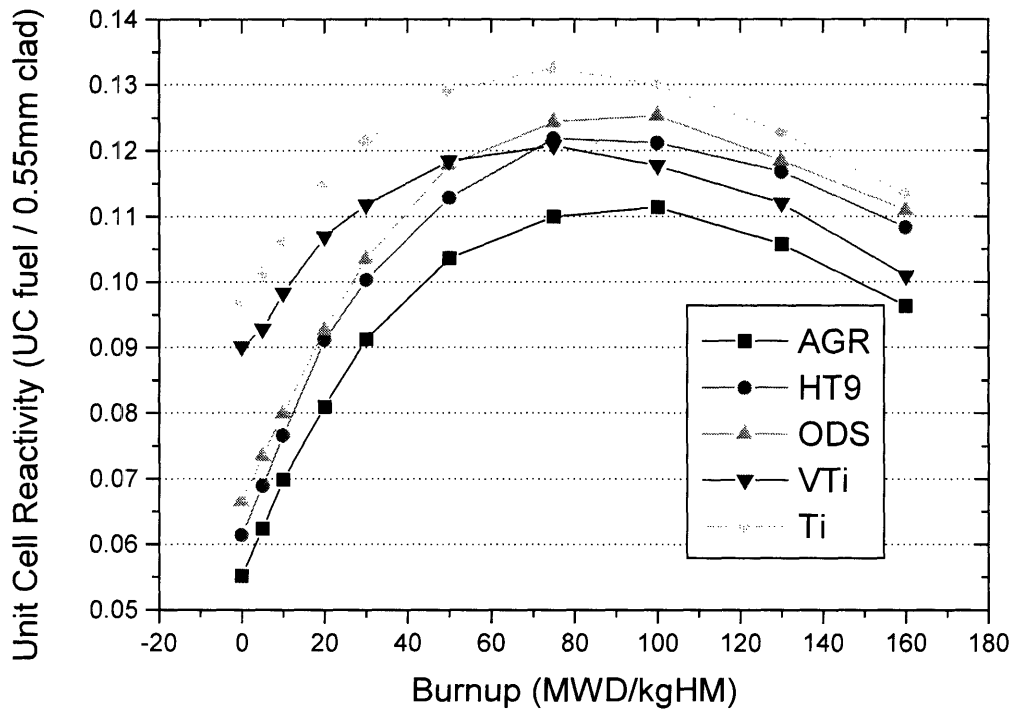


Figure 3.15 Reactivity History Comparison for Different Cladding Materials

This graph indicates that BOL studies can be deceptive. In the case of the V-20Ti alloy, the BOL reactivity is much higher than any of the other clad materials, yet, its shape is not parallel with the others and V-20Ti has the second lowest reactivity at high burnup. V-20Ti increases the BOL reactivity and achieves peak reactivity earlier in burnup. This is primarily due to the harder neutron spectrum and higher fertile fission rate due to the small slowing down power in the low density cladding material. The V-20Ti cladding peak is comparable with the HT-9 steel peak. The V-20Ti alloy may be more expensive to use for fuel and is not recommended based on its mediocre neutronic performance.

The MA956 ODS steel and Titanium are clear winners. Titanium achieves the highest peak reactivity of any of the cladding schemes, likewise for the highest BOL reactivity. On the other hand, MA956 ODS steel is commercially available and has a large chromium and aluminum content, which gives the material excellent oxidation resistance [34]. Therefore MA956 ODS steel is the recommended reference cladding material for the B&B GFR.

### **3.7. Gas Coolant Comparison**

The unit cell model developed for the fuel comparison was used to compare the trends in reactivity through burnup for helium and CO<sub>2</sub> coolants at different pressures. US fuel is used as a reference given its hard flux spectrum. Helium is tested at 8 MPa and 20 MPa; S-CO<sub>2</sub> is tested at 20 MPa. The results are used to determine the neutronic advantages associated with each coolant. Helium is lighter than carbon or oxygen independently, but with gases at the same molecular density, the CO<sub>2</sub> has three times the number density of helium. Additionally, the microscopic scattering cross section of helium is ~20% of that for carbon or oxygen. Therefore at different pressures each of these coolants will contribute differently to the flux spectrum and thus reactivity behavior through burnup.

The plot shown in Figure 3.16 portrays the flux spectra for three coolant cases. It is clear from the plot that the S-CO<sub>2</sub> cooled US fuel pin has the softest neutron flux spectrum. The helium at 20 MPa has a softer spectrum than the helium case at 8 MPa, but even at the same system pressure the helium cooled unit cell has a harder spectrum than S-CO<sub>2</sub>.

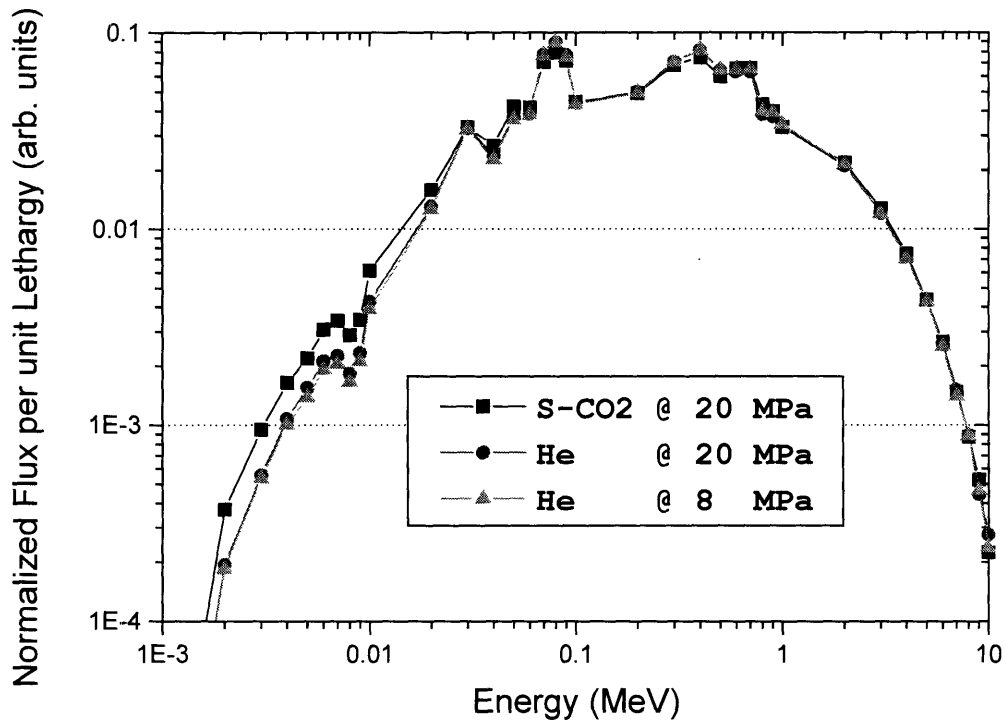


Figure 3.16 Gas Coolant Flux Comparisons

Helium is a weaker moderator than S-CO<sub>2</sub> even at the same pressure. This is because carbon and oxygen, even though they are heavier than helium, each have larger microscopic scattering cross sections, and there are three nuclei for each CO<sub>2</sub> molecule. The difference in spectrum hardness between 20 MPa and 8 MPa for the two helium cases is much less pronounced than the difference between helium and S-CO<sub>2</sub> at 20 MPa. Table 3-16 gives the average values for the relative slowing down power of helium and CO<sub>2</sub>.

Table 3-16 Slowing Down Power Comparison [21]

	$\sigma_s$ [b]	$\xi$	Avg. $\xi\sigma_s$ [b]	N (at 20 MPa) [molecules. / b-cm]	Avg. $\xi\Sigma_s$ [1/cm]
<b>He</b>	0.800	0.425	0.340	0.001940	0.000660
<b>CO<sub>2</sub></b>	13.000		1.869	0.001970	0.003682
<b>C</b>	4.600	0.158			
<b>O</b>	4.200	0.136			

Since the slowing down power of helium is smaller than that of S-CO<sub>2</sub>, using helium will increase the peak reactivity of the unit cell. Additionally, in the event of voiding (if leakage is not considered) the spectrum hardening from the loss of helium will be less acute than for S-CO<sub>2</sub>.

The reactivity penalty was also observed for every point in burnup by plotting the reactivity histories for each coolant case on the same set of axes. Figure 3.17 shows the reactivity histories for the three coolant cases studied.

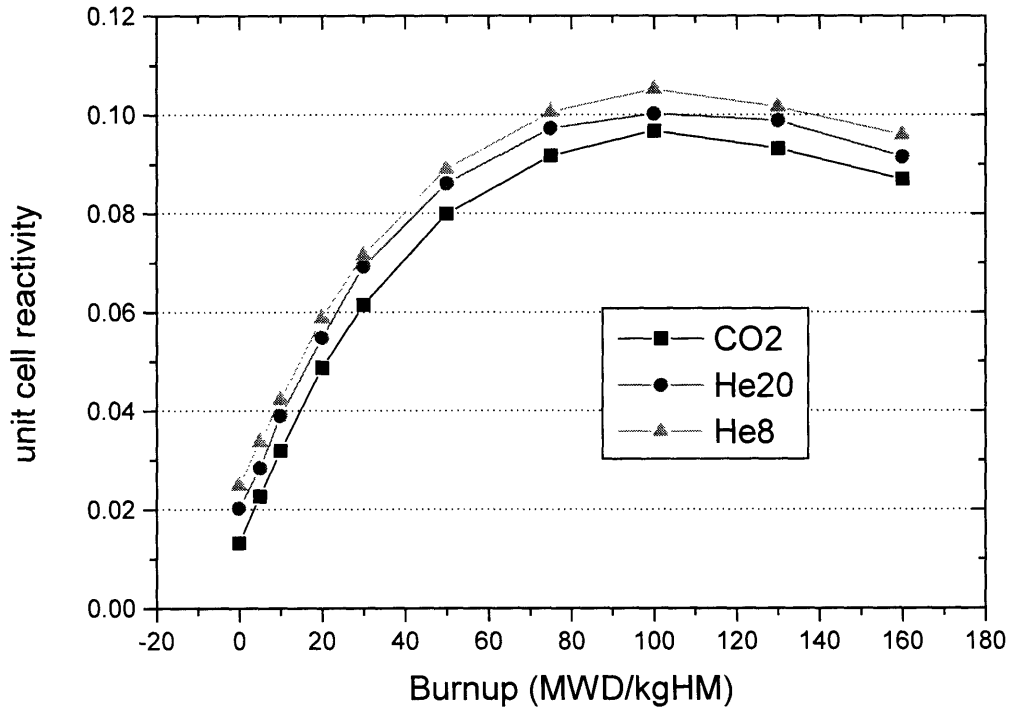


Figure 3.17 Reactivity Histories for Different Coolant Cases

The reactivity histories have similar shapes. The S-CO<sub>2</sub> is a slightly better moderator and contributes to spectrum softening, the spectrum softening in turn reduces the overall peak reactivity; the penalty is fairly small. The difference between the helium cooled case at 8 MPa and the S-CO<sub>2</sub> is only 0.009 on average. The improvement in conversion ratio associated with spectrum softening partially offsets the loss of reactivity from decreased <sup>239</sup>Pu worth. Figure 3.18 shows the conversion ratio as a function of burnup for the US fuel pin with helium coolant at 8 MPa and S-CO<sub>2</sub> at 20 MPa.



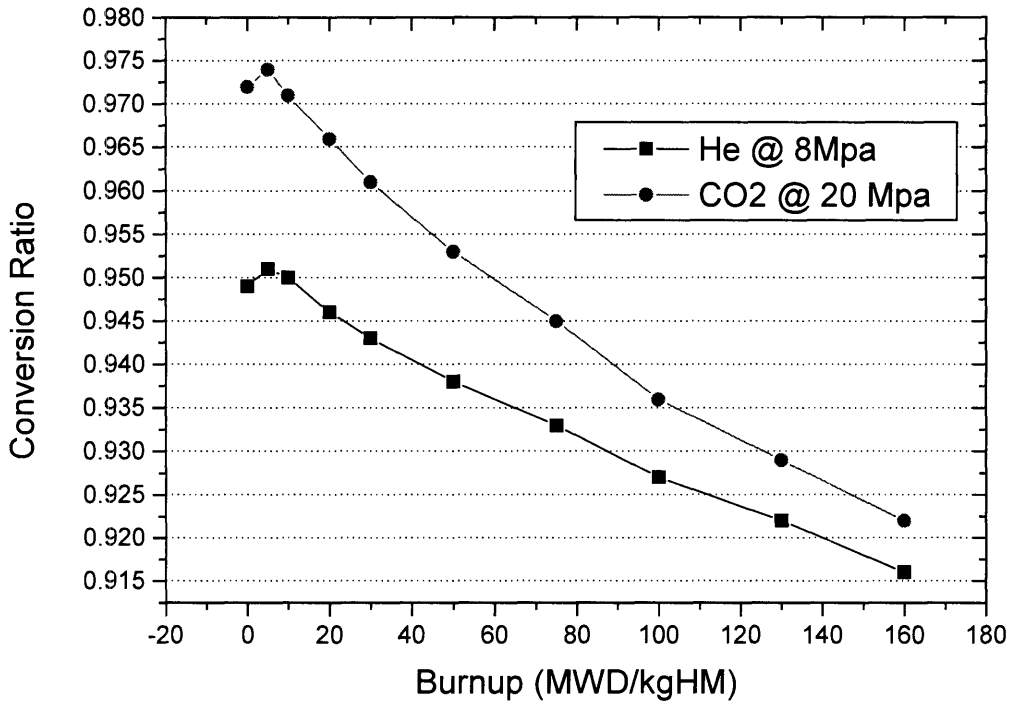


Figure 3.18 Conversion Ratio History for US fuel with different coolants.

It is expected that, by making slight changes to the core design, use of either coolant will permit B&B operation. Reoptimization of the core for potential B&B operation could involve slight adjustments in mass flow rate, average coolant temperature, or even volume fraction of coolant.

### 3.7.1. Comparison with Liquid Lead Coolant

To quantify the advantages of a GFR relative to a LFR, the unit cell models for U-10Zr and UC fuel were adapted to have liquid lead coolant instead of helium coolant. The unit cell models were then modeled with MCODE to compute the reactivity as a function of burnup analogous to the calculations described in previous chapters. The results are shown in Figure 3.19.

The highest reactivity curve is for U-10Zr fuel with helium coolant. The lead coolant softens the spectrum significantly, and therefore gas cooled systems have an advantage for a given fuel type. Though the difference between the U-10Zr fuel / Helium cooled reactivity history and the UC fuel / Lead cooled history is significant (~0.04), the difference between the UC fuel / Helium cooled reactivity history and the U-10Zr fuel / Lead cooled history is relatively small (~0.02). The  $U^{15}N$  fuel / Helium cooled case is more neutronically reactive than the U-10Zr / Lead cooled history.

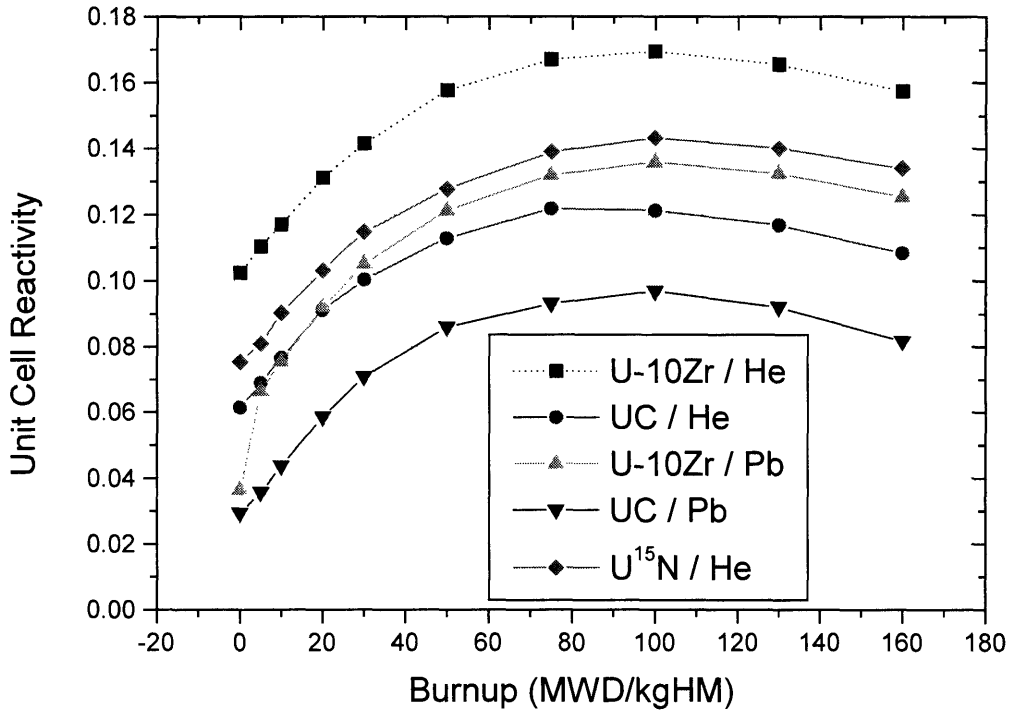


Figure 3.19 Lead vs. Helium Coolant Burnup Comparison<sup>19</sup>

### 3.8. Material Selections

Key parameters and physical phenomena that explain the reactivity behavior of different nuclear fuel types have been described. The application of those parameters and analyses for a variety of different fuels has allowed for the selection of a few potential fuels for a B&B GFR.

U<sup>15</sup>N appears to be an excellent fuel candidate for B&B reactor operation. However, more studies must be done into the economic feasibility of isotopic separation of <sup>15</sup>N from natural nitrogen. <sup>15</sup>N enrichment has been examined from the standpoint of UN fuel reprocessing, and the Japanese Nuclear Cycle Initiative (JNC) evaluated a gas phase absorption technique that appears to be technologically feasible [35].

UC also appears to be an adequate fuel candidate. The heavy metal density is slightly lower than that of U<sup>15</sup>N, and the fuel neutronic performance is not quite as good. However, the price of nitrogen enrichment may drive the design in the direction of UC fuel.

Metallic alloy fuels were also considered, and U-10Zr is a clear winner in terms of neutronic performance. Core designs that utilize this fuel, however, will have more stringent fuel temperature limits than cores with ceramic fuel.

<sup>19</sup> The metallic fuel and gas coolant combination (U-10Zr with Helium) is not realistic as fuel melting would likely occur in the reference configuration.

A cladding material, MA956 ODS, is selected based on good neutronic and material performance. Helium and S-CO<sub>2</sub> coolant were compared. There is a reactivity penalty associated with the S-CO<sub>2</sub> coolant, but it is not so large as to rule out the S-CO<sub>2</sub> cycle for a B&B GFR. Void reactivity worth of the coolant in the event of a LOCA is a more serious concern. Oxidation of exposed fuel may also rule out the use of S-CO<sub>2</sub> coolant with high performance fuels such as UC or U<sup>15</sup>N. In any event, an indirect cycle with helium as a primary coolant was eventually selected for a host of reasons.

### 3.9. Temperature Limits

Given the choice for cladding material, MA956 ODS, temperature limits must be set for steady state and transient conditions. While MA956 ODS irradiation experiments are scarce, engineering judgment and experience from the GCFR allows for rough limits to be established. Between the 1970 and 1980 several design changes were proposed for the GCFR demonstration plant designed by General Atomics. A proposed 300 MWe variant used 316 SS cladding material with a maximum steady state temperature of 700 °C [15]; and a later version for a 367 MWe unit used Austenitic SS (D9) cladding with a maximum steady state temperature of 750 °C [25].

The melting temperature for MA956 ODS is 1482 °C, and the material is creep resistant up to 1300 °C [34]. The fission gas in the fuel will be vented to avoid pressure induced stress in the clad, as well as to eliminate the need for a large fission gas plenum (which would increase friction pressure drop in the core). Therefore, there is little concern of pressure-induced stress in transient conditions.

Table 3-17 Cladding Temperature Limits (Hot Channel)

	Steady State	Anticipated Transients
Maximum Clad Temperature	750 °C	1300 °C

Creep is most likely the limiting phenomenon for the clad during anticipated transients. In this case we know that the material retains excellent creep resistance for many hours at high temperature (1300 °C). Similarly, the proposed fuel cladding temperature limit for the GCFR cladding under faulted conditions was 1300 °C [26]. Additionally, there is little loss of mechanical performance in ODS due to embrittlement as there is no Nickel, and thus drastically reduced helium production versus other alternatives, in the cladding. Therefore, the temperature limits in Table 3-17 are adopted for the B&B GFR cladding.

### 3.10. VIPAC Fuel Conductivity

VIPAC UC and U<sup>15</sup>N were selected as fuel forms for the B&B GFR. However, the conductivity of UC and U<sup>15</sup>N manufactured using VIPAC has not been extensively studied. Therefore, an approach was taken to approximate the fuel conductivity for these types of fuels. VIPAC UO<sub>2</sub> fuel has been studied and experiments have been conducted to determine the effect of burnup and temperature on fuel conductivity [14]. It was assumed that the thermal conductivity of VIPAC fuel is proportional to the thermal conductivity of the solid material, in other words, it was assumed that a temperature dependent ratio could be applied to the conductivity of UN and UC to arrive at an approximate thermal conductivity for the VIPAC U<sup>15</sup>N and UC fuel. Given the temperature dependent thermal conductivity for UO<sub>2</sub>, and the results of [14], a temperature

dependent ratio was calculated.<sup>20</sup> The expression for the ratio of VIPAC to solid UO<sub>2</sub> conductivity is shown in Equation (3.6).

$$k(VIPAC, UO_2) = rk(UO_2)$$

$$r = \frac{k(VIPAC, UO_2)}{k(UO_2)} = \frac{C(3.88001 - 0.00137T + 0.423 \times 10^{-6}T(T - 273)^2)}{\frac{3824}{129.4 + T} + 0.61256 \times 10^{-10}T^3}$$
(3.6)

Where T is the temperature in K

r is the ratio discussed above,

C is the fill gas factor, assumed 0.70 (i.e. 100% fission gas),

k(VIPAC, UO<sub>2</sub>) is the empirical correlation for VIPAC UO<sub>2</sub> conductivity in W/m-K, and

k(UO<sub>2</sub>) is the thermal conductivity of UO<sub>2</sub> from [63] in W/m-K.

Given the VIPAC conductivity ratio (r), it is possible to predict the temperature dependent thermal conductivity for UC and UN based on correlations for their respective solid pellet conductivities. Taking an expression for the thermal conductivity of UC from [38], Equation (3.7) shows the approximated thermal conductivity for VIPAC UC.

$$k(VIPAC, UC) = rk(UC)$$

$$k(VIPAC, UC) = \frac{0.70(3.88001 - 0.00137T + 0.423 \times 10^{-6}T(T - 273)^2)}{\frac{3824}{129.4 + T} + 0.61256 \times 10^{-10}T^3} (10.28 + 0.00972T - 0.188 \times 10^{-5}T^2)$$
(3.7)

A similar treatment is used for the thermal conductivity of VIPAC UN, given the conductivity of UN from [2]<sup>21</sup>, as shown in Equation (3.8).

$$k(VIPAC, UN) = rk(UN)$$

$$k(VIPAC, UN) = \frac{0.70(3.88001 - 0.00137T + 0.423 \times 10^{-6}T(T - 273)^2)}{\frac{3824}{129.4 + T} + 0.61256 \times 10^{-10}T^3} (0.70 + 0.028759500T - 0.968755 \times 10^{-5}T^2)$$
(3.8)

These formulae for the thermal conductivity are input in the thermal hydraulics model to calculate the fuel temperature in the hot channel. However, UC and UN both have significantly higher thermal conductivity than UO<sub>2</sub>, and the primary temperature constraint is that for the cladding

<sup>20</sup> The results in [14] account for burnup of the fuel by taking into account the fill gas volume occupied by fission gas; as a conservative measure the entire fill gas volume is assumed to be occupied by fission products, even though the fuel will be vented.

<sup>21</sup> The conductivity expression is dependent on the fraction of heavy metal that is plutonium; 5% was assumed, as the fuel starts with 0 at BOC and ends with ~10%. This is done so that the conductivity would be only temperature dependent and still representative of the fuel during irradiation.

material. Therefore, while only approximate for several reasons, this treatment for estimating the fuel conductivity is deemed suitable for current purposes.

### 3.11. Chapter 3 Summary

The purpose of the work reported in this chapter was to identify materials for the core design that would best facilitate B&B operation. Simple unit cell models and burnup calculations were used to compare a wide range of different fuel forms, many of which were proposed as part of the ANL Reduced Enrichment for Research and Test Reactors (RERTR) program. The RERTR fuels are high heavy metal density fuels, and high heavy metal density is the best indicator of good neutronic performance for a B&B reactor fuel.

The end result was that  $U^{15}N$  and UC were identified as the leading candidates for the B&B GFR based on their neutronic performance, and vibration-compaction (VIPAC) fuel manufacturing was identified as a good approach, since the fuel must withstand high burnup, high fluence neutron irradiation. The VIPAC fuel conductivity was estimated using an empirical approach based on experience with oxide VIPAC fuel.

MA 956 Oxide Dispersion Strengthened Stainless Steel (ODS) was selected as the cladding and structural material. ODS has an excellent blend of superior mechanical performance (based on its high melting temperature and creep resistance) and superior neutronic performance (given the low parasitic absorption cross section and very low helium production rates). Operating limits for the cladding peak temperatures under steady state and accident conditions (namely 750 °C and 1300 °C, respectively) were selected for the ODS based on its properties and experience from the GA GCFR design process during the 1970s.

As nitride and carbide fuels will likely oxidize in  $CO_2$  environments, it was not considered as a potential coolant, therefore helium was selected based on its relative neutron transparency (and hence improved neutronic performance) and extensive experience in other gas-cooled reactors. Helium and liquid metal coolants were compared showing that the neutron spectrum is noticeably harder with the gas coolant, warranting its preferential use for the B&B application.

Given the choice of fuel, cladding, and coolant two reactor design concepts were pursued. The first concept, or the demonstration concept was based on the more exotic nitride fuel, enriched in the isotope  $^{15}N$ , given that it is more neutronically reactive than carbide fuel, and hence would facilitate the design of a more conventional pin-type fueled reactor core. As the reactivity is directly related to the heavy metal loading, a second concept was pursued with the carbide fuel that uses an advanced fuel assembly design to increase the heavy metal loading without breaching the cladding temperature limits or severely limiting reactor thermal power.



## Chapter 4. Demonstration Core Overview

### 4.1. Introduction

Before describing the design of the B&B GFR Core, this chapter gives a basic overview of the demonstration B&B GFR reactor plant, as well as unique physical aspects of the core. Two B&B GFR cores are proposed in the current work. The first focuses on a pin-type assembly fuel design. The first design is the “demonstration” core. It is worth reiterating the unique reactor physics aspects of the B&B GFR. First, the fresh assemblies are subcritical, and therefore, these assemblies depend on sharing reactivity with partially burnt assemblies. Second, because of clad endurance limits, the assemblies are discharged near the burnup where they attain peak reactivity, therefore, the other partially burnt assemblies, over any given cycle, must breed in sufficient excess reactivity to overcome the difference between the fresh and discharged assemblies. The second aspect means that the reactivity swing (increase) over any given cycle will be large compared with more conventional reactors. Third, the reactivity limited burnup is the minimum burnup that fuel must reach to sustain core criticality, and the fourth is that the reactivity is proportional to the inverse of the heavy metal density, and hence the heavy metal loading in the fuel. Therefore, a B&B GFR that brings reactivity-limited burnup to a reasonable level (such as 150 MWD/kg<sub>HM</sub>) must utilize high heavy metal density fuels.

### 4.2. Fuel Assembly Design

The demonstration core utilizes U<sup>15</sup>N fuel (the most reactive fuel form, see section 3.3.1) in a tight pitch pin-type fuel assembly. Roughly 45% of the core volume is occupied by VIPAC U<sup>15</sup>N fuel to achieve a reactivity great enough to reduce the reactivity-limited discharge burnup to the design goal of 150 MWD/kg<sub>HM</sub>. Though 45% is a large fraction of the core volume, to achieve a similar B&B OTTO with alternative fuels, such as UC, even larger volume fractions would be required or a higher discharge burnup would be required. Since 150 MWD/kg<sub>HM</sub> is already a substantial increase over conventional reactors (threefold that of current LWRs), an innovative fuel assembly must be employed in advanced core concepts to increase the heavy metal loading without significantly compromising the thermal hydraulic performance of the core in terms of peak temperatures and core pressure drop.

The demonstration core is so named because it strives to illustrate the viability of the B&B OTTO cycle without extending fuel fabrication techniques far beyond current capabilities. However, this core must use an exotic and more expensive fuel form to achieve this goal.

The fuel is manufactured using a vibration-compaction process. Advanced VIPAC processes developed and tested in Russia with oxide fuel can achieve very high smear density (90-91% of the theoretical density). Post irradiation examination of experimental fuel assemblies tested in Russian fast reactors indicate that concerns over both chemical and thermochemical fuel-cladding interactions are practically eliminated and burnup is effectively limited by the choice of cladding material [41].

Each assembly contains 169 fuel pins arranged in a triangular pattern and each batch contains 102 fuel assemblies; the core is comprised of 6 batches. Reflector pellets, stacked to a total height of 25 cm, made of Zr<sub>3</sub>Si<sub>2</sub> are included at the upper and lower axial extremes of the active fuel region. A cross section of the fuel assembly is illustrated in Figure 4.1. The figure clearly shows the tightness of the fuel pin lattice.

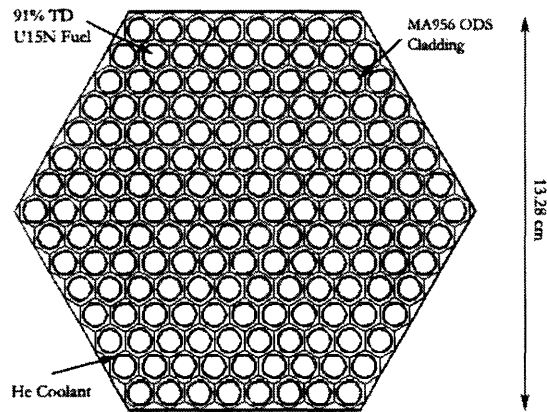


Figure 4.1 Horizontal Cross-sectional View of a Fuel Assembly

The core is arranged such that the fresh fuel assemblies are located near the core periphery. The reload assemblies are enriched to 5 a/o  $^{235}\text{U}$  in U. The multiplication factor of an infinite fresh assembly is approximately 0.8.

### 4.3. Balance of Plant

Initial investigations of the B&B GFR core focused on a supercritical carbon dioxide (S-CO<sub>2</sub>) Power Conversion System (PCS) studied previously at MIT [17,18]. In the base case, or first design iteration, the core was coupled to a S-CO<sub>2</sub> PCS with an intermediate printed circuit heat exchanger (PCHE). While the PCHE is ideally suited for this purpose [27], the S-CO<sub>2</sub> PCS is optimized for a core temperature rise of 150 °C. In an indirect cycle, the mass flow rate, and hence primary circulator work, required to cool the reactor core at such a low temperature rise is very large for a core having high fuel volume fraction and low coolant volume fraction. This significantly reduces the net efficiency for power production. Therefore, the B&B GFR, as many previously designed and operated gas-cooled reactors, utilizes a Steam Rankine PCS.

The balance of plant for the B&B GFR is modeled after the Advanced Gas-cooled Reactor (AGR). The schematic shown in Figure 4.2 is the plant layout for an AGR. The primary difference between the AGR and the B&B GFR is the core design, while the secondary side is essentially unchanged except for perhaps the size of the plant. The intermediate heat exchanger (IHx) is a standard steam generator.

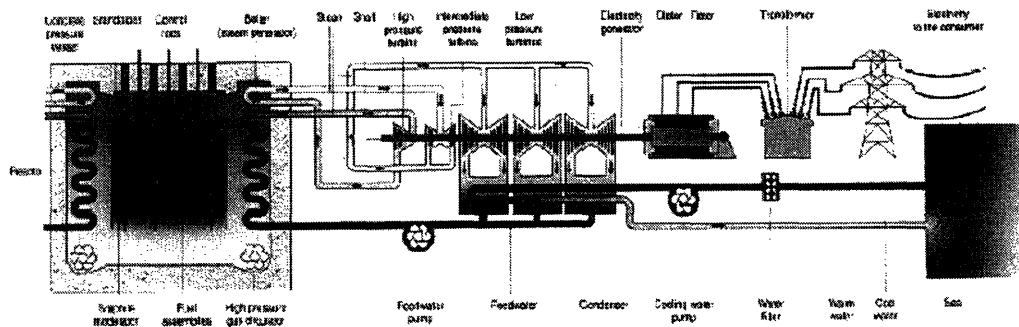


Figure 4.2 AGR Plant Layout [22]



The Steam Rankine PCS is a very mature and well understood technology, and previously used in a variety of operated gas-cooled reactors (Peach Bottom, Fort St. Vrain, British AGRs) and the reference balance of plant in several designs studied during the 1970s (General Atomics GCFR, High Temperature Gas Reactors, and the European Gas Breeder Reactor) [43].

The steam generator outlet temperature on the secondary side is 541 °C for the AGR with a temperature rise across the steam generator of 385 °C, corresponding to a 40% efficient Rankine-type PCS [63]. The log-mean temperature difference between the hot and cold fluids in the steam generator is assumed to be 20 °C for a high performance design, though no consideration is given to the specific design of the steam generator in the current work.

The B&B GFR also employs an active decay heat removal system and insulated reactor pressure vessel, though the specifics of these designs are also not given further consideration in the current work.

#### **4.4. Core Design Limitations and Strategies**

Several phenomena were identified early on as design constraints and key goals. To briefly recap the results from the material downselection, the peak cladding temperature in the steady state is limited to 750 °C and the helium velocity in the core is limited to 120 m/sec. The void reactivity worth is also limited to \$1 to avoid prompt criticality in the event of a loss of coolant accident. These characteristics of the core are dependent on design variables, one of which is the primary circuit pressure, which affects the mass flow rate, circulator power requirement, efficiency, and coolant void reactivity. An optimized design will strive to meet at least two of the three limitations listed here. Another limitation is that the core design should indicate safe operation according to the Quasi-Static method (discussion in section 2.2.5).

Having limited the coolant to helium, heat removal became a key area of focus, and as such, axial power shaping was investigated early on to determine if anything could be done given the stringent neutronic requirements of the B&B once-through-then-out fuel cycle (OTTO). As discussed in section 4.4.2, the aggressive plutonium breeding and high burnup makes axial power shaping through enrichment zoning a futile effort.

Lastly, the characteristics of the spent fuel from the B&B GFR were investigated using unit cell and infinite assembly models. The nature of spent fuel will affect potential alternative fuel cycles that may improve the economics of the system when proliferation resistant spent fuel treatment technologies can be applied.

##### **4.4.1. Primary Circuit Pressure**

The choice of the primary coolant pressure is dependent on a trade-off between the reactor physics and thermal hydraulic performance of the system. In essence, the higher the primary circuit pressure the smaller the required compressor work and the smaller the outlet helium velocity. From a thermal hydraulic standpoint, increased pressure increases the system efficiency by reducing the primary circulator power. From a structural integrity standpoint, increased pressure reduces helium velocity, and therefore reduces erosion rates.

From a reactor physics standpoint, however, the coolant void reactivity worth is dependent on the spectral shift associated with the change in coolant density between nominal operation and voided conditions. It is the goal of the design to limit the coolant void reactivity worth to less than \$1 for a helium cooled core. The void reactivity worth increases as the coolant density increases in the

nominal condition, hence, from a reactor physics standpoint it is best to reduce the primary circuit pressure to reduce the coolant void reactivity worth.

A reference EOEC B&B GFR core was analyzed by inspecting the difference in reactivity as the helium density is increased. The reactivity of the voided core was also calculated, and in doing the analysis, it was found that 10 MPa leads to a reactivity void worth of \$1 at the EOEC. Thus, 10 MPa was assumed to be the limiting pressure for this exact reason, and this value was later confirmed with MCNP calculations of the final design.

Next, at the maximum pressure allowable by the constraint on the coolant void reactivity worth, the circulator power is then minimized. The circulator power is dependent on the mass flow rate and density of the fluid; at high pressure the density is increased and the mass flow rate is reduced, thus, when operating at the highest allowable pressure the net electric energy that can be produced is maximum. However, for the purpose of establishing margins, a trade-off study is done where the coolant void worth is assumed to be proportional to the coolant density (noting that a loss of primary pressure would result in a coolant density  $\sim 1/100$  times the nominal density).

This is not a poor approximation given the available data. In the first design iteration (which was the S-CO<sub>2</sub> PCS case), the coolant density was 0.004130 g/cc and the void reactivity worth at BOC was 0.43\$. In the 10 MPa (Rankine PCS case) case the coolant density is 0.007620 g/cc and the void reactivity worth at the BOC is 0.80\$. The ratio of the densities is  $\sim 1.85$  and the ratio of the coolant void worth is  $\sim 1.86$ . Therefore, one can predict the net efficiency of the cycle based on the finite volume model and one can also estimate the coolant void reactivity worth for primary circuit pressures between 8 and 10 MPa. Table 4-1 summarizes the results of a series of coupled calculations. A finite volume model of a 2400 MW B&B GFR pin-type core was used to calculate helium outlet velocity, peak clad temperature, and the net efficiency for an AGR-type PCS for a variety of operating pressures. The 10 MPa void worth was used to estimate the void worth for the 9 MPa and 8 MPa cases. As shown in Table 4-1, there is an available design space between 10 and 9 MPa system pressure, as the velocity, temperature, and coolant void limits are all met in this range.

Table 4-1 Systematic Comparison for a 2400 MW<sub>th</sub> B&B GFR Core (pin-type)

primary system pressure	outlet velocity	peak clad temp.	net efficiency	estimated void worth (EOEC)
MPa	m/s	°C	%	\$
10	99	632	39.2	1.0
9	111	633	39.1	0.9
8	126	635	38.8	0.8

The system pressure does not have significant impact on the net efficiency of the cycle, nor the peak clad temperature. The limit of 120 m/sec on the helium velocity, however, is apparent between 8 and 9 MPa. Therefore, it is possible to reduce the EOEC void reactivity worth to  $\sim 90$  cents instead of  $\sim 100$  cents without compromising the plant efficiency or peak clad temperature or breaching the helium velocity limit.

However, an optimized design would entail reaching two of the three limitations. In this case, the power can be increased at a pressure of 10 MPa until the velocity at the core outlet reaches 120 m/sec; this would coincide with reaching the \$1 limit on coolant void reactivity.

In this case 10 MPa would limit the reactor power to ~2900 MWth before reaching 120 m/sec outlet velocity, and a primary circuit pressure of 9 MPa would limit the power to ~ 2400 MWth with similar efficiencies and cladding temperatures. However, the higher power density represents a reduction in fuel residency time of ~20% which is a significant cost savings from the fuel cycle standpoint. Therefore, Table 4-1 is not complete in that as the primary pressure is increased, the thermal power of the reactor can also be increased until the helium outlet velocity reaches the 120 m/s limit; the recommended primary circuit pressure is therefore 10 MPa.

#### 4.4.2. Axial Power Shaping

Smoothing the axial power profile is of interest in reactor design. This is particularly difficult in B&B reactors because power shifts towards high flux regions of the core as  $^{239}\text{Pu}$  is bred and then shifts away from regions where fissile material has been burnt. The natural tendency of the core to breed as well as burn leads to dynamic axial power distributions. An initial study was done to assess the power shape as a function of burnup for a pin with a uniform axial enrichment at the BOL. The results are depicted in Figure 4.3 in the form of a series of axial power shapes for a UC fuel unit cell.

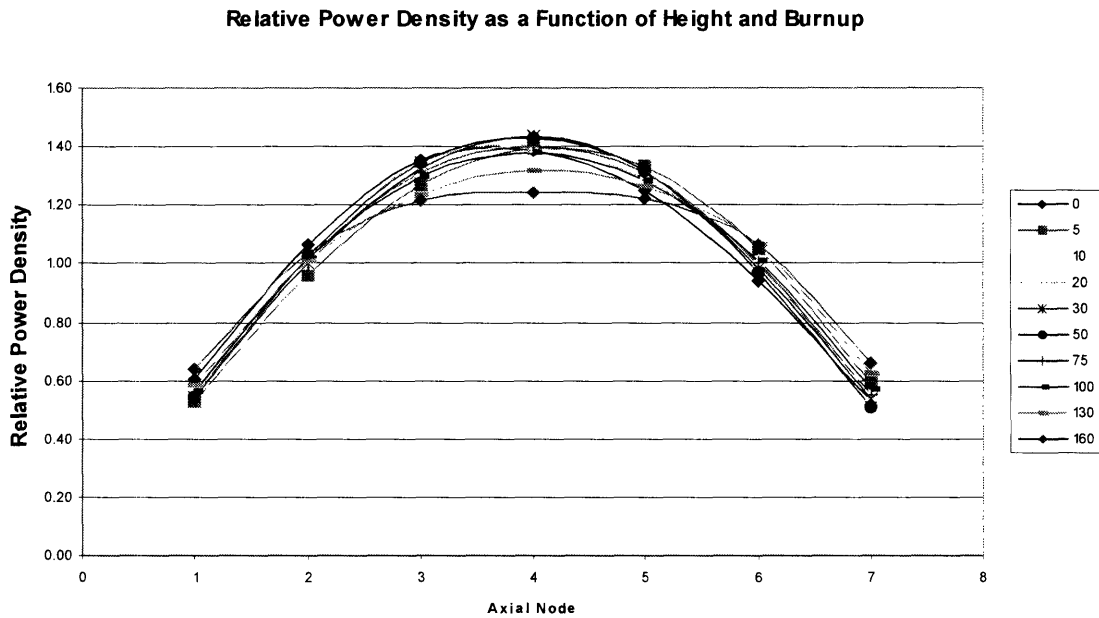


Figure 4.3 Axial Power Shape History for Uniform Fuel

The power peaking was calculated for each burnup step, and the maximum power peaking factor was assumed to be the maximum from those calculated for the burnup steps listed. In the base case, a constant axial enrichment of 10 a/o  $^{235}\text{U}$  in U was assumed. Table 4-2 summarizes the power peaking factors as a function of burnup, and the maximum is quoted.

Table 4-2 Power Peaking History for Uniform BOL Enrichment

Burnup [MWD/kgHM]	0	5	10	20	30	50	75	100	130	160	Axial Node	Enrichment
relative power	0.60	0.53	0.56	0.54	0.55	0.55	0.54	0.57	0.59	0.64	1	10 a/o
	1.06	0.96	1.00	1.02	1.00	1.02	1.02	1.02	1.01	1.04	2	10 a/o
	1.36	1.27	1.32	1.35	1.32	1.34	1.31	1.30	1.24	1.21	3	10 a/o
	1.39	1.40	1.40	1.40	1.43	1.43	1.40	1.38	1.32	1.25	4	10 a/o
	1.25	1.33	1.30	1.29	1.32	1.32	1.31	1.29	1.26	1.22	5	10 a/o
	0.94	1.05	1.01	0.99	0.98	0.97	1.00	1.01	1.07	1.07	6	10 a/o
	0.53	0.59	0.55	0.53	0.54	0.51	0.55	0.57	0.63	0.66	7	10 a/o
peaking factor	1.36	1.37	1.37	1.38	1.40	1.40	1.38	1.35	1.30	1.23	MAX	1.40

The power increases in the middle axial expanse of the fuel right before the middle of life, ~60 MWD/kg<sub>HM</sub>, before peak reactivity is achieved. The maximum power peaking factor is 1.40, and may be larger for values between 30 and 50 MWD/kg<sub>HM</sub>. A test was done to try and reduce the maximum power peaking factor. Enrichment was zoned axially to initially shift the power towards the top and bottom of the core. The same procedure was then used again to develop the power shapes as a function of burnup. Figure 4.4 illustrates the zoned power histories.

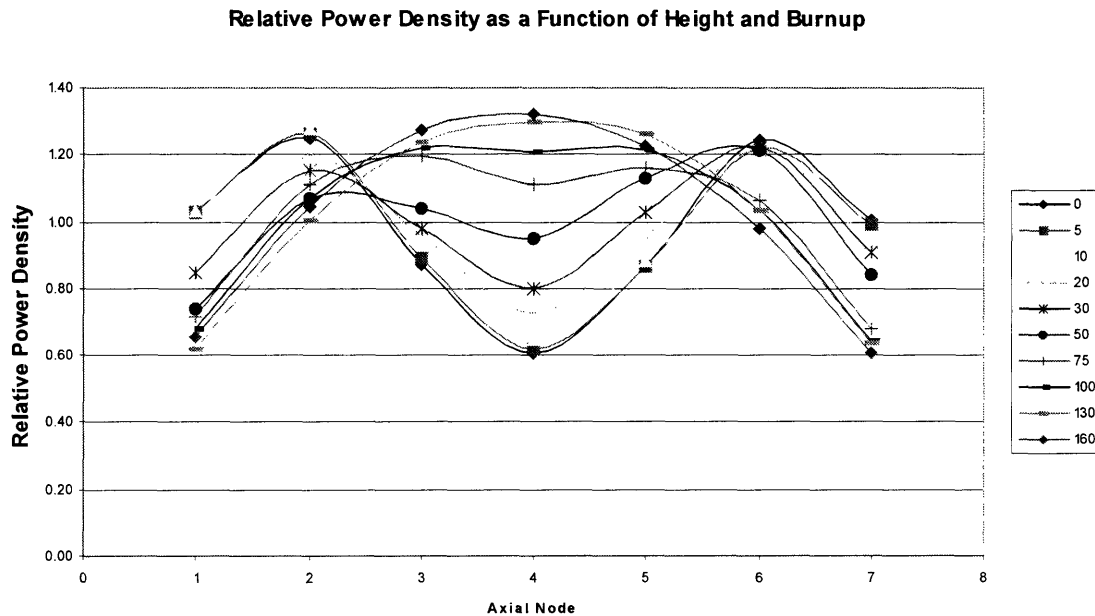


Figure 4.4 Axial Power Shape History for Enrichment-Zoned BOL Fuel

The general trend in the power is to burn to a chopped cosine shape. The high flux in the center of the fuel breeds more <sup>239</sup>Pu in the center towards the BOL, and by the EOL the power is being produced predominantly by <sup>239</sup>Pu fission. Since <sup>239</sup>Pu is more aggressively bred in the central region of the core, the power will always burn in the direction of a cosine curve. The power

peaking factor was then evaluated as a function of burnup again, and Table 4-3 gives the enrichment zones as well as the power peaking factors.

Table 4-3 Power Peaking History for Zoned Enrichment

Burnup [MWD/kgHM]	0	5	10	20	30	50	75	100	130	160	Axial Node	Enrichment
relative power	1.03	1.03	1.03	0.92	0.84	0.74	0.72	0.68	0.62	0.66	<b>1</b>	12 a/o
	1.25	1.26	1.28	1.19	1.15	1.07	1.11	1.07	1.00	1.04	<b>2</b>	11 a/o
	0.87	0.89	0.93	0.96	0.98	1.04	1.19	1.22	1.24	1.27	<b>3</b>	9 a/o
	0.60	0.62	0.65	0.73	0.80	0.95	1.11	1.21	1.30	1.32	<b>4</b>	7 a/o
	0.87	0.87	0.88	0.96	1.03	1.13	1.16	1.21	1.26	1.22	<b>5</b>	9 a/o
	1.24	1.22	1.17	1.22	1.22	1.21	1.06	1.03	1.03	0.98	<b>6</b>	11 a/o
	1.00	0.99	0.94	0.94	0.90	0.84	0.68	0.64	0.64	0.61	<b>7</b>	12 a/o
peaking factor	1.27	1.28	1.30	1.23	1.23	1.22	1.19	1.21	1.28	1.30	<b>MAX</b>	1.30

The average enrichment is still 10 a/o. The power peaking factor was reduced by a small amount to 1.30, but this was done at the expense of increasing the power peaking factor at BOL by creating two power peaks near the top and bottom of the core. The power peaking factor at the BOL is large (1.27) and gets smaller as the power shape approaches a cosine shape. By the EOL, however, the axial power shape has reached a chopped cosine and the power peaking factor reaches 1.30 again.

Recall that for different enrichments, the  $^{239}\text{Pu}$  number density approached a similar asymptotic value at high burnup (approximately 10% of heavy metal for UC fuel). For axial enrichment zoning, the BOL power can be flattened, but as the core burns out, the  $^{239}\text{Pu}$  number density profile axially will begin to flatten. The  $^{239}\text{Pu}$  concentration will flatten because each axial zone of the fuel will approach its asymptotic plutonium concentration at high burnup (> 60 MWD/kg<sub>HM</sub> local burnup). Since the average discharge burnup is large (150 MWD/kg<sub>HM</sub>), it is likely that each axial location along the fuel pin (except for the axial extremes) is near its asymptotic plutonium concentration, thus effectively flattening the axial profile of fissile species concentration. The plutonium concentration profile would result, therefore, in an axial power peaking factor similar to that for a uniform enrichment case at long burnup regardless of the initial enrichment zoning.

Though the power peaking factor was reduced somewhat, this was done at the expense of BOL reactivity because neutron leakage increases when power is shifted towards the top and bottom of the core. The expense to the neutron economy also occurs at the beginning of irradiation for any significant reduction in long-term power peaking reduction, and this is exactly the point during irradiation where the fuel is least reactive. Since the axial power shape will approach a cosine shape, enrichment zoning at BOL to flatten the power profile is futile in terms of minimizing the power peaking factor at every burnup.

Another approach that would seem promising to shape axial power is to zone the fuel density, as opposed to the enrichment, axially by including an inert matrix or diluent. However, the reactivity is directly related to the heavy metal loading, and therefore, an approach to flatten the axial power shape by zoning the loading (and hence designing a fuel element without the maximum allowable loading) is also a futile effort for the B&B GFR.

#### 4.4.3. Fission Gas Venting

The requirement for fission gas venting is derived from several constraining phenomena, particularly the need to reduce reactor pressure drop by eliminating the need for large fission gas plena at the extremes of the fuel assemblies, and to reduce the pressure induced stress on the irradiated cladding in the steady state as well as in the event of a loss of primary pressure.

Fission gas venting is a mature and demonstrated technology. Fission gas venting was successfully implemented for the Dounreay fast reactor [67] and was proposed for the GA GCFR design of the 1970's [25,26,15]. Given the benefits, and that this technology is well understood, fission gas venting is adopted for the B&B GFR. Although the current work does not encompass the design of the fission gas manifold or off-gas system, it is likely that the GA GCFR design would serve as the reference conceptual design for this system.

#### 4.4.4. Spent Fuel Characteristics

B&B GFR spent fuel typically has a large fissile fraction of plutonium (> 80%). A principal objective is to economically extract more energy in a highly-proliferation-resistant mode in which the final spent fuel plutonium also has a smaller fissile fraction. While the current work deals only with B&B mode GFR fuel, the same approach may be applicable to other fast reactor concepts.

In the present calculations, an HT-9 stainless steel clad, helium cooled, UC fuel pin in a GFR unit cell was burned to 130 MWD/kgHM using MCODEv1, cooled for 5 years using ORIGEN2.1, and then subjected to an AIROX type treatment, removing volatile fission products, previously shown to be removable [48]. The 5 year cooling period would correspond to 4 years after GFR irradiation before the AIROX treatment is applied, to allow for fuel fabrication, which becomes important in later economic assessment of such a fuel management strategy.

The resulting oxide fuel was then modeled as a standard Westinghouse PWR fuel pin. The fuel was burnt to 60 MWD/kgHM using CASMO-4 in a standard Westinghouse 17x17 PWR fuel assembly. Another case where 50% standard 4.4% enriched oxide fuel and 50% treated B&B GFR fuel are mixed in an assembly was run with CASMO-4. Table 4-4 summarizes some of the relevant data for the initial and final fuel compositions for treated fuel. In the PWR case, the table refers to the whole assembly of treated GFR fuel.

Table 4-4 Spent Fuel Fissile Content

	<b>B&amp;B GFR In</b>	<b>B&amp;B GFR out</b>	<b>PWR in</b>	<b>PWR Out</b>
<b>w/o <sup>235</sup>U in HM</b>	5	2.51	2.51	1.60
<b>w/o Pu in HM</b>	0	9.65	9.62	7.84
<b>w/o Fissile Pu in Total Pu</b>	0	86.8	87.0	73.3
<b>Burnup, MWD/kgHM</b>	0	130	0	50

The infinite medium eigenvalues as a function of burnup are shown in Figure 4.5. For comparison purposes, the burnup histories for a 4.4% <sup>235</sup>U enriched fuel assembly, and a 4.4%

$^{235}\text{U}$  enriched fuel assembly with burnable poison pins are shown. The most noteworthy feature in the burnup histories of the treated GFR fuel is the initial rise in eigenvalue.

In the hard GFR spectrum, some fission products with strong thermal and epithermal absorption cross sections, but weak fast absorption cross sections, accumulate to much higher concentrations than in LWRs. The primary contribution to fission product poisoning in the LWR fuel produced from spent GFR fuel at early burnup in the PWR is  $^{149}\text{Sm}$ . The  $^{149}\text{Sm}$ , however, quickly burns out in the thermal PWR spectrum. In essence, fission products such as  $^{149}\text{Sm}$  are self-generated LWR burnable poison.

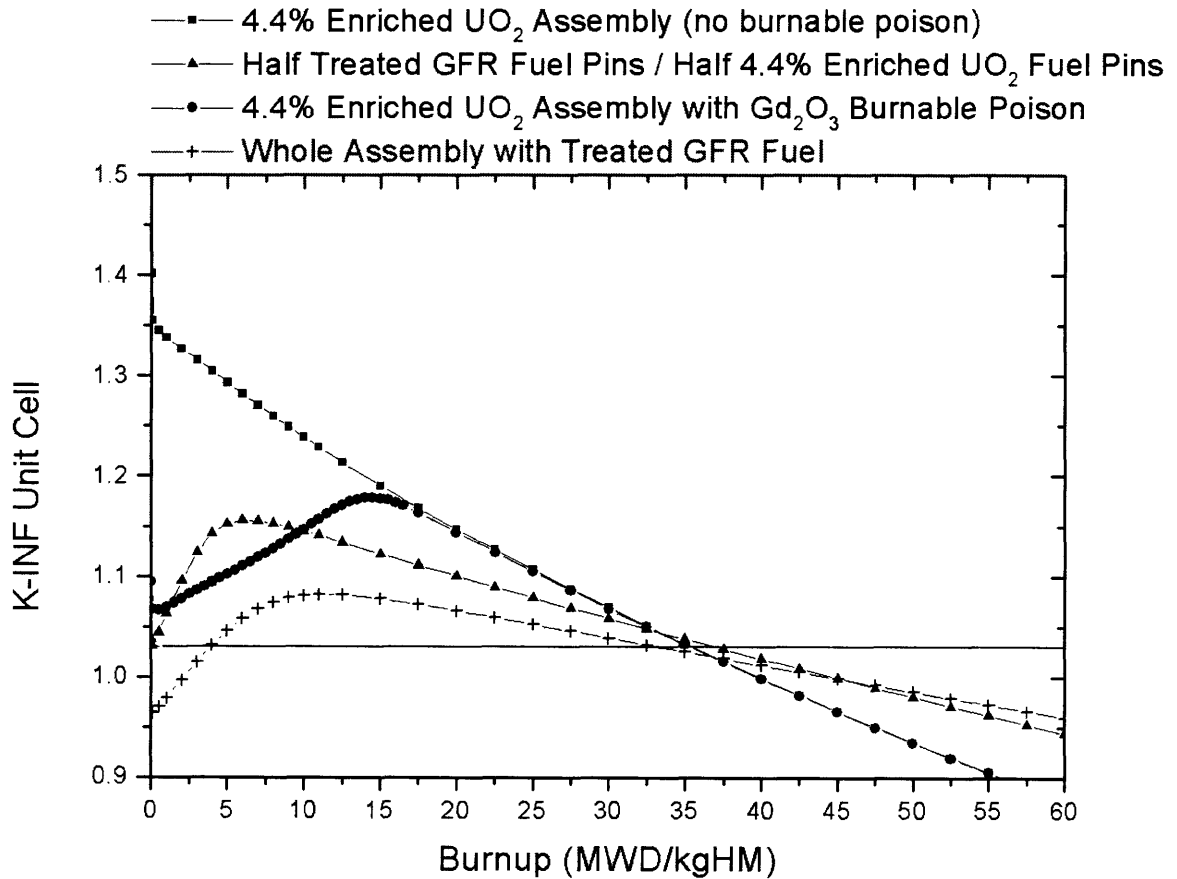


Figure 4.5  $k_{\text{inf}}$  as a Function of Burnup for Different PWR Cases.

The second point of note is the burnup where the single-batch-burned mixed fuel assemblies reach  $k_{\text{inf}}$  of 1.03 (to allow for leakage): around 35 MWD/kg<sub>HM</sub> for all cases. This would permit attaining discharge burnup on the order of 50 MWD/kg<sub>HM</sub> in a 3-batch management scheme. The corresponding full power refueling interval is approximately 18 months.

While reactivity feedback was not investigated, the basic feasibility of employing minimally-processed B&B GFR spent fuel for LWR reuse has been confirmed. The treated spent fuel from

the B&B GFR when combined with standard fuel pins in an assembly will emulate a PWR assembly with burnable poison. However, other compositions and configurations may prove superior. The CARDIO process in which UC fuel is oxidized by treatment with CO<sub>2</sub> has not been as fully examined as AIROX treatment of UO<sub>2</sub> fuel. There is some evidence, not yet fully established or replicated, that fission product poison removal during the CARDIO processing is enhanced beyond what is taken credit for here [48].

#### **4.5. Chapter 4 Summary**

This chapter briefly describes some of the design choices leading to the final design of the demonstration B&B GFR core and plant. The fuel assembly is a pin-type design aimed at achieving a large heavy metal loading to facilitate B&B operation with U<sup>15</sup>N VIPAC fuel. The core is coupled to an AGR type Rankine Power Conversion System (PCS). This particular PCS was selected for the design as opposed to competing technologies, such as the S-CO<sub>2</sub> PCS because the large temperature rise across the steam generator for the Rankine Steam Plant allows for reduced primary coolant flow rates and hence reduced primary circulator power.

The neutronic characteristics and material composition of the fuel are also discussed in terms of hard spectrum irradiation. It was found that the axial power shape will tend to a chopped cosine shape during burnup regardless of the initial axial enrichment profile, thus precluding the use of enrichment zoning to flatten axial power shape. Additionally, in the hard spectrum reactor, the concentration of fissile plutonium at the end of irradiation is substantial, and could potentially be used in a LWR.

Based on these preliminary observations, a full core was designed to meet the neutronic requirements and material limitations of the B&B GFR core. The three following chapters will discuss the neutronic design of the reactor core, the assessments of its thermal hydraulic performance, and lastly the nuclear fuel cycle costs associated with the demonstration concept.



## Chapter 5. Demonstration Core Physics

### 5.1. Introduction

The design of the demonstration B&B GFR core began with an initial investigation into the neutronics for a full core design, and as such, the design evolved over two stages. The first stage involved a rapid assessment of the physics for a preliminary design, and the second stage involved the refinement of the design to better meet the other neutronic and thermal hydraulic requirements.

The most striking difference between the preliminary and final designs of the demonstration core is the rated power. The preliminary design was conducted in the near absence of coupled thermal hydraulic calculations in order to first check the feasibility of the physics before committing to further work in the areas of thermal hydraulics and economics. The preliminary demonstration core design was conducted in the context of a reference super-critical CO<sub>2</sub> secondary power conversion system and a rated power of 3200 MW<sub>th</sub>. The uncontrolled reactivity (i.e. the evolution of core eigenvalue without the control rods being inserted or withdrawn during irradiation) was of key interest in validating the B&B concept.

While the final rated power for the design hinged on the thermal hydraulics, the weak absorption in the fission products due to the hardness of the neutron spectrum essentially divorced the neutronic performance from the power density, and thus, at any given power level the reactivity history for the core when plotted against burnup (as opposed to effective full power time) would remain essentially unchanged. Section 5.2 covers the results of the preliminary core design while section 5.3 describes the refinements of the design in terms of important neutronic phenomena that were not considered during the preliminary stages.

### 5.2. Preliminary Core Design

The preliminary design of the demonstration core focused on an approach to sustain criticality at the beginning of each cycle from startup until the core reached equilibrium. While 3200 MW<sub>th</sub> was selected as the reference power level, the reactivity history is essentially independent of the power density over a large range because of the hardness of the neutron spectrum. In order to achieve this, a multi-batch strategy was developed. Given the large difference in the reactivity of fresh and discharged assemblies as dictated by the burnup goal of 150 MWD/kg<sub>HM</sub>, a six batch scheme was adopted to promote reactivity sharing.

While the control devices were not modeled, the preliminary design included seven control rod assembly (CRA) locations. Figure 5.1 shows a diagram of the preliminary core design with the batch locations numbered as well as the location of the CRAs.

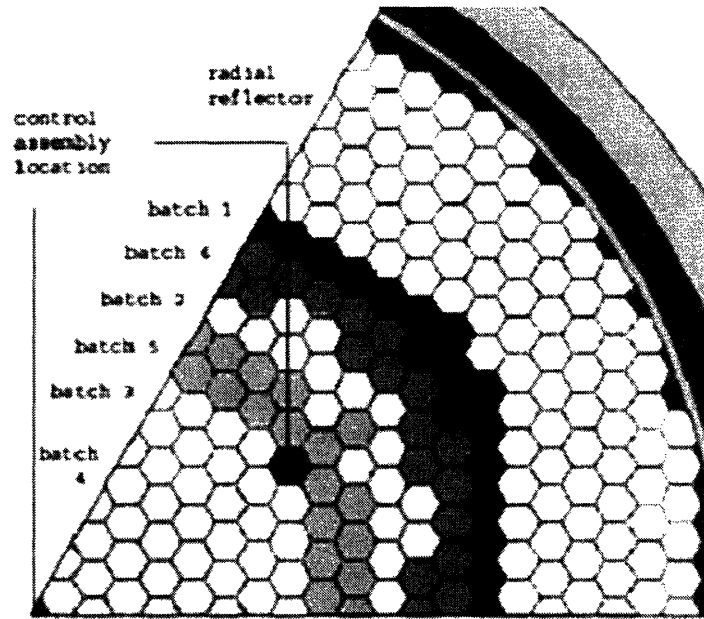


Figure 5.1 Preliminary Core Design 1/6<sup>th</sup> Symmetric Model

The 1<sup>st</sup> and 2<sup>nd</sup> batch locations are near the radial periphery of the core. These batches are the lowest reactivity batches, and are placed in the outer batch locations in order to act as radial blankets. This strategy allows for the partially burnt assemblies closer to the core center to act as a seed. If the fresh batches were included in the center of the core, the detriment to the reactivity at the BOC would be insurmountable given their negative infinite medium reactivity.

The batches are arranged in concentric rings for several reasons. The fuel during its campaign through irradiation is advanced by batch location as shown in Figure 5.1. The 6<sup>th</sup> batch is located at the core periphery between the 1<sup>st</sup> and 2<sup>nd</sup> batches in order to increase the neutron flux in the low reactivity, fresh batches to promote plutonium production in these batches. The 3<sup>rd</sup> and 4<sup>th</sup> batches comprise the center of the reactor core. During irradiation, reactivity rapidly builds up in the 2<sup>nd</sup> batch in particular; when transferred to the 3<sup>rd</sup> batch location, these fuel assemblies build reactivity more slowly during irradiation, as they are approaching their asymptotic plutonium concentration.

Therefore the evolution of the power shape during irradiation is more benign and by placing these highly reactive batches at the core center, the core reactivity is increased. The final pattern for the fuel shuffling through a campaign has the fuel move inward radially towards the center of the core as plutonium concentration increases (to sustain criticality) and then the batches move outward (to promote radial flux flattening and higher plutonium production rates in fresh batches).

A convenient benefit of this multi-batch approach is that each batch is essentially confined to a radial “ring” about the center of the core, and as such will experience essentially the same neutron flux throughout the batch. The major exception would perhaps be the fourth batch, which constitutes the center of the core. Therefore, in modeling the core, a major simplifying assumption was made: that the composition and incremental burnup for each assembly in a batch is the same after each burnup step in the MCODE calculation. Given the memory constraints of the MIT Echelon Beowulf Computing Cluster, it is unlikely that a higher fidelity solution would

be tenable regardless. Recall that the memory constrained the geometry of the model such that the radial reflector could only be modeled with a single homogenous cell taken at 80% of the nominal density of the  $Zr_3Si_2$  in order to account for coolant channels.

### 5.2.1. Fuel Assembly Specifications

The core is comprised of 612 fuel assemblies in six equally sized batches. Each fuel assembly contains 169 fuel pins, as depicted in Figure 4.1. The fuel pins are MA 956 ODS clad with a VIPAC  $U^{15}N$  center. The fuel is taken at 91% of the theoretical density. Table 5-1 summarizes the assembly and core geometry. On a unit cell basis, the fuel occupies 50% of the volume of the repeating cell. However, there is additional coolant in the assembly at the edge of the assembly. If the fuel volume fraction in the active core is calculated based on the fraction of volume occupied by fuel in the assembly that value is 47.6%.

Table 5-1 Preliminary Design Demonstration Core Geometry

Fuel Form	$U^{15}N$	
Fuel Pins per Assembly	169	
Pin Outer Diameter	0.82	cm
Clad Thickness	0.04	cm
Pin Pitch	1.00	cm
Assembly Flat-to-Flat	13.28	cm
Active Core Height	200	cm
Equivalent Core Diameter	350	cm
Fuel Volume Fraction	47.6	v/o
Cladding Volume Fraction	10.8	v/o
Coolant Volume Fraction	41.6	v/o

Above and below the active core region, there are axial reflectors. The axial reflector material,  $Zr_3Si_2$ , is the same material used in the radial reflector. The axial reflector extends 25 cm above and below the fuel inside the fuel pin.

### 5.2.2. Uncontrolled Reactivity History

Several MCODE calculations were performed to model the evolution of the core through many cycles. After seven cycles were modeled the core reached equilibrium, thus any further cycle calculations would generate the same result as the 7<sup>th</sup> cycle. At startup, the core is fueled entirely with enriched uranium fuel having a core average enrichment of 8.2 a/o; some of the batches in the startup core are enriched to as high as 10 a/o  $^{235}U$  in U. The startup core configuration and fuel reload sequence are summarized in Table 5-2. The enrichment is graded in order to emulate the equilibrium cycle.

Table 5-2 Startup and Reload Sequence

Cycle Loading (a/o <sup>235</sup> U in U)			
Batch	BOC1	BOC2	BOCn
1	5	5	5
2	6	from 1	from 1
3	8	from 2	from 2
4	10	from 3	from 3
5	10	from 4	from 4
6	10	from 5	from 5

Though the reload sequence remains the same during each cycle, the 7<sup>th</sup> cycle is the first cycle after all the startup core assemblies have been discharged. During irradiation of the assemblies, the fuel composition for any initial enrichment approaches the same asymptotic behavior as discussed at greater lengths in section 1.3; thus the core rapidly approaches equilibrium.

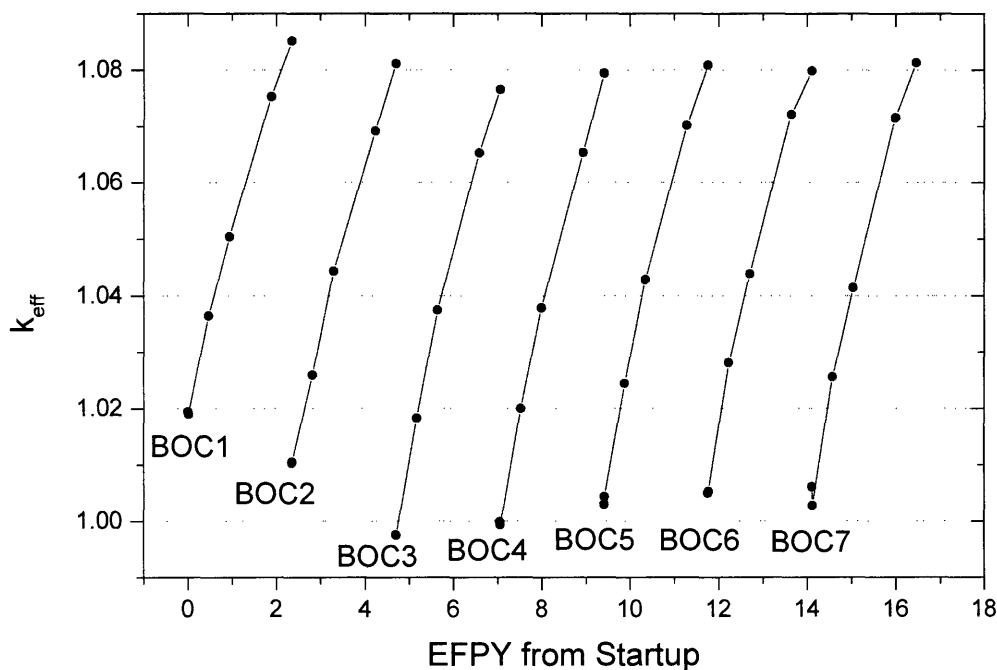


Figure 5.2 Preliminary Design Demonstration Core Reactivity History

Figure 5.2 shows the trend in the full core reactivity as a function of EFPY from startup. The standard deviation of all data points is 0.0006. No control devices are modeled, thus during any cycle the reactivity increases significantly. The core is designed such that the reactivity at BOC is unity. During irradiation the reactivity increases as plutonium is bred in the core; the reactivity increases because the reactor is breeding more plutonium than it is burning at all points during

burnup. The reactivity swing is necessarily large because the oldest assembly has a large plutonium content, and subsequently when this fuel is discharged and fresh fuel included at the core periphery, the excess reactivity in the remaining assemblies must be sufficient to overcome the difference between the oldest batch and fresh batch reactivity.

In the subject reload sequence, the reactivity at the beginning of the 3<sup>rd</sup> cycle (BOC3) is actually slightly less than unity, 0.997(5). While increasing the startup enrichment of the fuel in the 2<sup>nd</sup> batch location can easily accommodate this discrepancy, it is important to note that the modeling technique will underestimate the reactivity slightly due to plutonium drift.

### 5.2.3. **Assembly Power History in Equilibrium**

The multi-batch reload sequence was designed to optimize several competing goals. First, the scheme must promote reactivity sharing between partially burnt and fresh fuel assemblies in order to breed plutonium in low reactivity assemblies. Second, partially burnt assemblies are progressively moved towards the center of the core in order to sustain core criticality over multiple (six) cycles. Third, the power shape should remain fairly constant during irradiation to enable the use of fixed flow orificing to improve power conversion efficiency. Fourth, the radial power shape should be as flat as possible to maximize core power density. As a consequence of the current multi-batch reload scheme, the power history for the average assembly varies significantly between fuel reload and subsequent shuffling but is fairly constant during irradiation.

Figure 5.3 shows the power history for an assembly during irradiation. Step increases are incurred where the assembly is moved from one batch location to the next. The highest thermal power occurs in the 4<sup>th</sup> batch, and the lowest in the 1<sup>st</sup> batch. This calculation is done for the equilibrium cycle in the uncontrolled preliminary core model; in practice control rod clusters would be inserted predominantly in the 3<sup>rd</sup> or 4<sup>th</sup> batches to control reactivity and tailor radial power shape.

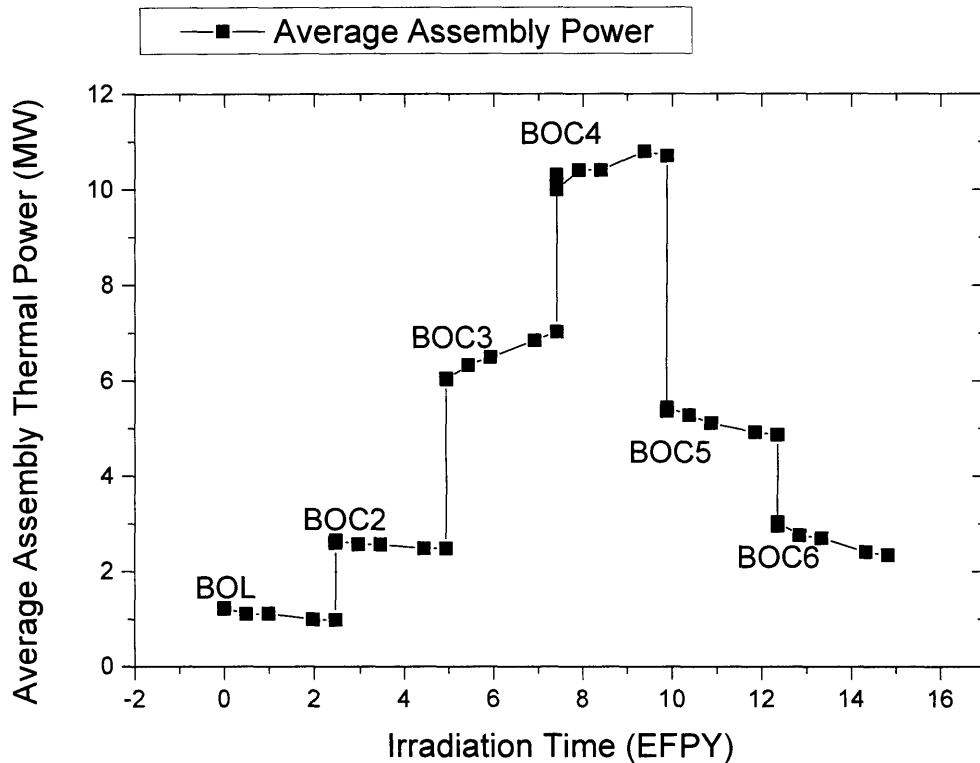


Figure 5.3 Demonstration Core Assembly Power History

The step variation in power between cycles occurs because of the multi-batch reload scheme. The fuel assemblies during irradiation are moved from the periphery of the core, to the center of the core, and then outward radially again. The power shape, however, during each cycle remains fairly constant with a slight inward shift of thermal power during each cycle, thus the slopes of the power are slightly positive in the 3<sup>rd</sup> and 4<sup>th</sup> cycles and slightly negative elsewhere, indicating a subtle, but nonnegligible radially inward shift of reactor power during a single cycle. Despite this shift, the goal to maintain a roughly constant power shape appears tenable, thus allowing for efficient flow orificing with fixed orifices in the core grid plate.

#### 5.2.4. Delayed Neutron Fraction

The delayed neutron fraction of the core was calculated for the BOEC (BOC7) and EOEC (EOC7) by comparing the core eigenvalue with and without delayed neutron cross sections. The B&B GFR spectrum is exceptionally hard compared with other fast reactor concepts, yielding a very large fertile fission fraction. The spectra for each batch are plotted in Figure 5.4. The most salient feature is the large portion of the flux near the 1 MeV threshold for <sup>238</sup>U fission.

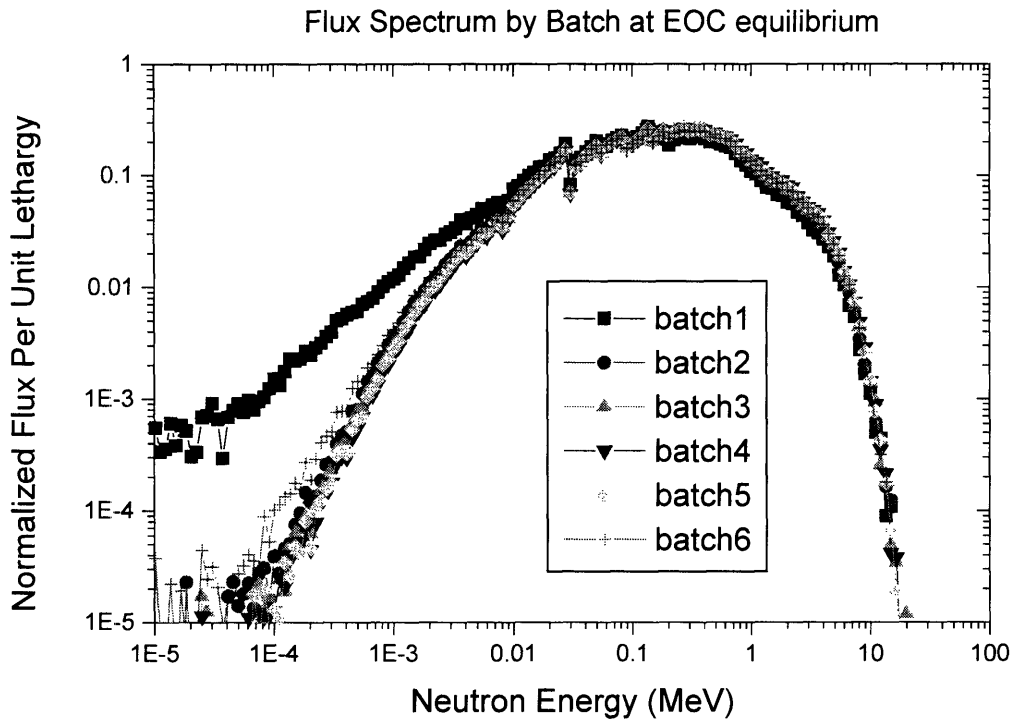


Figure 5.4 B&B GFR Neutron Flux Spectra

The delayed neutron fraction was calculated by determining the reactivity worth of the delayed neutrons. The result was then compared to a simplistic approximation. The estimated delayed neutron fraction was calculated by weighting the  $^{239}\text{Pu}$  and  $^{238}\text{U}$  delayed neutron yields by the fissile and fertile fission fractions, respectively. This approximation, while capturing the effect of predominant isotopes, neglects  $^{235}\text{U}$  and the host of other actinides that build up in the core during irradiation. Table 5-3 summarizes the calculated delayed neutron fraction as well as the estimated delayed neutron fraction.

The estimated  $\beta$  is a very good approximation for the calculated  $\beta$  near EOEC, once the concentration of  $^{235}\text{U}$  from the initial loading in the fresh assemblies becomes small compared to the concentration of  $^{239}\text{Pu}$  bred during the cycle. At BOC, the estimated  $\beta$  is somewhat lower than the actual because it treats all fission in fissile species as  $^{239}\text{Pu}$  fission, which has a lower delayed neutron yield than  $^{235}\text{U}$ . Overall, the very strong contribution of  $^{238}\text{U}$  to the total number of fissions, and the very large delayed neutron yield of  $^{238}\text{U}$  fission contributes to an overall core  $\beta$  near that of a typical PWR.

Table 5-3 Delayed Neutron Fraction

Fertile Fission Fraction Equilibrium U <sup>15</sup> N B&B GFR Core		
Batch	BOEC	Cycle Burnup of 20 MWD/kg <sub>HM</sub>
1	23%	21%
2	27%	25%
3	25%	23%
4	23%	22%
5	22%	21%
6	21%	20%
Average FFF	24%	22%
Estimated $\beta$	0.0054	0.0052
Calculated $\beta^*$	0.0060	0.0054 <sup>**</sup>

\* standard deviation (std-dev) is < 0.0003.

\*\* The quoted  $\beta$  here is calculated for 25 MWD/kg<sub>HM</sub> of core average burnup.

### 5.2.5. Control

The preliminary core design included seven control rod assemblies (CRA). The final design includes several more control elements, however, the preliminary design was used to evaluate potential control schemes for the reactor. Given the strict requirements on the neutron economy, designing a successful control scheme is critical to the illustrating the feasibility of the B&B concept. To that end, spectral shift control via insertable moderator as well as neutron absorbers were investigated to see which approach best met the neutronic requirements.

#### 5.2.5.1. Moderator vs. Absorber

Preliminary study of spent fuel reuse options indicate that strong thermal and epithermal absorbers accrue in the B&B GFR fuel during irradiation, namely <sup>149</sup>Sm. Hence the buildup of <sup>149</sup>Sm was investigated using the equilibrium cycle MCODEv1 calculation.

The material composition of the fuel in each batch during the equilibrium cycle was plotted at each burnup step. For the partially burnt batches, the burnup step was added to the cumulative burnup of the preceding batch. Thus, using just one cycle calculation, the full history of a fuel assembly can be plotted. The linear aspect of the curves shown in Figure 5.5 clearly illustrates two things. First, as the data from each batch (of 17454 kg<sub>HM</sub>) aligns along the linear trend, this is evidence that the cycle is in fact the equilibrium cycle. Second, the linearity also indicates that for a discharge burnup of 150 MWD/kg<sub>HM</sub>, and likely even higher burnup, the concentration of rare earth metal neutron absorbers does not saturate.



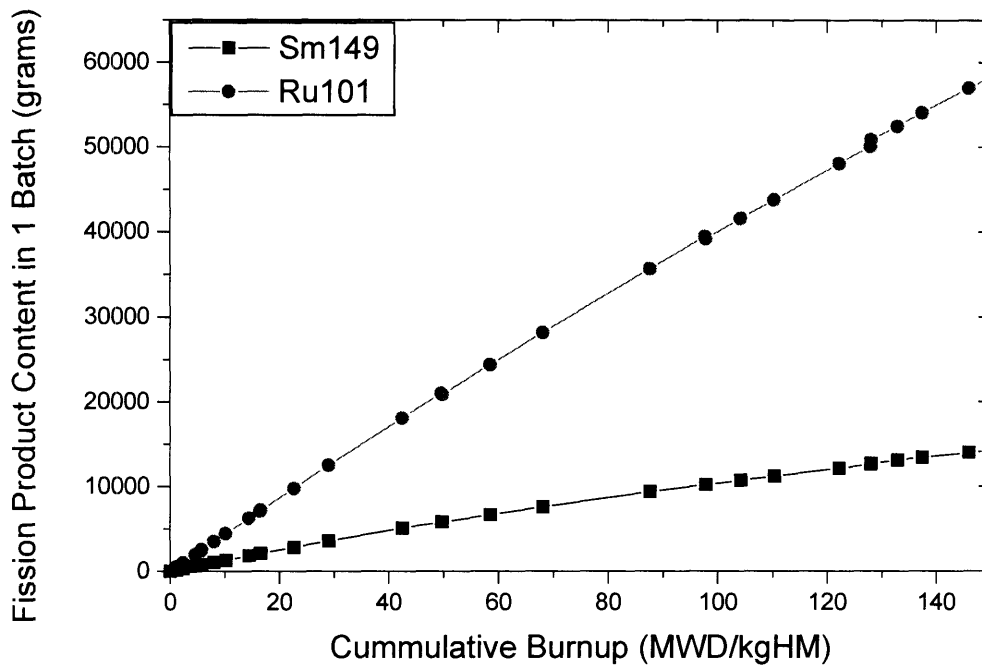


Figure 5.5 The Buildup of <sup>149</sup>Sm and <sup>101</sup>Ru During GFR Irradiation

Understanding the nature of thermal poison buildup in GFR fuel is essential for two reasons. The first being that as the discharge burnup increases, the feasibility of recycling the B&B GFR spent fuel into LWRs is compromised, and secondly, softening the spectrum in partially burnt assemblies may reduce the reactivity as the rare earth metals preferentially absorb slower epithermal neutrons. This motivated an investigation of the use of moderator for reactor control. Moderating control pins or assemblies would have several affects on the neutron economy, in particular, by softening the neutron spectrum: first the rods would reduce the fertile fission fraction and increase the <sup>238</sup>U capture rate; secondly the rods would increase absorption in fission products such as samarium; and thirdly, the moderation may lead to increased or decreased <sup>239</sup>Pu fission depending on the degree of the softening of the spectrum.

The reactivity swing is approximately 0.08 (or 15-17 \$). The control devices must be sufficient to reduce the reactivity by this amount. To evaluate the worth of different control schemes the BOL core (after initial fission product poisoning) is modeled statically with fully inserted control rods. Moderators and absorbers were both evaluated to see if spectral shift is a reasonable approach to reactivity control of the B&B GFR. The spectral shift might be advantageous depending on the effects of the shift on the neutron economy.

The results of the calculations are summarized in Table 5-4. Flux spectra of interesting cases are plotted to show any spectral shift from the base case (for the 1<sup>st</sup> batch, or fresh batch only) in Figure 5.6. In general, whereas moderators tend to increase the epithermal flux, poison materials harden the neutron spectrum.

Table 5-4 Core Eigenvalues for Various Control Materials

control material	keff	notes	reactivity change	negative worth (fully inserted)
2 x ZrD <sub>2</sub>	0.95044	(double density)	0.050377	\$10.72
<sup>6</sup> Li <sub>2</sub> O	0.86778	(no <sup>7</sup> Li)	0.132966	\$28.29
<sup>7</sup> LiD	0.97149	(no <sup>6</sup> Li)	0.029345	\$6.24
B <sub>4</sub> C	0.91122	(natural B)	0.089563	\$19.06
C	0.98730		0.013548	\$2.88
Li <sub>2</sub> O	0.97226	(natural Li)	0.028575	\$6.08
Li <sub>3</sub> N	0.97793	(natural Li)	0.022910	\$4.87
ZrD <sub>2</sub>	0.96919		0.031643	\$6.73
ZrH <sub>2</sub>	1.00068		0.000180	\$0.04
½ ZrH <sub>2</sub>	1.00566	(batches 1-3 only)	-0.004796	-\$1.02
2 x ½ ZrD <sub>2</sub>	0.96232	(batches 4-6) (2x den)	0.038507	\$8.19
<b>BOC (rods out)</b>	1.00086	<b>Cycle Swing</b>	0.08	

The ZrH<sub>2</sub> and ZrD<sub>2</sub> moderator options are the most interesting. These illustrate that moderation has the strongest negative reactivity affect in the older batches, which was initially expected. The plutonium concentration in the oldest batches is higher, and moderation may potentially increase the reactivity in these batches by promoting plutonium absorption relative to uranium absorption. However, the oldest batches are heavily poisoned with fission products that contribute strongly to parasitic absorption upon spectrum softening. Additionally, upon softening, the plutonium worth is reduced because of the decreasing absorption yield with neutron energy, and the overall utilization is reduced because the fission product resonances compete for neutrons.

In the fresh batches, if a moderator with too much slowing down power is inserted, the spectrum may develop a thermal peak near the control rods, and thus contribute to a <sup>235</sup>U absorption advantage in the fresh batches; this is undesirable because it will lead to rapid burnout of the initial fissile loading before the plutonium can reach a high enough concentration to sustain criticality. Therefore, very strong moderators, or moderators heavy in hydrogen are not recommended. <sup>7</sup>Li and D are more likely to shift the spectrum into the resonance region without creating a significant thermal peak.

It is likely that moderator control may only account for 10\$ of the 16\$ required, but 10\$ is still quite significant. However, given that the B&B GFR reactivity swing is necessarily large, moderator control was abandoned for the current work for several reasons. First, there is no identified moderating material that can contribute enough negative reactivity to fully control the reactor. Second, there are no fission products in the startup core, further degrading moderator control rod worth. Third, while moderation may increase the conversion ratio, poison control elements harden the neutron spectrum, and therefore, poison elements, as contrary as it may seem, have the potential to improve the long term neutron economy according to an evaluation of the neutron economy performance index: Y (see section 1.3), whereas moderators hurt neutronic performance by reducing <sup>239</sup>Pu worth and contributing to the rapid burnout of <sup>235</sup>U in fresh assemblies.

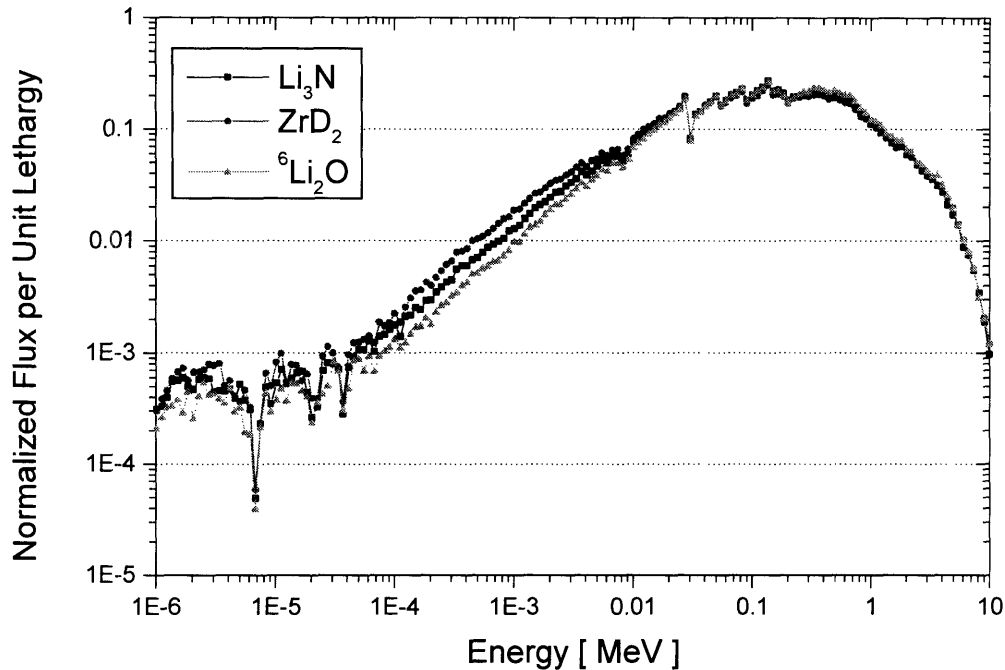


Figure 5.6 Spectral Shift for Some Control Materials

Spectral shift control, however, remains an interesting alternative for fast reactors with a less pronounced reactivity swing than the B&B GFR of interest.

Poison control was investigated at greater length, and particularly the effects of neutron absorption in poison on the long-term trends in reactivity to ensure that the poison control strategy does not infringe on the reactor's ability to breed in reactivity.

### 5.3. Final Design

Thermal Hydraulic calculations for the preliminary core design indicated several faults in the design that required refinements. The first is that the rated power, given the power cycle, was too high to avoid breaching the peak clad temperature limitations. Secondly, even as power density was reduced to meet the cladding temperature limits, the very small core temperature rise consistent with a S-CO<sub>2</sub> PCS meant that the circulator power was exceptionally large to meet the mass flow rate requirements, and thus, the net efficiency was significantly degraded. The approach to solving these problems was to switch from the S-CO<sub>2</sub> PCS to an AGR Rankine PCS (see section 4.3), and thus increase the core temperature rise from 150 °C to 385 °C [17,63]; additionally, flow orificing had to be adopted to reduce the requirements for primary circulator power to attain acceptable net power conversion efficiency. Thirdly, to meet the peak clad temperature requirements, the radial power peaking factor had to be reduced for the core power to achieve an economically reasonable level given the large size and high heavy metal loading for the core.

The core was redesigned to reduce the radial power peaking factor in the demonstration core from the preliminary design. The preliminary design had the 6<sup>th</sup> batch near the outer periphery between the 1<sup>st</sup> and 2<sup>nd</sup> batch locations, to increase the flux near the fresh assemblies, and promote plutonium breeding in the subcritical fresh assemblies. The redesigned core shifts the 6<sup>th</sup> batch assemblies inward by one batch location and moves the 2<sup>nd</sup> batch outward. This means the core is divided clearly into seed and blanket regions as shown in Figure 5.7.

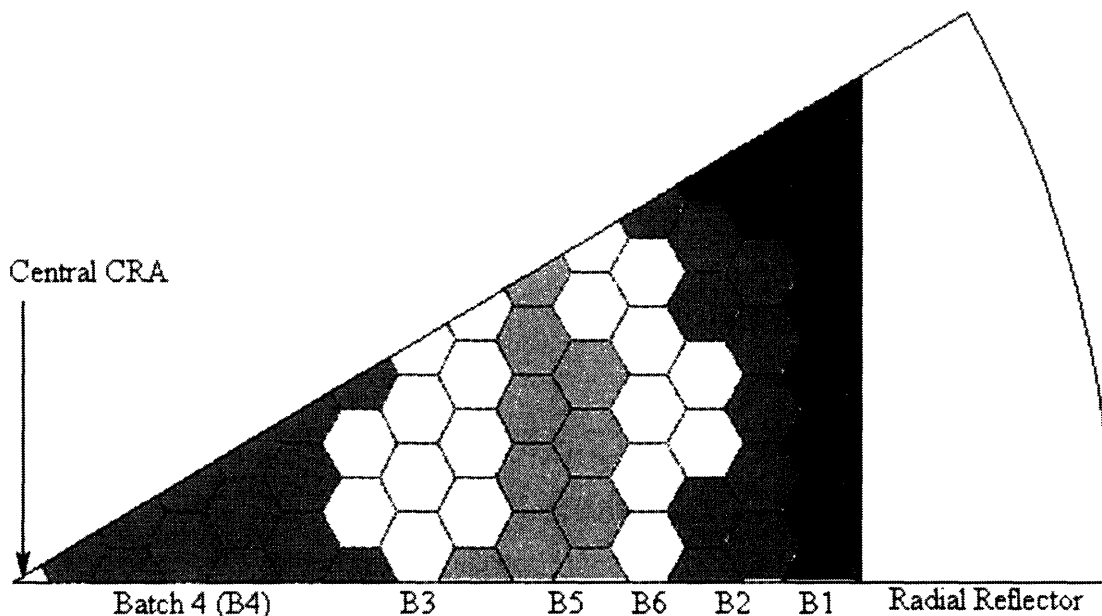


Figure 5.7 Demonstration Core Final Design Layout

The increased power fraction in the 6<sup>th</sup> batch location reduces the power fraction in the 4<sup>th</sup> batch, and thereby reduces the radial power peaking factor from 2.2 to 1.7. Though shifting the 6<sup>th</sup> batch inward, and thus to a higher flux region of the core increases the reactivity, the fresh fuel experiences a somewhat lower flux, and therefore does not have the same <sup>239</sup>Pu concentration when the 2<sup>nd</sup> batch is advanced to the 3<sup>rd</sup> batch location. In the preliminary design the second batch accrues 19.5 MWD/kg<sub>HM</sub> of burnup (<sup>239</sup>Pu concentration of  $8.0 \times 10^{-4}$  #/b-cm) before advancing to the 3<sup>rd</sup> batch location, in the final design the accrued burnup in the 2<sup>nd</sup> batch is only 16.5 MWD/kg<sub>HM</sub> (<sup>239</sup>Pu concentration of  $7.6 \times 10^{-4}$  #/b-cm). The design change, therefore, while reducing the radial power peaking at the BOC does change the evolution of the power shape during burnup. The preliminary design's multi-batch shuffling sequence was specifically selected to ensure a benign shift in the power shape during irradiation.

In the preliminary design the 3<sup>rd</sup> and 4<sup>th</sup> batches were close enough to their discharge burnup that the plutonium concentration, while increasing, was not increasing rapidly during a given cycle, and therefore the power shape held relatively constant over a given cycle. In the redesign, the 3<sup>rd</sup> batch rapidly builds up plutonium over the equilibrium cycle, and therefore the radial power peaking factor goes from 1.74 at BOEC to 2.05 at EOEC. Recall that the plutonium concentration, and thus reactivity as a function of burnup was a rapidly increasing function for a burnup less than 60 MWD/kg<sub>HM</sub>; after this burnup the fuel has "forgotten" its original enrichment.

This would present a problem in effectively implementing an orificing strategy to reduce the pumping work. While there is a simplified method for predicting the pump work savings for the

ideal case, if the power shape were to evolve significantly during a cycle, the effectiveness of orificing would be degraded significantly or fuel assemblies' orifices would have to be changed regularly. The strategy for reactor control was thus evaluated to see if using inward biased control (instead of a bank of control rods through-out the entire core) could be used to flatten the radial power profile during burnup.

### 5.3.1. Poison Control and Fuel Assembly Design

Assessment of control strategies for the preliminary design indicated that seven CRAs were insufficient to provide the very large negative reactivity worth for the control devices that would be required to overcome the large reactivity swing over any given cycle. However, the neutronic requirements for the core leave little design margin in terms of removing fuel assemblies for more CRA locations. Therefore, a distributed control rod approach was adopted as opposed to a CRA approach. This would mean that the control elements were not as effectively self shielded, and therefore, control could be accomplished by removing a few fuel rods per assembly as opposed to removing several assemblies from the core.

Additionally, by moving the 6<sup>th</sup> batch location inward, the BOC reactivity was somewhat increased because the 6<sup>th</sup> batch has a substantial plutonium concentration and was moved to a slightly higher worth region of the core. Therefore, several fuel pins in each assembly were removed and replaced with control rods and the six CRA locations between the 3<sup>rd</sup> and 5<sup>th</sup> batches were removed, thus shifting assemblies inward one assembly location along the core diagonals. The CRA at the core center remained. Figure 5.8 shows the final fuel assembly design with the control rod locations marked. The control rods were dubbed "fingers" as each and every assembly has a control cluster of a handful of individual pins extending into the core. This approach resembles the approach taken for PWRs more than the CRA approach taken in conventional fast reactors.

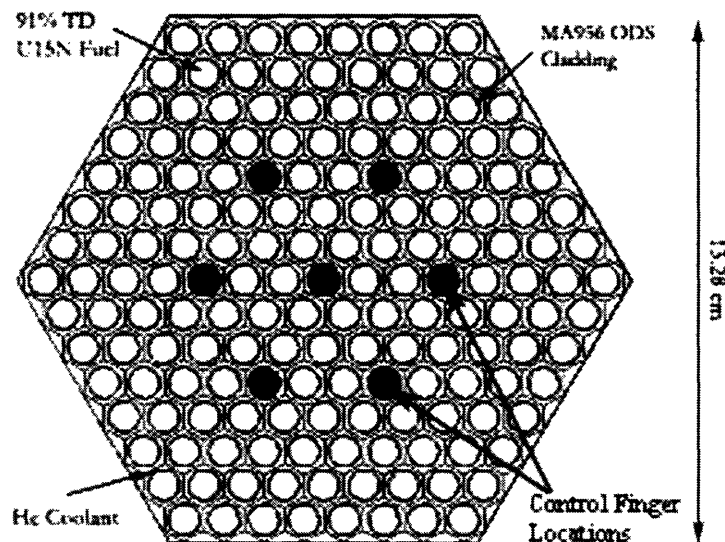


Figure 5.8 Final Fuel Assembly Design with a Control Cluster

As the reactivity is intimately related to the heavy metal loading, a very dense absorber was selected for the poison material to avoid any further reduction in the assembly heavy metal loading than necessary. Tantalum diboride ( $TaB_2$ ) with highly enriched boron (90 a/o  $^{10}B$  in B)

was selected for the poison given its strong neutron absorption cross section for epithermal energies. The TaB<sub>2</sub> material is clad in 0.02 cm thick ODS with 0.02 cm thick ODS guide tubes. The poison finger guide tube is the same outer diameter as a fuel pin.

The MCNP model of the final demonstration core design and MCODE input file are included in Appendix E and Appendix F respectively. The core model is 1/12<sup>th</sup> symmetric. While ENDFB6 cross sections at 900K are used for the actinides, one caveat is that the boron cross sections used are JEF2.2 cross section sets for 1000K, as the maximum temperature available using prebroadened ENDFB6 cross sections sets for boron was 600K.

The volume fraction of fuel is reduced as some fuel pins are removed from each assembly, and the volume fractions are summarized in Table 5-5. The structural volume fraction includes the volume occupied by control finger guide tubes, as well as any coolant that is within the guide tubes.

Table 5-5 Final Design Demonstration Core Geometry

Fuel Form	U <sup>15</sup> N	
Fuel Pins per Assembly	162	
Pin Outer Diameter	0.82	cm
Clad Thickness	0.04	cm
Pin Pitch	1.00	cm
Assembly Flat-to-Flat	13.28	cm
Active Core Height	200	cm
Equivalent Core Diameter	350	cm
Fuel Volume Fraction	45.6	v/o
Structural Volume Fraction	12.8	v/o
Coolant Volume Fraction	41.6	v/o

#### 5.3.1.1. Impact on Neutron Economy

The uncontrolled reactivity history for the final core design is shown in Figure 5.9. It is basically consistent with the preliminary design. The impact of the control clusters on the neutron economy was evaluated using data from the EOEC (EOC8) MCNP calculations for the poison controlled U<sup>15</sup>N pin-core. It has been shown that while neutrons are being lost to capture in poison (~ -8%), the associated spectrum hardening offsets these lost neutrons by improving the fertile fission fraction, thus allowing in some sense a storage of neutrons by reducing the destruction rate of plutonium by substituting direct <sup>238</sup>U fission, hence also reducing conversion ratio (~ -3%).

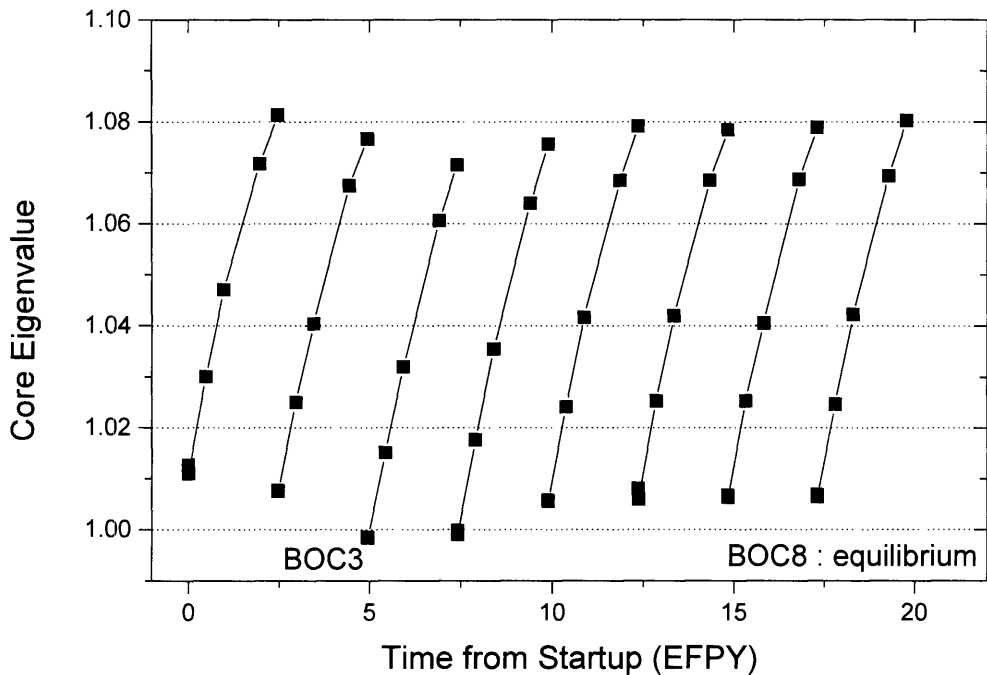


Figure 5.9 Final Design Demonstration Core Reactivity History<sup>22</sup>

The neutrons being discarded in this case, are largely neutrons that were being uneventfully captured. Additionally, one can see that the fission to absorption ratio for the  $^{239}\text{Pu}$  increases, and thus fewer  $^{239}\text{Pu}$  nuclei will be required to sustain the same criticality. The increase in fission to absorption ( $\sim 2\%$ ) is very nearly the same as the reduction in conversion ratio. A calculation for the metric of neutron economy ( $Y$ ) is summarized in Table 5-6. The results indicate that the insertion of the  $\text{TaB}_2$  poison control clusters does not significantly compromise the neutron economy, and therefore, without doing exhaustive critical burnup calculations, the current design was judged as acceptable.

<sup>22</sup> standard deviation of all data points < 0.0006

Table 5-6 Neutron Economy Performance with Poison Control

	EOEC Rods out	EOEC Rods in	Units	% change
$\sigma_f$ 49 (41)	1.6530	1.6321	b	-1.3%
$\sigma_\gamma$ 49 (41)	0.3290	0.2806	b	-14.7%
$\sigma_a$ 49 (41)	1.9820	1.9127	b	-3.5%
$\sigma_f$ 28 (41)	0.0428	0.0472	b	10.2%
$\sigma_\gamma$ 28 (41)	0.2284	0.2083	b	-8.8%
$\sigma_a$ 28 (41)	0.2712	0.2555	b	-5.8%
Conv. Ratio	1.1796	1.1475		-2.7%
$k_{eff}$	1.0741	0.9934		-7.5%
N49	0.0022	0.0022	#/b-cm	
N28	0.0252	0.0252	#/b-cm	
$\sigma_f/\sigma_a$ 49	0.83	0.85		2.3%
$\sigma_f/\sigma_a$ 28	0.16	0.18		17.0%
$\nu$ average	2.83	2.83		
1/Y	1.213	1.004		-17.3%
Y	0.82	1.00		20.9%

In conclusion, analysis shows that while conversion ratio is reduced by 3% when reactivity is reduced using poison control, it is likely to have a very small impact on the neutron economy, and likely within the margin left by the conservative treatment of plutonium drift.

### 5.3.1.2. Impact on Radial Power Shape

The demonstration core utilizes inward biased control elements to control the reactivity. During irradiation the assemblies' control clusters are separated into two banks, the first bank are the control pin clusters in the 3<sup>rd</sup>, 4<sup>th</sup>, and 5<sup>th</sup> batches and the CRA in the center of the core, and the second bank is the core periphery (or the control clusters in batches 1, 2, and 6).

During a given cycle the uncontrolled core reactivity increases considerably (~6900 pcm for equilibrium cycles), however, during operation the control elements are inserted into the core, such that the control elements in the first bank are essentially fully inserted at the EOEC.

The first bank fully inserted at the EOEC yields a radial power peaking factor of 1.77, which is comparable to the 1.74 at the BOEC. Therefore, an orificing strategy can easily be optimized for the cycle taking into account that the first bank of control elements shifts the radial power outward during burnup.



Table 5-7 Impact of Control Clusters on Radial Power Peaking

Peaking Factor by Region	BOEC	EOEC (uncontrolled)	EOEC (clusters inserted)
1	0.25	0.20	0.28
2	0.47	0.40	0.50
3	1.21	1.45	1.38
4	1.74	2.05	1.77
5	1.32	1.13	1.19
6	1.01	0.77	0.88

The essential result is that the shift of the 6<sup>th</sup> batch one batch location inward reduces the BOEC radial power peaking factor, but the insertion of the first control bank during irradiation holds the power shape fairly constant, with noticeable deviation only in the 3<sup>rd</sup> and 6<sup>th</sup> batches over the cycle.

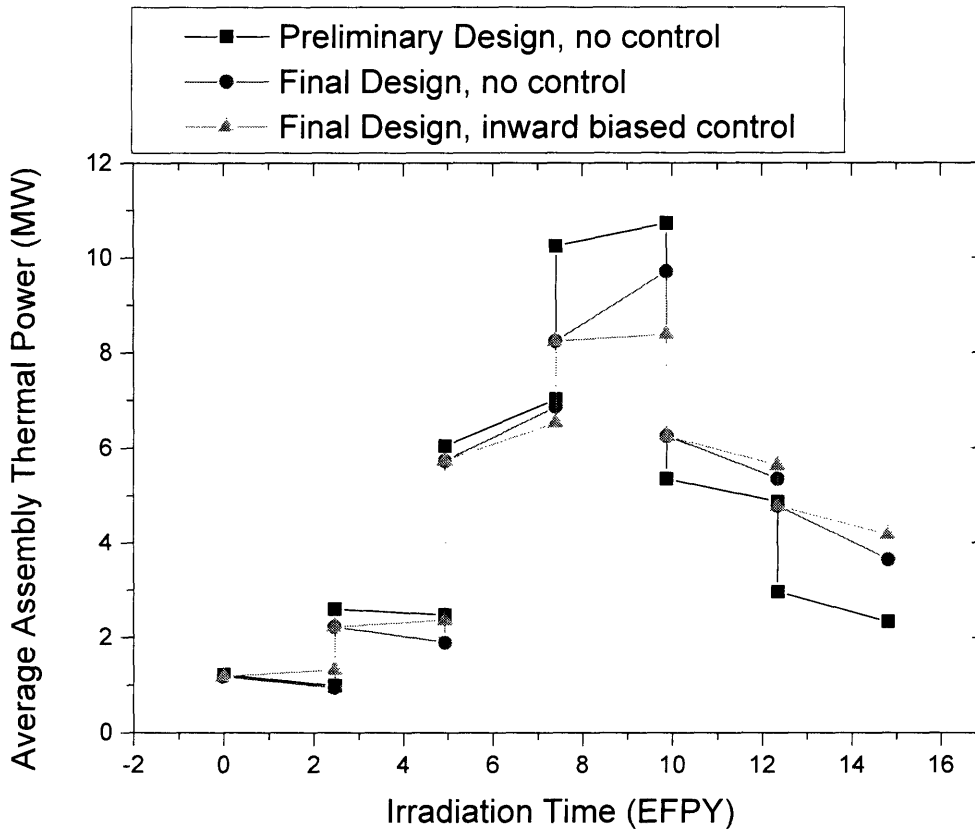


Figure 5.10 Power History Comparison

The aim in the final design for the multi-batch shuffle sequence was to reduce the radial power peaking relative to the preliminary design. By moving the 6<sup>th</sup> batch inward one batch location, the uncontrolled reactor calculation showed a reduction in radial power peaking, as shown in

Figure 5.10. However, as the power in the 4<sup>th</sup> batch noticeable grew during irradiation it effectively prevented the use of flow orificing to reduce the primary circulator work. Therefore, the inward biased control bank approach to control reactivity was adopted. As evidenced by the relative flatness of the power history for the controlled final design (shown in Figure 5.10), the inward biased approach would enable effective use of flow orificing. Therefore the multi-batch shuffling sequence and control scheme were accepted for the demonstration core.

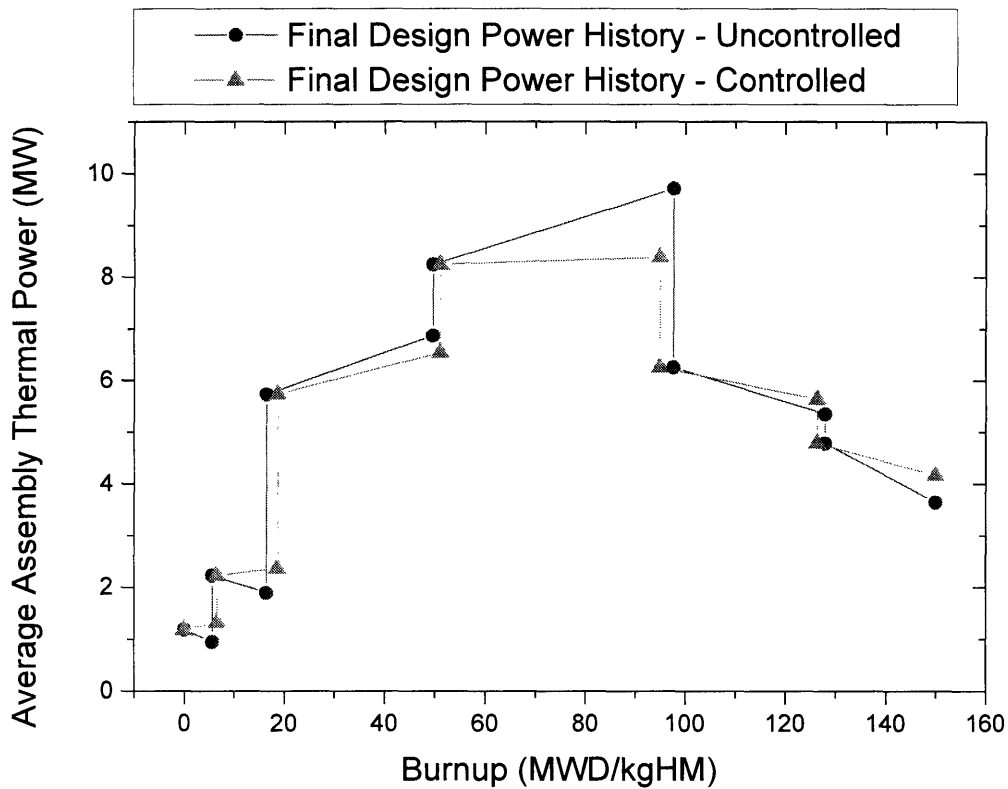


Figure 5.11 Power History versus Burnup

Figure 5.11 shows the power history for an assembly in the final design versus its burnup. The controlled and uncontrolled calculations are shown to stress the benefits of the current control strategy. The flattening of the power during irradiation allows for effective flow orificing without the need for frequent adjustment of the orifices. Therefore, grid plate orificing, as opposed to assembly orificing will likely be sufficient. Despite the small shifts in power shape, an ideal orificing approximation was still used when calculating the characteristics of the thermal hydraulic performance of the core.

Another benefit of the current approach is that the oldest assemblies (those in the 5<sup>th</sup> and 6<sup>th</sup> batch locations) experience a lower power density, thus alleviating some of the thermal stress on the assemblies with the highest accrued fluence.

### 5.3.2. Quasi-Static Analysis

The integral safety performance of the demonstration core (46 v/o U<sup>15</sup>N fuel) was evaluated using a quasi-static method and compared to the performance of the IFR and ABR (metal cooled fast reactors). The method uses a reactivity balance to determine the steady state fuel and coolant temperatures following a variety of postulated accidents. In particular, loss of flow, loss of ultimate heat sink, and control rod ejection are evaluated to establish an envelope. The GFR is somewhat less constrained in that coolant freezing is not a concern.

An advantage of the ODS material is that during transients the cladding can retain strength and creep resistance for long periods of time (many hours) at temperatures of 1300 °C [34]. Individual reactivity feedback parameters were calculated as prescribed in section 2.2.5. The parameters are the Doppler coefficient, the fuel thermal expansion coefficient (assuming clad-fuel bonding for VIPAC), the coolant temperature coefficient (derived as a coolant density coefficient and adjusted using the ideal gas relationship), the control rod driveline expansion reactivity coefficient, and lastly, the core radial thermal expansion coefficient (or flowering coefficient). The B&B GFR core spacers should be designed to enable radial expansion of the core.

The maximum perturbation in the reactor coolant outlet temperature was taken as the difference between the maximum cladding temperature (1300 °C) and the peak cladding temperature under normal operating conditions (641 °C) for the 2900 MW<sub>th</sub> core. The details of the steady state thermal hydraulic calculation for the peak clad temperature is discussed in Chapter 6.

A set of six or seven MCNP calculations is required for each point during irradiation. The results of these MCNP calculations are summarized in Table 5-8. The results also indicate the uncertainty in the individually calculated parameters.

Table 5-8 Calculated Reactivity Feedback Parameters and Uncertainty

Demonstration B&B GFR Case Description	Eigenvalue	Standard Deviation	Derived Quantity	Units	Value	Standard Deviation
BOL Nominal	1.01323	0.00017	$\Delta\rho_{\text{VOID}}$	\$	0.330	0.030
BOL Without Delayed Neutrons	1.00429	0.00016	$\beta$		0.00882	0.00023
BOL 300 K Cross Sections	1.01766	0.00016	$\alpha_{\text{D}}$	pcm/K	-0.565	0.030
BOL Fuel Thermally Expanded	1.01222	0.00018	$\alpha_{\text{e}}$	pcm/K	-0.148	0.036
BOL Core Radially Expanded	1.01114	0.00100	$\alpha_{\text{R}}$	pcm/K	-0.153	0.074
BOL Coolant Voided	1.01623	0.00020	$\alpha_{\text{Co}}$	pcm/K	0.0045	0.0004
Estimated Maximum CRA Worth			$\Delta\rho_{\text{TOP}}$	pcm	206	4
BOEC Nominal	1.00760	0.00017	$\Delta\rho_{\text{VOID}}$	\$	0.814	0.053
BOEC Without Delayed Neutrons	1.00132	0.00024	$\beta$		0.00623	0.00029
BOEC 300 K Cross Sections	1.01200	0.00018	$\alpha_{\text{D}}$	pcm/K	-0.567	0.032
BOEC Fuel Thermally Expanded	1.00683	0.00017	$\alpha_{\text{e}}$	pcm/K	-0.114	0.036
BOEC Core Radially Expanded	1.00711	0.00017	$\alpha_{\text{R}}$	pcm/K	-0.036	0.018
BOEC Coolant Voided	1.01278	0.00018	$\alpha_{\text{Co}}$	pcm/K	0.0078	0.0004
Estimated Maximum CRA Worth			$\Delta\rho_{\text{TOP}}$	pcm	80	2
EOEC Nominal (uncontrolled)	1.08082	0.00012	$\Delta\rho_{\text{VOID}}$	\$	1.021	0.050
EOEC Without Delayed Neutrons	1.07494	0.00016	$\beta$		0.00544	0.00019
EOEC 300 K Cross Sections	1.08540	0.00017	$\alpha_{\text{D}}$	pcm/K	-0.513	0.023
EOEC Fuel Thermally Expanded	1.08043	0.00017	$\alpha_{\text{e}}$	pcm/K	-0.050	0.027
EOEC Core Radially Expanded	1.07897	0.00010	$\alpha_{\text{R}}$	pcm/K	-0.119	0.010
EOEC Coolant Voided	1.08735	0.00020	$\alpha_{\text{Co}}$	pcm/K	0.0086	0.0003
EOEC Highest Worth CRA Inserted	1.07853	0.00016	$\Delta\rho_{\text{TOP}}$	pcm	196	17

Based on these parameters and steady state temperature limits, the feedback can be assessed; the limits are calculated and shown in Table 5-9, along with the appropriate ratios of the macroscopic coefficients. A margin factor ( $\gamma$ ) of 2/3 and a fuel temperature difference ( $\Delta T_f$ ) of 230 °C were used in these analyses.

Table 5-9 Reactivity Feedback Parameters for Several Fast Reactor Designs

		Demo. B&B GFR			ABR [55]		IFR [66]
		BOL	BOEC	EOEC	BOL	EOL	AVG
A	cents	-19	-25	-24	-10	-8	-31
B	cents	-22	-23	-28	-22	-19	-35
C	cents/K	-0.10	-0.11	-0.12	-0.27	-0.23	-0.25
A/B		0.84	1.09	0.85	0.47	0.41	0.88
CΔTc/B		1.70	1.90	1.70	1.14	1.11	1.10
ΔpTOP/B		0.53	0.28	0.64	0.69	0	0
A/B limits		x < 1.14			< 1.25		< 1
CΔTc/B limits		x > 1			1 < x < 1.8		1 < x < 2
ΔpTOP/B limits		x < 1.14			< 1.25		< 1
β		0.00882	0.00623	0.00544	0.0024	0.0023	0.0035
αD	1e-3 c/K	-64	-91	-94	-55	-85	-120
αe	1e-3 c/K	-17	-18	-9	-60	0	-90
αCo	1e-3 c/K	1	1	2	30	40	180
αRD	1e-3 c/K	0	0	0	-10	0	0
αR	1e-3 c/K	-17	-6	-22	-180	-180	-220

The results of the calculations indicate that the GFR can be operated safely. In general, the reactor is less sensitive to changes in the coolant density than metal cooled reactors and the GFR is not as constrained because strong negative feedbacks do not pose a threat in terms of coolant freezing (as in the ABR and IFR). However, the GFR depends on active cooling and decay heat removal, additionally, coolant depressurization under large break loss of coolant accident conditions may occur very rapidly. Therefore, these assessments should be taken as an indication of semi-passive self-regulation as opposed to fully passive.

The EOEC control rod ejection accident posed a challenge, as initially the reactivity worth of the central control rod assembly was enough to breach the third limit (the TOP, however, was within the limit when  $\gamma$  was set to unity). However, by switching to two independently driven dual entry control rod drives, the reactivity worth of the ejection was reduced by a factor of two, thus putting the GFR comfortably within its safety envelope; furthermore two independent SCRAM systems are specified in accordance with usual fast reactor practice. Therefore, the final design for the B&B GFR demonstration core includes a full set of control element insertions from both the top and bottom of the core.

### 5.3.3. Core Flooding

Introducing the Rankine PCS prompted the discussion of the reactivity consequences of core flooding. Therefore, several cases were analyzed using core models at several points in life. Some key results are summarized in Table 5-10. MCNP was used to investigate the change in core eigenvalue between the nominal and flooded conditions with and without control rods. It was found that in equilibrium there is substantial negative feedback from enhanced absorption by fission products such as  $^{149}\text{Sm}$ . Figure 5.12 shows a plot of the core eigenvalue with the control rods withdrawn for the EOEC core as either  $\text{H}_2\text{O}$  or  $\text{D}_2\text{O}$  is added to the coolant. Regardless of the density of the water added between 0.1 g/cc and 1.1 g/cc, the result is a negative reactivity insertion. The curve is increasing towards lower density, because this is approaching the voided condition where the reactivity is \$1 higher than the nominal condition.

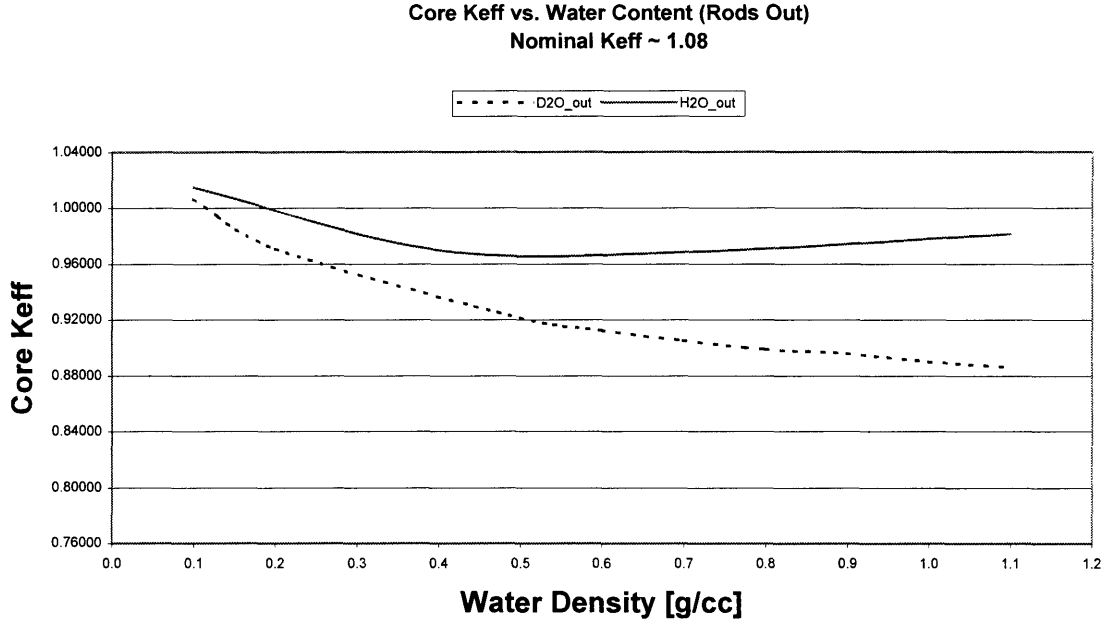


Figure 5.12 Effect of Core Flooding on EOEC Core Eigenvalue (Poison Withdrawn)

The negative reactivity insertion at the EOEC is magnified when the control rods are inserted to a subcritical position ( $k_{eff} \sim 0.98$ ). This is because the  $^{10}\text{B}$  absorption cross section increases as the spectrum becomes softer; as illustrated in Figure 5.13. The same trend with increasing reactivity towards lower water density was also observed. As the water becomes more dense, however, the spectrum becomes even more thermal and the substantial plutonium content contributes to a positive effect despite increasing  $^{10}\text{B}$  and fission product negative reactivity worth.

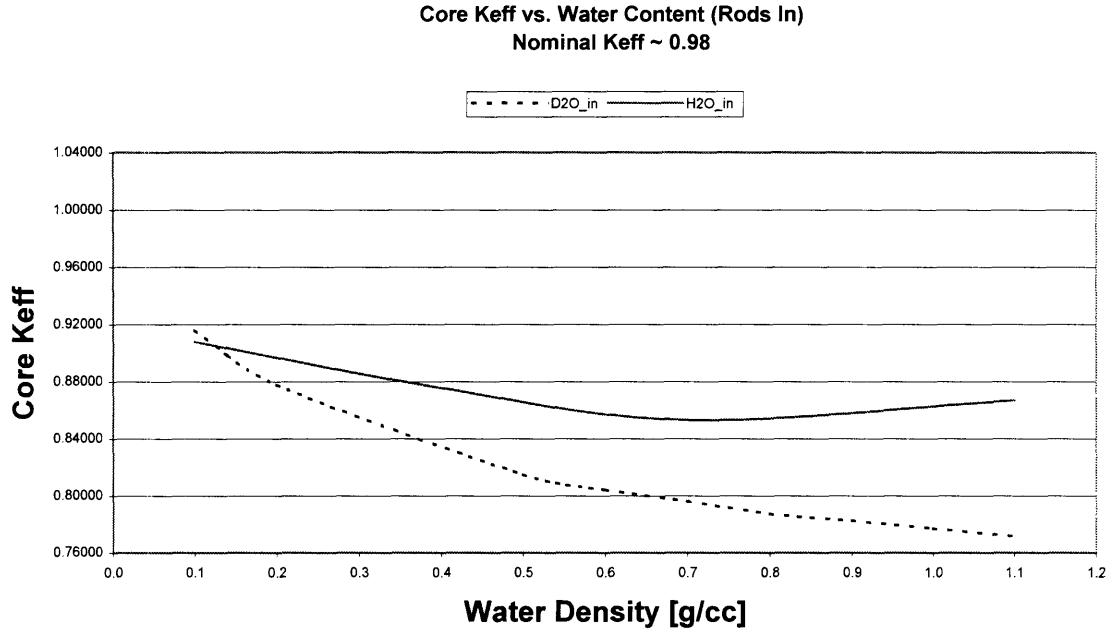


Figure 5.13 Effect of Core Flooding on EOEC Core Eigenvalue (Poison Inserted)

However, Table 5-10 indicates there are some concerns over the consequences of flooding the core at the very BOL, where there are no fission products such as samarium or xenon in the fuel. In this case it was found that full water flooding of the core contributes to a strong positive reactivity effect.

The potential accident under current consideration is a failure of the steam generator that leads to a flow of water into the primary system and eventual flooding of the core. There are several reasons why this is highly unlikely to lead to a prompt criticality accident. Firstly, the concern only arises at the BOL when there is little <sup>149</sup>Sm in the core. Secondly, the primary coolant pressure is higher than the secondary PCS pressure and thus an outflow of helium is expected. Thirdly, decay heat would surely lead to boiling and thus water density ~ 1 g/cc is unlikely to occur.

Table 5-10 Reactivity Consequences of Core Flooding

Condition	Core keff	std-dev
EOEC Rods Out	1.07411	0.0006
EOEC Rods In	0.92264	0.0004
BOL Rods Out	1.00656	0.0006
BOL Rods In	0.84186	0.0005
BOL with FP Rods Out	1.00489	0.0006
BOL Rods Out Water Flooded	1.35067	0.0003
BOL Rods In Water Flooded	1.07142	0.001
BOL with FP Rods In Water Flooded	1.07246	0.001
EOEC Rods In Water Flooded	0.86690	0.0009
EOEC Rods Out Water Flooded	0.98144	0.0009

However, the very large reactivity insertion from flooding at the BOL is a hypothetical concern. One proposed solution is to use a diluent in the fresh fuel that approximates the fission products. In this case samarium is an ideal candidate, as the leading epithermal absorber at points later in life is  $^{149}\text{Sm}$ , though any burnable poison could likely serve as a surrogate for the fission products.

A sample case was analyzed using natural samarium diluent. The fuel was modified to remove 1% of the uranium (all  $^{238}\text{U}$ ). Each  $^{238}\text{U}$  nucleus was then replaced with 0.13  $^{149}\text{Sm}$  nuclei. This is a conservative approach as all other isotopes of natural samarium are effectively ignored. The enrichment is thus slightly increased, but the inventory of  $^{235}\text{U}$  is the same. This is only done for the 4<sup>th</sup>, 5<sup>th</sup>, and 6<sup>th</sup> batches (the formerly 10 a/o enriched, now 11 a/o enriched startup batches). Table 5-11 summarizes the findings of this initial analysis.

Table 5-11 Samarium Diluent and Startup Flooding

Condition	keff	std-dev
1% Sm Dry	1.01410	0.00046
1% Sm Flooded SCRAM	0.95884	0.00076
1% Sm Flooded NO SCRAM	1.20081	0.00112
No Diluent Dry	1.01461	0.00064
No Diluent Flooded SCRAM	1.07142	0.00110
No Diluent Flooded NO SCRAM	1.35067	0.00025
No Diluent SCRAM	0.84186	0.00052

The analysis indicates that even modest diluent fractions (1-3%) would be sufficient to completely eliminate any concerns over prompt criticality accidents near the BOL due to water ingress from the PCS, at 1% the safety is still contingent upon SCRAM.

#### 5.3.4. Cladding Irradiation

Cladding fluence was calculated, but this alone is an incomplete measure for cladding material damage, therefore, helium concentration (peak and average) as well as displacements per atom (DPA) (peak and average) at the point of discharge were also calculated. The DPA was calculated using two models, the first is the Lindhard model [16] to characterize the displacement cascade for stainless steel, and the second was the Half-Nelson model [16] to characterize the displacement cascade in Iron.

The  $(n,\alpha)$  cross section was also calculated, so the EOEC helium concentration could be calculated. The ratio of the appm of helium to DPA was calculated, as was the ratio of DPA to atomic fraction burnup. (burnup in a/o is  $\sim 1/10$  the burnup in  $\text{MWD}/\text{kg}_{\text{HM}}$ ). The metrics were then compared with those of the Commissariat a l'Energie Atomique (CEA) GFR studies quoted in reference [13]. Table 5-12 summarizes calculations of the helium concentration during several stages of burnup as well as the DPA. Recall from section 2.2.4.2 that the pin cell and full core models predict the same cladding fluence, and therefore, unit cell models were judged appropriate for these calculations.



Table 5-12 U<sup>15</sup>N Pin Model Fluence and DPA Calculation

U <sup>15</sup> N PIN	Lindhard	Half-Nelson	(n,α)	Heppm DPA	Burnup MWD kgHM	Φ > 0.1 n/b	Φ > 1 n/b	Total Φ n/b	Helium Concen. ppm	avg DPA	Atomic Burnup a/o	DPA Burnup
step	b	b	b	ppm								
0	267	209	2.92E-5	0.11	0	0	0	0			0	
1	267	209	2.92E-5	0.11	0.1	0.001	0.000	0.001	0	0	0.01	21
2	267	209	2.84E-5	0.11	10	0.052	0.009	0.088	3	21	1	21
3	272	213	3.06E-5	0.11	40	0.193	0.032	0.322	10	78	4	19
4	281	220	3.29E-5	0.12	70	0.313	0.053	0.517	17	129	7	18
5	286	223	3.64E-5	0.13	100	0.427	0.074	0.700	25	178	10	18
6	289	225	3.72E-5	0.13	130	0.540	0.094	0.879	33	226	13	17
7	290	226	3.75E-5	<b>0.13</b>	150	0.615	0.108	0.998	<b>37</b>	<b>257</b>	15	17
8	291	226	3.64E-5	0.12	180	0.728	0.129	1.177	43	305	18	17
9	291	226	3.80E-5	<b>0.13</b>	225	0.902	0.161	1.453	<b>55</b>	<b>376</b>	22.5	17

In order to compare the B&B GFR to conventional fast reactors, a unit cell model was created for a SS316 clad LMFBR fuel pin [63]. The cladding DPA and helium concentration were calculated using the same approach as for the B&B GFR. While the DPA per unit burnup is essentially the same, of particular interest is the ratio of the helium concentration in appm to the DPA. For the B&B GFR the maximum value of this ratio is 0.13 (versus approximately 0.4 for the LMFBR). Helium buildup results in cladding embrittlement, but the absence of nickel (which has a substantial (n,α) cross section in a hard spectrum) in the cladding nearly makes helium buildup concerns moot.

The average DPA quoted in Table 5-12 linearly averages the cross section from the Lindhard and Half-Nelson models, and is 257 DPA at the discharge burnup, thus representing the average DPA for discharged fuel. The value at a burnup of 225 MWD/kgHM is also quoted to give a measure of the DPA for the cladding at the axial power peak (376 DPA). The DPA is significantly higher for the B&B GFR than for the CEA GFR described in reference [13]. This is most likely due to two reasons, one being the harder neutron spectrum. The B&B GFR neutron spectrum is harder because there is no diluent or matrix to soften the neutron spectrum and the number of displacements per primary knock out atom increases with energy due to displacement cascades (or secondary knock outs). The second, of course, is the higher discharge burnup and thus higher fluence.

The ratio of DPA to burnup is 10 – 13 for the CEA reference cores [13] and 17 for the B&B GFR. Yielding an overall DPA that is approximately 4 – 5 times as great. However, the burnup is triple that of the CEA GFR, and one of the essential design goals for the B&B GFR. It should be noted that the CEA GFR burnup is low because of the use of an innovative UC-SiC cercer fuel to allow for very high temperature operation [13].

DPA usually results in enhanced creep [54] and the ODS has improved creep resistance relative to other stainless steels [34], therefore, it is still not clear what the ramifications of the high fluence and hard spectrum really are. If the Half-Nelson model is used (less conservative) the ratio of DPA to burnup is reduced to below 15, and much closer that of the CEA GFR.

## 5.4. Chapter 5 Summary

The demonstration B&B GFR core design was evaluated using several neutronic calculations. The results of these calculations lead to the evolution of the design from the preliminary to final stages. In the final design a control rod strategy was developed based on a distributed control rod approach. In this approach each fuel assembly has several control rod insertion guide tubes with  $TaB_2$  control pins (fingers). The control strategy was designed, additionally, to maintain the radial power shape roughly constant through burnup.

Once the final design met the neutronic requirements for B&B operation, its safety was evaluated by calculating reactivity feedback parameters and core eigenvalue for a series of potential accident scenarios. The Quasi-Static method, developed for the ANL Integral Fast Reactor concept, was applied to the demonstration B&B GFR core. It was found that by switching to dual entry control rods (i.e. from both the top and bottom of the core), and using active decay heat removal, that the system would be self-regulating, and thus safe under all significant potential accidents.

Coolant voiding and core flooding were also investigated. The coolant void reactivity worth limit was \$1, and it was found that the core reaches this limit only at the end of the equilibrium cycle. The effects of core flooding (i.e. cool liquid water ingress from the Steam Rankine PCS) were only of concern near BOL where there are few or no strong epithermal neutron absorbing fission products in the core. Therefore, if core flooding is a credible threat, adding a small amount of poison such as samarium to the startup core will eliminate the risk of prompt criticality arising from water ingress; the concentration will depend on whether SCRAM can be assured.

Given that the core meets the neutronic requirements, the thermal hydraulic and economic performance of the demonstration concept were also evaluated, as discussed in the subsequent two chapters.

## Chapter 6. Demonstration Core Thermal Hydraulics

### 6.1. Introduction

The thermal hydraulic evaluation of the B&B GFR core included determination of the peak clad temperature, helium outlet velocity, primary circulator work, average helium density, and fuel temperature to feedback into the physics calculations, thus enabling the refinement from the preliminary to the final design. The calculations also served to determine the limiting thermal power of the reactor. Finally, as Quasi-Static analyses confirm semi-self-regulation for the demonstration core, the time for blow down was calculated to determine the safety implications of a void reactivity of 1\$.

### 6.2. Steady State Operation

The three imposed limits are on the peak clad temperature, helium velocity, and coolant void reactivity worth. Having established that the 10 MPa operating pressure is the limiting pressure given the coolant void worth, the thermal power input in the finite volume thermal hydraulic model (FVM) was updated until either the peak clad or helium velocity limit was met.

Table 6-1 shows the numerical input parameters into the FVM. Recall that seven pin locations in each assembly are dedicated to the control cluster guide tubes. While the output includes the temperature profiles for the fuel, clad, and coolant, the primary interest is in the peak temperatures and the core pressure drop. The core pressure drop is an essential value of interest as it dictates the required primary circulator power and thus the cycle efficiency.

Table 6-1 Input into the Demonstration Core FVM

Core/Global Parameters	Symbol	Formula
Pin Locations per Assembly	n	169
Fuel Pins per Assembly	n'	162
Core Height	L	200 cm
Axial Reflector Length	R	25 cm
Assembly Flat-to-Flat Length	FTF	13.28 cm
Pin Pitch	p	1.00 cm
Pin Diameter	D	0.82 cm
Fuel Diameter	d <sub>in</sub>	0.74 cm
Number of Assemblies	N	612
Equivalent Core Temperature Rise	$\Delta T_{eq}$	218 °C (= 385/1.77)
Operating Pressure	P <sub>op</sub>	10 MPa
Thermal Power	P <sub>th</sub>	2900 MW
Axial Power Peaking Factor	APPF	1.44
Radial Power Peaking Factor	RPPF	1.77
Spacer Drag Coefficient	K <sub>sp</sub>	0.6
Helium IHX Outlet Temperature	T <sub>i</sub>	176 °C

The output for the hot channel is of key interest, and the numerical results are summarized in Table 6-2. The helium outlet velocity with flow orificing is 121.45 m/sec, however, the thermal power was not changed to reduce the velocity to exactly 120 m/sec; the very small difference was judged to be an acceptable discrepancy given the relative crudeness of the model. The peak clad

temperature is well within the 750 °C limit ( $< 650$  °C), and the primary circulator power with ideal orificing is an acceptable 53 MWe. With a secondary PCS efficiency of 40%, the gross electrical generation is 1181 MWe, and the net is 1128 MWe, giving a net efficiency for the reactor plant of 38.9%, very near the 40% goal.

Table 6-2 Demonstration Core Hot Channel FVM Output

Hot Channel Calculation Result	Value	Units
Average Linear Heat Rate	258.87	W/cm
Peak Linear Heat Rate	373.46	W/cm
Mass Flow Rate per Pin	25.91	g/sec/pin
Core Mass Flow Rate	2568.88	kg/sec
Core Pressure Drop	380.13	kPa
Primary Circulator Power	93.57	MW
Circulator Power with Ideal Orificing	52.86	MW
Spacer Pressure Drop Fraction	0.22	
Average Film Temperature Drop	130	°C
Peak Clad Temperature	641.21	°C
Average Clad Temperature	504.76	°C
Peak Fuel Temperature	845	°C
Average Fuel Temperature	696	°C
Average Helium Density	7.55	kg/m <sup>3</sup>
Average Heat Transfer Coefficient	0.88	W/cm <sup>2</sup> -°C
Helium Outlet Velocity	121.45	m/sec
Helium Average Velocity	91.56	m/sec

The average channel calculation is also used to determine the degree of orificing required. The mass flow rate in the average orificed channel is reduced by dividing by the radial power peaking factor, thus forcing the temperature rise in the average channel to be the same as the temperature rise in the hot channel. In doing so, the difference in pressure drop between the hot channel and the average orificed channel is the additional pressure drop that must be supplied by the assembly orifice. In this case, it is calculated to be 251 kPa.

Lastly, the fuel temperature is of interest. The fuel temperature is not close to any limits imposed by materials, but is an important parameter in the coupling between the thermal hydraulic and neutronic analysis of the reactor core. While a temperature of 900K was assumed for the MCNP input, a calculation of the average fuel temperature with flow orificing yields a value of 601 °C or 873K. Therefore, the available 900K ENDFB6 cross sections are the most appropriate choice for the model. Additionally, the average channel calculation is important for determining the average difference between the fuel temperature and the coolant temperature, as it is a factor in the Quasi-Static analysis of the core. In this case the average fuel temperature is ~600 °C and the average coolant temperature in the average orificed channel is 370 °C, yielding an average temperature difference of 229 °C. A temperature difference of 230 °C was used in the Quasi-Static analysis described in section 5.3.2.

### 6.3. Loss of Coolant and Blowdown Time

A limit for the coolant void reactivity worth of \$1 was imposed for the design. This limit is meant to avert the threat of prompt criticality in the event of a loss of coolant accident. However, this reactivity is not instantaneously added in the event of a pipe break. Therefore, the time it

takes for the coolant to blow down was estimated to give a better understanding of the safety implications of a \$1 coolant void reactivity worth for the B&B GFR.

The system pressure is high (10 MPa) compared to atmospheric pressure (~0.1 MPa) and therefore, in the event of a break the coolant flow from the primary system into the containment will be choked.

If frictional pressure losses at the break are ignored, the gas is assumed to expand isentropically, and the flow is assumed to be one dimensional, then the critical velocity of the flow for an ideal gas can be calculated as shown in Equation (6.1) [68].

$$u = \sqrt{\gamma RT} \tag{6.1}$$

Where  $u$  is the speed of sound,  
 $T$  is the temperature of the gas at the site of the break,  
 $R$  is the gas constant for the escaping gas, and  
 $\gamma$  is the ratio of the specific heat at constant pressure to the specific heat at constant volume (1.67 for monatomic ideal gases such as helium)

While the critical velocity for the escaping helium can be calculated at the time the break initiates, during the blowdown process the pressure of the primary side decreases, and subsequently, the density of the coolant decreases during blowdown. Because the density is decreasing, and the velocity is constant, the mass flow rate for the escaping coolant decreases after the break.

Therefore, one must account for the time dependence of the mass flow rate in calculating the time it takes to evacuate the primary coolant. The mass flow rate is shown in Equation (6.2) [68].

$$\frac{dM}{dt} = \rho_i A u \frac{p}{p_i} \tag{6.2}$$

Where  $M$  is the mass of coolant in the primary system,  
 $\rho$  is the coolant density at the time of the break,  
 $p$  is the primary pressure,  
 $A$  is the size of the break (area),  
 $u$  is the critical velocity, and  
 $i$  denotes the initial conditions for the gas.

Here, we define the time it takes to blow down as the time it takes for the pressure in the primary system to decrease to the point where the flow is no longer choked. In other words, the time it would take for the primary system to blow down to a pressure that is the product of the critical pressure ratio and the outside pressure (atmospheric). Using this definition, the blowdown time is given by Equation (6.3).

$$t_{bd} = \frac{-\ln\left(CPR \frac{p_{ref}}{p_i}\right) CPR^{\left(\frac{1}{\gamma}\right)}}{\sqrt{\gamma RT_i \left(CPR^{\left(\frac{\gamma-1}{\gamma}\right)}\right)}} \left(\frac{V}{A}\right) \quad (6.3)$$

Where  $t_{bd}$  is the blowdown time,  
 CPR is the critical pressure ratio,  
 V is the primary coolant volume,  
 $p_{ref}$  is the containment pressure (assumed ~ 1atm),  
 $p_i$  is the operating pressure, and  
 $T_i$  is the helium temperature.

Noting that the critical pressure ratio is related to the ratio of specific heats as shown in Equation (6.4) [68], the result of Equation (6.3) can be further simplified.

$$CPR = \left(2 \frac{1}{1+\gamma}\right)^{\left(\frac{\gamma}{\gamma-1}\right)} \quad (6.4)$$

The final result for the blowdown time is shown in Equation (6.5). The blowdown time depends on several key variables: the helium pressure and temperature at the time of the break, the size of the break, the volume of the primary coolant, and the pressure in the containment.

$$t_{bd} = \frac{-\ln\left(\left(2 \frac{1}{1+\gamma}\right)^{\left(\frac{\gamma}{\gamma-1}\right)} \frac{p_{ref}}{p_i}\right) \left(2 \frac{1}{1+\gamma}\right)^{\left(\frac{1}{1-\gamma}\right)}}{\sqrt{\frac{2\gamma RT_i}{1+\gamma}}} \left(\frac{V}{A}\right) \quad (6.5)$$

The blowdown time was calculated for various helium temperatures and break sizes. The volume of the primary coolant was assumed to be 761 m<sup>3</sup> (which is the value for the GA GCFR) [19]. The average helium temperature is 372 °C for the demonstration core, however, the blowdown time was calculated for temperatures of 176 °C (cold, zero power condition), and 568 °C (maximum helium temperature). Break sizes of 1 in<sup>2</sup>, 10 cm<sup>2</sup>, and 0.1 m<sup>2</sup> were examined. The results for the blowdown time calculation are summarized in Table 6-3.

Table 6-3 GFR Loss of Coolant Blowdown Times

Helium Temperature	GA GCFR Volume	B&B GFR Volume	small break (1 in <sup>2</sup> ) blowdown time	medium break (10 cm <sup>2</sup> ) blowdown time	large break (0.1 m <sup>2</sup> ) blowdown time
°C	m <sup>3</sup>	m <sup>3</sup>	min	min	sec
		approx. order			
176	761		149	10	58
372	761		124	8	48
568	761		108	7	42
176		1000	196	13	76
372		1000	163	11	63
568		1000	142	9	55

A volume of 1000 m<sup>3</sup> was also included in the analysis to represent a rough estimate of the B&B GFR primary circuit volume. The results indicate that the blowdown time for a medium sized break could be as long as ~10 minutes. Thus, during a loss of coolant accident the reactivity is increased over a period of time on the order of a minute to several minutes, allowing some time for negative reactivity feedback to compensate (such as core radial expansion) or even direct operator intervention.

#### 6.4. Chapter 6 Summary

Thermal hydraulic calculations for the final design of the demonstration core were completed to determine the peak cladding temperature, core pressure drop, and helium outlet velocity. These calculations demonstrate that a thermal power of 2900 MW is achievable without breaching the cladding temperature or helium velocity limits. The peak cladding temperature in steady state is more than 100 °C below the limit. Additionally, an analysis was carried out to determine the time it takes for the reactor pressure vessel to blow down; it was found that the time it takes is on the order of minutes, and therefore, in the event of coolant depressurization there is time for negative reactivity feedback mechanisms such as core flowering to compensate for the positive reactivity affect of voiding.





## Chapter 7. Demonstration Core Fuel Cycle Economics

### 7.1. Introduction

While the B&B GFR is designed without the need for any type of spent fuel reprocessing or reuse, the high fissile plutonium concentration in the fuel at discharge makes the spent fuel valuable, especially if proliferation resistant fuel cycle options are employed. Here, four fuel cycle options are postulated for the demonstration core.

First, as a general matter, the GFR spent fuel contains fissile plutonium with concentrations of ~8a/o in the heavy metal. The plutonium is ~80%  $^{239}\text{Pu}$ . The fuel also has a substantial concentration of fission products, particularly a large (non-saturating) quantity of  $^{149}\text{Sm}$ .

The first option considered was the once-through option, labeled OTTO. Given the high variability in the cost of highly enriched nitrogen in the literature, several cases were examined for each postulated fuel cycle option. The second option considered was to use an AIROX type reprocessing technique on the GFR spent fuel and then load the spent fuel into an LWR, labeled AIROX in the case studies that follow.

Nitrogen recovery was also considered as a way to improve the economics of the fuel cycle as the price of HEN is considerable. The recovery is assumed to coincide with the AIROX treatment of the fuel and was furthermore assumed to occur without any change in the cost of spent fuel treatment.

The last option considered was to separate some of the treated spent fuel for direct reuse in the GFR. In the direct reuse option (labeled split), spent fuel would be divided into two equal parts. The first part would undergo conversion to oxide and be used in a PWR; the second part would be blended with depleted U and refabricated as GFR fuel for a second campaign in the B&B GFR. The cost of the depleted U is neglected. Given the very hard spectrum of the GFR and thus small absorption cross sections for fission products, no spent fuel chemical separations are required for direct reuse in the GFR.

The technical feasibility for PWR disposition of the spent fuel has been illustrated and covered in section 4.4.4.

### 7.2. Cost of Generation

The technical feasibility of direct reuse in the GFR using the split option was assessed based on infinite assembly reactivity calculations. The infinite BOL assembly reactivity of potential direct reuse fuel was compared to that of a fresh assembly, and the results are tabulated in Table 7-1. That each infinite assembly calculation yields similar eigenvalues indicates that splitting and reusing the spent fuel directly in the B&B GFR is feasible from a neutronics standpoint, and likely to have little impact on the performance of the reference core.

Table 7-1 Infinite Assembly Reactivity at BOL for Direct Fuel Reuse in the GFR

Infinite Assembly	k	std-dev
Fresh Reload Fuel	0.77382	0.00040
EOC1 Split Fuel	0.78675	0.00046
EOEC Split Fuel	0.79305	0.00037

It was found that the spent fuel from the 1<sup>st</sup> cycle and from the equilibrium cycle can potentially be reused as fresh fuel once split and blended with 50% <sup>238</sup>U. The reactivity will be slightly higher if natural, or even depleted, uranium is used.

Since the cost of HEN is uncertain, given the high level of JAERI interest and recent progress in the area of HEN production, a series of economic comparisons were carried out. The results are shown for a 2900 MWth demonstration core in Table 7-2. The price of HEN was varied between 0 1994 USD/g and 1,000 1994 USD/g. However, estimates for the price of HEN range from as low as \$100/g [60] to as high as \$1,000/g [35,47] in 1998 USD.

Table 7-2 Alternative Fuel Cycle Economic Assessment

	Demo. B&B GFR OTTO	Demo. B&B GFR and AIROX	PWR AIROX with HEN Recovery	PWR AIROX, HEN Recovery and Split	Reference LWR OTTO
HEN Price	Fuel Cycle Cost	Fuel Cycle Cost	Fuel Cycle Cost	Fuel Cycle Cost	Fuel Cycle Cost
USD/g	mills/kWhre	mills/kWhre	mills/kWhre	mills/kWhre	mills/kWhre
0	3.86	3.74		3.71	6.72
30	6.69	6.57	6.23	6.07	6.72
100	13.31	13.19	12.09	11.59	6.72
500	51.11	50.99	45.56	43.12	6.72
1000	98.37	98.25	87.39	82.54	6.72

Table 7-2 clearly shows that the demonstration core is hardly economic at the current price estimates for HEN and would require complicated fuel cycles. As JAERI research in the area of HEN production is rapidly progressing, the demonstration core fuel cycle should not be immediately abandoned. A second series of calculations summarized in Table 7-3 were carried out to determine the price of HEN where the demonstration core fuel cycle costs and the fuel cycle costs for a typical LWR would be the same. These prices range between 30 and 40 1994 USD/gHEN.

Table 7-3 Breakeven HEN Unit Cost

Input Variables	Units	Symbol	LWR Reference Value	Demo. B&B GFR OTTO	Demo. B&B GFR AIROX	AIROX with HEN Recovery	AIROX, HEN Recovery and Split
Discharge Burnup	MWD/kg <sub>HM</sub>	B <sub>d</sub>	50	150	150	150	150
Net Efficiency	%	η	33	40	40	40	40
Cycle Length	EFY	T	1.5	2.5	2.5	2.5	2.5
Number of Batches		n	2.68	6	6	6	6
Capacity Factor		CF	0.9	0.9	0.9	0.9	0.9
Enrichment	w/o	x <sub>p</sub>	4.5	5	5	5	5
Fuel Cycle Cost	mills/kWhre		6.72	6.72	6.72	6.72	6.72
Required Price of HEN	USD/gHEN		N/A	30.26	31.55	35.83	38.22

Although the demonstration core illustrates the feasibility of the B&B concept, it, however, is not economically competitive currently due to the very high cost of HEN. The equilibrium fuel cycle costs are going to be much lower than the costs for the startup core fuel assemblies because the enrichment for these assemblies is higher (as high as 10 a/o) and these assemblies are discharged after only a few cycles. The highest enriched batches, at 10 a/o enrichment, are all discharged within the first three fuel cycles. Thus, the economic competitiveness of the demonstration core is further impeded by the necessity for highly reactive startup fuel assemblies. The costs for startup were not calculated for the demonstration core given the already expensive equilibrium fuel cycle costs.

The cost estimates for free HEN indicate that if B&B can be achieved with a less expensive fuel form, such as UC, there are significant economic benefits, thus warranting further investigation of UC fuel in the B&B GFR. The costs associated for a B&B GFR startup core with this type of fuel are discussed in Chapter 11.

The UC fuel, however, is less neutronically reactive than the  $U^{15}N$  fuel form, and will therefore require an innovative new fuel assembly design to facilitate a larger loading of heavy metal to meet the neutronic requirements for B&B.

### **7.3. Chapter 7 Summary**

This chapter discusses the economics of the demonstration core fuel cycle. The very high price for highly enriched nitrogen makes the demonstration core fuel cycle unattractive unless the unit cost of HEN can be reduced to ~30 1994 USD/gHEN. Even at this level, fuel reprocessing, reuse, and nitrogen recovery may be required to ensure economic competitiveness with today's light water reactor fuel cycles.

If HEN were much cheaper, there are real economic benefits to operating in the B&B mode despite the long fuel residency times, thus strongly motivating investigation of alternative fuels such as uranium carbide.



# Chapter 8. Advanced Core Overview

## 8.1. Introduction

For a reactor to operate in the B&B mode, the core must have a large heavy metal loading to sustain criticality through cycle lengths allowable by structural material performance. With a large heavy metal loading in each assembly, and a discharge burnup of 150 MWD/kg<sub>HM</sub> it is essential, from an economic perspective, for the core to operate at high power density. The Tube-in-Duct (TID) fuel assembly is proposed as a means to meet the competing fuel design requirements for service in a B&B GFR [50,73].

The TID fuel assembly is a hexagonal array of coolant tubes surrounded by a VIPAC UC fuel inside a vented assembly duct. The fuel volume fraction in the TID fuel assembly is higher than that achievable with a standard pin-type assembly without compromising the peak cladding temperature. The design also eliminates the need for pin spacers which helps in minimizing the core pressure drop. The conceptual TID assembly is shown in Figure 8.1. The fuel and axial reflector are both VIPAC and fission gases are vented into an off-gas system.

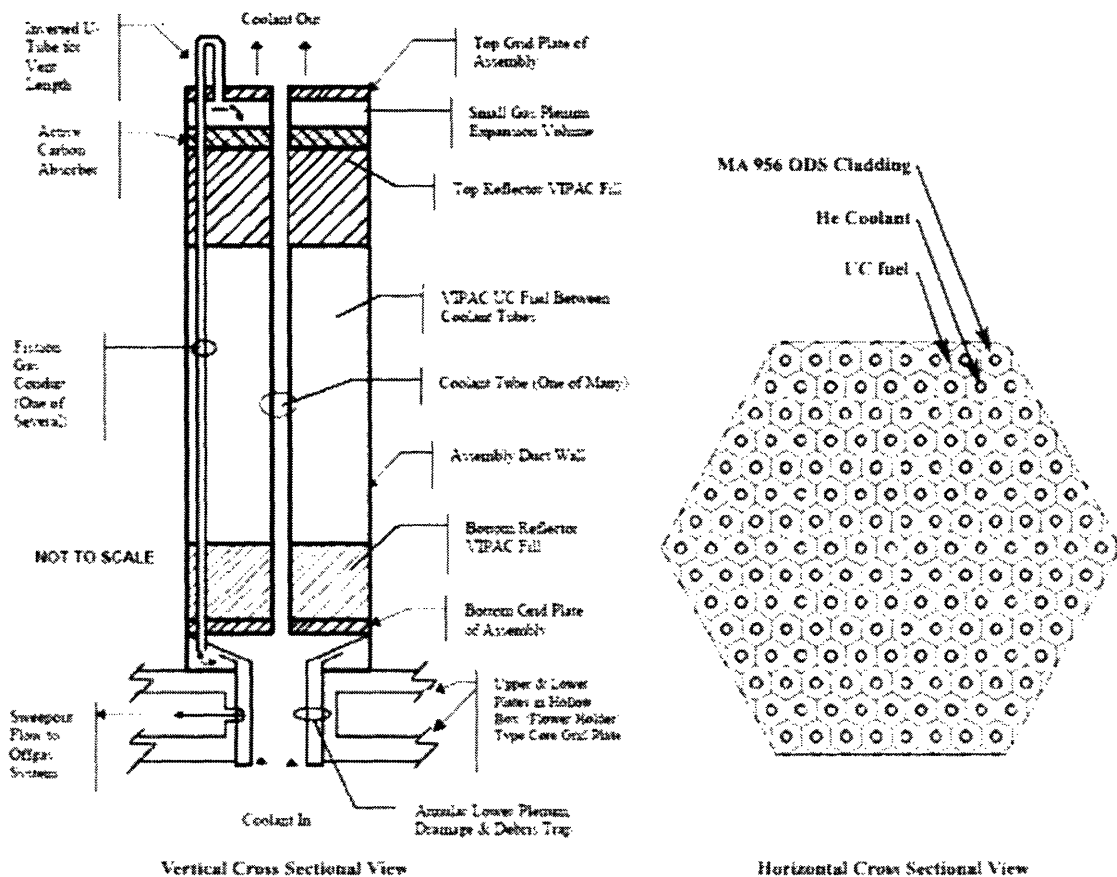


Figure 8.1 TID Conceptual Diagram

## 8.2. Fuel Volume Fraction

MCNP4c3 and ORIGEN2.2 were used to evaluate the BOC eigenvalue and reactivity history of the TID fuel assembly for various enrichments and coolant channel dimensions. The purpose of this work was to establish the desired fuel volume fraction for a TID assembly, where the neutronic performance mirrors that of the demonstration core's  $U^{15}N$  pin assemblies.

An MCNP model was created for a UC fueled, MA956 ODS steel clad, helium cooled TID fuel assembly. The assembly had mirror boundary conditions on the edge of the ODS duct radially, and allowed for neutron leakage through the upper and lower axial  $Zr_3Si_2$  reflectors. The reference assembly model has a flat-to-flat distance of 13.3 cm, 169 coolant channels, and 8 axial fuel zones. This model was also used to calculate the axial power peaking factor.

The BOC assembly eigenvalue was calculated for enrichments of 5 a/o and 10 a/o  $^{235}U$ . The coolant channel inner radius was varied between 0.15 cm and 0.45 cm. For coolant channel radii of 0.15 cm, 0.30 cm, and 0.40 cm MCODE was used to simulate the burnup of the assembly to 300 MWD/kg<sub>HM</sub>. These cases were evaluated solely to compare the physics performance; in practice one would vary pin pitch at constant coolant tube diameter.

Figure 8.2 shows a plot based on BOC assembly reactivity calculations. The reactivity is plotted against the ratio of the theoretical heavy metal density to the homogenous heavy metal density (the heavy metal density smeared over the whole assembly volume). The curves clearly illustrate the dependence of the reactivity on the heavy metal density. As the two BOC curves are nearly linear, one can easily predict the BOC reactivity based on the initial enrichment using a linear model.

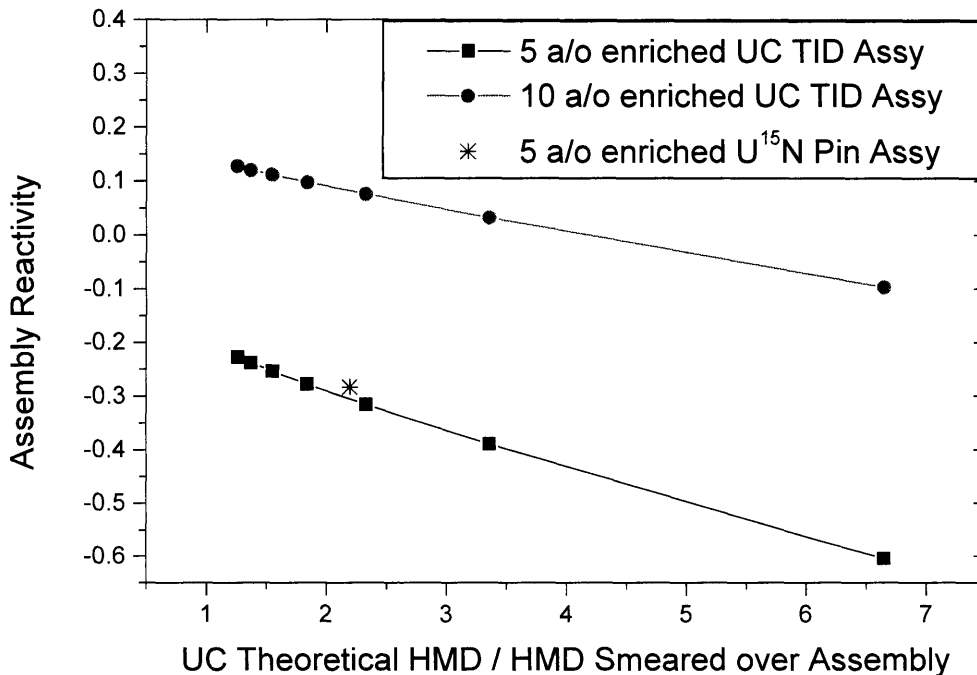


Figure 8.2 BOC Infinite Medium Reactivity Assessment for TID Fuel

The BOC eigenvalue for the demonstration core fuel assembly is also shown as a reference. The next set of analyses were carried out on several cases to illustrate the behavior of the 5a/o enriched fuel during burnup. As Figure 8.3 illustrates, increasing the volume fraction to much larger than 60% only yields a reactivity benefit on the order of 200 pcm. Additionally, it is worth noting that the reactivity difference between the different cases is fairly constant throughout burnup. Therefore it is possible to predict the burnup trend for the TID fuel based on the coolant or fuel volume fraction and BOC reactivity. Additionally, a  $U^{15}N$  fueled pin assembly is also shown to illustrate the competitiveness of the TID concept in terms of meeting the requirements for B&B operation.

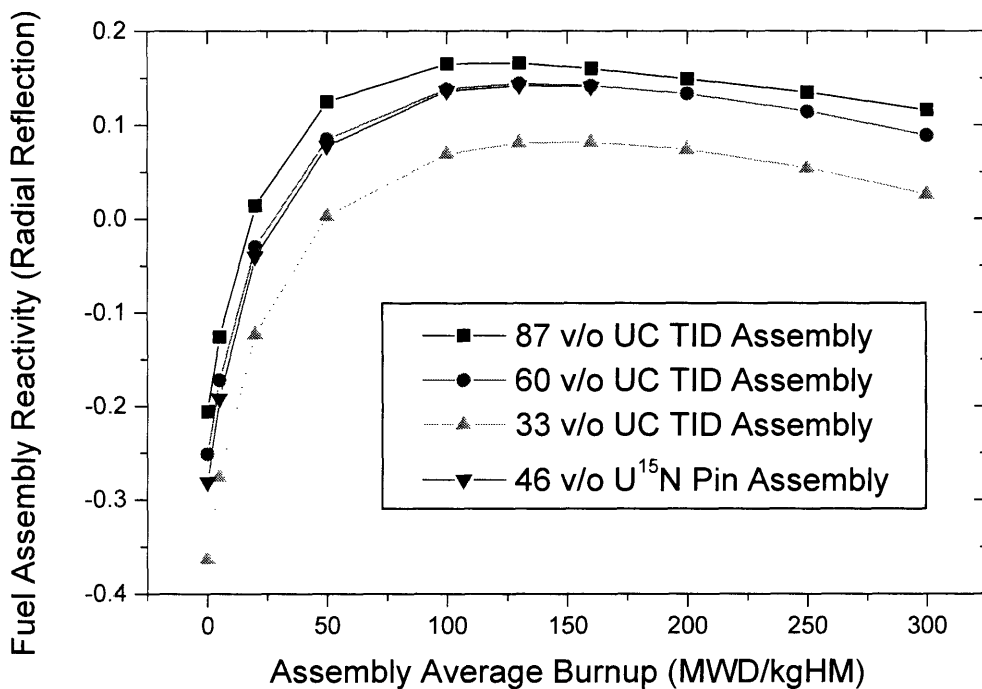


Figure 8.3 Burnup Histories for Various Fuel Volume Fractions.

The  $U^{15}N$  fueled pin assembly evaluated in Chapter 5 has been shown to enable B&B operation with a discharge burnup of 150 MWD/kg<sub>HM</sub>. To achieve B&B operation with UC, the results of these analyses show that ~60 v/o fuel will be required with the TID assembly to avoid the need for spent fuel recycle or raising the burnup limit. Given the necessary volume fraction, a series of thermal hydraulic calculations were performed to ensure that the TID assembly would not result in exceeding the peak clad temperature, or maximum helium velocity limits.

### 8.3. Advanced Core Primary Coolant Pressure

The advanced core is comprised of UC fueled tube-in-duct fuel assemblies. The TID assembly, while conferring the physics benefits of high heavy metal density, will require slightly higher operating pressure to keep within the limits on clad temperature and helium velocity.

Physics analyses of the TID fuel assembly indicate that 60 v/o fuel will be required to match the performance of the 46 v/o pin-type assembly with U<sup>15</sup>N fuel. Therefore, a parametric analysis was conducted before completing a full core design to check the feasibility from a thermal-hydraulic standpoint of designing a TID fuel assembly that will match the physics performance of the demonstration core.

Table 8-1 shows a comparison between several test cases for the TID assembly based on the same core temperature rise as the demonstration core. The table shows the coolant channel diameter, pitch, volume fractions, peak clad temperature, helium outlet velocity, the assembly flat-to-flat dimension and the operating pressure.

Table 8-1 Parametric Comparison for the TID Assembly

	<b>D</b>	<b>P</b>	<b>v/o F</b>	<b>v/o Co</b>	<b>peak Tcl</b>	<b>He v out</b>	<b>FTF</b>	<b>Pop</b>
	<b>cm</b>	<b>cm</b>	<b>%</b>	<b>%</b>	<b>°C</b>	<b>m/s</b>	<b>cm</b>	<b>MPa</b>
case 1	0.80	1.35	61.6	31.7	712	138	13.3	10.0
case 2	1.00	1.64	60.6	33.8	778	131	13.2	10.0
case 3	1.28	2.10	61.8	33.9	888	131	13.3	10.0
case 4	0.80	1.35	61.6	31.7	711	125	13.3	11.0
case 5	0.80	1.35	61.6	31.7	711	119	13.3	11.5
case 6	0.80	1.35	61.6	31.7	710	114	13.3	12.0

The results indicate that to simultaneously meet the temperature and velocity limits with the same core size and reload strategy as the demonstration core an operating pressure of 11.5 MPa or higher is required (case 5). However, previous experience with the demonstration core indicates that the EOEC void reactivity will be ~\$1 at 10 MPa; since the TID coolant inventory is reduced by approximately 1/3, the pressure can likely be increased by a similar percentage and maintain approximately the same coolant void worth. Therefore, the primary pressure for the advanced core is taken as 11.5 MPa.

#### 8.4. Core Design Considerations and Lessons Learned

The control scheme for the demonstration core, i.e. distributed control elements in each assembly, is not practical for the advanced core given the design of the tube-in-duct fuel assemblies. Therefore, there was no clear alternative to the CRA approach to control the excess reactivity. Hence, during the initial stages of the core design it is essential to include many CRA locations, due to which the final advanced core design will be larger radially than the its demonstration core predecessor, and the discharge burnup was increased to 165 MWD/kg<sub>HM</sub>. Furthermore, moderator control was not investigated for the advanced core based on its poor performance in the demonstration core.

Yet, while there are some areas where solutions and strategies applied to the demonstration core will not be acceptable for the advanced core, the similarity in the reactivity histories between the pin and TID assemblies allows for the adoption of essentially the same multi-batch fuel shuffling sequence. Additionally, high fuel cost figures calculated for the demonstration core motivate investigation of the advanced concept. Though some parameters such as cycle duration will differ between the demonstration and advanced cores, the potential economic advantage of the concept is significant. Based on this preliminary neutronic and thermal hydraulic assessment, there is a viable design space for a UC fueled B&B GFR.



The same balance of plant is used for the advanced as for the demonstration core. Since CRAs must be included in the core, the radial size of the core was increased (from ~350 cm to ~400 cm) to make room for CRA locations, and the increased radius reduces the radial leakage. As the necessity for the CRA locations reduces the fuel volume fraction in the core, the reactivity-limited burnup will be somewhat higher (165 MWD/kg<sub>HM</sub> instead of 150 MWD/kg<sub>HM</sub> in the demonstration core). The batch shuffling sequence remains essentially the same as the demonstration core, except that 6 assemblies from each batch are removed to make room for CRAs, giving a total of 37 CRAs, including the one at the center of the core.

The advanced core geometry is summarized in Table 8-2. The structural volume fraction includes volume dedicated to the control rod assemblies and interassembly spacing (6 mm).

Table 8-2 Advanced Core Geometry

Fuel Form	UC	
Channels per Assembly	91	
Channel Diameter	0.80	cm
Clad Thickness	0.04	cm
Channel Pitch	1.45	cm
Assembly Flat-to-Flat	14.8	cm
Active Core Height	200	cm
Equivalent Core Diameter	396	cm
Fuel Volume Fraction	54.5	v/o
Structural Volume Fraction	18.0	v/o
Coolant Volume Fraction	27.5	v/o

It is likely that a non-negligible fraction of the heat will be transferred to coolant flowing in the interassembly volume, and therefore, an area of future work would optimize the interassembly spacing to make use of bypass flow through this region in order to minimize the peak fuel, duct and cladding temperatures. However, assessment for the thermal hydraulics was done using two single channel calculations as discussed in section 2.3.2.

## 8.5. Chapter 8 Summary

Initial investigation into the tube-in-duct fuel assemblies involved coupled thermal hydraulic finite volume calculations and infinite assembly neutronic calculations to determine assembly dimensions and primary coolant pressure before undertaking a full core design.

The neutronic calculations indicate that a ~60 v/o fuel fraction (on an assembly basis) will be required to enable B&B mode operation with a UC fueled GFR. At this high a fuel volume fraction, a coolant pressure of at least 11.5 MPa is required to meet the cladding temperature and helium velocity limits. Additionally, the tube-in-duct fuel assembly will not allow for control rod insertion points inside the assembly, therefore a control rod assembly scheme was adopted, in which case several more CRA locations must be added to the full core design relative to the demonstration core, thus requiring either the displacement of fuel assemblies or an increase in the size of the core.



## Chapter 9. Advanced Core Physics

### 9.1. Introduction

Full core modeling for the advanced core began after relatively sophisticated scoping analyses were conducted using an infinite assembly MCNP model coupled with the finite volume thermal hydraulic model. The final core design was input into MCNP and the core layout is shown in Figure 9.1. The model is  $1/12^{\text{th}}$  symmetric radially, and reflected about the axial midplane, thus representing only  $1/24^{\text{th}}$  of the actual core.

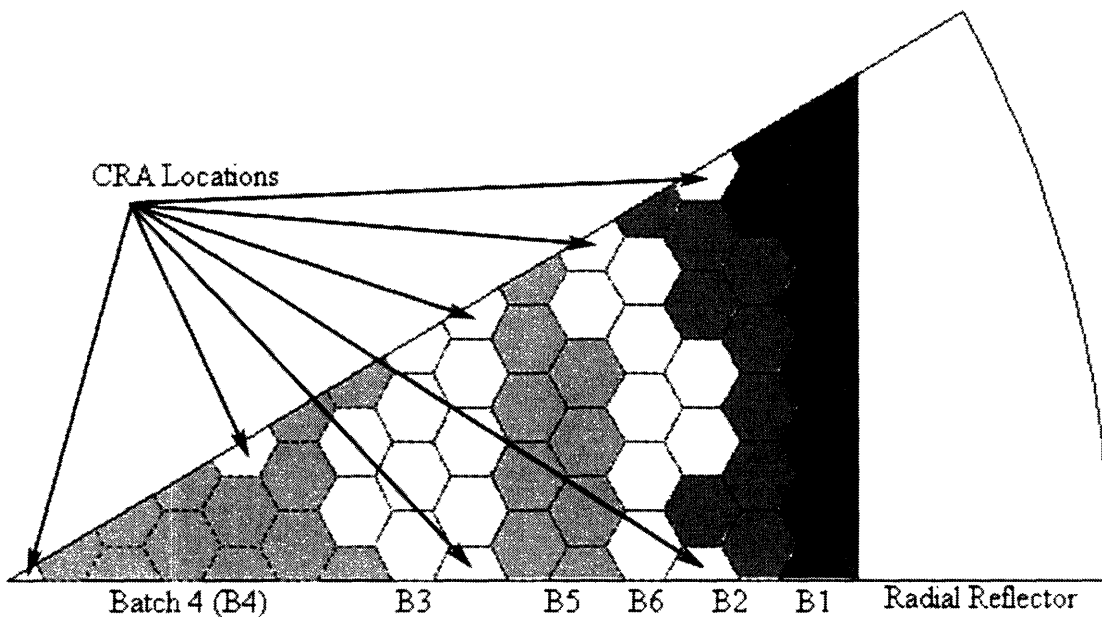


Figure 9.1 Advanced Core Layout

The MCNP and MCODEv2 input file for the advanced core model are shown in Appendix G. The primary physics parameters of interest are: the uncontrolled reactivity history, the impact of the control rod assemblies on the neutron economy, a Quasi-Static analysis of the core, and an assessment of the cladding damage due to irradiation. All of these are meant to verify the feasibility of the concept. In many respects the neutronic performance of the advanced core is only subtly different from that of the demonstration core.

The core thermal power is  $2400 \text{ MW}_{\text{th}}$ , whereas the demonstration core thermal power was  $2900 \text{ MW}_{\text{th}}$ . The lower thermal power, and higher heavy metal loading for a slightly larger discharge burnup results in a longer cycle length (4.7 EFPY for the advanced core and 2.5 for the demonstration core). This is an important distinction, because increased carrying charges for the longer fuel residency time will erode some of the economic benefits of the advanced core, though still remaining competitive relative to a LWR.

As dual entry control devices were identified for the demonstration core as advantageous for several reasons, the advanced core model is axially symmetric about the midplane. Therefore, as control elements are inserted from the top of the model, the neutronic calculation reflects control elements being inserted simultaneously from the bottom of the core.

## 9.2. Uncontrolled Reactivity History

The uncontrolled reactivity history for the advanced core was calculated using MCODEv2. Again, the advanced core design uses the lessons learned in the demonstration core design and operates with the same startup enrichment zoning, reload enrichment, and multi-batch shuffling sequence as for the final design of the demonstration core. The BOC3 reactivity, just as in the demonstration core, is still the lowest of any cycle. An addition cycle was calculated, cycle 8, to further illustrate that the core had reached equilibrium in the 7<sup>th</sup> cycle.

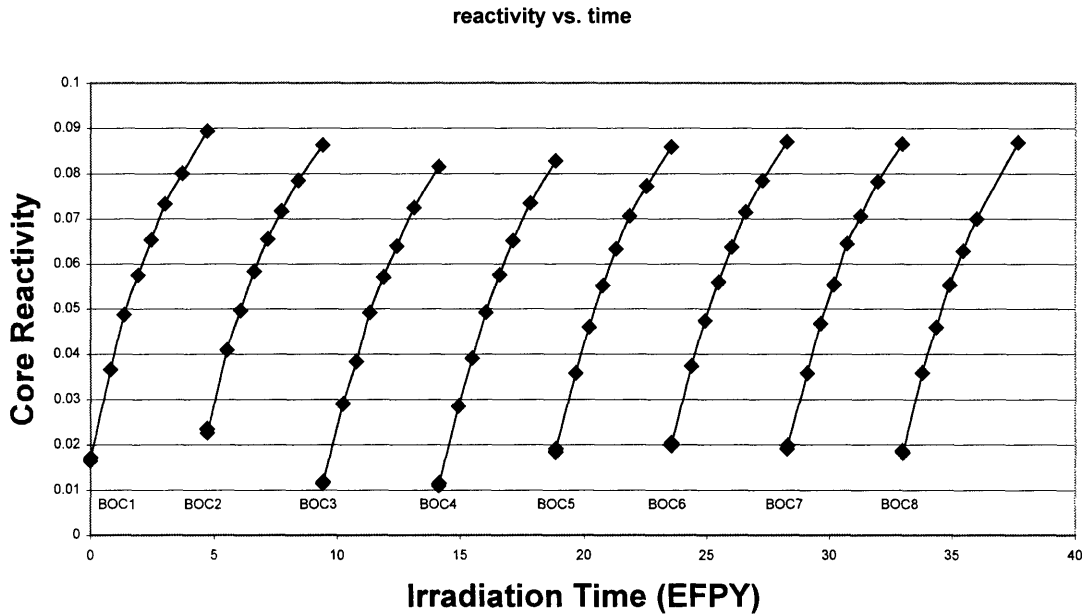


Figure 9.2 Advanced Core Uncontrolled Reactivity History

On average the fuel accrues 27.5 MWD/kg<sub>HM</sub> of burnup during each cycle, which is 1720 EFPD long. The Burnup Accrual Discrepancy (BAD) discussed in 2.2.4.5 describes why it is important to specify burnup steps in MCODEv2 in EFPD instead of burnup; to quantify this error, the burnup accrued in the last cycle of the MCODEv2 calculation is calculated to be 29 MWD/kg<sub>HM</sub>. This discrepancy arises because MCODEv2 calculates the burnup by dividing by the heavy metal mass at the beginning of the cycle calculation, and the heavy metal mass for the partially burnt assemblies is lower than the initial heavy metal mass.

## 9.3. Reactivity Control

The advanced core makes use of 37 CRAs distributed throughout the core model as shown in Figure 9.1. The control material is highly enriched boron carbide (96 a/o <sup>10</sup>B in B) designated HE B<sub>4</sub>C. The HE B<sub>4</sub>C control assemblies are arranged in a TID geometry identical to the fuel assemblies, with an equal number of equally sized coolant channels for calculational purposes. Detailed design of the HE B<sub>4</sub>C control assemblies is left for future work.

The HE B<sub>4</sub>C control elements were inserted in the EOC MCNP model to assess the impact of the control elements on the neutron economy using the metric of neutron economy (Y) exactly as in the case for the demonstration core. The calculation of the metric is summarized in Table 9-1.

Table 9-1 Neutron Economy Performance of Advanced B&B Concept

	EOEC Rods out	EOEC Rods in		% change
$\sigma_{f49}$ (41)	1.6740	1.6610	b	-0.8%
$\sigma_{\gamma49}$ (41)	0.3528	0.3121	b	-11.5%
$\sigma_{a49}$ (41)	2.0268	1.9731	b	-2.6%
$\sigma_{f28}$ (41)	0.0470	0.0530	b	12.8%
$\sigma_{\gamma28}$ (41)	0.2343	0.2167	b	-7.5%
$\sigma_{a28}$ (41)	0.2813	0.2697	b	-4.1%
CR	1.1574	1.1016		-4.8%
$k_{eff}$	1.0941	0.9662		-11.7%
N49	0.0022	0.0022	#/b-cm	
N28	0.0223	0.0223	#/b-cm	
$\sigma_f/\sigma_a$ 49	0.83	0.84		1.9%
$\sigma_f/\sigma_a$ 28	0.17	0.20		17.7%
$\nu$ average	2.84	2.85		
1/Y	1.098	0.875		-20.3%
Y	0.91	1.14		25.5%

It was found that there is very little difference in the impact of poison control on the advanced core relative to the demonstration core, and the current control scheme was accepted.

#### 9.4. Quasi-Static Analysis

A Quasi-Static analysis was conducted for the advanced core. The eigenvalue and coefficient calculation is summarized in Table 9-2. One of the key assumptions in this analysis is that the base plate for the advanced core is designed to enable radial expansion, and thus the flowering of the fuel elements.

The advanced core, unlike the demonstration core however, fails to fall within the limit dictated by transient overpower without scram. Therefore, the advanced core, with the current control rod assembly approach is not self regulating following a control rod ejection accident at EOEC. This is because the geometry of the tube-in-duct fuel assemblies forces the core design to use several control rod assemblies instead of many distributed control elements. Given the large reactivity swing, at the EOEC the central CRA has ~4 times more reactivity than would fall within the prescribed limits as shown in Table 9-3. The only potential solution is to increase the number of CRAs in the core such as to significantly reduce the relative worth of a single CRA.

Table 9-2 Calculated Reactivity Feedback Parameters and Uncertainty

Advanced B&B GFR Case Description	Eigenvalue	Standard Deviation	Derived Quantity	Units	Value	Standard Deviation
BOL Nominal	1.01658	0.00033	$\Delta\rho_{\text{VOID}}$	\$	0.352	0.051
BOL Without Delayed Neutrons	1.00777	0.00022	$\beta$		0.00867	0.00039
BOL 300 K Cross Sections	1.02412	0.00030	$\alpha_{\text{D}}$	pcm/K	-0.952	0.056
BOL Fuel Thermally Expanded	1.01406	0.00025	$\alpha_{\text{e}}$	pcm/K	-0.366	0.060
BOL Core Radially Expanded	1.01462	0.00030	$\alpha_{\text{R}}$	pcm/K	-0.142	0.032
BOL Coolant Voided	1.01974	0.00028	$\alpha_{\text{Co}}$	pcm/K	0.0041	0.0006
Estimated Maximum CRA Worth			$\Delta\rho_{\text{TOP}}$	pcm	249	5
BOEC Nominal	1.01904	0.00025	$\Delta\rho_{\text{VOID}}$	\$	0.624	0.066
BOEC Without Delayed Neutrons	1.01254	0.00027	$\beta$		0.00638	0.00036
BOEC 300 K Cross Sections	1.02492	0.00029	$\alpha_{\text{D}}$	pcm/K	-0.740	0.048
BOEC Fuel Thermally Expanded	1.01512	0.00026	$\alpha_{\text{e}}$	pcm/K	-0.568	0.052
BOEC Core Radially Expanded	1.01608	0.00025	$\alpha_{\text{R}}$	pcm/K	-0.214	0.027
BOEC Coolant Voided	1.02319	0.00028	$\alpha_{\text{Co}}$	pcm/K	0.0053	0.0005
Estimated Maximum CRA Worth			$\Delta\rho_{\text{TOP}}$	pcm	112	2
EOEC Nominal (~critical configuration)	0.99179	0.00034	$\Delta\rho_{\text{VOID}}$	\$	0.564	0.104
EOEC Without Delayed Neutrons	0.98680	0.00032	$\beta$		0.00503	0.00047
EOEC 300 K Cross Sections	0.99548	0.00038	$\alpha_{\text{D}}$	pcm/K	-0.491	0.068
EOEC Fuel Thermally Expanded	0.98935	0.00030	$\alpha_{\text{e}}$	pcm/K	-0.373	0.069
EOEC Core Radially Expanded	0.98886	0.00031	$\alpha_{\text{R}}$	pcm/K	-0.224	0.035
EOEC Coolant Voided	0.99459	0.00029	$\alpha_{\text{Co}}$	pcm/K	0.0038	0.0006
EOEC Highest Worth CRA Ejected	1.01377	0.00032	$\Delta\rho_{\text{TOP}}$	pcm	2186	47

The coefficient ratios were calculated and are shown in Table 9-3. A side-by-side comparison of the coefficients between the demonstration and advanced cores shows that the advanced core has consistently stronger negative feedback and consistently weaker positive feedback. While these differences are small, they are noticeable and easily explained.

Table 9-3 Demonstration and Advanced Core Reactivity Feedback

		Adv. B&B GFR			Demo. B&B GFR		
		BOL	BOEC	EOEC	BOL	BOEC	EOEC
A	cents	-35	-47	-40	-19	-25	-24
B	cents	-36	-52	-50	-22	-23	-28
C	cents/K	-0.17	-0.24	-0.22	-0.10	-0.11	-0.12
A/B		0.99	0.90	0.79	0.84	1.09	0.85
CΔTc/B		1.82	1.75	1.66	1.70	1.90	1.70
Δρ <sub>TOP</sub> /B		0.40	0.17	4.34	0.53	0.28	0.64
A/B limits		x < 1			x < 1.14		
CΔTc/B limits		x > 1			x > 1		
Δρ <sub>TOP</sub> /B limits		x < 1			x < 1.14		
β		0.00867	0.00638	0.00503	0.00882	0.00623	0.00544
α <sub>D</sub>	1e-3 c/K	-110	-116	-98	-64	-91	-94
α <sub>e</sub>	1e-3 c/K	-42	-53	-44	-17	-18	-9
α <sub>Co</sub>	1e-3 c/K	0.5	0.8	0.8	1	1	2
α <sub>RD</sub>	1e-3 c/K	0	0	0	0	0	0
α <sub>R</sub>	1e-3 c/K	-16	-34	-45	-17	-6	-22

The dominant negative reactivity feedback parameters for the advanced core are the Doppler coefficient and the fuel thermal expansion coefficient. As for the Doppler, the carbon in the UC TID fueled advanced core is a stronger neutron moderator than <sup>15</sup>N, leading to a somewhat softer neutron flux spectrum for the advanced core, as evidenced by the stronger conversion ratio calculated during the assessment of control devices. The Doppler coefficient for the advanced core is therefore somewhat larger because a larger portion of the neutron flux is in the resonance region compared to the demonstration core.

The fuel thermal expansion coefficient is driven by the expansion of the cladding material as it is assumed that the fuel is bonded to the cladding. In the demonstration core, the expansion of the fuel elements constricts the coolant passages through the core, and thus reduces axial neutron streaming paths through the coolant. In the advanced core case, the fuel thermal expansion coefficient is more negative because the expansion of the cladding material increases, as opposed to decreases, the coolant passages through the core, and is therefore coupled with an increase in axial leakage.

The only positive feedback parameter in either the demonstration or advanced core concepts is the coolant temperature coefficient. While each core has a positive coolant void reactivity, since the advanced core has a significantly reduced coolant inventory compared to the demonstration core, this coefficient is smaller. Thus the advanced core has consistently stronger negative feedback in parallel with weaker positive feedback.

Therefore, while an alternative control scheme must be devised in order for the advanced core to be self regulating (with active decay heat removal), the stronger negative feedback relative to the demonstration core is an encouraging attribute of the advanced core. Additionally, the smaller coolant void reactivity (0.60\$) of the advanced core warrants further investigation of this concept, as increased primary system pressure and increased thermal power will likely improve the economic performance of the fuel cycle.

## 9.5. Cladding Irradiation

A unit cell model was used to assess the cladding irradiation, fluence, DPA, and helium buildup. As the discharge burnup is 165 MWD/kg<sub>HM</sub>, linearly interpolation was used to determine the DPA and helium concentration. Given that the physics behavior of the advanced and demonstration cores are essentially the same, there are only small differences in the effects of irradiation on the cladding material.

The helium concentration is somewhat higher in the advanced core (67 ppm vs. 55 ppm for the demonstration core) and the peak DPA is slightly, though not much, greater (411 for the advanced, 376 for the demonstration). Table 9-4 summarizes these calculations.

Table 9-4 UC TID Model Fluence and DPA Calculation

UC TID	Lindhard	Half-Nelson	(n,α)	Heppm DPA	Burnup MWD kgHM	Φ > 0.1	Φ > 1	Total Φ	Helium Concen. ppm	avg DPA	Atomic Burnup a/o	DPA Burnup
step	b	b	b	ppm		n/b	n/b	n/b				
0	273	213	3.40E-05	0.12	0	0	0	0			0	
1	273	213	3.40E-05	0.12	0.1	0.001	0.000	0.001	0	0	0.01	21
2	273	212	3.41E-05	0.13	10	0.050	0.009	0.086	3	21	1	21
3	279	217	3.70E-05	0.13	40	0.185	0.034	0.313	12	77	4	19
4	290	224	4.09E-05	0.14	70	0.301	0.057	0.503	21	129	7	18
5	294	227	4.15E-05	0.14	100	0.410	0.078	0.681	28	177	10	18
6	298	230	4.35E-05	0.15	130	0.518	0.100	0.853	37	225	13	17
7	299	230	4.45E-05	0.15	150	0.590	0.114	0.969	43	256	15	17
8	300	231	4.41E-05	0.15	180	0.700	0.136	1.144	50	303	18	17
9	300	231	4.33E-05	0.14	225	0.868	0.170	1.411	61	374	22.5	17

The close agreement in these results is expected given the essentially identical trends in cladding fluence as calculated by MCODEv1 and MCODEv2 for these two types of models, as discussed in section 2.2.4. Therefore, the cladding performance under irradiation of the TID fuel is approximately the same as that for the demonstration core.

## 9.6. Chapter 9 Summary

Neutronic analyses of the advanced core confirm the basic feasibility of sustaining B&B mode operation with UC fuel. The TID fuel design enables high heavy metal loading in the core, and by slightly increasing the core size (from 350 to 400 cm equivalent diameter) and burnup (from 150 MWD/kg<sub>HM</sub> to 165 MWD/kg<sub>HM</sub>) relative to the demonstration core, essentially the same reactivity history can be achieved.

Control rod assemblies were investigated as a means to control excess reactivity for the advanced core. These assemblies are sufficient to suppress the reactivity swing over the cycle and they are not detrimental to the long term neutron economy. However, as there are only 37 CRAs, the threat of rod ejection poses a serious concern. The advanced core is nearly self-regulating according to the Quasi-Static analysis, but would require redesigning the control scheme to a more distributed technique. An area for future work on this concept will involve the exploration of interassembly control, similar in many ways to Boiling Water Reactor control blades.



Lastly, the cladding damage from irradiation was assessed. While the slightly higher discharge burnup results in a proportionally higher DPA (~400), the overall cladding performance is practically the same as for the demonstration core.

Aside from the control scheme, which may warrant future investigation, the advanced core design is taken for more in depth thermal hydraulic analysis as is. As the system pressure may be increased before reaching the void limit, two cases were examined with the thermal hydraulic model to establish an envelope for the available design space set by the various materials and neutronic limits as discussed in much greater detail in Chapter 10.



## Chapter 10. Advanced Core Thermal Hydraulics

### 10.1. Introduction

This chapter discusses the thermal hydraulic performance of the advanced core. The base case for the advanced core is for a thermal power of 2400 MW and a primary system pressure of 11.5 MPa. The pressure was selected as to meet the helium velocity requirements based on preliminary scoping analyses. The performance of the base case final design is described in section 10.2.

Neutronic calculations, however, confirm that the base case advanced core has a coolant void reactivity worth less than 0.65\$. Therefore, a second case was analyzed as well. In the second case, the primary system pressure was increased to 17 MPa. At this pressure, it is predicted that the coolant void reactivity worth would be less than but nearly 1\$. For the higher pressure case, the thermal power could be increased to 3400 MW before breaching any of the limits on temperature or velocity, as discussed in section 10.3.

### 10.2. The 2400 MW Base Case

The thermal hydraulic performance of the reactor core was analyzed using essentially the same methodology as for the demonstration core. The input parameters into the finite volume model (FVM) are shown in Table 10-1. Again, only the final iteration is shown, where the core thermal power is adjusted until reaching a performance limit, in this case the limit of 120 m/sec for the helium outlet velocity. For the given configuration, the limiting thermal power is 2400 MW<sub>th</sub>.

Table 10-1 Advanced Core FVM Input Parameters

Core/Global Parameters	Symbol	Formula
Coolant Channel Locations per Assembly	n	91
Coolant Channels per Assembly	n'	91
Core Height	L	200 cm
Axial Reflector Length	R	25 cm
Assembly Flat-to-Flat Length	FTF	14.8 cm
Channel Pitch	p	1.45 cm
Channel Inner Diameter	D <sub>c,i</sub>	0.80 cm
Channel Outer Diameter	D <sub>c,o</sub>	0.88 cm
Number of Assemblies	N	576
Equivalent Core Temperature Rise	$\Delta T_{eq}$	218 °C (= 385/1.77)
Operating Pressure	P <sub>op</sub>	11.5 MPa
Thermal Power	P <sub>th</sub>	2400 MW
Axial Power Peaking Factor	APPF	1.44
Radial Power Peaking Factor	RPPF	1.77 <sup>23</sup>
Spacer Drag Coefficient	K <sub>sp</sub>	0.6
Primary Circulator Inlet Temperature	T <sub>i</sub>	176 °C

<sup>23</sup> Assumed the same as for the demonstration core based on similar fuel assembly neutronic calculations and fuel shuffling sequence.

The coolant, cladding, and fuel temperature profiles are shown for the hot and average channels in Figure 10.1 and Figure 10.2 respectively. As the average channel is orificed, the temperature rise across both of these channels is the same, and the film temperature difference increases with the local power density.

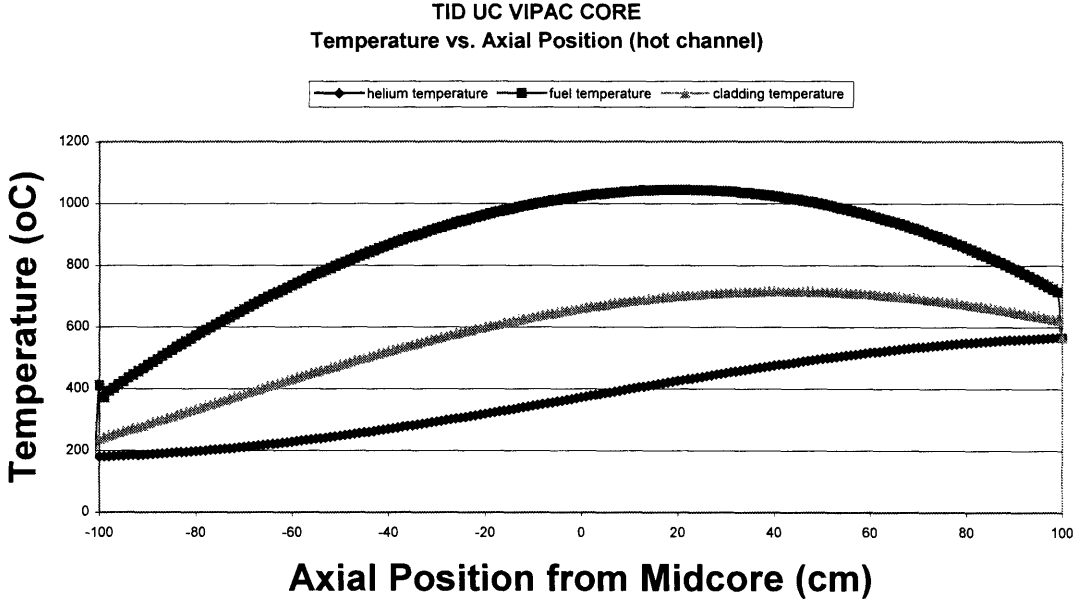


Figure 10.1 Advanced Core Hot Channel Temperature Profile

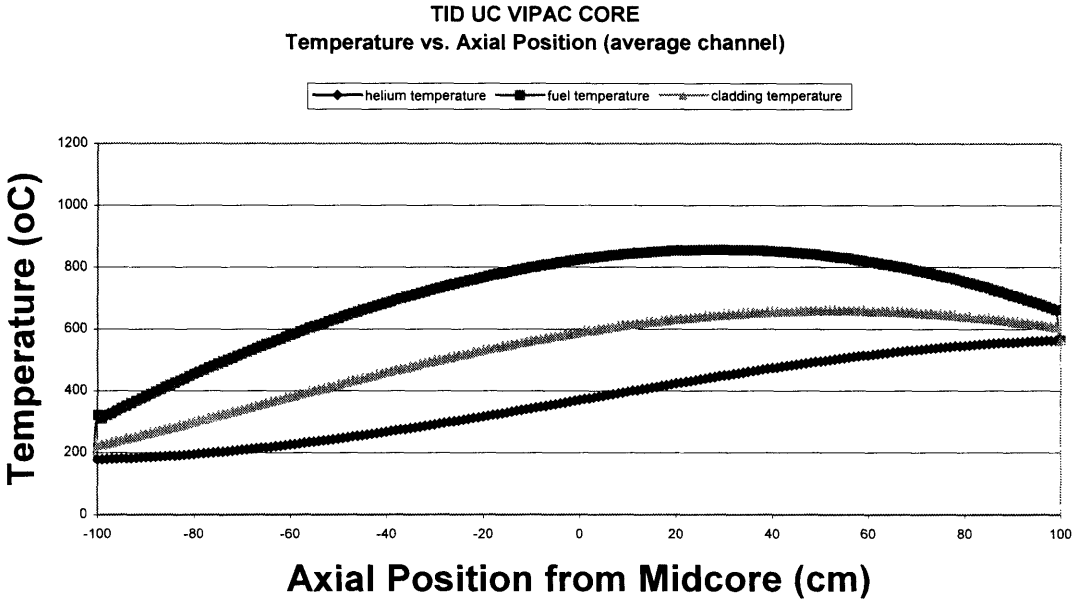


Figure 10.2 Advanced Core Average Channel (orificed) Temperature Profile

The peak cladding temperature is 716 °C, which is within the 750 °C limit, and the outlet velocity is 127 m/sec. The helium velocity is somewhat above the 120 m/sec limit, but judged appropriate given the small difference and that the model does not take credit for bypass flow in the interassembly area. Table 10-2 summarizes the output of the FVM.

Table 10-2 Advanced Core FVM Output

Hot Channel Calculation Result	Value	Units
Average Linear Heat Rate	405.22	W/cm
Peak Linear Heat Rate	568.90	W/cm
Mass Flow Rate per Channel	40.47	g/sec/pin
Core Mass Flow Rate	2121.23	kg/sec
Core Pressure Drop	290.82	kPa
Primary Circulator Power	51.13	MW
Circulator Power with Ideal Orificing	28.89	MW
Form Pressure Drop Fraction	0.18	
Average Film Temperature Drop	204	°C
Peak Clad Temperature	715.93	°C
Average Clad Temperature	577.30	°C
Peak Fuel Temperature	1044	°C
Average Fuel Temperature	861	°C
Average Helium Density	8.75	kg/m <sup>3</sup>
Average Heat Transfer Coefficient	0.94	W/cm <sup>2</sup> -°C
Helium Outlet Velocity	126.69	m/sec
Helium Average Velocity	96.12	m/sec

While the temperatures are somewhat higher for the advanced core than the demonstration core for the cladding and coolant, the reduced coolant mass flow rate leads to a reduced primary circulator power and hence a net power conversion efficiency of 39.3%. The reactor power is reduced somewhat (from 2900 MW<sub>th</sub> to 2400 MW<sub>th</sub>) relative to the demonstration core, however the basic feasibility of the design has been verified by modeling the thermal hydraulic performance and neutronic performance of the advanced core concept.

### 10.3. The 3400 MW High Pressure & High Power Case

A second variant of the advanced core was studied. This variant is based on a significantly higher primary system pressure. As was discussed in Chapter 8, the primary system pressure was selected as to meet the helium velocity and cladding temperature limits for a 2400 MW design. However, subsequent reactor physics analyses show that for this case the coolant void reactivity worth is < 0.65\$. As the coolant inventory is much smaller compared with the demonstration core, this result is not unexpected.

Since the coolant void reactivity worth is lower than \$1, the primary system pressure could be increased until reaching the void limit. Though no neutronic analyses have been conducted to confirm this, it is expected that the primary pressure could be increased by a factor of 100/65 or to 17.7 MPa, and still not breach the void worth limit. This should remain an area for future work should interest in the B&B GFR persist.

However, thermal hydraulic calculations were done assuming that the primary system pressure was 17 MPa. At this pressure, the reactor thermal power was increased in the FVM until either

the helium velocity or peak cladding temperature limits were reached. This occurred for both limits simultaneously at 3400 MW. At this power level the net electric power generation is 1340 MWe.

Table 10-3 summarizes the input parameters for the high pressure, high power variant of the advanced core design.

Table 10-3 High Pressure & Power Advanced Core FVM Input Parameters

Core/Global Parameters	Symbol	Formula
Coolant Channel Locations per Assembly	n	91
Coolant Channels per Assembly	n'	91
Core Height	L	200 cm
Axial Reflector Length	R	25 cm
Assembly Flat-to-Flat Length	FTF	14.8 cm
Channel Pitch	p	1.45 cm
Channel Inner Diameter	$D_{c,i}$	0.80 cm
Channel Outer Diameter	$D_{c,o}$	0.88 cm
Number of Assemblies	N	576
Equivalent Core Temperature Rise	$\Delta T_{eq}$	218 °C (= 385/1.77)
Operating Pressure	$P_{op}$	17.0 MPa
Thermal Power	$P_{th}$	3400 MW
Axial Power Peaking Factor	APPF	1.44
Radial Power Peaking Factor	RPPF	1.77
Spacer Drag Coefficient	$K_{sp}$	0.6
Primary Circulator Inlet Temperature	$T_i$	176 °C

In the high pressure, high power variant, the peak clad temperature (as shown in Table 10-4) is 747 °C (essentially the 750 °C limit) and the helium outlet velocity is 121 m/sec (essentially the 120 m/sec limit) and the expected EOEC coolant void reactivity worth is less than but nearly \$1. This would then represent the optimized advanced core design.

Table 10-4 High Pressure & Power Advanced Core FVM Output

Hot Channel Calculation Result	Value	Units
Average Linear Heat Rate	574.06	W/cm
Peak Linear Heat Rate	805.94	W/cm
Mass Flow Rate per Channel	57.33	g/sec/pin
Core Mass Flow Rate	3005.07	kg/sec
Core Pressure Drop	376.83	kPa
Primary Circulator Power	63.42	MW
Circulator Power with Ideal Orificing	35.83	MW
Form Pressure Drop Fraction	0.19	
Average Film Temperature Drop	231	°C
Peak Clad Temperature	747.27	°C
Average Clad Temperature	603.60	°C
Peak Fuel Temperature	1188	°C
Average Fuel Temperature	974	°C
Average Helium Density	12.96	kg/m <sup>3</sup>
Average Heat Transfer Coefficient	1.24	W/cm <sup>2</sup> -°C
Helium Outlet Velocity	120.94	m/sec
Helium Average Velocity	91.89	m/sec

An area of future work remains for this second advanced core variant in the neutronic evaluation. However, it is expected that the neutronic performance will not differ significantly from the 2400 MW base case. If this design change were accepted the fuel cycle length would be reduced from 4.7 EFPY to a more economical 3.3 EFPY.

#### 10.4. Chapter 10 Summary

Thermal hydraulic analysis of the 2400 MW advanced core confirms that the cladding temperature and helium velocity limits are met. However, by reducing the thermal power from 2900 MW in the demonstration core to 2400 MW in the advanced core, while simultaneously increasing the heavy metal loading relative to the demonstration core, the cycle length for the advanced core is substantially longer (4.7 EFPY for the advanced core, 2.5 EFPY for the demonstration core).

Upon examining the neutronic behavior of the advanced core, it was noted that the coolant void reactivity worth is only ~0.65\$ at the BOEC and ~0.55\$ at the EOEC. If the coolant void reactivity worth is assumed to be proportional to the primary system pressure, then the pressure could likely be increased to 17 MPa or higher without compromising the 1\$ coolant void reactivity worth limit. At 17 MPa primary system pressure, the reactor thermal power could be increased to 3400 MW from 2400 MW without exceeding the cladding temperature or helium velocity limits, and thus allow for a more economically attractive fuel cycle.

The 3400 MW case represents the optimized design where every limit is reached simultaneously. The base case and the 3400 MW case illustrate that there is a substantial open design space for the advanced GFR core. The 2400 MW and 3400 MW cases were both analyzed using the FVM to demonstrate the technical feasibility of either design as well as to establish the envelope of the

design space. These two cases were both examined in terms of their economic performance relative to a LWR fuel cycle in the following chapter.



# Chapter 11. Advanced Core Fuel Cycle Economics

## 11.1. Introduction

The fuel cycle costs associated with the advanced B&B GFR were evaluated relative to the fuel cycle costs for a conventional LWR. The investigation of the demonstration core economics revealed that substantial economic benefits could be attained if one eliminates the need for highly enriched nitrogen. This chapter discusses the advanced core fuel cycle economics, which eliminates the requirement for highly enriched nitrogen. Both the 2400 MW base case and 3400 MW case were examined: the former to establish a likely fuel cycle cost and the latter to establish the lowest achievable fuel cycle cost.

Sustainability is also addressed in this chapter. By increasing the fuel discharge burnup (to 165 MWD/kg<sub>HM</sub>) relative to a typical LWR (50 MWD/kg<sub>HM</sub>) and increasing the power conversion efficiency from 33% to 40%, the requirements for uranium ore per unit of electricity generated is substantially lower for the advanced core than for a LWR.

## 11.2. Cost of Generation

In the advanced core the power density is reduced, thus resulting in a longer fuel residency time, which translates directly into higher carrying charges over the cycle. While substantial savings are still realizable, the results summarized in Table 11-1 indicate that back end fuel cycle alternatives are not likely to be economically worthwhile given the very long time horizon between fresh fuel purchase and discharge.

Table 11-1 Advanced B&B GFR Fuel Cycle Cost Assessment

Input Variables	Units	Symbol	LWR Reference Value	Advanced B&B GFR OTTO	Advanced B&B GFR AIROX
Discharge Burnup	MWD/kg <sub>HM</sub>	B <sub>d</sub>	50	165	165
Net Efficiency	%	η	33	40	40
Cycle Length	EFPY	T	1.5	4.7	4.7
Number of Batches		n	2.68	6	6
Capacity Factor		CF	0.9	0.9	0.9
Enrichment	w/o	x <sub>p</sub>	4.5	5	5
Fuel Cycle Cost	mills/kWhre		6.72	5.11	5.07

The analyses indicate that even in the once-through mode the advanced core, having no need for highly enriched nitrogen, does offer a real economic benefit compared with the LWR fuel cycle (both in equilibrium mode). For the advanced core, AIROX treatment of the equilibrium cycle spent fuel for reuse in the GFR is not recommended as it offers only a slight economic advantage and significantly increases the complexity of an otherwise simple and economically competitive fuel cycle.

While the equilibrium cycle fuel costs are very attractive compared with that of a typical PWR, the fuel cycle costs associated with the startup core will be significantly higher than for the equilibrium cycle. The startup core has batches enriched to as high as 10 a/o <sup>235</sup>U in U that are irradiated for fewer than six cycles. Therefore, the levelized costs associated with the first five batches were calculated. They are calculated for the base case of 2400 MW and for the high

power variant (3400 MW) briefly discussed in section 10.3. These calculations assume reuse of the spent GFR fuel to create LWR fuel reloads, and the results are summarized in Table 11-2.

Table 11-2 Startup Fuel Cycle Costs With LWR Reuse

Startup Core Batch	Thermal Power [ MWth ]	Average Burnup [ MWD/kgHM ]	Enrichment at BOL [ a/o ]	Fuel Costs with AIROX/PWR Reuse [ mills/kWhre ]
<b>Base Case (2400 MW)</b>				
1 <sup>st</sup> discharged batch	2400	27	10	20
2 <sup>nd</sup> discharged batch	2400	54	10	13
3 <sup>rd</sup> discharged batch	2400	81	10	11
4 <sup>th</sup> discharged batch	2400	108	8	8.2
5 <sup>th</sup> discharged batch	2400	135	6	6.1
6 <sup>th</sup> discharge batch (EQ)	2400	150	5	5.0
Average for Startup Core				10.6
<b>High Power Case (3400 MW)</b>				
1 <sup>st</sup> discharged batch	3400	27	10	18
2 <sup>nd</sup> discharged batch	3400	54	10	11
3 <sup>rd</sup> discharged batch	3400	81	10	9.3
4 <sup>th</sup> discharged batch	3400	108	8	6.7
5 <sup>th</sup> discharged batch	3400	135	6	4.9
6 <sup>th</sup> discharged batch (EQ)	3400	150	5	4.0
Average for Startup Core				9.4

Table 11-2 shows several important features of the B&B GFR fuel cycle. First, the fuel cycle costs for the first batch are much higher than the equilibrium batches, however, the fuel cycle costs become competitive with a LWR after the 4<sup>th</sup> batch is discharged. AIROX and LWR recycle were investigated for these batches given their high levels of enrichment, however, direct recycle into the GFR should also be investigated. Direct recycle eliminates the need for fission product separation, as well as conversion of the fuel form from carbide to oxide. The fuel would, however, require refabrication or a process step to repair irradiation induced cladding damage.

The second result of the startup core fuel cycle cost comparison is that the high power core offers significant economic advantages compared to the base case. By increasing the system pressure and thermal power the high power core saves approximately 1 mill/kWhre.

### 11.3. Sustainability

The uranium ore requirements for a conventional LWR and the advanced B&B GFR are dramatically different. The mass of uranium mined to produce one MWDe of power is used as a measure of the relative sustainability of B&B GFR compared to today's LWRs. Using the reference LWR described in Table 11-1 and the equations described in section 2.4.1, the sustainability index can be calculated according to Equation (11.1).

$$S = \frac{M_{ore}}{M_{fab} B_d \eta} \quad (11.1)$$

Where S is the sustainability index,  
 $M_{ore}$  is the mass of natural uranium mined in kgU<sub>NAT</sub>,  
 $M_{fab}$  is the mass of heavy metal to be irradiated in kgU,  
 $B_d$  is the discharge burnup in MWD/kg<sub>HM</sub>, and  
 $\eta$  is the net efficiency of power conversion.

For a typical LWR, the sustainability index is 0.62 kgU<sub>NAT</sub>/MWD<sub>e</sub>. For the advanced core operating in OTTO mode, the sustainability index is 0.17 kgU<sub>NAT</sub>/MWD<sub>e</sub>. The B&B GFR reduces the need for natural uranium by a factor greater than 3.5. The natural uranium demand could be further reduced by implementing AIROX treatment of the GFR spent fuel and reuse in a LWR. Reuse in the GFR itself would result in even greater savings.

#### 11.4. Chapter 11 Summary

The equilibrium cycle fuel cost for the advanced B&B GFR core is ~5.1 mills/kWhre. The high fuel costs for the startup batches warranted a reinvestigation of AIROX treatment and recycle into a PWR. It was found that even with AIROX and sale to a PWR that the fuel costs associated with the first few batches are significantly higher than for the equilibrium batch, and decrease as the initial enrichment decreases and discharge burnup increases, until finally approaching the equilibrium costs.

AIROX processing does not reduce the costs for the first few batches to a level near that for a PWR. Without AIROX treatment and subsequent sale of the spent GFR fuel to a PWR, the 1<sup>st</sup> discharged batch fuel cycle cost is ~22 mills/kWhre. Therefore, AIROX and resale to a PWR only saves ~2 mills/kWhre for the early batches. While the costs for refabrication or cladding annealing are uncertain, these approaches would allow for direct reuse in the GFR without any fuel reprocessing and should be investigated.

In once-through-then-out fuel cycle operation, the advanced B&B GFR core reduces the demand for natural uranium by a factor of 3.6 compared to a conventional light water reactor; generating 5.9 MWD<sub>e</sub>/kgU<sub>NAT</sub> compared to 1.6 MWD<sub>e</sub>/kgU<sub>NAT</sub> for a typical LWR. The advanced core simultaneously meets the GenIV goals of improved fuel cycle economics as well as improved sustainability – all without any need for spent fuel reprocessing, thus preserving the proliferation resistance inherent in the OTTO fuel cycle.



## Chapter 12. Summary and Conclusions

### 12.1. Overview

A Breed and Burn Gas-cooled Fast Reactor (B&B GFR) was designed to have a once-through fuel cycle. B&B refers to the equilibrium operation of a reactor where low enriched uranium (5 a/o) reload assemblies are required, yet in-situ plutonium breeding sustains discharge burnup on the order of 150 MWD/kg<sub>HM</sub> without the need for spent fuel reprocessing. Two reactor concepts were developed and evaluated against the Generation IV International Forum (GIF) goals of improved sustainability, economics, safety, and proliferation resistance. The first concept, or “demonstration” concept, is based on uranium nitride pin-type fuel in a tight pitch hexagonal lattice (~50 v/o fuel). The nitrogen is enriched to greater than 99% in the isotope <sup>15</sup>N. The 2900 MW<sub>th</sub> demonstration core uses vibrationally compacted (VIPAC) U<sup>15</sup>N fuel clad in MA 956 oxide dispersion strengthened stainless steel (ODS). The core is 200 cm in active height, and 350 cm in equivalent diameter. Coupled thermal hydraulic and neutronic analysis confirmed the feasibility of the B&B demonstration core, however, there were strong economic motivations to employ uranium carbide fuel. In the second, or “advanced,” concept an innovative tube-in-duct vented fuel assembly was designed to enable B&B operation with UC fuel. The fuel volume fraction was increased to ~60 v/o, the discharge burnup was slightly increased to 165 MWD/kg<sub>HM</sub>, and the core diameter was increased to 400 cm. Both concepts build on extensive experience from previous gas cooled reactor designs and employ steam Rankine power conversion systems. Modeling of the B&B GFR confirmed its semi-passive safe operation under a host of postulated accident scenarios, as well as the economic advantages to B&B mode operation.

### 12.2. Introduction

Breed and Burn refers to a once-through-then-out fuel cycle where low enriched uranium fuel is irradiated until reaching a burnup of approximately 150 MWD/kg<sub>HM</sub> without the need for any spent fuel reprocessing, recycle, or reuse. B&B is not a new concept. B&B was first mentioned in 1958 by Feinberg [23], studied in 1970 by Fischer, et al. [24] with collaborators at MIT [39], [3], and a lead cooled alloy version has been recently explored by Toshinsky, et al. in the 1990s [64]. Though research has been conducted that indicates that B&B may be possible with natural uranium, such proposed fuel cycles are complicated and require extremely long residency times and complex fuel shuffling sequences. Ryu and Sekimoto have recently described a pebble bed approach with online refueling, yet still requiring extra-long fuel residency times [56].

The current NERI funded research has focused on the design of a Gas-cooled Fast Reactor (GFR) operating in a Breed and Burn (B&B) fuel cycle mode. The B&B fuel cycle meets the GenIV goals of sustainability, economics, and proliferation resistance by increasing fuel burnup without the need for spent fuel reprocessing, recycle, or reuse of any kind.

The neutronic requirements for B&B are strict and require an ultra-hard neutron spectrum. Therefore, the GFR is ideally suited for this fuel cycle. In the present work the B&B GFR concept evolved into two practical reactor designs, both of which build on extensive previous gas-cooled reactor design experience.

The first version is the “demonstration” concept using highly neutronically reactive U<sup>15</sup>N fuel in a hexagonal pin fuel array that is nearly 50 v/o fuel. The core is helium cooled, with an outlet temperature of 570 °C. The helium primary circuit is coupled to a steam Rankine power conversion system essentially identical to that for the British Advanced Gas-cooled Reactors.

One advantage of the low coolant temperature compared to other GenIV GFR concepts is that it allows for the use of oxide dispersion strengthened stainless steels (ODS) in core. The fuel is manufactured using advanced vibration compaction techniques, clad in ODS, and vented in order to achieve the high burnup goal.

The second version, the “advanced” concept, builds on the experience of the demonstration concept to develop a B&B GFR without the need for expensive  $U^{15}N$  fuel. In order to substitute the nitride fuel with carbide, significantly higher heavy metal loadings are required (60 v/o fuel for UC versus 50 v/o fuel for  $U^{15}N$ ) which are not practically achievable with a conventional pin fuel array. Therefore, an innovative tube-in-duct assembly design was proposed to achieve B&B operation with the less neutronically reactive carbide fuel. The advanced core offers significantly reduced natural uranium requirements and lower equilibrium fuel cycle costs (5 mills/kWhre) compared with conventional light water reactors (7 mills/kWhre), as the burnup is tripled for the same reload enrichment.

The B&B GFR designs, though requiring active decay heat removal, are semi-self-regulating from a reactivity feedback standpoint and are designed to withstand all plausible accident scenarios, including loss of flow, loss of heat sink, and transient overpower, all without scram. Reactor pressure vessel blowdown (LOCA) was investigated and while the B&B GFR has a low positive coolant void reactivity (less than 1\$), the added reactivity during blow down is compensated through other strong negative reactivity feedback mechanisms, thereby allowing for the safe operation of the B&B GFR.

### 12.3. Theory and Methods

In the B&B GFR fresh reload assemblies are enriched to 5%  $^{235}U$  in U. In a fast reactor, this type of fuel is subcritical, and during normal operation will require reactivity sharing with other assemblies in order to produce power. However, during operation in a very hard neutron spectrum, a significant quantity of the  $^{238}U$  transmutes to  $^{239}Pu$ . The plutonium in partially burnt assemblies is the source of excess reactivity to share with fresh assemblies. A wide range of fuel forms was examined to determine the fuel candidates with the highest B&B potential.

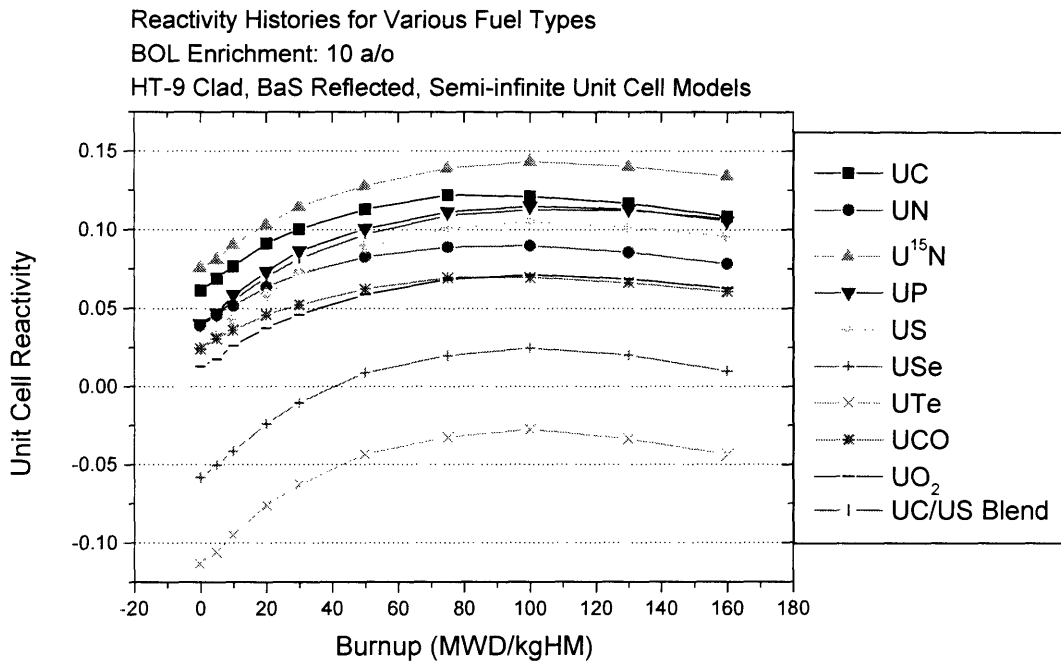


Figure 12.1 Comparison of Fuels' Reactivity History

MCODE, a MCNP-ORIGEN coupling program, was used to calculate the reactivity as a function of burnup for semi-infinite pin cell models. These models were used to compare a wide range of different fuel forms, many of which were proposed as part of the ANL Reduced Enrichment for Research and Test Reactors (RERTR) program [32]. The RERTR fuels are high heavy metal density fuels, and high heavy metal density is an indicator of good neutronic performance for a B&B reactor fuel. Figure 12.1 shows these histories for many ceramic fuels. The histories are roughly parallel indicating that most fuels will experience similar breeding gains and that the peak reactivity is the best metric for good neutronic performance. The buildup and then slow fall in reactivity during irradiation arises as fissile plutonium rapidly builds up to an asymptotic concentration and the fission product inventory is continuously increasing. U<sup>15</sup>N and UC were identified as the leading candidates for the B&B GFR.

By comparing the fuels at the beginning of irradiation it was found, as shown in Figure 12.2, that the reactivity is directly related to the heavy metal density of the fuel, and hence, that the reactivity of an assembly is inversely proportional to the fuel loading.

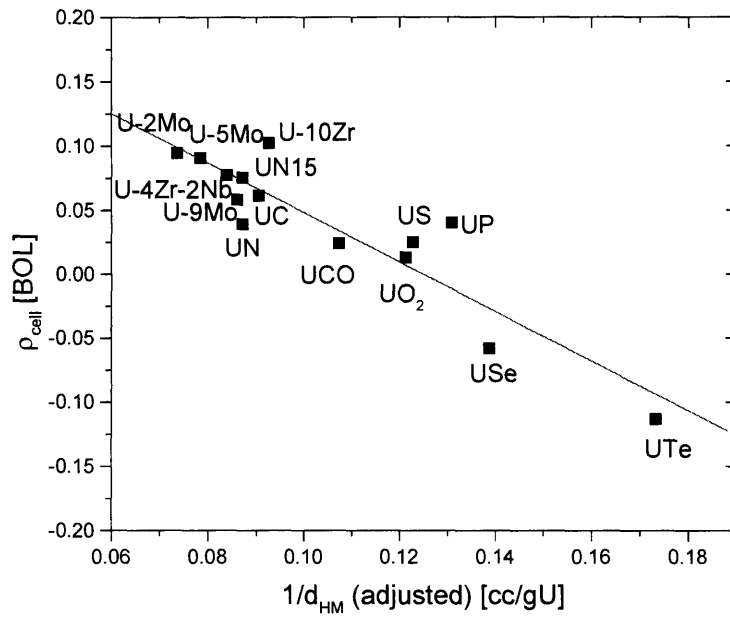


Figure 12.2 Relationship between Reactivity and Heavy Metal Density

Figure 12.3 shows the effects of fuel enrichment on the reactivity history using a UC test case. Since the enrichment at the BOC is only ~5% and the fuel reaches atomic burnup on the order of ~15%, the long-term, high burnup trends in reactivity will be dictated purely by the <sup>238</sup>U content and the spectrum. Also, while changing the enrichment from 5% to 10% may represent a 100% change in the <sup>235</sup>U content, it is only ~5% change in the <sup>238</sup>U content; in essence, the long-term trend in fuel reactivity will be nearly completely independent of the initial enrichment. This motivated the investigation of natural uranium fueled B&B concepts in the past.



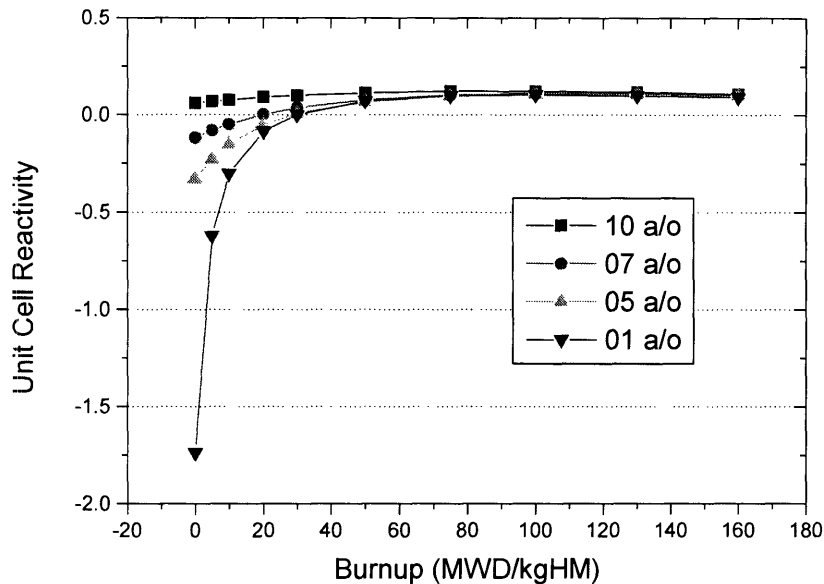


Figure 12.3 Impact of Enrichment on High Burnup Reactivity

However, because the reactivity increases during irradiation, the reactivity-limited burnup is the minimum burnup (as opposed to maximum in conventional reactors) that the fuel must attain to sustain criticality once it is discharged and replaced with subcritical fresh fuel. The integral of the reactivity is what determines the limitations on discharge burnup and fuel residency, and as such, the current work focuses on using enriched (5 a/o) uranium fuel in order to reduce the reactivity limited burnup to the design goal of  $\sim 150$  MWD/kg<sub>HM</sub> burnup at discharge.

Based on the fuel comparison, two design concepts were pursued. The demonstration concept focuses on the U<sup>15</sup>N fuel while the advanced concept focuses on the less expensive, less neutronically reactive UC fuel.

#### 12.4. Demonstration Core: Fuel and Core Design

There are four unique reactor physics aspects of the B&B GFR that dictate many features of the core design. First, the fresh assemblies are subcritical, and therefore, these assemblies depend on sharing reactivity with partially burnt assemblies. Second, because of clad endurance limits, the assemblies are discharged near the burnup where they attain peak reactivity, therefore, the other partially burnt assemblies, over any given cycle, must breed in sufficient excess reactivity to overcome the difference between the fresh and discharged assemblies. The second aspect means that the reactivity swing (increase) over any given cycle will be large compared with conventional reactors. Third, the reactivity limited burnup is the minimum burnup that fuel must reach to sustain core criticality, and the fourth is that the reactivity is proportional to the inverse of the heavy metal density, and hence the heavy metal loading in the fuel. Therefore, a B&B GFR that enables reactivity-limited burnup of a reasonable level (such as the goal of 150 MWD/kg<sub>HM</sub>) must utilize high heavy metal density fuels.

Vibration-compaction (VIPAC) fuel manufacturing was identified as a good approach, since the fuel must withstand high burnup, high fluence neutron irradiation. MA 956 ODS was selected as the cladding and structural material. ODS has an excellent blend of superior mechanical performance (based on its high melting temperature and creep resistance) and superior neutronic performance (given the low parasitic absorption cross section and very low helium production rates). Operating limits for the cladding peak temperatures under steady state and accident conditions (namely 750 °C and 1300 °C, respectively) were selected for the ODS based on its properties [34] and experience from the GA GCFR design process during the 1970s [25].

A tight-pitch hexagonal fuel pin array was designed to meet the neutronic requirements for the demonstration core, while meeting the steady state thermal hydraulic limits. With a primary system pressure of 10 MPa and a core thermal power of 2900 MW<sub>th</sub>, the peak cladding temperature is 640 °C in steady state, and the helium outlet velocity is 120 m/sec. Figure 12.4 shows a schematic of the demonstration core fuel assembly.

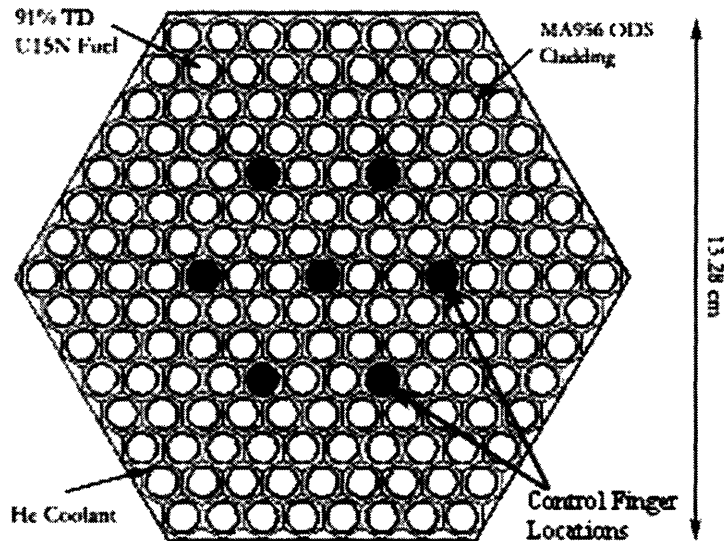


Figure 12.4 Demonstration Core Fuel Assembly

The fuel assemblies are designed so that each has seven control rod locations. These rods form a cluster of control fingers that constitute the reactivity control devices for the core. There are control insertions at both the top and bottom of the core to increase the system safety and reliability. The core design is summarized in Table 12-1. The core layout and batch shuffling sequence are shown in Figure 12.5.

Table 12-1 Demonstration Core Geometry

Fuel Form	U <sup>15</sup> N	
Fuel Pins per Assembly	162	
Pin Outer Diameter	0.82	cm
Clad Thickness	0.04	cm
Pin Pitch	1.00	cm
Assembly Flat-to-Flat	13.28	cm
Active Core Height	200	cm
Equivalent Core Diameter	350	cm
Fuel Volume Fraction	45.6	v/o
Structural Volume Fraction	12.8	v/o
Coolant Volume Fraction	41.6	v/o

The core model is 1/12<sup>th</sup> symmetric. The multi-batch reload sequence and control strategy was designed to optimize several competing goals. First, the scheme must promote reactivity sharing between partially burnt and fresh fuel assemblies in order to breed plutonium in low reactivity assemblies. Second, partially burnt assemblies are progressively moved towards the center of the core in order to sustain core criticality over multiple (six) cycles. Third, the power shape should remain fairly constant during irradiation to enable the use of fixed flow orificing to improve power conversion efficiency. Fourth, the radial power shape should be as flat as possible to maximize core power density. As a consequence of the current multi-batch reload scheme, the power history for the average assembly varies significantly between fuel reload and subsequent shuffling but is fairly constant during irradiation.

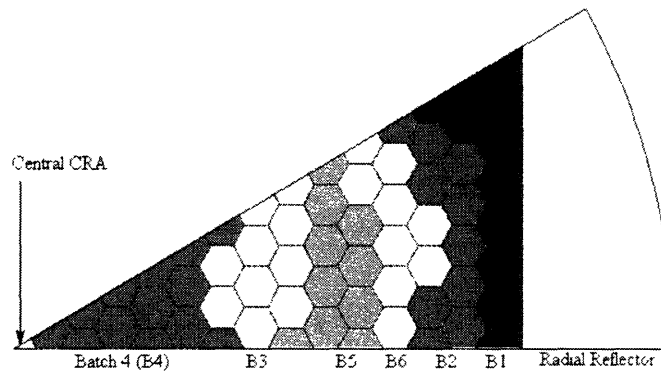


Figure 12.5 Demonstration Core Layout

In the current approach, the uncontrolled reactivity history for the core over multiple cycles is shown in Figure 12.6. The startup core is fueled with several batches ranging in enrichment from 5 to 10 a/o <sup>235</sup>U in U. The startup core loading and refueling sequence are summarized in Table 12-2.

Table 12-2 Startup Core and Fuel Shuffle Sequence

Cycle Loading (a/o <sup>235</sup> U in U)			
Batch	BOC1	BOC2	BOCn
1	5	5	5
2	6	from 1	from 1
3	8	from 2	from 2
4	10	from 3	from 3
5	10	from 4	from 4
6	10	from 5	from 5

For this startup core configuration, and multi-batch reload sequence, the uncontrolled reactivity is plotted in Figure 12.6. The key features of the plot are that by the 8<sup>th</sup> cycle the core has reached its equilibrium cycle and that at the beginning of the 3<sup>rd</sup> cycle the core is slightly subcritical (with an eigenvalue of 0.997(5)). While increasing the enrichment in the 2<sup>nd</sup> batch would certainly increase the reactivity at this stage in life, the current startup configuration is meant to rapidly advance the core model to its equilibrium cycle. Furthermore, this small discrepancy is within the margin of uncertainty arising from conservative model simplicity.

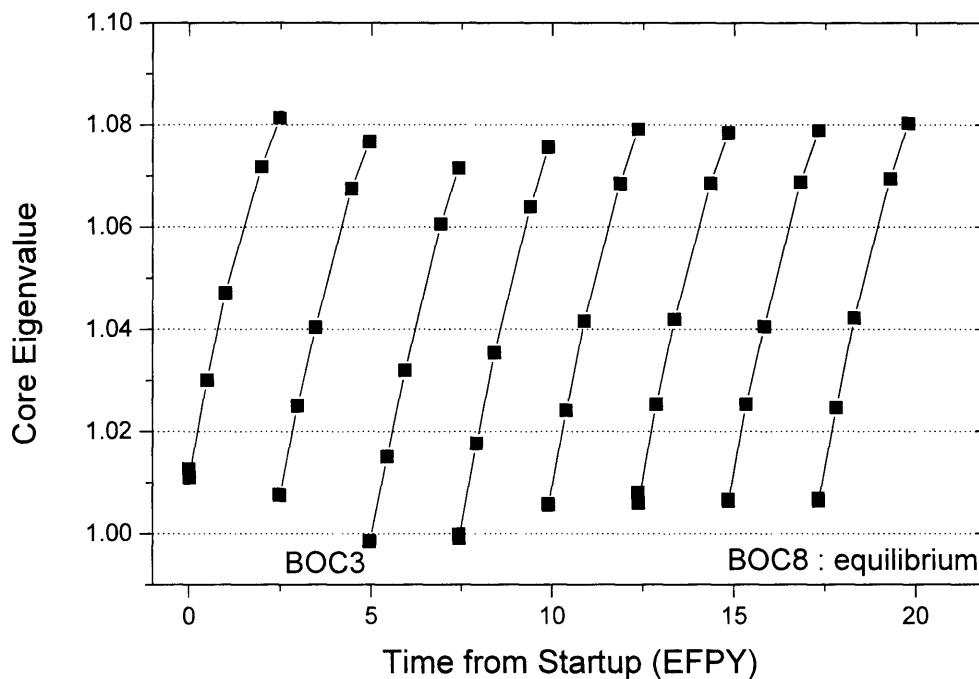


Figure 12.6 Demonstration Core Uncontrolled Reactivity History

#### 12.4.1. Safety

The Quasi-Static method, first developed for the design of the integral fast reactor (IFR) was used to evaluate the ability of the demonstration core to self-regulate during accident scenarios [66]. Specifically, loss of heat sink, loss of flow, and unexpected transient overpower (all without scram) were used to establish an envelope of accident conditions. Additionally, loss of primary pressure (LOCA) was considered. The Quasi-Static method uses the reactivity balance shown in Equation (12.1) to determine steady state core conditions after a perturbation.

$$0 = \Delta\rho_{ext} + \delta T_m C + \left(\frac{P}{F} - 1\right)B + (P - 1)A \quad (12.1)$$

Where  $\Delta\rho_{ext}$  is the change in reactivity from external sources (i.e. control rods),  
 $P$  is the normalized power (at nominal power  $P$  is unity),  
 $F$  is the normalized flow (at nominal flow rate  $F$  is unity), and  
 $\delta T_m$  is the change from nominal coolant inlet temperature.

The lumped reactivity feedback parameters are calculated based on individual reactivity feedback mechanisms as shown in Equation (12.2).

$$\begin{aligned} A &= (\alpha_D + \alpha_e)\Delta T_f \\ B &= (\alpha_D + \alpha_e + \alpha_{Co} + 2\alpha_{RD} + 2\alpha_R)\frac{\Delta T_c}{2} \\ C &= \alpha_D + \alpha_e + \alpha_{Co} + \alpha_R \end{aligned} \quad (12.2)$$

Where  $\Delta T_f$  is the difference in temperature between the fuel and coolant [K],  
 $\Delta T_c$  is the temperature rise across the core at steady state conditions [K],  
 $\alpha_D$  is the Doppler coefficient [ $\ell$ /K],  
 $\alpha_e$  is the fuel thermal expansion reactivity coefficient [ $\ell$ /K],  
 $\alpha_{Co}$  is the coolant temperature coefficient [ $\ell$ /K],  
 $\alpha_{RD}$  is the control rod drive line coefficient [ $\ell$ /K], and  
 $\alpha_R$  is the radial thermal expansion coefficient (core flowering) [ $\ell$ /K].

The steady state core conditions following the aforementioned accidents are related to the ratios of the lumped feedback parameters. Based on the limiting fuel temperatures and temperature data from a series of steady state thermal hydraulic evaluations, specific coefficient ratios were calculated and compared with their appropriate limits at various points in life. The results are tabulated in and the B&B GFR is compared to two metal cooled reactors (the Actinide Burner Reactor and the Integral Fast Reactor).

Table 12-3 Quasi-Static Analysis of the Demonstration Core

		Demo. B&B GFR			ABR[55]		IFR[66]
		BOL	BOEC	EOEC	BOL	EOL	AVG
A	cents	-19	-25	-24	-10	-8	-31
B	cents	-22	-23	-28	-22	-19	-35
C	cents/K	-0.10	-0.11	-0.12	-0.27	-0.23	-0.25
A/B		0.84	1.09	0.85	0.47	0.41	0.88
CΔTc/B		1.70	1.90	1.70	1.14	1.11	1.10
ΔρTOP/B		0.53	0.28	0.64	0.69	0	0
A/B limits		x < 1.14			< 1.25		< 1
CΔTc/B limits		x > 1			1 < x < 1.8		1 < x < 2
ΔρTOP/B limits		x < 1.14			< 1.25		< 1
β		0.00882	0.00623	0.00544	0.0024	0.0023	0.0035
αD	1e-3 c/K	-64	-91	-94	-55	-85	-120
αe	1e-3 c/K	-17	-18	-9	-60	0	-90
αCo	1e-3 c/K	1	1	2	30	40	180
αRD	1e-3 c/K	0	0	0	-10	0	0
αR	1e-3 c/K	-17	-6	-22	-180	-180	-220

While meeting the self-regulating criteria, the demonstration core requires active decay heat removal, and is therefore considered semi-passively self-regulating. Additionally, it is worth noting that the design of the B&B GFR is less constrained than metal cooled reactors in that the reactor can be designed with strong negative reactivity feedback parameters without the risk of coolant freezing. The control rod driveline thermal expansion is always a negative reactivity feedback mechanism because the reactor pressure vessel is insulated. Hence, it was neglected in the current analyses to add conservatism.

Coupled thermal hydraulic and neutronic calculations indicate that the coolant void reactivity worth is a maximum at the EOEC, and is approximately 1\$. Pressure vessel blowdown, however, will take anywhere from one to several minutes; thereby allowing time for other negative reactivity feedback to compensate. However, the transient nature of rapid blowdown will have to be investigated further to fully assure the B&B GFR safety.

#### 12.4.2. Economics

While the demonstration core offers much higher burnup for a similar level of enrichment compared to a conventional LWR, the uncertain, but likely high price for highly enriched nitrogen (HEN) motivated the evaluation of several fuel cycle options. Many of these options included possible end use options for the spent fuel. The base case is the once-through-then-out fuel cycle (OTTO), but AIROX treatment of the B&B GFR spent fuel, and subsequent reuse in a LWR was also considered. Additionally, recovery of the HEN in combination with either LWR reuse or direct GFR reuse was evaluated. The purpose of these calculations was to determine the breakeven price of HEN where the B&B GFR equilibrium fuel cycle costs would match those for today's LWRs.

Table 12-4 Demonstration Core Cost of Generation and Alternative Fuel Cycles

Input Variables	Units	Symbol	LWR Reference Value	Demo. B&B GFR OTTO	Demo. B&B GFR AIROX	AIROX with HEN Recovery	AIROX, HEN Recovery and Split
Discharge Burnup	MWD/kg <sub>HM</sub>	B <sub>d</sub>	50	150	150	150	150
Net Efficiency	%	η	33	40	40	40	40
Cycle Length	EFPY	T	1.5	2.5	2.5	2.5	2.5
Number of Batches		n	2.68	6	6	6	6
Capacity Factor		CF	0.9	0.9	0.9	0.9	0.9
Enrichment	w/o	x <sub>p</sub>	4.5	5	5	5	5
Fuel Cycle Cost	mills/kWhre		6.72	6.72	6.72	6.72	6.72
Required Price of HEN	USD/gHEN		N/A	30.26	31.55	35.83	38.22

Current price estimates for HEN range between 100 USD/g to 1000 USD/g [35,47]. However, these calculations show that the demonstration core would only be economical if the price of HEN were between 30 and 40 USD/g. The economic analysis clearly motivates examination of an advanced GFR concept that allows B&B mode operation without the requirement for HEN. Therefore, the UC fueled advanced concept was developed.

### 12.5. Advanced Core Fuel and Core Design

Since the reactivity is related to the heavy metal density, to substitute U<sup>15</sup>N with UC in the B&B GFR core, some design changes are necessary to compensate for the lower reactivity. The fuel assembly must have a much higher heavy metal loading to enable B&B operation. Additionally, the burnup is slightly increased (10%) to 165 MWD/kg<sub>HM</sub> and the core size is somewhat increased (350 cm to 400 cm equivalent diameter). The combination of these design changes and the innovative tube-in-duct concept allow for B&B mode operation with UC fuel.

The tube-in-duct concept effectively inverts a pin-type fuel assembly. In the tube-in-duct (TID) assembly coolant flows through channels that are surrounded by fuel, instead of coolant flowing in between separate fuel pins. The TID assembly schematic is shown in Figure 12.7.

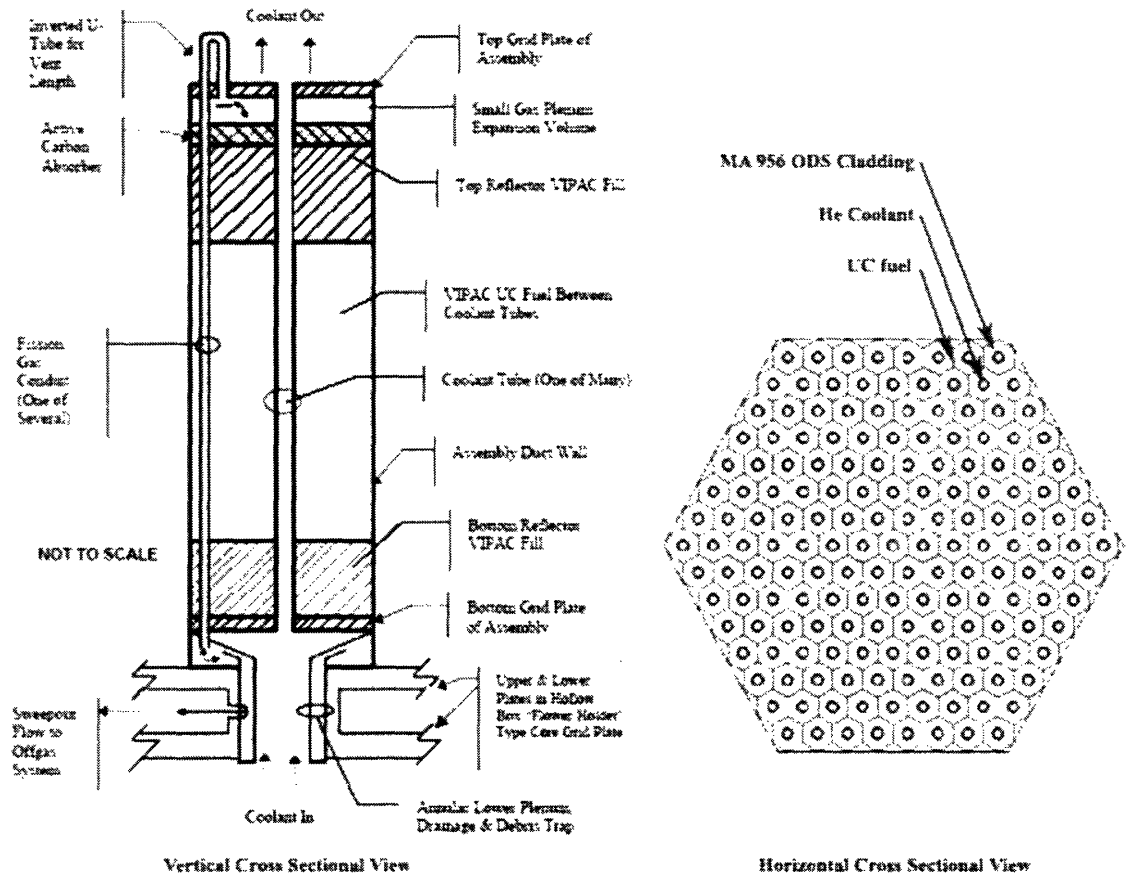


Figure 12.7 Tube-in-Duct Fuel Assembly Schematic

Using the TID assembly, coupled thermal hydraulic and neutronic calculations show that volume fractions of nearly 60 v/o and a primary system pressure of 11.5 MPa or greater are required to sustain B&B operation. Table 12-5 summarizes the geometry for the advanced core concept.

Table 12-5 Advanced Core Geometry

Fuel Form	UC	
Channels per Assembly	91	
Channel Diameter	0.80	cm
Clad Thickness	0.04	cm
Channel Pitch	1.45	cm
Assembly Flat-to-Flat	14.8	cm
Active Core Height	200	cm
Equivalent Core Diameter	396	cm
Fuel Volume Fraction	54.5	v/o
Structural Volume Fraction	18.0	v/o
Coolant Volume Fraction	27.5	v/o



The layout of the advanced core is essentially identical to that of the demonstration core except for one distinct difference. Six assemblies from each batch are removed to make room for control rod assembly locations. The reference design for the advanced core makes use of 74 control rod assemblies, 37 inserted from above the core and 37 from below. By removing these assemblies, the fuel volume fraction is approximately 55% instead of the 45% in the demonstration core.

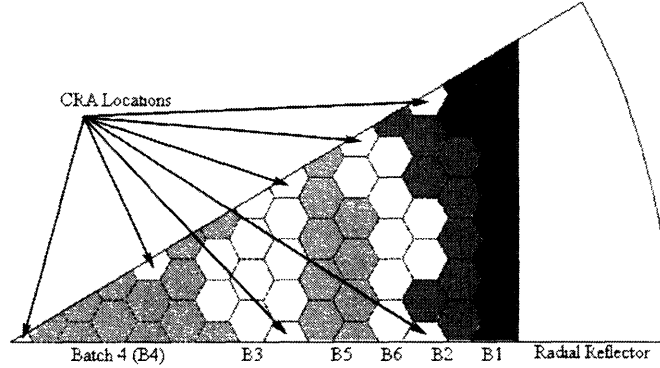


Figure 12.8 Advanced Core Layout

The reactivity history for the uncontrolled core is shown in Figure 12.9. The results essentially mirror those from the demonstration core, thus verifying that B&B mode operation can be achieved with a UC fueled GFR. However, the combination of a lower thermal power (2400 MW<sub>th</sub>), higher heavy metal loading, and slightly higher burnup results in a longer cycle length. The cycle length of the demonstration core is 2.5 EFPY and 4.7 EFPY for the advanced core.

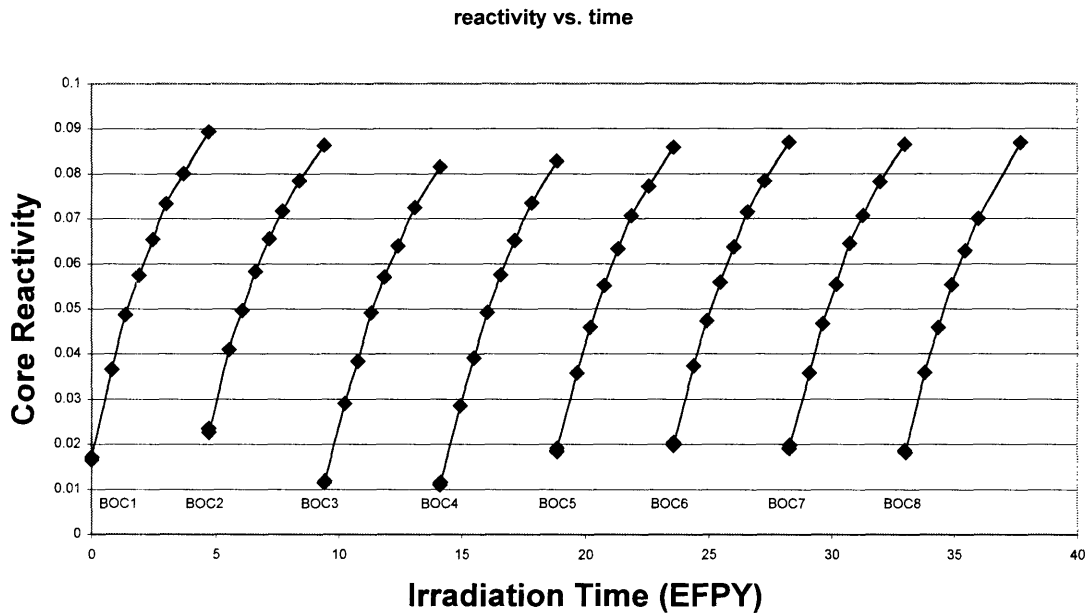


Figure 12.9 Advanced Core Uncontrolled Reactivity History

### 12.5.1. Safety

The Quasi-Static method was applied to the advanced core and it was found that control rod ejection at the EOEC posed a major risk to the safe operation of the advanced core. The design solution is to adopt a distributed interassembly control scheme. As the demonstration core control scheme mirrored that of a PWR, the advanced B&B GFR core would achieve self-regulation under all accident scenarios by adopting a BWR-like interassembly control approach. The CRA approach developed for the reference design concentrates the poison in a few high worth assemblies.

Table 12-6 Quasi-Static Analysis of the Advanced Core

		Adv. B&B GFR		
		BOL	BOEC	EOEC
A	cents	-35	-47	-40
B	cents	-36	-52	-50
C	cents/K	-0.17	-0.24	-0.22
A/B		0.99	0.90	0.79
CΔTc/B		1.82	1.75	1.66
ΔρTOP/B		0.40	0.17	4.34
A/B limits		x < 1		
CΔTc/B limits		x > 1		
ΔρTOP/B limits		x < 1		
β		0.00867	0.00638	0.00503
αD	1e-3 c/K	-110	-116	-98
αe	1e-3 c/K	-42	-53	-44
αCo	1e-3 c/K	0.5	0.8	0.8
αRD	1e-3 c/K	0	0	0
αR	1e-3 c/K	-16	-34	-45

The cladding temperature is slightly higher (715 °C), therefore the limits for LOHS and TOP are reduced from 1.14 in the demonstration core to 1 for the advanced core. Despite the large reactivity worth associated with control rod ejection at the EOEC (which could be corrected with a control rod design change) the advanced core has consistently stronger negative reactivity feedback than the demonstration core, mainly due to a slightly softer neutron spectrum and the design of the assembly itself. The advanced core also has a lower void reactivity worth (~0.6\$ versus ~0.9\$ in the demonstration core).

### 12.5.2. Economics

The advanced B&B GFR once-through-then-out fuel cycle was compared to a conventional LWR, and the results are summarized in Table 12-7. The advanced core, in equilibrium, offers significant economic benefits compared to conventional LWR. Furthermore, the combination of higher burnup and higher power conversion efficiency reduce the need for uranium ore by a factor of 3.5, thus improving the sustainability of the OTTO fuel cycle relative to a LWR.

Table 12-7 Advanced Core Cost of Generation

<b>Input Variables</b>	<b>Units</b>	<b>LWR Reference Value</b>	<b>Advanced B&amp;B GFR OTTO</b>
Discharge Burnup	MWD/kg <sub>HM</sub>	50	165
Net Efficiency	%	33	40
Cycle Length	EFPY	1.5	4.7
Number of Batches		2.68	6
Capacity Factor		0.9	0.9
Enrichment	w/o	4.5	5
Fuel Cycle Cost	mills/kWhre	6.72	5.11

## 12.6. Conclusions

The demonstration and advanced concepts illustrate the feasibility of designing a practical B&B GFR. The advanced concept builds on the experience developed in the demonstration core design and illustrates the benefits of B&B mode operation. Table 12-8 briefly summarizes some of the unique attributes of the B&B GFR concept described in the current work as well as key findings related to core design and fuel management.

The advanced B&B GFR meets the GIF goal for improved sustainability by reducing the uranium ore requirement by a factor of 3.5 relative to today's LWRs. By achieving much higher fuel burnup for approximately the same level of enrichment, the B&B GFR also meets the goal for enhanced fuel cycle economics.

The B&B GFR cores described in the present work were successfully designed to be semi-passive self-regulating systems, thus demonstrating that it is possible to design a B&B GFR system that will be safe and reliable. Lastly, the nature of the once-through-then-out fuel cycle makes the B&B GFR more proliferation resistant than conventional breeder reactors that typically require spent fuel reprocessing and separation of the transuranics.

In conclusion, the demonstration and advanced concepts prove that a B&B GFR system can be designed by building on an already extensive base of gas-cooled reactor experience and still achieve all of the goals set forth by the GIF.

Table 12-8 Summary of B&B GFR Core Attributes

Attribute	Manifestation	Ramification
Large , low leakage core needed	2400+ MWth rating results	Not suitable concept for small reactors
High heavy metal loading is required	High heavy metal density fuels (UC or U15N) are used	The fuels are not chemically compatible with CO <sub>2</sub> , motivating the use of chemically inert He
	High fuel volume fraction and low coolant volume fraction	Only moderate power densities can be achieved, and the fuel residency time is long
Fresh and partially burnt assemblies must share reactivity	A 6 batch fuel management scheme is adopted. At startup the average enrichment is 8% and reload assemblies are 5% enriched	Burnup of ~15 a/o (fuel endurance, not reactivity, limited)
		With LWR recycle, a burnup of ~19 a/o
		With direct GFR reuse (split option), a burnup of ~24 a/o
Large core temperature rise needed to reduce core pressure drop	Best coupled to a Rankine power conversion system	The primary circulator power is modest, enabling efficient use of a secondary PCS
		Water ingress from the PCS is a reactivity concern near the BOL
Long term breeding	Fuel achieves peak reactivity only shortly before discharge	Large core reactivity swing (increase) over a cycle
		Incentives motivate fuel refabrication and reuse in the GFR core
	At long irradiation, the axial fissile content distribution is uniform	Enrichment zoning cannot reduce axial power peaking over entire fuel residency
		High plutonium content at discharge, approximately 80% of which is <sup>239</sup> Pu
Very high fertile fission fraction due to hard spectrum	b is large because of <sup>238</sup> U delayed fission neutrons	Once-through spent fuel can be loaded into LWRs
		Separative reprocessing would raise proliferation issues
Direct fertile fission is necessary given the strict neutron economy	Void reactivity is limited to \$1	Spectrum hardening increases achievable reactivity, allowing poison control
Mechanically robust, and neutronically transparent cladding is preferred	MA 956 ODS Stainless Steel is the preferred cladding material	ODS may adequately reduce creep at temperatures ~750 oC
		ODS has no nickel, and therefore lower helium production than SS316
Fission products do not saturate	High concentration of <sup>149</sup> Sm at discharge	Multipass spent fuel cannot be recycled into LWRs
		Core flooding at EOC results in a negative reactivity insertion

## Chapter 13. Recommendations for Future Work

### 13.1. TID Fuel Assembly Fabrication, Systems, and Associated Costs

The innovative tube-in-duct fuel assembly is a necessary feature of the advanced B&B GFR core. The current work has focused on the physics, thermal hydraulics, and economics of the advanced core, however, given the scope of the research, little work was done on the mechanical design or manufacturing of the tube-in-duct fuel assembly, nor an integrated performance assessment of a conceptual fission gas collection system. Mechanical performance under stresses and irradiation, as well as system integration should be investigated further. In the current work, the fabrication costs associated with the tube-in-duct assembly were assumed the same as for LWR fuel.

The motivation behind the tube-in-duct assembly was to achieve B&B operation with a cheaper fuel form than  $U^{15}N$ , namely UC. While calculations indicate that there is significant cost savings for the equilibrium fuel cycle, future work must include the design of a fission gas collection system for the TID assembly. Fabrication costs of the tube-in-duct assembly and associated venting systems should be examined at greater length to verify the technical feasibility as well as the economic advantages of the advanced core relative to the demonstration core.

Furthermore, the associated plant systems for the tube-in-duct fuel assembly warrant further investigation. While extensive work was done on vented fuel pins during the design of the GA GCFR [25] and vented fuel pins were actually deployed at the Dounreay fast reactor [67], comprehensive analyses should be conducted to assess the transfer of this technology to the tube-in-duct configuration.

Vented fuel assemblies will likely be advantageous for any high-pressure, high-burnup GFR, whether operating in the B&B mode or not, unless block-type, self-supporting fuel assemblies (e.g. cermet, cermet, or metmet) can be developed.

### 13.2. Verifying Temperature, Irradiation, and Velocity Limits

In conducting the design of the B&B GFR core several limits were imposed on the cladding and coolant. In the case of the cladding temperature and irradiation limits were imposed. While these two limits are likely to be, and should be, coupled there is not enough experience with irradiation of ODS to verify the current limits. While creep, embrittlement, and loss of strength are key materials issues for any cladding material, experimental data would be required to fully understand the coupling between cladding temperature, irradiation, and mechanical performance of the ODS.

During irradiation the cladding may suffer from material creep arising from atomic displacement and embrittlement due to helium buildup from  $(n,\alpha)$  reactions. Calculations show that even at burnup as high as 150 MWD/kg<sub>HM</sub>, the helium concentration is roughly a factor of four lower than (1980s era) LMFBR cladding at the same burnup, therefore, creep and loss of strength will likely be the key materials issues affecting the endurance limits for the cladding material.

The fuel assemblies are vented and thus the cladding experiences a much lower pressure-induced stress compared to other fast reactors. At the same time however, the operating temperature between 600 and 750 °C may lead to a loss of strength during irradiation. The irradiation also creates atomic displacements. At higher temperatures the displacements may rapidly self anneal, thus there is a coupling between the temperature limit and the irradiation limit. As there is no clear indication how the strength of ODS, or the creep resistance of ODS will behave under long-

term hard spectrum neutron irradiation, future work should include rigorous modeling of cladding performance under irradiation at a variety of temperatures ranging between 600 °C and 750 °C, coupled with a relevant experimental program.

In addition, annealing at an even higher temperature should be studied to see if assembly lifetime could be extended, since the burnup is limited only by the materials endurance; and the fuel could sustain criticality for even longer duration (higher than 350 MWD/kg<sub>HM</sub>). If an annealing treatment can repair radiation induced damage in the cladding, then direct reuse of spent fuel into the GFR should be investigated. Direct reuse of the low burnup, first few discharged assemblies should be investigated because they have significantly higher fuel cycle costs than the equilibrium assemblies.

Research in this area should be pursued not merely for the B&B GFR, but to gain a better understanding of the true limits imposed by cladding endurance given the affects of both temperature and irradiation on overall mechanical performance.

Similarly, a maximum outlet velocity limit was imposed, ~120 m/sec, based on the GA GCFR design. The helium velocity affects mechanical performance of the fuel assemblies via two phenomena. The first is flow-induced vibrations. At high helium velocities, the fuel assemblies will rattle and thus lead to fretting and wear of the pins at spacer locations. The second mechanism is erosion. The high speed flow may lead to high rates of material erosion, and thus compromise the cladding performance. While both of these phenomena pose a real concern in the demonstration core, the primary concern for the tube-in-duct assembly is erosion. The design of the tube-in-duct assembly makes it relatively insensitive (i.e. stiff) in terms of vibrations. Therefore, more work should be done, particularly on the tube-in-duct fuel assembly to verify the limit on helium velocity.

### **13.3. 3400 MW Advanced Core Design**

Initial investigations were made into the possibility of uprating the advanced core thermal power to 3400 MW from the base case of 2400 MW. The base case primary circuit pressure is 11.5 MPa and the coolant void reactivity worth is approximately 0.65\$. The limit on coolant void reactivity worth is taken to be 1\$, therefore, it is likely that the primary system pressure (and hence thermal power) could be increased without breaching the void worth limit.

While thermal hydraulic calculations and fuel cycle economic calculations indicate that this uprated design would still meet the cladding temperature and helium velocity limits, while outperforming the base case economically, supporting neutronic calculations would have to be done to conclusively prove that the void reactivity worth remains below 1\$. Additionally, transient coupled neutronic and thermal hydraulic calculations should be done in order to establish a void reactivity worth limit.

In the current assessment, the self-regulating operation could only be achieved at full pressure. Secondly, calculations for reactor pressure vessel blowdown time indicate that several other negative reactivity feedback mechanisms may play a substantial role in counteracting the positive reactivity associated with coolant voiding. A more rigorous investigation into system performance may indicate that a 17 MPa primary pressure and associated void reactivity worth is not detrimental to the overall safety of the uprated system.

Such an analysis, however, is outside the scope of the current work, which is to develop a practical reactor system to verify the B&B concept. An uprated power design will ultimately

hinge on better establishing the operational limits for the core in terms of temperature, irradiation, void worth, and velocity.

### **13.4. Advanced Core Interassembly Control and Cooling**

Initial neutronic investigation of the advanced B&B GFR core indicated that in the event of a control assembly run out, the reactor would not be self-regulating according to the Quasi-Static method. This is contrary to experience in the design of the demonstration core. The demonstration core uses distributed control clusters throughout the core in each fuel assembly, similar to a PWR. However, there was no clear means for implementing the same strategy for the advanced core. Therefore, the advanced core was designed with 37 control rod assembly locations and highly enriched boron carbide control TID assemblies. The ejection of the central control assembly at the EOEC poses a challenge.

As distributed control is one means of reducing the risk associated with control rod run out (as there are more control elements, each with a smaller worth, and less-coupled to one another), a similar approach might be adopted for the advanced core. The only area in-core available for distributed control is the area between adjacent fuel assemblies. While the distributed control scheme for the demonstration core mimicked that for a PWR, the advanced core distributed control scheme would be more similar to that of a boiling water reactor in that it would require inserting control blades (e.g. Y shaped blades) in the interassembly spaces.

While only conceptual, future investigation of this concept is warranted as it has the potential to significantly improve the safety of the advanced core by enabling self-regulation, and semi-passive operation. The term semi-passive is used because active decay heat removal is still a necessity for both the demonstration and advanced cores.

Adopting this control scheme, however, will involve a significant degree of coupled thermal hydraulic and neutronic analysis. While no credit was taken for interassembly cooling in the current work, and an interassembly spacing of 6 mm was assumed, by including control elements in this area the heat transfer through the duct walls will be significantly different from the base case analyzed here.

Future work should examine the possibility of optimizing the interassembly spacing to maximize the benefits from flow in the interassembly area, while still enabling the use of control elements between the assemblies. Distributed control elements, particularly dual entry assemblies, increase redundancy and mitigate reactivity transients due to the failure of a single drive; however, future work should focus on an optimization of the control strategy which takes into account additional technical and economic factors associated with including a large number of control rod drives in the final design.

### **13.5. SiC as a Cladding Material**

The current B&B GFR concepts focus on stainless steel cladding and a Rankine Steam plant power conversion system. Therefore, the B&B GFR operates at core outlet temperatures on the order of 600 °C. By using different cladding materials the B&B GFR core could be upgraded to higher temperatures, which may facilitate direct Brayton power conversion or even hydrogen production, either of which requires significantly higher core outlet temperatures.

In order to meet the goal for higher core outlet temperatures, SiC should be investigated as a potential cladding material. Some preliminary neutronic studies indicate that MA956 ODS and SiC have similar physics characteristics during irradiation at the same volume fraction. A 10 a/o

UC fueled pin cell model was used to investigate the difference in reactivity histories between a pin clad with ODS and SiC. While Figure 13.1 shows that ODS achieves a higher peak reactivity, SiC has a higher reactivity at the BOL, and the overall performance is similar. However, these studies were carried out with the same clad thickness (0.55 mm). This may be possible in a vented TID assembly, since the cladding is under very little pressure-induced stress, but a detailed assessment is required.

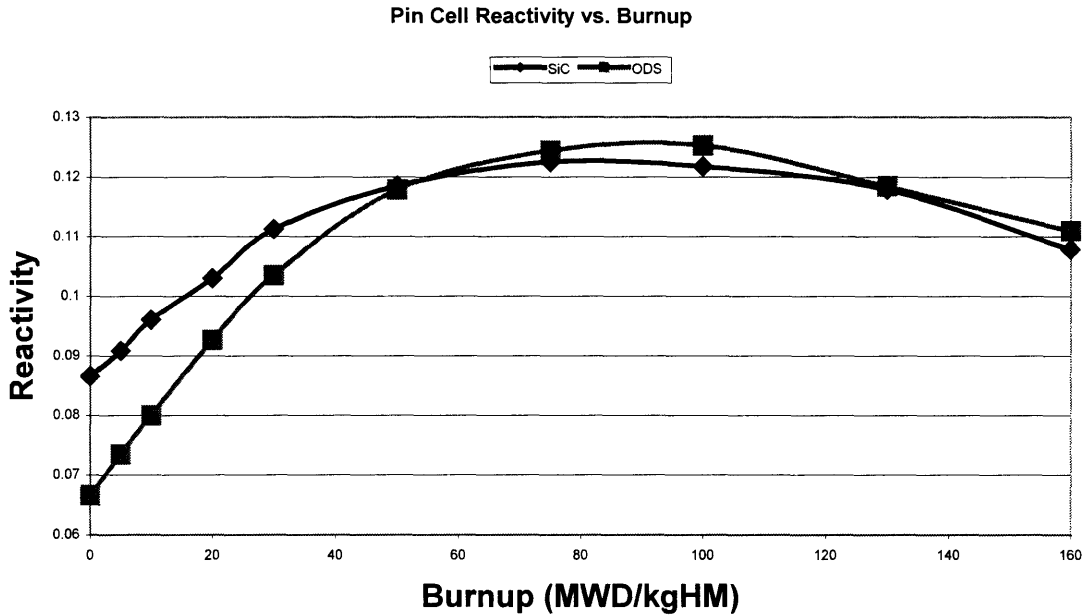


Figure 13.1 ODS and SiC Cladding Comparison

At the present time one must assume that if SiC is to be a viable cladding material, it is likely that the cladding thickness may have to be larger than for stainless steels. Hence, a second comparison was made between ODS and SiC where the SiC density is doubled to simulate the effect of a doubly thick cladding. Cases were run for both 5 a/o and 10 a/o BOL enrichments for UC fuel.



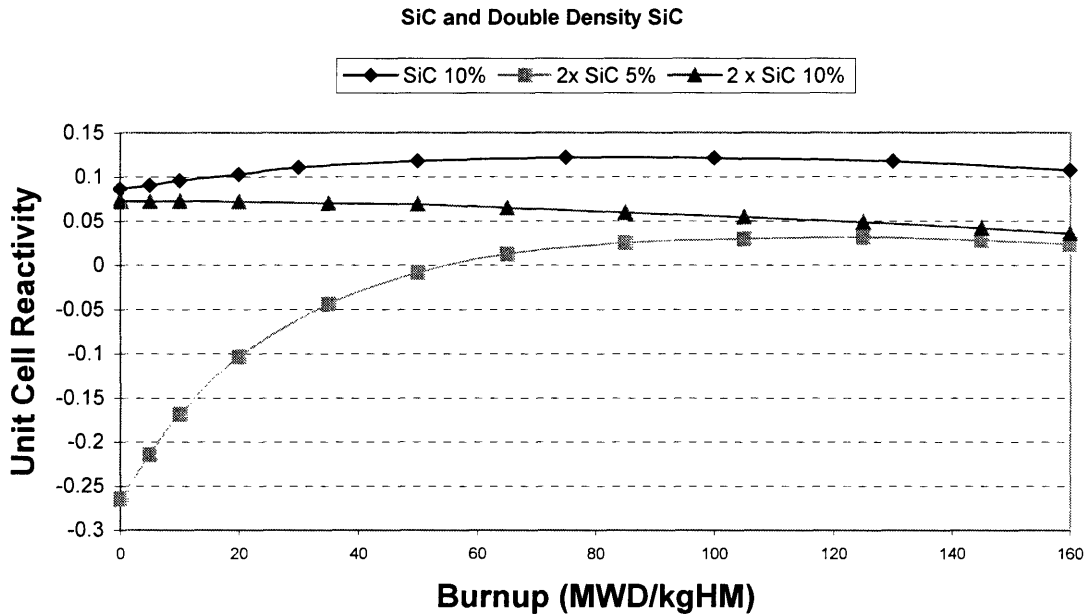


Figure 13.2 SiC at Double Thickness Reactivity History

Figure 13.2 shows three reactivity histories. The uppermost history is the same shown in Figure 13.1 for SiC at its normal density. The two histories below the uppermost are for SiC at double its normal density. The middle curve is for the 10 a/o enrichment history and the lower curve is for the 5 a/o enrichment history. As expected, during irradiation the two histories begin to converge as they approach their asymptotic plutonium concentration, however, at the BOL, the 10 a/o enriched, double density SiC case has very nearly the same reactivity as that for the normal density, but then declines monotonically during irradiation – unlike the normal density case. This reversal in the irradiation trend is most likely due to spectrum softening that results, ultimately, in lower achievable peak reactivity. The metric of neutron economy ( $Y$ ) was calculated for the 10 a/o enriched cases, first for the SiC at nominal density, and the SiC at double density as shown in Table 13-1.

Table 13-1 SiC Effect on Neutron Economy

	SiC Normal Density	SiC Double Density		Difference
Burnup	5 MWD/kgHM	5 MWD/kgHM		
$\sigma_f$ 49 (11)	1.7621	1.9070	b	8.2%
$\sigma_\gamma$ 49 (11)	0.4688	0.6380	b	36.1%
$\sigma_a$ 49 (11)	2.2309	2.5450	b	14.1%
$\sigma_f$ 28 (11)	0.0474	0.0462	b	-2.6%
$\sigma_\gamma$ 28 (11)	0.2565	0.2820	b	10.0%
$\sigma_a$ 28 (11)	0.3039	0.3282	b	8.0%
CR	0.9222	0.9389		1.8%
$k_{eff}$	1.0999	1.0781		-2.0%
N49	0.0002	0.0002	#/b-cm	
N28	0.0236	0.0237	#/b-cm	
$\sigma_f/\sigma_a$ 49	0.79	0.75		-5.1%
$\sigma_f/\sigma_a$ 28	0.16	0.14		-9.8%
$\nu$ average	2.56	2.53		
1/Y	4.836	5.692		17.7%
Y	0.21	0.18		-15.0%

Increasing the SiC content in the core significantly impacts the neutron economy. Therefore, while SiC is an attractive cladding alternative for other GFRs at present, its applicability for application in the B&B GFR will depend on achieving sufficient strength and fission product retention with SiC at comparable thicknesses to stainless steel alternatives (e.g. 0.4 – 0.6 mm)

### 13.6. Improved VIPAC Conductivity Models

VIPAC carbide and nitride fuels were examined in the current work. The conductivities for these materials were estimated based on experience with VIPAC oxide fuel. The treatment to estimate the VIPAC conductivity is mostly conjectural at the current stage, but deemed acceptable given the relatively low temperature of operation. Though the fuel temperature is not a limitation for the current B&B GFR designs, high temperature variations of the B&B concept will require a more rigorous and thorough approach for estimating the conductivity of irradiated UC or UN VIPAC fuel. Additionally, a better treatment for the cladding-fuel contact resistance should be implemented in more future validation of the B&B GFR concept.

### 13.7. Increase Power Density by Power Shaping

There are several design optimizations that could be investigated in order to allow for increased power density. Radial power shaping would be the most promising option, as there is no clear axial power shaping solution that does not involve reducing fuel loading. In terms of radial power shaping, however, different fuel shuffling sequences could be investigated to promote reactivity sharing and power flattening by adopting a scheme that arranges partially burnt assemblies in a more uniform distribution throughout the central region of the core, akin to a checker board reload pattern common in LWRs.

# Appendices

## Preamble

A large portion of the Appendices is devoted to essential MCNP4c input decks. The purpose of these Appendix entries is to enable the easy replication of results present in this thesis. Refer to the MCNP4c Manual for format and identity of all entries in the MCNP input decks described in the appendices (reference [40]). For a better understanding of CASMO-4 input files refer to the CASMO-4 primer (reference [69]).

## List of Appendices

Appendix A	Homogenous ZPR-9 Quarter Assembly Model MCNP input .....	200
Appendix B	Heterogeneous ZPR-9 Quarter Assembly Model MCNP input .....	205
Appendix C	Irradiation Damage Tube-in-Duct Pin Cell Model.....	210
Appendix D	CASMO-4 Sample Input Deck for a Mixed PWR Assembly .....	216
Appendix E	B&B GFR Demonstration Core Final Design MCNP Input File.....	218
Appendix F	Demonstration Core MCODEv1 Input File.....	237
Appendix G	Advanced B&B GFR MCNP Model and MCODEv2 Input .....	238



```

78 78 78 78 78 78 78 78 78 78 78 78 51 51 51 51 78 78 78 78 78 78 78
78 78 78 78 78 78 78 78 78 78 78 78 51 51 51 51 78 78 78 78 78 78 78
78 78 78 78 78 78 78 78 78 78 51 51 51 51 51 78 78 78 78 78 78 78 78
78 78 78 78 78 78 78 78 51 51 51 51 51 78 78 78 78 78 78 78 78 78 78
51 51 51 51 51 51 51 51 51 51 78 78 78 78 78 78 78 78 78 78 78 78 78
51 51 51 51 51 51 51 51 51 78 78 78 78 78 78 78 78 78 78 78 78 78 78
51 51 51 51 51 78 78 78 78 78 78 78 78 78 78 78 78 78 78 78 78 78 78
78 78 78 78 78 78 78 78 78 78 78 78 78 78 78 78 78 78 78 78 78 78 78
78 78 78 78 78 78 78 78 78 78 78 78 78 78 78 78 78 78 78 78 78 78 78
130 13 -1.168e-3 -2 imp:n=1 lat=1 u=79 fill=0:22 0:22 0:0 $Core
11 11 11 11 11 11 11 11 11 21 21 21 31 41 41 41 41 41 51 51 51 79 79
11 11 11 11 11 11 11 11 11 22 22 22 31 41 41 41 41 41 51 51 51 79 79
11 11 11 11 11 11 11 11 11 23 23 23 31 41 41 41 41 41 51 51 51 79 79
11 11 11 11 11 11 11 11 11 21 21 21 31 41 41 41 41 41 51 51 51 79 79
11 11 11 11 11 11 11 11 22 22 22 31 31 41 41 41 41 41 51 51 51 79 79
11 11 11 11 11 11 11 23 23 23 23 31 41 41 41 41 41 41 51 51 51 79 79
11 11 11 11 11 21 21 21 21 31 31 41 41 41 41 41 41 41 51 51 51 79 79
11 11 11 11 11 23 21 21 22 22 31 41 41 41 41 41 41 41 51 51 51 79 79
11 11 11 11 22 23 21 22 23 31 31 41 41 41 41 41 41 51 51 51 79 79 79
21 22 23 21 22 23 21 22 31 41 41 41 41 41 41 41 51 51 51 79 79 79 79
21 22 23 21 22 23 31 31 31 41 41 41 41 41 41 41 51 51 51 79 79 79 79
21 22 23 21 31 31 31 41 41 41 41 41 41 41 51 51 51 79 79 79 79 79
31 31 31 31 31 41 41 41 41 41 41 41 41 51 51 51 79 79 79 79 79 79 79
41 41 41 41 41 41 41 41 41 41 41 41 41 51 51 51 79 79 79 79 79 79 79
41 41 41 41 41 41 41 41 41 41 41 41 51 51 51 79 79 79 79 79 79 79 79
41 41 41 41 41 41 41 41 41 41 41 51 51 51 79 79 79 79 79 79 79 79 79
41 41 41 41 41 41 41 41 41 51 51 51 51 79 79 79 79 79 79 79 79 79 79
41 41 41 41 41 41 51 51 51 51 51 79 79 79 79 79 79 79 79 79 79 79 79
51 51 51 51 51 51 51 51 51 51 79 79 79 79 79 79 79 79 79 79 79 79 79
51 51 51 51 51 51 51 51 79 79 79 79 79 79 79 79 79 79 79 79 79 79 79
51 51 51 51 51 51 79 79 79 79 79 79 79 79 79 79 79 79 79 79 79 79 79
79 79 79 79 79 79 79 79 79 79 79 79 79 79 79 79 79 79 79 79 79 79 79
79 79 79 79 79 79 79 79 79 79 79 79 79 79 79 79 79 79 79 79 79 79 79
1005 0 -35 +501 +502 fill=77 imp:n=1 $axial reflector
1004 0 -34 +501 +502 fill=78 imp:n=1 $axial blanket
1001 0 -31 +501 +502 fill=79 imp:n=1 $core
1002 0 -32 +501 +502 fill=78 imp:n=1 $axial blanket
1003 0 -33 +501 +502 fill=77 imp:n=1 $axial reflector
9999 0 (31 32 33 34 35):-501:-502 imp:n=0 $void
c
c end cell specification

c surface specification
c
1 rpp -0.15875 0.15875 -2.54 2.54 -1000 +1000
2 rpp -2.38125 2.69875 -2.54 2.54 -1000 +1000
31 rpp 0 114.300 0 114.300 -61.04 +61.04
32 rpp 0 114.300 0 114.300 61.04 91.52
33 rpp 0 114.300 0 114.300 91.52 107.32
34 rpp 0 114.300 0 114.300 -91.52 -61.04
35 rpp 0 114.300 0 114.300 -107.32 -91.52
*501 px 1e-5
*502 py 1e-5
c
c end surface specification

c material specification
m13 08016.50c 0.30
07014.50c 0.70
m11 26000.50c 13.2544 $Fe
28000.50c 1.2056 $Ni
24000.50c 2.6337 $Cr
25055.50c 0.2107 $Mn
08016.50c 14.8674 $O

```

	42000.50c	0.2258	\$Mo
	92235.60c	0.0126	\$U235
	92238.60c	5.8098	\$U238
	94238.60c	0.0006	\$Pu238
	94239.60c	0.8842	\$Pu239
	94240.60c	0.1171	\$Pu240
	94241.60c	0.0130	\$Pu241
	94242.60c	0.0019	\$Pu242
	95241.60c	0.0052	\$Am241
m12	26000.50c	8.3648	\$Fe
	28000.50c	1.0667	\$Ni
	24000.50c	2.3563	\$Cr
	25055.50c	0.1870	\$Mn
	08016.50c	15.6918	\$O
	92235.60c	0.0175	\$U235
	92238.60c	8.1763	\$U238
m21	26000.50c	15.3744	\$Fe
	28000.50c	1.3240	\$Ni
	24000.50c	2.8669	\$Cr
	25055.50c	0.2291	\$Mn
	08016.50c	13.8596	\$O
	42000.50c	0.3022	\$Mo
	92235.60c	0.0122	\$U235
	92238.60c	5.5423	\$U238
	94238.60c	0.0007	\$Pu238
	94239.60c	1.1832	\$Pu239
	94240.60c	0.1569	\$Pu240
	94241.60c	0.0163	\$Pu241
	94242.60c	0.0024	\$Pu242
	95241.60c	0.0094	\$Am241
m22	26000.50c	15.3744	\$Fe
	28000.50c	1.3240	\$Ni
	24000.50c	2.8669	\$Cr
	25055.50c	0.2291	\$Mn
	08016.50c	13.8596	\$O
	42000.50c	0.3022	\$Mo
	92235.60c	0.0122	\$U235
	92238.60c	5.5423	\$U238
	94238.60c	0.0007	\$Pu238
	94239.60c	1.1832	\$Pu239
	94240.60c	0.1569	\$Pu240
	94241.60c	0.0163	\$Pu241
	94242.60c	0.0024	\$Pu242
	95241.60c	0.0094	\$Am241
m23	26000.50c	15.3744	\$Fe
	28000.50c	1.3240	\$Ni
	24000.50c	2.8669	\$Cr
	25055.50c	0.2291	\$Mn
	08016.50c	13.8596	\$O
	42000.50c	0.3022	\$Mo
	92235.60c	0.0122	\$U235
	92238.60c	5.5423	\$U238
	94238.60c	0.0007	\$Pu238
	94239.60c	1.1832	\$Pu239
	94240.60c	0.1569	\$Pu240
	94241.60c	0.0163	\$Pu241
	94242.60c	0.0024	\$Pu242
	95241.60c	0.0094	\$Am241
m24	26000.50c	8.8520	\$Fe
	28000.50c	1.1384	\$Ni
	24000.50c	2.4963	\$Cr
	25055.50c	0.1975	\$Mn
	08016.50c	15.8164	\$O
	92235.60c	0.0176	\$U235

```

m25      92238.60c  8.2170 $U238
         26000.50c  8.8520 $Fe
         28000.50c  1.1384 $Ni
         24000.50c  2.4963 $Cr
         25055.50c  0.1975 $Mn
         08016.50c 15.8164 $O
         92235.60c  0.0176 $U235
m26      92238.60c  8.2170 $U238
         26000.50c  8.8520 $Fe
         28000.50c  1.1384 $Ni
         24000.50c  2.4963 $Cr
         25055.50c  0.1975 $Mn
         08016.50c 15.8164 $O
         92235.60c  0.0176 $U235
m31      92238.60c  8.2170 $U238
         26000.50c 18.9341 $Fe
         28000.50c  1.4606 $Ni
         24000.50c  3.1381 $Cr
         25055.50c  0.2515 $Mn
         08016.50c 11.8173 $O
         42000.50c  0.4521 $Mo
         92235.60c  0.0111 $U235
         92238.60c  4.9782 $U238
         94238.60c  0.0008 $Pu238
         94239.60c  1.7718 $Pu239
         94240.60c  0.2351 $Pu240
         94241.60c  0.0227 $Pu241
         94242.60c  0.0032 $Pu242
         95241.60c  0.0178 $Am241
m32      26000.50c  9.0957 $Fe
         28000.50c  1.1743 $Ni
         24000.50c  2.5663 $Cr
         25055.50c  0.2027 $Mn
         08016.50c 15.7200 $O
         92235.60c  0.0175 $U235
         92238.60c  8.1763 $U238
m41      26000.50c  8.6832 $Fe
         28000.50c  1.1136 $Ni
         24000.50c  2.4478 $Cr
         25055.50c  0.1938 $Mn
         08016.50c 18.5944 $O
         92235.60c  0.0198 $U235
         92238.60c  9.2582 $U238
m51      26000.50c 55.3173 $Fe
         28000.50c  6.9735 $Ni
         24000.50c 15.6724 $Cr
         25055.50c  1.5646 $Mn
         08016.50c  1.9709 $O
c end material specification
ksrc    0.001 0.001 0.001
mode    n
kcode   20000 1.0 50 150
prcnp   150 150 150
print
f114:n  101 111 201 202 203 211 212 213 301 311 401 501 601
e114:n  1.000E-11 6.220E-10 6.874E-10 7.597E-10 8.396E-10 9.279E-10
        1.026E-09 1.133E-09 1.253E-09 1.384E-09 1.530E-09 1.691E-09
        1.869E-09 2.065E-09 2.282E-09 2.522E-09 2.788E-09 3.081E-09
        3.405E-09 3.763E-09 4.159E-09 4.596E-09 5.079E-09 5.614E-09
        6.204E-09 6.856E-09 7.578E-09 8.374E-09 9.255E-09 1.023E-08
        1.130E-08 1.249E-08 1.381E-08 1.526E-08 1.686E-08 1.864E-08
        2.060E-08 2.276E-08 2.516E-08 2.780E-08 3.073E-08 3.396E-08
        3.753E-08 4.148E-08 4.584E-08 5.066E-08 5.599E-08 6.188E-08
        6.839E-08 7.558E-08 8.353E-08 9.231E-08 1.020E-07 1.128E-07

```

1.246E-07 1.377E-07 1.522E-07 1.682E-07 1.859E-07 2.054E-07  
2.271E-07 2.509E-07 2.773E-07 3.065E-07 3.387E-07 3.743E-07  
4.137E-07 4.572E-07 5.053E-07 5.585E-07 6.172E-07 6.821E-07  
7.538E-07 8.331E-07 9.207E-07 1.018E-06 1.125E-06 1.243E-06  
1.374E-06 1.518E-06 1.678E-06 1.854E-06 2.049E-06 2.265E-06  
2.503E-06 2.766E-06 3.057E-06 3.378E-06 3.734E-06 4.126E-06  
4.560E-06 5.040E-06 5.570E-06 6.156E-06 6.803E-06 7.519E-06  
8.310E-06 9.184E-06 1.015E-05 1.122E-05 1.240E-05 1.370E-05  
1.514E-05 1.673E-05 1.849E-05 2.044E-05 2.259E-05 2.496E-05  
2.759E-05 3.049E-05 3.370E-05 3.724E-05 4.116E-05 4.549E-05  
5.027E-05 5.556E-05 6.140E-05 6.786E-05 7.500E-05 8.288E-05  
9.160E-05 1.012E-04 1.119E-04 1.236E-04 1.367E-04 1.510E-04  
1.669E-04 1.845E-04 2.039E-04 2.253E-04 2.490E-04 2.752E-04  
3.041E-04 3.361E-04 3.715E-04 4.105E-04 4.537E-04 5.014E-04  
5.541E-04 6.124E-04 6.768E-04 7.480E-04 8.267E-04 9.136E-04  
1.010E-03 1.116E-03 1.233E-03 1.363E-03 1.506E-03 1.665E-03  
1.840E-03 2.033E-03 2.247E-03 2.484E-03 2.745E-03 3.033E-03  
3.352E-03 3.705E-03 4.095E-03 4.525E-03 5.001E-03 5.527E-03  
6.108E-03 6.751E-03 7.461E-03 8.246E-03 9.113E-03 1.007E-02  
1.113E-02 1.230E-02 1.359E-02 1.502E-02 1.660E-02 1.835E-02  
2.028E-02 2.241E-02 2.477E-02 2.738E-02 3.026E-02 3.344E-02  
3.695E-02 4.084E-02 4.514E-02 4.988E-02 5.513E-02 6.093E-02  
6.733E-02 7.442E-02 8.224E-02 9.089E-02 1.005E-01 1.110E-01  
1.227E-01 1.356E-01 1.499E-01 1.656E-01 1.830E-01 2.023E-01  
2.236E-01 2.471E-01 2.731E-01 3.018E-01 3.335E-01 3.686E-01  
4.074E-01 4.502E-01 4.975E-01 5.499E-01 6.077E-01 6.716E-01  
7.422E-01 8.203E-01 9.066E-01 1.002E+00 1.107E+00 1.224E+00  
1.352E+00 1.495E+00 1.652E+00 1.826E+00 2.018E+00 2.230E+00  
2.464E+00 2.724E+00 3.010E+00 3.326E+00 3.676E+00 4.063E+00  
4.490E+00 4.963E+00 5.484E+00 6.061E+00 6.699E+00 7.403E+00  
8.182E+00 9.042E+00 1.000E+01 1.105E+01 1.221E+01 1.350E+01  
1.492E+01 1.649E+01 1.822E+01 2.000E+01



## Appendix B Heterogeneous ZPR-9 Quarter Assembly Model MCNP input

```

c MCNP Model of ZPR9 GCFR Critical Assembly
c
c
c Core is in 3 Zones
c 1 Radial Blanket
c 6 Axial Blankets
c 2 Axial Reflectors
c 1 Radial Reflector
c
c SST drawer / matrix ~ 0.1 cm thickness
c
c create stacks of 1/8" x 2" thick boxes
c     0.3175 cm x 5.08 cm thick
c
c cell specification
c
1  11  -7.73      -1  u=1 imp:n=1 tmp=0.258e-7 $U308 /
2  12  -13.8     -1  u=2 imp:n=1 tmp=0.258e-7 $Pu /
3  13  -1.168e-3 -1  u=3 imp:n=1 tmp=0.258e-7 $Void /
4  14  -4.9      -1  u=4 imp:n=1 tmp=0.258e-7 $Fe203 /
5  15  -7.7      -1  u=5 imp:n=1 tmp=0.258e-7 $$SST /
6  16  -18.1493  -1  u=6 imp:n=1 tmp=0.258e-7 $U238 /
7  17  -2.1828   -1  u=7 imp:n=1 tmp=0.258e-7 $B4C /
c
c
c
1001 0  -1  imp:n=1 lat=1 u=110 fill= -7:8 0:0 0:0 $Core 1 Fuel
      1 1 3 3 3 3 4 2 2 4 3 3 3 3 1 1
1011 0  -1  imp:n=1 lat=1 u=120 fill= -7:8 0:0 0:0 $Core 1 Axial Blanket 1
      1 1 3 3 3 3 1 1 1 6 3 3 3 3 1 1
1012 0  -1  imp:n=1 lat=1 u=130 fill= -7:8 0:0 0:0 $Core 1 Poison
      1 1 7 7 7 7 4 2 2 4 3 3 3 3 1 1
2001 0  -1  imp:n=1 lat=1 u=210 fill= -7:8 0:0 0:0 $Core 2 Fuel 1
      1 1 3 3 4 2 2 4 3 3 3 3 1 1 3 3
2002 0  -1  imp:n=1 lat=1 u=220 fill= -7:8 0:0 0:0 $Core 2 Fuel 2
      4 2 2 4 3 3 3 3 1 1 3 3 4 2 2 4
2003 0  -1  imp:n=1 lat=1 u=230 fill= -7:8 0:0 0:0 $Core 2 Fuel 3
      3 3 3 3 1 1 3 3 4 2 2 4 3 3 3 3
2011 0  -1  imp:n=1 lat=1 u=240 fill= -7:8 0:0 0:0 $Core 2 Axial Blanket 1
      1 1 3 3 1 1 1 6 3 3 3 3 1 1 3 3
2012 0  -1  imp:n=1 lat=1 u=250 fill= -7:8 0:0 0:0 $Core 2 Axial Blanket 2
      1 1 1 1 3 3 3 3 1 1 3 3 1 1 1 6
2013 0  -1  imp:n=1 lat=1 u=260 fill= -7:8 0:0 0:0 $Core 2 Axial Blanket 3
      3 3 3 3 1 1 3 3 1 1 1 6 3 3 3 3
3001 0  -1  imp:n=1 lat=1 u=310 fill= -7:8 0:0 0:0 $Core 3 Fuel 1
      3 3 4 2 2 4 3 3 3 3 4 2 2 4 3 3
3011 0  -1  imp:n=1 lat=1 u=320 fill= -7:8 0:0 0:0 $Core 3 Axial Blanket 1
      3 3 1 1 1 1 3 3 3 3 1 1 1 6 3 3
4001 0  -1  imp:n=1 lat=1 u=410 fill= -7:8 0:0 0:0 $Radial Blanket 1
      1 1 1 1 3 3 3 3 1 1 1 1 6 3 3 3
5001 0  -1  imp:n=1 lat=1 u=510 fill= -7:8 0:0 0:0 $Radial Reflector 1
      5 5 5 5 5 5 5 5 5 5 5 5 5 5 5 5
6001 0  -1  imp:n=1 lat=1 u=610 fill= -7:8 0:0 0:0 $Axial Reflector 1
      5 5 5 5 5 5 5 5 5 5 5 5 5 5 5 5
7777 0  -1  imp:n=1 lat=1 u=777 fill= -7:8 0:0 0:0 $Void
      3 3 3 3 3 3 3 3 3 3 3 3 3 3 3 3
101  15 .814987e-1  -11  imp:n=1 lat=1 u=11 fill=-1:1 -1:1 0:0
      610 610 610
      610 110 610
      610 610 610
111  15 .814987e-1  -11  imp:n=1 lat=1 u=12 fill=-1:1 -1:1 0:0
      610 610 610

```

```

610 120 610
610 610 610
112 15 .814987e-1 -11 imp:n=1 lat=1 u=13 fill=-1:1 -1:1 0:0
610 610 610
610 130 610
610 610 610
201 15 .814987e-1 -11 imp:n=1 lat=1 u=21 fill=-1:1 -1:1 0:0
610 610 610
610 210 610
610 610 610
202 15 .814987e-1 -11 imp:n=1 lat=1 u=22 fill=-1:1 -1:1 0:0
610 610 610
610 220 610
610 610 610
203 15 .814987e-1 -11 imp:n=1 lat=1 u=23 fill=-1:1 -1:1 0:0
610 610 610
610 230 610
610 610 610
211 15 .814987e-1 -11 imp:n=1 lat=1 u=24 fill=-1:1 -1:1 0:0
610 610 610
610 240 610
610 610 610
212 15 .814987e-1 -11 imp:n=1 lat=1 u=25 fill=-1:1 -1:1 0:0
610 610 610
610 250 610
610 610 610
213 15 .814987e-1 -11 imp:n=1 lat=1 u=26 fill=-1:1 -1:1 0:0
610 610 610
610 260 610
610 610 610
301 15 .814987e-1 -11 imp:n=1 lat=1 u=31 fill=-1:1 -1:1 0:0
610 610 610
610 310 610
610 610 610
311 15 .814987e-1 -11 imp:n=1 lat=1 u=32 fill=-1:1 -1:1 0:0
610 610 610
610 320 610
610 610 610
401 15 .814987e-1 -11 imp:n=1 lat=1 u=41 fill=-1:1 -1:1 0:0
610 610 610
610 410 610
610 610 610
501 15 .814987e-1 -11 imp:n=1 lat=1 u=51 fill=-1:1 -1:1 0:0
610 610 610
610 510 610
610 610 610
601 15 .814987e-1 -11 imp:n=1 lat=1 u=61 fill=-1:1 -1:1 0:0
610 610 610
610 610 610
610 610 610
701 13 -1.168e-3 -11 imp:n=1 lat=1 u=77 fill=-1:1 -1:1 0:0
610 610 610
610 777 610
610 610 610
110 15 .814987e-1 -2 imp:n=1 lat=1 u=76 fill=0:22 0:22 0:0 $Axial Reflector
61 61 61 61 61 61 61 61 61 61 61 61 77 77 77 77 77 77 77 77 77 77
61 61 61 61 61 61 61 61 61 61 61 61 77 77 77 77 77 77 77 77 77 77
61 61 61 61 61 61 61 61 61 61 61 61 77 77 77 77 77 77 77 77 77 77
61 61 61 61 61 61 61 61 61 61 61 61 77 77 77 77 77 77 77 77 77 77
61 61 61 61 61 61 61 61 61 61 61 61 77 77 77 77 77 77 77 77 77 77
61 61 61 61 61 61 61 61 61 61 61 61 77 77 77 77 77 77 77 77 77 77
61 61 61 61 61 61 61 61 61 61 61 61 77 77 77 77 77 77 77 77 77 77
61 61 61 61 61 61 61 61 61 61 61 61 77 77 77 77 77 77 77 77 77 77
61 61 61 61 61 61 61 61 61 61 61 61 77 77 77 77 77 77 77 77 77 77
61 61 61 61 61 61 61 61 61 61 61 61 77 77 77 77 77 77 77 77 77 77
61 61 61 61 61 61 61 61 61 61 61 61 77 77 77 77 77 77 77 77 77 77
61 61 61 61 61 61 61 61 61 61 61 61 77 77 77 77 77 77 77 77 77 77
61 61 61 61 61 61 61 61 61 61 61 61 77 77 77 77 77 77 77 77 77 77
61 61 61 61 61 61 61 61 61 61 61 61 77 77 77 77 77 77 77 77 77 77

```



```

11 11 11 11 11 11 11 11 11 11 22 22 22 31 41 41 41 41 41 51 51 51 77 77
11 11 11 11 11 11 11 11 11 11 23 23 23 31 41 41 41 41 41 51 51 51 77 77
11 11 11 11 11 11 11 11 11 21 21 21 31 41 41 41 41 41 51 51 51 77 77
11 11 77 11 11 11 11 11 22 22 22 31 31 41 41 41 41 41 51 51 51 77 77
11 11 11 11 11 11 11 23 23 23 31 41 41 41 41 41 41 51 51 51 77 77
11 11 11 11 11 11 22 23 21 21 31 31 41 41 41 41 41 41 51 51 77 77 77
11 11 11 11 11 23 23 21 22 22 31 41 41 41 41 41 41 51 51 51 77 77 77
11 11 11 11 22 23 21 22 23 31 31 41 41 41 41 41 41 51 51 51 77 77 77
21 22 23 21 22 23 21 22 31 41 41 41 41 41 41 51 51 51 77 77 77 77
21 22 23 21 22 23 31 31 31 41 41 41 41 41 41 51 51 51 77 77 77 77
21 22 23 21 31 31 41 41 41 41 41 41 41 41 51 51 51 77 77 77 77
31 31 31 31 31 41 41 41 41 41 41 41 41 51 51 51 77 77 77 77 77 77
41 41 41 41 41 41 41 41 41 41 41 41 41 51 51 51 51 77 77 77 77 77
41 41 41 41 41 41 41 41 41 41 41 41 51 51 51 51 77 77 77 77 77 77
41 41 41 41 41 41 41 41 41 41 41 51 51 51 51 77 77 77 77 77 77 77
41 41 41 41 41 41 41 41 41 51 51 51 51 51 77 77 77 77 77 77 77 77
41 41 41 41 41 41 51 51 51 51 51 77 77 77 77 77 77 77 77 77 77 77
51 51 51 51 51 51 51 51 51 51 51 77 77 77 77 77 77 77 77 77 77 77
51 51 51 51 51 51 51 51 77 77 77 77 77 77 77 77 77 77 77 77 77 77
51 51 51 51 51 77 77 77 77 77 77 77 77 77 77 77 77 77 77 77 77 77
77 77 77 77 77 77 77 77 77 77 77 77 77 77 77 77 77 77 77 77 77 77
77 77 77 77 77 77 77 77 77 77 77 77 77 77 77 77 77 77 77 77 77 77
7005 0 -35 +501 +502 fill=76 imp:n=1 $axial reflector
7004 0 -34 +501 +502 fill=78 imp:n=1 $axial blanket
7001 0 -31 +501 +502 fill=80 imp:n=1 $score bottom
7000 0 -30 +501 +502 fill=79 imp:n=1 $score top
7002 0 -32 +501 +502 fill=78 imp:n=1 $axial blanket
7003 0 -33 +501 +502 fill=76 imp:n=1 $axial reflector
9999 0 (31 32 33 34 35):-501:-502 imp:n=0 $void
c
c end cell specification

c surface specification
c
1 rpp -0.15875 0.15875 -2.54 2.54 -1000 +1000
11 rpp -2.28125 2.59875 -2.44 2.44 -1000 +1000
2 rpp -2.38125 2.69875 -2.54 2.54 -1000 +1000
30 rpp 0 114.300 0 114.300 -61.04 0
31 rpp 0 114.300 0 114.300 0 +61.04
32 rpp 0 114.300 0 114.300 61.04 91.52
33 rpp 0 114.300 0 114.300 91.52 107.32
34 rpp 0 114.300 0 114.300 -91.52 -61.04
35 rpp 0 114.300 0 114.300 -107.32 -91.52
*501 px 1e-5
*502 py 1e-5
c
c end surface specification

c material specification
m11 92235.60c -0.1781 $U235
92238.60c -84.6419 $U238
08016.50c -15.18 $O
m12 42000.50c -16.76 $Mo
92235.60c -1.02 $U235
92238.60c -462.40 $U238
94238.60c -0.11 $Pu238
94239.60c -163.46 $Pu239
94240.60c -21.75 $Pu240
94241.60c -0.54525 $Pu241
94242.60c -0.36 $Pu242
95241.60c -2.91475 $Am241
26000.50c -36 $Fe
28000.50c -5.49 $Ni
24000.50c -9.71 $Cr

```

	25055.50c	-0.875	\$Mn
	08016.50c	-0.367	\$O
m13	08016.50c	0.30	\$O
	07014.50c	0.70	\$N
m14	26000.50c	-70.35	\$Fe
	08016.50c	-29.61	\$O
m15	26000.50c	55.3173	\$Fe
	28000.50c	6.9735	\$Ni
	24000.50c	15.6724	\$Cr
	25055.50c	1.5646	\$Mn
	08016.50c	1.9709	\$O
m16	92238.60c	-99.789	
	92235.60c	-0.221	
m17	26000.50c	-13.65682	\$Fe
	28000.50c	-2.019366	\$Ni
	24000.50c	-3.490238	\$Cr
	25055.50c	-0.275196	\$Mn
	08016.50c	-0.14424	\$O
	06000.50c	-43.5566	\$C
	05010.60c	-27.71962	\$B10
	05011.60c	-123.6029	\$B11
	14000.60c	-0.156608	\$Si
c end material specification			
ksrc	0.001	0.001	0.001
mode	n		
kcode	2000	1.0	70 170
prtmp	170	170	170
print			

## Appendix C Irradiation Damage Tube-in-Duct Pin Cell Model

```
c deck by Pete Yarsky
c
c 4.13.2005
c
c the purpose of this deck is to use a very simple reflected
c unitcell model in order to calculate the fluence on the
c cladding for a TID assembly.
c
c the calculation uses MCODE2 to perform burnup steps and
c meanwhile accrues the flux per source neutron per second in
c the fuel as well as the cladding.
c
c the deck also includes tallies for the fission cross-section
c as well as the energy yield from fission in order to compute
c the flux multiplication factor.
c
c define the fuel cell (fuel, cladding, and coolant)
c
c here the fuel volume is an essential parameter; while the
c volume fraction of cladding and fuel is essential to
c accurately predicting the ratio of the fluxes, in order to
c apply the FMF the correct volumes must be used, or the
c heavy metal mass must be adjusted accordingly.
c
c for the purposes of making this model more universal the
c cladding for a single cell (including the correct axial
c height) should be used. This of course, will neglect the
c duct wall.
c
c an approximate method for calculating the duct fluence will
c be to multiply the clad fluence by the ratio of the duct
c volume to the cladding volume per assembly
c
c the fuel is 200cm tall. The cladding thickness is 0.04cm.
c the total volume of the cell is  $\sqrt{3}/2$  pitch2 height.
c
c volume of the cell =  $\sqrt{3}/2$  (0.725x2)2 200 = 364.16cc
c volume of the coolant = 200 pi IR2 = 100.53 cc
c volume of the cladding = 200 pi (OR2 - IR2) = 21.11 cc
c volume of the fuel = 364.16 - 100.53 - 21.11 = 242.52 cc
c
c coolant volume fraction = 0.276
c
c The unit cell will include white boundary conditions for
c reflection
c
c
c IMPORTANT PRECONDITIONS
c (1) must change the fuel number density in 2 locations
c (2) update geometry in the surface cards
c (2a) for the hex geometry, changing the pitch is sufficient
c the input for the hex card is p/2
c (3) update the power density in the MCODE2 input
c (4) the burnup goes to 225 MWD/kgIHM for peak fluence
c (5) recalculate the volumes
c (6) fuel volume must be included in MCODE2 input
c
c INPUT DATA REQUIRED
c different for UC and (U,Pu,MA)O2 fueled versions
c (1) coolant channel pitch
c (2) cladding OR
c (3) cladding IR
```

```

c (4) coolant density
c (5) fuel density
c (6) fuel composition
c (7) peak burnup
c (8) power density (W/gIHM)
c (9) core height
c
c
c CELL CARDS
c
  1  1  5.987e-02 +2 -3    imp:n=1  vol=242.52 $ fuel
  2  2  -7.2      +1 -2 -3  imp:n=1  vol=21.11 $ ODS cladding
  3  3  -0.00876  -1 -3    imp:n=1  vol=100.53 $ He coolant
  99 0          +3      imp:n=0          $ VOID
c
c END OF CELL CARDS
c
c
c SURFACE CARDS
c
c FUEL PIN GEOMETRY
c
  1      cz          +0.40          $ cladding inner R
  2      cz          +0.44          $ cladding inner R
c
c FUEL ASSEMBLY GEOMETRY
c
c          bottom      vector to top  facet vector
c                                     pitch/2,0,0
3+  hex  0 0 -0.5      0 0 1          0.725 0 0
c
c END OF SURFACE CARDS
c
c
c DATA CARDS - INCLUDING MATERIALS
c
c UC fuel at 5 a/o enrichment
c
m1      6000.60c  0.0294850
      92235.86c  0.00141425
      92238.86c  0.02801075
c
c ODS steel cladding
c
m2      26000.50c  -0.745      $ Fe
      24000.50c  -0.200      $ Cr
      13027.60c  -0.045      $ Al
      22000.60c  -0.005      $ Ti
      6000.50c   -0.0005     $ C
      39089.60c  -0.00394     $ Y
      8016.50c   -0.00106     $ O
c
c He coolant
c
m3      2004.50c   1.0          $Helium Coolant
c
c END OF MATERIAL CARDS
c
c TALLY SPECIFICATION
c
F104:N  1 2

```

```

E104:N 0.1 1 10 T
FC104 fuel and cladding flux (1/sn) fast, threshold and total
C
F114:N 1 2
FC114 total integrated flux
C
F124:N 1
FML24 (5.987e-02 1 (-6))
FC124 macroscopic fission cross section (1/cm)
C
c above the multiplier is NFUEL (atoms/b-cm) same as in cell card
C
F134:N 1
FML34 (5.987e-02 1 (-8 -6) (-7 -6))
FC134 fission Q (MeV/fission) fission yield (n/fission)
C
C
F144:N 2
FML144 (1 2 (103) (107) (2) (104) (105) (106))
FC144 (n,p) (n,alpha) scattering (n,d) (n,t) (n,3He)
C
c energy weighted fluence
c 174 the fluence is weighted by energy and scattering xsection - integrated
c 194 Lindhard model for stainless steel - integrated
c 204 half-Nelson model for iron - integrated
C
C
F174:N 2
FML174 (1 2 (2))
DE174 LOG
1e-9
1e-8
1e-7
1e-6
1e-5
1e-4
1e-3
1e-2
1e-1
1
10
100
DF174 LOG
1e-9
1e-8
1e-7
1e-6
1e-5
1e-4
1e-3
1e-2
1e-1
1
10
100
FC174 energy and scattering weighted fluence - integral
C
C
C
F194:N 2
FML194 0.66
E194 1.01e-4
1.67e-4
2.75e-4

```



4.54e-4  
7.49e-4  
1.23e-3  
2.03e-3  
3.36e-3  
5.53e-3  
9.12e-3  
1.50e-2  
2.48e-2  
4.09e-2  
6.74e-2  
1.11e-1  
1.83e-1  
3.02e-1  
4.98e-1  
8.21e-1  
1.35  
2.23  
3.68  
6.07  
10  
100  
T  
EML94 0  
0.28  
0.22  
0.12  
2.18  
6.03  
5.46  
9.38  
20.9  
41.3  
34.4  
35.4  
185  
111  
206  
250  
297  
529  
635  
861  
1370  
2000  
2450  
2840  
3140  
FC194 Lindhard  
C  
C  
F204:N 2  
FM204 0.66  
E204 1.01e-4  
1.67e-4  
2.75e-4  
4.54e-4  
7.49e-4  
1.23e-3  
2.03e-3  
3.36e-3  
5.53e-3  
9.12e-3  
1.50e-2

```

2.48e-2
4.09e-2
6.74e-2
1.11e-1
1.83e-1
3.02e-1
4.98e-1
8.21e-1
1.35
2.23
3.68
6.07
10
100
T
EM204 0
0
0
0
0
0
0
7.4
10.6
36.8
18.2
9.4
234
90.9
177
198
260
455
578
650
882
1241
1433
1433
1433
FC204 Half-Nelson
c
c
c END OF TALLY SPECIFICATION
c
ksrc 0 0 0
mode n
kcode 4000 1.0 25 75
prinp 75 75 75
print

c mcode2 input
c
c
mce /home/yarsky/bin/mcnp1.exe
c mcnp xs summary
mcxs /home/yarsky/bin/mcode2/mcnpxs.sum.endf
c opt (0=no source, 1=source every mcnp, 2=source all through)
mcs 1
c executable
orge /usr/local/bin/origen22/origen22
c org-library-path decay gamma
orgl /usr/local/bin/origen22/LIBS DECAY.LIB GXUO2BRM.LIB
c

```

```

c m# vol(cc) org-xs-lib imp temp mcrp-xs-opt ntal
c                                     (K) optional optional
c                                     1=original(default), 2=new
c 1 242.52 FFTFC.LIB 0.999 900 2
c optional tally specification
c tal
c
c since vol is for the cell watts here is
c (W/gIHM) (gIHM/cc) (cc/cell) = 16 (11.8) (242.52)
c pow = 45788 watts / cell
c
pow 45788 $ watts (in this case watts/cell)
c
nor 1 $ 1=flux(iterated) 2=flux(once)
c
cor 1 $ predictor-corrector, 0=OFF, 1=ON (1 mcrp) default, 2=ON (2 mcrp)
c
c depletion description
c opt days/BU rel-pow-level NMD
c D/E (absolute) (default 1, negative means decay only) (default 20)
dep E 0 1 40
0.1 1 40
10 1 40
40 1 40
70 1 40
100 1 40
130 1 40
150 1 40
180 1 40
225 1 40
sta $ start pint, default 0
end $ end point, default max

```

## Appendix D CASMO-4 Sample Input Deck for a Mixed PWR Assembly

```
TTL *Nominal PWR case
TFU=900,TMO=583.1,BOR=0.0,VOI=0.0,IDE='B+B'
BOX 6.550,0.7000E-05/304=100
FUE,1,10.302/3.860142,92234=0.048,92238=83.870358,8000=11.861
FUE,2,10.302/4.4045,92234=0.048,92238=77.6855,8000=12.661,7300=6.0
FUE 3 /5.47E+20
08000= 5.24E+22
38088= 8.93E+19
39089= 1.11E+20
42095= 1.78E+20
42097= 1.83E+20
42098= 2.13E+20
43099= 4.46E+19
42100= 2.18E+20
44101= 1.77E+20
44102= 2.29E+20
45103= 1.56E+20
44104= 1.50E+20
46105= 9.63E+19
46106= 9.82E+19
46108= 4.61E+19
47109= 2.85E+19
52130= 7.77E+19
55133= 2.11E+19
54134= 2.55E+20
55135= 2.39E+20
54136= 2.30E+20
55137= 1.44E+20
56138= 2.23E+20
57139= 2.10E+20
58140= 2.05E+20
59141= 1.93E+20
58142= 1.79E+20
60143= 1.63E+20
60144= 1.61E+20
60145= 1.11E+20
60146= 1.09E+20
61147= 3.01E+18
61148= 2.02E+12
61149= 4.88E+13
62147= 5.74E+19
60148= 5.96E+19
62149= 2.91E+19
62151= 1.41E+19
63153= 8.92E+18
90232= 2.03E+14
90233= 3.02E+05
91231= 1.45E+13
91233= 1.73E+12
92232= 2.00E+13
92233= 5.46E+14
92234= 2.23E+18
92236= 3.32E+20
92237= 3.10E+14
92238= 1.85E+22
92239= 2.28E+13
93236= 6.02E+14
93237= 5.00E+19
93238= 4.30E+13
94238= 1.48E+19
94239= 1.78E+21
94240= 2.50E+20
```

```

94241= 1.18E+19
94242= 1.15E+18
95241= 7.62E+18
95242= 1.80E+12
95243= 6.36E+16
96242= 3.77E+14
96243= 1.71E+15
96244= 6.70E+15
96245= 5.41E+14
PIN,1,.4096,.4178,.4750/"1","AIR","CAN"
PIN,2,.5690,.6147/"COO","BOX"
PIN,3,.4096,.4178,.4750/"2","AIR","CAN"
PIN,4,.4096,.4178,.4750/"3","AIR","CAN"
PRE,155.1296
PDE 104.5 'KWL'
PWR,17,1.260,21.50,,,,,8
DEP -80
LPI
  2
  4 4
  4 1 1
  2 4 4 2
  4 4 1 4 1
  4 1 4 1 4 2
  2 4 1 2 1 4 4
  4 1 4 1 4 1 4 1
  1 4 1 1 1 4 1 1 1
*LST,1,0,0,0
STA
END

```

## Appendix E B&B GFR Demonstration Core Final Design MCNP Input File

```
B&B GFR Hex Pitch Core,
c Peter Yarsky
c 9.30.04
c
c PURPOSE:
c The purpose of this MCNP model is to do burnup calculations on a full
c core model of a Breed and Burn reactor.
c
c PRECONDITIONS:
c The geometry is a hexagonal pitch cylindrical fuel rod array
c high pressure helium cooled. The cladding material is ODS and
c the fuel material is enriched uranium nitride-15.
c
c 5 a/o enriched UN15 fuel (BOC)
c Fuel is taken at 91% Theoretical Density (VIPAC)
c
c GRADED ENRICHMENT BOL
c 01: 5 a/o
c 02: 6 a/o
c 03: 8 a/o
c 04: 10a/o
c 05: 10a/o
c 06: 10a/o
c
c The initial assumption is 6 batch reloading of assemblies,
c The initial startup core is purely uranium fuel.
c
c startup core uses uranium enrichment gradient to simulate equilibrium
c
c A Zirconium Silicide reflector is included at the
c top and bottom of the core.
c
c FUEL CELLS
c
c mt density
11 11 6.217e-02
   -4 u=11 imp:n=1 vol = 1421370 $ fuel
13 3 -7.2 +4 -5 u=11 imp:n=1 tmp=1.000e-7 $ ODS cladding
14 2 -0.007620 +5 u=11 imp:n=1 tmp=0.710e-7 $ He coolant
21 12 6.217e-02
   -4 u=22 imp:n=1 vol = 1421370 $ fuel
23 3 -7.2 +4 -5 u=22 imp:n=1 tmp=1.000e-7 $ ODS cladding
24 2 -0.007620 +5 u=22 imp:n=1 tmp=0.710e-7 $ He coolant
31 13 6.217e-02
   -4 u=33 imp:n=1 vol = 1421370 $ fuel
33 3 -7.2 +4 -5 u=33 imp:n=1 tmp=1.000e-7 $ ODS cladding
34 2 -0.007620 +5 u=33 imp:n=1 tmp=0.710e-7 $ He coolant
41 14 6.217e-02
   -4 u=44 imp:n=1 vol = 1421370 $ fuel
43 3 -7.2 +4 -5 u=44 imp:n=1 tmp=1.000e-7 $ ODS cladding
44 2 -0.007620 +5 u=44 imp:n=1 tmp=0.710e-7 $ He coolant
51 15 6.217e-02
   -4 u=55 imp:n=1 vol = 1421370 $ fuel
53 3 -7.2 +4 -5 u=55 imp:n=1 tmp=1.000e-7 $ ODS cladding
54 2 -0.007620 +5 u=55 imp:n=1 tmp=0.710e-7 $ He coolant
61 16 6.217e-02
   -4 u=66 imp:n=1 vol = 1421370 $ fuel
63 3 -7.2 +4 -5 u=66 imp:n=1 tmp=1.000e-7 $ ODS cladding
64 2 -0.007620 +5 u=66 imp:n=1 tmp=0.710e-7 $ He coolant
c
c REFLECTOR
c
```

```

c
c AXIAL
c
81 4 0.08918 -4      u=88 imp:n=1 $ axial reflector
83 3 -7.2      +4 -5  u=88 imp:n=1 tmp=1.000e-7 $ ODS cladding
84 2 -0.007620 +5      u=88 imp:n=1 tmp=0.710e-7 $ He coolant
c
c RADIAL
c
99 4 0.07134
505 -501 +402 -405 61 62 imp:n=1 tmp=0.710e-7 $ radial reflector
c
c CONTROL
c
71 6 0.03706 -4 +6  u=77 imp:n=1 $ poison
72 4 0.08918 -4 -7  u=77 imp:n=1 $ diluent
73 3 -7.2      +4 -5 6 u=77 imp:n=1 $ ODS cladding
74 3 -7.2      4 -5 -7 u=77 imp:n=1 $ ODS cladding
75 3 -7.2      7 -6 -5 +9 u=77 imp:n=1 $GuideTube
77 2 -0.007620 -9 -6 7 u=77 imp:n=1 $ He fill
78 2 -0.007620 +5      u=77 imp:n=1 $ He coolant
c
c Assembly Definitions
c
101 2 -0.007620 -21      $ batch 01
      imp:n=1 u=01 lat=2 fill=-8:8 -8:8 0:0
      00 00 00 00 00 00 00 00 01 01 01 01 01 01 01 01
      00 00 00 00 00 00 00 00 01 11 11 11 11 11 11 11
      00 00 00 00 00 00 00 00 01 11 11 11 11 11 11 11
      00 00 00 00 00 01 11 11 11 11 11 11 11 11 11 11
      00 00 00 00 01 11 11 11 11 11 11 11 11 11 11 11
      00 00 00 01 11 11 11 11 11 77 11 11 77 11 11 11
      00 00 01 11 11 11 11 11 11 11 11 11 11 11 11 11
      00 01 11 11 11 11 11 11 11 11 11 11 11 11 11 11
      01 11 11 11 11 11 77 11 11 77 11 11 77 11 11 11
      01 11 11 11 11 11 11 11 11 11 11 11 11 11 11 01
      01 11 11 11 11 11 11 11 11 11 11 11 11 11 01 00
      01 11 11 11 11 11 77 11 11 77 11 11 11 11 01 00
      01 11 11 11 11 11 11 11 11 11 11 11 11 01 00 00
      01 11 11 11 11 11 11 11 11 11 11 11 11 01 00 00
      01 11 11 11 11 11 11 11 11 11 01 00 00 00 00 00
      01 01 01 01 01 01 01 01 01 00 00 00 00 00 00 00
102 2 -0.007620 -21      $ batch 02
      imp:n=1 u=02 lat=2 fill=-8:8 -8:8 0:0
      00 00 00 00 00 00 00 00 02 02 02 02 02 02 02 02
      00 00 00 00 00 00 00 00 02 22 22 22 22 22 22 22
      00 00 00 00 00 00 00 00 02 22 22 22 22 22 22 22
      00 00 00 00 00 02 22 22 22 22 22 22 22 22 22 22
      00 00 00 02 22 22 22 22 22 77 22 22 77 22 22 22
      00 00 02 22 22 22 22 22 22 22 22 22 22 22 22 22
      00 02 22 22 22 22 22 22 22 22 22 22 22 22 22 22
      02 22 22 22 22 77 22 22 77 22 22 77 22 22 22 22
      02 22 22 22 22 22 22 22 22 22 22 22 22 22 02 00
      02 22 22 22 22 77 22 22 77 22 22 22 22 02 00 00
      02 22 22 22 22 22 22 22 22 22 22 22 02 00 00 00
      02 22 22 22 22 22 22 22 22 22 22 02 00 00 00 00
      02 22 22 22 22 22 22 22 22 22 02 00 00 00 00 00
      02 02 02 02 02 02 02 02 00 00 00 00 00 00 00 00
103 2 -0.007620 -21      $ batch 03
      imp:n=1 u=03 lat=2 fill=-8:8 -8:8 0:0

```

```

00 00 00 00 00 00 00 00 03 03 03 03 03 03 03 03
00 00 00 00 00 00 00 00 03 33 33 33 33 33 33 33
00 00 00 00 00 00 03 33 33 33 33 33 33 33 33 33
00 00 00 00 00 03 33 33 33 33 33 33 33 33 33 33
00 00 00 03 33 33 33 33 77 33 33 77 33 33 33 33
00 00 03 33 33 33 33 33 33 33 33 33 33 33 33 33
00 03 33 33 33 33 33 33 33 33 33 33 33 33 33 33
03 33 33 33 33 77 33 33 77 33 33 77 33 33 33 33
03 33 33 33 33 33 33 33 33 33 33 33 33 33 33 00
03 33 33 33 33 77 33 33 77 33 33 33 33 33 33 00
03 33 33 33 33 33 33 33 33 33 33 33 03 00 00 00
03 33 33 33 33 33 33 33 33 33 33 03 00 00 00 00
03 33 33 33 33 33 33 33 33 33 03 00 00 00 00 00
03 03 03 03 03 03 03 03 03 00 00 00 00 00 00 00
104 2 -0.007620 -21 $ batch 04
    imp:n=1 u=04 lat=2 fill=-8:8 -8:8 0:0
00 00 00 00 00 00 00 04 04 04 04 04 04 04 04 04
00 00 00 00 00 00 04 44 44 44 44 44 44 44 44 44
00 00 00 00 00 04 44 44 44 44 44 44 44 44 44 44
00 00 00 00 04 44 44 44 44 44 44 44 44 44 44 44
00 00 04 44 44 44 44 44 77 44 44 77 44 44 44 44
00 00 04 44 44 44 44 44 44 44 44 44 44 44 44 44
00 04 44 44 44 44 44 44 44 44 44 44 44 44 44 44
04 44 44 44 44 77 44 44 77 44 44 77 44 44 44 44
04 44 44 44 44 44 44 44 44 44 44 44 44 44 44 00
04 44 44 44 44 44 44 44 44 44 44 44 44 44 00 00
04 44 44 44 44 77 44 44 77 44 44 44 44 04 00 00
04 44 44 44 44 44 44 44 44 44 44 44 04 00 00 00
04 44 44 44 44 44 44 44 44 44 04 00 00 00 00 00
04 44 44 44 44 44 44 44 44 04 00 00 00 00 00 00
04 04 04 04 04 04 04 04 04 00 00 00 00 00 00 00
105 2 -0.007620 -21 $ batch 05
    imp:n=1 u=05 lat=2 fill=-8:8 -8:8 0:0
00 00 00 00 00 00 00 05 05 05 05 05 05 05 05 05
00 00 00 00 00 00 05 55 55 55 55 55 55 55 55 55
00 00 00 00 00 05 55 55 55 55 55 55 55 55 55 55
00 00 00 00 05 55 55 55 55 55 55 55 55 55 55 55
00 00 05 55 55 55 55 55 77 55 55 77 55 55 55 55
00 00 05 55 55 55 55 55 55 55 55 55 55 55 55 55
00 05 55 55 55 55 55 55 55 55 55 55 55 55 55 55
05 55 55 55 55 77 55 55 77 55 55 77 55 55 55 55
05 55 55 55 55 55 55 55 55 55 55 55 55 55 55 00
05 55 55 55 55 55 55 55 55 55 55 55 55 55 00 00
05 55 55 55 55 77 55 55 77 55 55 55 55 05 00 00
05 55 55 55 55 55 55 55 55 55 55 55 05 00 00 00
05 55 55 55 55 55 55 55 55 55 05 00 00 00 00 00
05 55 55 55 55 55 55 55 55 05 00 00 00 00 00 00
05 05 05 05 05 05 05 05 05 00 00 00 00 00 00 00
106 2 -0.007620 -21 $ batch 06
    imp:n=1 u=06 lat=2 fill=-8:8 -8:8 0:0
00 00 00 00 00 00 00 06 06 06 06 06 06 06 06 06
00 00 00 00 00 00 06 66 66 66 66 66 66 66 66 66
00 00 00 00 00 06 66 66 66 66 66 66 66 66 66 66
00 00 00 00 06 66 66 66 66 66 66 66 66 66 66 66
00 00 00 06 66 66 66 66 66 66 66 66 66 66 66 66
00 00 00 06 66 66 66 66 66 66 66 66 66 66 66 66
00 00 06 66 66 66 66 66 66 66 66 66 66 66 66 66
00 00 06 66 66 66 66 66 66 66 66 66 66 66 66 66

```



```
00 06 66 66 66 66 66 66 66 66 66 66 66 66 66 06
06 66 66 66 66 77 66 66 77 66 66 77 66 66 66 66 06
06 66 66 66 66 66 66 66 66 66 66 66 66 66 66 06 00
06 66 66 66 66 66 66 66 66 66 66 66 66 66 66 06 00 00
06 66 66 66 66 77 66 66 77 66 66 66 66 06 00 00 00 00
06 66 66 66 66 66 66 66 66 66 66 66 06 00 00 00 00 00
06 66 66 66 66 66 66 66 66 66 66 06 00 00 00 00 00 00
06 66 66 66 66 66 66 66 66 66 06 00 00 00 00 00 00 00
06 66 66 66 66 66 66 66 66 06 00 00 00 00 00 00 00 00
06 06 06 06 06 06 06 06 00 00 00 00 00 00 00 00 00 00
```

C

C NON FUEL

C

```
107 2 -0.007620 -21 $ axial reflector
imp:n=1 u=07 lat=2 fill=-8:8 -8:8 0:0
00 00 00 00 00 00 00 00 07 07 07 07 07 07 07 07 07
00 00 00 00 00 00 00 00 07 77 77 77 77 77 77 77 77
00 00 00 00 00 00 07 77 77 77 77 77 77 77 77 77 07
00 00 00 00 00 07 77 77 77 77 77 77 77 77 77 77 07
00 00 00 00 07 77 77 77 77 77 77 77 77 77 77 77 07
00 00 00 07 77 77 77 77 77 77 77 77 77 77 77 77 07
00 00 07 77 77 77 77 77 77 77 77 77 77 77 77 77 07
00 07 77 77 77 77 77 77 77 77 77 77 77 77 77 77 07
07 77 77 77 77 77 77 77 77 77 77 77 77 77 77 77 07
07 77 77 77 77 77 77 77 77 77 77 77 77 77 77 77 07 00
07 77 77 77 77 77 77 77 77 77 77 77 77 77 77 77 07 00 00
07 77 77 77 77 77 77 77 77 77 77 77 77 77 77 77 07 00 00 00
07 77 77 77 77 77 77 77 77 77 77 77 77 77 77 77 07 00 00 00
07 77 77 77 77 77 77 77 77 77 77 77 77 77 77 77 07 00 00 00
07 77 77 77 77 77 77 77 77 77 77 77 77 77 77 77 07 00 00 00
07 07 07 07 07 07 07 07 00 00 00 00 00 00 00 00 00 00
```

```
108 2 -0.007620 -21 $ axial reflector
imp:n=1 u=08 lat=2 fill=-8:8 -8:8 0:0
00 00 00 00 00 00 00 00 08 08 08 08 08 08 08 08 08 08
00 00 00 00 00 00 00 08 88 88 88 88 88 88 88 88 88 08
00 00 00 00 00 00 08 88 88 88 88 88 88 88 88 88 88 08
00 00 00 00 00 08 88 88 88 88 88 88 88 88 88 88 88 08
00 00 00 08 88 88 88 88 88 88 88 88 88 88 88 88 88 08
00 00 08 88 88 88 88 88 88 88 88 88 88 88 88 88 88 08
00 08 88 88 88 88 88 88 88 88 88 88 88 88 88 88 88 08
08 88 88 88 88 88 88 88 88 88 88 88 88 88 88 88 88 08
08 88 88 88 88 88 88 88 88 88 88 88 88 88 88 88 88 08 00
08 88 88 88 88 88 88 88 88 88 88 88 88 88 88 88 88 08 00 00
08 88 88 88 88 88 88 88 88 88 88 88 88 88 88 88 88 08 00 00 00
08 88 88 88 88 88 88 88 88 88 88 88 88 88 88 88 88 08 00 00 00
08 88 88 88 88 88 88 88 88 88 88 88 88 88 88 88 88 08 00 00 00
08 88 88 88 88 88 88 88 88 88 88 88 88 88 88 88 88 08 08 08 08
```

C

C Core Definition

C

```
209 2 -0.007620 -31 u=14 lat=2
imp:n=1 fill=0:19 -10:10 0:0
00 00 00 00 00 00 00 00 00 00 00 00 00 00 00 00 14 14 14 14
00 00 00 00 00 00 00 00 00 00 00 00 00 00 00 00 14 14 14 14
00 00 00 00 00 00 00 00 00 00 00 00 00 00 00 00 14 14 14 14
00 00 00 00 00 00 00 00 00 00 00 00 00 00 00 08 14 14 14 14
00 00 00 00 00 00 00 00 00 00 00 08 08 08 08 14 14 14 14 14
00 00 00 00 00 00 00 00 00 08 08 08 08 08 08 14 14 14 14 14
00 00 00 00 00 00 00 08 08 08 08 08 08 08 08 14 14 14 14 14
00 00 00 00 00 08 08 08 08 08 08 08 08 08 14 14 14 14 14
```

```

00 00 00 00 08 08 08 08 08 08 08 08 08 08 08 08 14 14 14 14 14
00 00 08 08 08 08 08 08 08 08 08 08 08 08 08 08 14 14 14 14 14
08 08 08 08 08 08 08 08 08 08 08 08 08 08 08 08 14 14 14 14 14
00 08 08 08 08 08 08 08 08 08 08 08 08 08 08 08 14 14 14 14 14
00 00 08 08 08 08 08 08 08 08 08 08 08 08 08 08 14 14 14 14 14
00 00 00 08 08 08 08 08 08 08 08 08 08 08 08 14 14 14 14 14 14
00 00 00 00 08 08 08 08 08 08 14 14 14 14 14 14 14 14 14 14 14
00 00 00 00 00 08 08 08 08 14 14 14 14 14 14 14 14 14 14 14 14
00 00 00 00 00 00 08 08 08 14 14 14 14 14 14 14 14 14 14 14 14
00 00 00 00 00 00 00 08 14 14 14 14 14 14 14 14 14 14 14 14 14
00 00 00 00 00 00 00 00 14 14 14 14 14 14 14 14 14 14 14 14 14
00 00 00 00 00 00 00 00 14 14 14 14 14 14 14 14 14 14 14 14 14
210 2 -0.007620 -31 u=12 lat=2
      imp:n=1 fill=0:19 -10:10 0:0
00 00 00 00 00 00 00 00 00 00 00 00 00 00 00 00 12 12 12 12
00 00 00 00 00 00 00 00 00 00 00 00 00 00 00 00 12 12 12 12
00 00 00 00 00 00 00 00 00 00 00 00 00 00 00 00 12 12 12 12
00 00 00 00 00 00 00 00 00 00 00 00 00 00 01 12 12 12 12 12
00 00 00 00 00 00 00 00 00 00 00 00 02 02 01 12 12 12 12 12
00 00 00 00 00 00 00 00 00 00 05 06 02 02 01 12 12 12 12 12
00 00 00 00 00 00 00 00 03 05 05 06 06 02 01 12 12 12 12 12
00 00 00 00 00 04 03 03 05 05 06 06 02 01 12 12 12 12 12
00 00 00 00 04 04 03 03 03 05 05 06 02 01 12 12 12 12 12
07 04 04 04 04 04 03 05 05 06 02 01 12 12 12 12 12 12 12
00 04 04 04 04 03 03 03 05 06 06 02 01 01 12 12 12 12 12 12
00 00 04 04 03 03 03 05 05 06 02 02 01 12 12 12 12 12 12 12
00 00 00 04 03 03 05 05 06 06 02 01 12 12 12 12 12 12 12 12
00 00 00 00 03 05 05 06 06 02 01 12 12 12 12 12 12 12 12 12
00 00 00 00 00 05 06 02 02 01 12 12 12 12 12 12 12 12 12 12
00 00 00 00 00 02 02 01 12 12 12 12 12 12 12 12 12 12 12 12
00 00 00 00 00 00 01 12 12 12 12 12 12 12 12 12 12 12 12 12
00 00 00 00 00 00 00 12 12 12 12 12 12 12 12 12 12 12 12 12
00 00 00 00 00 00 00 12 12 12 12 12 12 12 12 12 12 12 12 12
00 00 00 00 00 00 00 12 12 12 12 12 12 12 12 12 12 12 12 12
131 0          +61 +62 -505 402 -403 fill=14 imp:n=1 $ bottom-reflector
130 0          +61 +62 -505 403 -404 fill=12 imp:n=1 $ core
132 0          +61 +62 -505 404 -405 fill=14 imp:n=1 $ top-reflector
c
c REST OF MODEL
c
c
301 3 -7.2          -501          61 62 401 -402 imp:n=1 $ lower plate
302 3 -7.2          -501          61 62 405 -406 imp:n=1 $ upper plate
403 2 -0.007620          -501 61 62 406 -407 imp:n=1 $ chimney
404 2 -0.007620          -503 61 62 400 -401 imp:n=1 $ l.plenum
405 3 -7.2          501 -502 61 62 401 -407 imp:n=1 $ core barrel
406 2 -0.007620 502 -503 61 62 401 -407 imp:n=1 $ downcomer
407 3 -7.2          503 -504 61 62 400 -407 imp:n=1 $ vessel wall
1000 0          -61:-62: 504:-400:407 imp:n=0 $ outside
c end of cell specification

c
c surface specification
c
c FUEL PIN GEOMETRY
c
1      cz          +0.25          $ coolant channel R
3      cz          +0.35          $ fuel OR
4      cz          +0.37          $ gap OR / Clad IR
5      cz          +0.41          $ Clad OR
8      cz          +0.45          $ Reflector Sleeve
9      cz          +0.39          $ Guide Tube

```

```

c
c CONTROL RODS
c
c      pz      +99      $ Moderator (in = -
100)
c      pz      -99      $ Diluent (in =
+100)
c
c FUEL ASSEMBLY GEOMETRY
c
c      bottom      vector to top      facet vector
c
c      hex 0 0 -500      0 0 1000      0.5 0 0
c
c CORE GEOMETRY
c
c      assembly area = sqrt(3)/2 FTF^2 = (23/3)^2 pitch^2 3 sqrt(3)/2 = 529/6 sqrt(3)
pitch^2
c
c      bottom      vector to top      angle = 30 degrees
c      FTF = (8 - 1 + 2/3) sqrt(3) pitch
c      sqrt(3) FTF/4 , FTF/4 , 0
c
c      hex 0 0 -500      0 0 1000      5.75 3.319764049 0
c
c      -sqrt(3)
c
c *61 p 1 -1.732051 0 0      $ symmetry
c *62 py 1E-5      $ symmetry
c
c REST OF MODEL GEOMETRY
c
c      pz      -360.0      $ bottom boundary
c      pz      -128.00      $ lower plate-
bottom
c      pz      -125.000      $ axial-reflector-
bottom
c      pz      -100.000      $ core-bottom
c      pz      100.000      $ core-top
c      pz      125.000      $ axial-reflector-
top
c      pz      128.000      $ top plate
c      pz      350.000      $ top boundary
c      cz      225      $ barrel in (32)
c      cz      228      $ barrel out (3)
c      cz      238      $ vessel in (10)
c      cz      253      $ vessel out (15)
c      hex 0 0 -125 0 0 250 169 0 0      $ radial reflector
in
c      end of surface specification

c
c      data specification
c
c MATERIALS
c fuel
c m11 007015.60c 0.031084529      $ N15
c      35081.55c 1.0000e-24      $ begin_mcode_FP
c      36083.50c 1.0000e-24
c      36084.50c 1.0000e-24
c      37085.55c 1.0000e-24
c      37087.55c 1.0000e-24
c      39089.60c 1.0000e-24

```

40090.62c 1.0000e-24  
40091.96c 1.0000e-24  
40092.62c 1.0000e-24  
40093.50c 1.0000e-24  
40094.62c 1.0000e-24  
40096.62c 1.0000e-24  
41095.96c 1.0000e-24  
42095.50c 1.0000e-24  
42096.96c 1.0000e-24  
42097.60c 1.0000e-24  
42098.50c 1.0000e-24  
c 42100.50c 1.0000e-24  
43099.50c 1.0000e-24  
44100.96c 1.0000e-24  
44101.50c 1.0000e-24  
44102.60c 1.0000e-24  
44103.50c 1.0000e-24  
44104.96c 1.0000e-24  
45103.50c 1.0000e-24  
46104.96c 1.0000e-24  
46105.50c 1.0000e-24  
46106.96c 1.0000e-24  
46108.50c 1.0000e-24  
46110.96c 1.0000e-24  
47109.60c 1.0000e-24  
48110.62c 1.0000e-24  
48111.62c 1.0000e-24  
48112.62c 1.0000e-24  
48113.60c 1.0000e-24  
48114.62c 1.0000e-24  
49115.60c 1.0000e-24  
50117.96c 1.0000e-24  
51121.96c 1.0000e-24  
51123.96c 1.0000e-24  
52125.96c 1.0000e-24  
52128.96c 1.0000e-24  
52130.96c 1.0000e-24  
53127.60c 1.0000e-24  
53129.60c 1.0000e-24  
54128.62c 1.0000e-24  
54130.62c 1.0000e-24  
54131.50c 1.0000e-24  
54132.62c 1.0000e-24  
54134.62c 1.0000e-24  
54136.62c 1.0000e-24  
55133.60c 1.0000e-24  
55134.60c 1.0000e-24  
55135.60c 1.0000e-24  
55137.60c 1.0000e-24  
56132.96c 1.0000E-24  
56135.96c 1.0000e-24  
56136.96c 1.0000e-24  
56134.62c 1.0000e-24  
56137.62c 1.0000e-24  
56138.60c 1.0000e-24  
57139.60c 1.0000e-24  
58140.96c 1.0000e-24  
58142.96c 1.0000e-24  
59141.50c 1.0000e-24  
60142.96c 1.0000e-24  
60143.50c 1.0000e-24  
60144.96c 1.0000e-24  
60145.50c 1.0000e-24  
60146.96c 1.0000e-24

	60148.50c	1.0000e-24	
	60150.96c	1.0000e-24	
	61147.50c	1.0000e-24	
	61148.60c	1.0000e-24	
	62147.50c	1.0000e-24	
	62148.96c	1.0000e-24	
	62149.50c	1.0000e-24	
	62150.50c	1.0000e-24	
	62151.50c	1.0000e-24	
	62152.50c	1.0000e-24	
	62154.96c	1.0000e-24	
	63151.60c	1.0000e-24	
	63152.50c	1.0000e-24	
	63153.60c	1.0000e-24	
	63154.50c	1.0000e-24	
	64154.60c	1.0000e-24	
	64155.60c	1.0000e-24	
	64156.60c	1.0000e-24	
	64157.60c	1.0000e-24	
	64158.60c	1.0000e-24	
	65159.96c	1.0000e-24	
	66160.96c	1.0000e-24	
	66161.96c	1.0000e-24	
	66162.96c	1.0000e-24	\$ end_mcode_FP
	90232.86c	1.0000e-24	\$ begin_mcode_ACT
	90233.35c	1.0000e-24	
	91231.60c	1.0000e-24	
	91233.50c	1.0000e-24	
	92232.60c	1.0000e-24	
	92233.86c	1.0000e-24	
	92234.86c	1.0000e-24	
	92235.86c	.1554226471e-2	
	92236.86c	1.0000e-24	
	92237.86c	1.0000e-24	
	92238.86c	.2953030294e-1	
	92239.35c	1.0000e-24	
	93235.35c	1.0000e-24	
	93236.35c	1.0000e-24	
	93237.82c	1.0000e-24	
	93238.35c	1.0000e-24	
	94237.86c	1.0000e-24	
	94238.86c	1.0000e-24	
	94239.86c	1.0000e-24	
	94240.86c	1.0000e-24	
	94241.86c	1.0000e-24	
	94242.86c	1.0000e-24	
	95241.82c	1.0000e-24	
	95242.82c	1.0000e-24	
	95243.10c	1.0000e-24	
	96242.82c	1.0000e-24	
	96243.10c	1.0000e-24	
	96244.82c	1.0000e-24	
	96245.60c	1.0000e-24	\$ end_mcode_ACT
m12	007015.60c	0.031084529	\$ N15
	35081.55c	1.0000e-24	\$ begin_mcode_FP
	36083.50c	1.0000e-24	
	36084.50c	1.0000e-24	
	37085.55c	1.0000e-24	
	37087.55c	1.0000e-24	
	39089.60c	1.0000e-24	
	40090.62c	1.0000e-24	
	40091.96c	1.0000e-24	
	40092.62c	1.0000e-24	
	40093.50c	1.0000e-24	

c 40094.62c 1.0000e-24  
40096.62c 1.0000e-24  
41095.96c 1.0000e-24  
42095.50c 1.0000e-24  
42096.96c 1.0000e-24  
42097.60c 1.0000e-24  
42098.50c 1.0000e-24  
42100.50c 1.0000e-24  
43099.50c 1.0000e-24  
44100.96c 1.0000e-24  
44101.50c 1.0000e-24  
44102.60c 1.0000e-24  
44103.50c 1.0000e-24  
44104.96c 1.0000e-24  
45103.50c 1.0000e-24  
46104.96c 1.0000e-24  
46105.50c 1.0000e-24  
46106.96c 1.0000e-24  
46108.50c 1.0000e-24  
46110.96c 1.0000e-24  
47109.60c 1.0000e-24  
48110.62c 1.0000e-24  
48111.62c 1.0000e-24  
48112.62c 1.0000e-24  
48113.60c 1.0000e-24  
48114.62c 1.0000e-24  
49115.60c 1.0000e-24  
50117.96c 1.0000e-24  
51121.96c 1.0000e-24  
51123.96c 1.0000e-24  
52125.96c 1.0000e-24  
52128.96c 1.0000e-24  
52130.96c 1.0000e-24  
53127.60c 1.0000e-24  
53129.60c 1.0000e-24  
54128.62c 1.0000e-24  
54130.62c 1.0000e-24  
54131.50c 1.0000e-24  
54132.62c 1.0000e-24  
54134.62c 1.0000e-24  
54136.62c 1.0000e-24  
55133.60c 1.0000e-24  
55134.60c 1.0000e-24  
55135.60c 1.0000e-24  
55137.60c 1.0000e-24  
56132.96c 1.0000E-24  
56135.96c 1.0000e-24  
56136.96c 1.0000e-24  
56134.62c 1.0000e-24  
56137.62c 1.0000e-24  
56138.60c 1.0000e-24  
57139.60c 1.0000e-24  
58140.96c 1.0000e-24  
58142.96c 1.0000e-24  
59141.50c 1.0000e-24  
60142.96c 1.0000e-24  
60143.50c 1.0000e-24  
60144.96c 1.0000e-24  
60145.50c 1.0000e-24  
60146.96c 1.0000e-24  
60148.50c 1.0000e-24  
60150.96c 1.0000e-24  
61147.50c 1.0000e-24  
61148.60c 1.0000e-24

	62147.50c	1.0000e-24	
	62148.96c	1.0000e-24	
	62149.50c	1.0000e-24	
	62150.50c	1.0000e-24	
	62151.50c	1.0000e-24	
	62152.50c	1.0000e-24	
	62154.96c	1.0000e-24	
	63151.60c	1.0000e-24	
	63152.50c	1.0000e-24	
	63153.60c	1.0000e-24	
	63154.50c	1.0000e-24	
	64154.60c	1.0000e-24	
	64155.60c	1.0000e-24	
	64156.60c	1.0000e-24	
	64157.60c	1.0000e-24	
	64158.60c	1.0000e-24	
	65159.96c	1.0000e-24	
	66160.96c	1.0000e-24	
	66161.96c	1.0000e-24	
	66162.96c	1.0000e-24	\$ end_mcode_FP
	90232.86c	1.0000e-24	\$ begin_mcode_ACT
	90233.35c	1.0000e-24	
	91231.60c	1.0000e-24	
	91233.50c	1.0000e-24	
	92232.60c	1.0000e-24	
	92233.86c	1.0000e-24	
	92234.86c	1.0000e-24	
	92235.86c	.1865071765e-2	
	92236.86c	1.0000e-24	
	92237.50c	1.0000e-24	
	92238.86c	.29219457647e-1	
	92239.35c	1.0000e-24	
	93235.35c	1.0000e-24	
	93236.35c	1.0000e-24	
	93237.82c	1.0000e-24	
	93238.35c	1.0000e-24	
	94237.86c	1.0000e-24	
	94238.86c	1.0000e-24	
	94239.86c	1.0000e-24	
	94240.86c	1.0000e-24	
	94241.86c	1.0000e-24	
	94242.86c	1.0000e-24	
	95241.82c	1.0000e-24	
	95242.82c	1.0000e-24	
	95243.10c	1.0000e-24	
	96242.82c	1.0000e-24	
	96243.10c	1.0000e-24	
	96244.82c	1.0000e-24	
	96245.60c	1.0000e-24	\$ end_mcode_ACT
m13	007015.60c	0.031084529	\$ N15
	35081.55c	1.0000e-24	\$ begin_mcode_FP
	36083.50c	1.0000e-24	
	36084.50c	1.0000e-24	
	37085.55c	1.0000e-24	
	37087.55c	1.0000e-24	
	39089.60c	1.0000e-24	
	40090.62c	1.0000e-24	
	40091.96c	1.0000e-24	
	40092.62c	1.0000e-24	
	40093.50c	1.0000e-24	
	40094.62c	1.0000e-24	
	40096.62c	1.0000e-24	
	41095.96c	1.0000e-24	
	42095.50c	1.0000e-24	

c 42096.96c 1.0000e-24  
42097.60c 1.0000e-24  
42098.50c 1.0000e-24  
42100.50c 1.0000e-24  
43099.50c 1.0000e-24  
44100.96c 1.0000e-24  
44101.50c 1.0000e-24  
44102.60c 1.0000e-24  
44103.50c 1.0000e-24  
44104.96c 1.0000e-24  
45103.50c 1.0000e-24  
46104.96c 1.0000e-24  
46105.50c 1.0000e-24  
46106.96c 1.0000e-24  
46108.50c 1.0000e-24  
46110.96c 1.0000e-24  
47109.60c 1.0000e-24  
48110.62c 1.0000e-24  
48111.62c 1.0000e-24  
48112.62c 1.0000e-24  
48113.60c 1.0000e-24  
48114.62c 1.0000e-24  
49115.60c 1.0000e-24  
50117.96c 1.0000e-24  
51121.96c 1.0000e-24  
51123.96c 1.0000e-24  
52125.96c 1.0000e-24  
52128.96c 1.0000e-24  
52130.96c 1.0000e-24  
53127.60c 1.0000e-24  
53129.60c 1.0000e-24  
54128.62c 1.0000e-24  
54130.62c 1.0000e-24  
54131.50c 1.0000e-24  
54132.62c 1.0000e-24  
54134.62c 1.0000e-24  
54136.62c 1.0000e-24  
55133.60c 1.0000e-24  
55134.60c 1.0000e-24  
55135.60c 1.0000e-24  
55137.60c 1.0000e-24  
56132.96c 1.0000E-24  
56135.96c 1.0000e-24  
56136.96c 1.0000e-24  
56134.62c 1.0000e-24  
56137.62c 1.0000e-24  
56138.60c 1.0000e-24  
57139.60c 1.0000e-24  
58140.96c 1.0000e-24  
58142.96c 1.0000e-24  
59141.50c 1.0000e-24  
60142.96c 1.0000e-24  
60143.50c 1.0000e-24  
60144.96c 1.0000e-24  
60145.50c 1.0000e-24  
60146.96c 1.0000e-24  
60148.50c 1.0000e-24  
60150.96c 1.0000e-24  
61147.50c 1.0000e-24  
61148.60c 1.0000e-24  
62147.50c 1.0000e-24  
62148.96c 1.0000e-24  
62149.50c 1.0000e-24  
62150.50c 1.0000e-24



```

62151.50c 1.0000e-24
62152.50c 1.0000e-24
62154.96c 1.0000e-24
63151.60c 1.0000e-24
63152.50c 1.0000e-24
63153.60c 1.0000e-24
63154.50c 1.0000e-24
64154.60c 1.0000e-24
64155.60c 1.0000e-24
64156.60c 1.0000e-24
64157.60c 1.0000e-24
64158.60c 1.0000e-24
65159.96c 1.0000e-24
66160.96c 1.0000e-24
66161.96c 1.0000e-24
66162.96c 1.0000e-24 $ end_mcode_FP
90232.86c 1.0000e-24 $ begin_mcode_ACT
90233.35c 1.0000e-24
91231.60c 1.0000e-24
91233.50c 1.0000e-24
92232.60c 1.0000e-24
92233.86c 1.0000e-24
92234.86c 1.0000e-24
92235.86c .2486762353e-2
92236.86c 1.0000e-24
92237.50c 1.0000e-24
92238.86c .28597767059e-1
92239.35c 1.0000e-24
93235.35c 1.0000e-24
93236.35c 1.0000e-24
93237.82c 1.0000e-24
93238.35c 1.0000e-24
94237.86c 1.0000e-24
94238.86c 1.0000e-24
94239.86c 1.0000e-24
94240.86c 1.0000e-24
94241.86c 1.0000e-24
94242.86c 1.0000e-24
95241.82c 1.0000e-24
95242.82c 1.0000e-24
95243.10c 1.0000e-24
96242.82c 1.0000e-24
96243.10c 1.0000e-24
96244.82c 1.0000e-24
96245.60c 1.0000e-24 $ end_mcode_ACT
m14 007015.60c 0.031084529 $ N15
35081.55c 1.0000e-24 $ begin_mcode_FP
36083.50c 1.0000e-24
36084.50c 1.0000e-24
37085.55c 1.0000e-24
37087.55c 1.0000e-24
39089.60c 1.0000e-24
40090.62c 1.0000e-24
40091.96c 1.0000e-24
40092.62c 1.0000e-24
40093.50c 1.0000e-24
40094.62c 1.0000e-24
40096.62c 1.0000e-24
41095.96c 1.0000e-24
42095.50c 1.0000e-24
42096.96c 1.0000e-24
42097.60c 1.0000e-24
42098.50c 1.0000e-24
c 42100.50c 1.0000e-24

```

43099.50c 1.0000e-24  
44100.96c 1.0000e-24  
44101.50c 1.0000e-24  
44102.60c 1.0000e-24  
44103.50c 1.0000e-24  
44104.96c 1.0000e-24  
45103.50c 1.0000e-24  
46104.96c 1.0000e-24  
46105.50c 1.0000e-24  
46106.96c 1.0000e-24  
46108.50c 1.0000e-24  
46110.96c 1.0000e-24  
47109.60c 1.0000e-24  
48110.62c 1.0000e-24  
48111.62c 1.0000e-24  
48112.62c 1.0000e-24  
48113.60c 1.0000e-24  
48114.62c 1.0000e-24  
49115.60c 1.0000e-24  
50117.96c 1.0000e-24  
51121.96c 1.0000e-24  
51123.96c 1.0000e-24  
52125.96c 1.0000e-24  
52128.96c 1.0000e-24  
52130.96c 1.0000e-24  
53127.60c 1.0000e-24  
53129.60c 1.0000e-24  
54128.62c 1.0000e-24  
54130.62c 1.0000e-24  
54131.50c 1.0000e-24  
54132.62c 1.0000e-24  
54134.62c 1.0000e-24  
54136.62c 1.0000e-24  
55133.60c 1.0000e-24  
55134.60c 1.0000e-24  
55135.60c 1.0000e-24  
55137.60c 1.0000e-24  
56132.96c 1.0000E-24  
56135.96c 1.0000e-24  
56136.96c 1.0000e-24  
56134.62c 1.0000e-24  
56137.62c 1.0000e-24  
56138.60c 1.0000e-24  
57139.60c 1.0000e-24  
58140.96c 1.0000e-24  
58142.96c 1.0000e-24  
59141.50c 1.0000e-24  
60142.96c 1.0000e-24  
60143.50c 1.0000e-24  
60144.96c 1.0000e-24  
60145.50c 1.0000e-24  
60146.96c 1.0000e-24  
60148.50c 1.0000e-24  
60150.96c 1.0000e-24  
61147.50c 1.0000e-24  
61148.60c 1.0000e-24  
62147.50c 1.0000e-24  
62148.96c 1.0000e-24  
62149.50c 1.0000e-24  
62150.50c 1.0000e-24  
62151.50c 1.0000e-24  
62152.50c 1.0000e-24  
62154.96c 1.0000e-24  
63151.60c 1.0000e-24

	63152.50c	1.0000e-24	
	63153.60c	1.0000e-24	
	63154.50c	1.0000e-24	
	64154.60c	1.0000e-24	
	64155.60c	1.0000e-24	
	64156.60c	1.0000e-24	
	64157.60c	1.0000e-24	
	64158.60c	1.0000e-24	
	65159.96c	1.0000e-24	
	66160.96c	1.0000e-24	
	66161.96c	1.0000e-24	
	66162.96c	1.0000e-24	\$ end_mcode_FP
	90232.86c	1.0000e-24	\$ begin_mcode_ACT
	90233.35c	1.0000e-24	
	91231.60c	1.0000e-24	
	91233.50c	1.0000e-24	
	92232.60c	1.0000e-24	
	92233.86c	1.0000e-24	
	92234.86c	1.0000e-24	
	92235.86c	.3108452941e-2	
	92236.86c	1.0000e-24	
	92237.50c	1.0000e-24	
	92238.86c	.2797607647e-1	
	92239.35c	1.0000e-24	
	93235.35c	1.0000e-24	
	93236.35c	1.0000e-24	
	93237.82c	1.0000e-24	
	93238.35c	1.0000e-24	
	94237.86c	1.0000e-24	
	94238.86c	1.0000e-24	
	94239.86c	1.0000e-24	
	94240.86c	1.0000e-24	
	94241.86c	1.0000e-24	
	94242.86c	1.0000e-24	
	95241.82c	1.0000e-24	
	95242.82c	1.0000e-24	
	95243.10c	1.0000e-24	
	96242.82c	1.0000e-24	
	96243.10c	1.0000e-24	
	96244.82c	1.0000e-24	
	96245.60c	1.0000e-24	\$ end_mcode_ACT
m15	007015.60c	0.031084529	\$ N15
	35081.55c	1.0000e-24	\$ begin_mcode_FP
	36083.50c	1.0000e-24	
	36084.50c	1.0000e-24	
	37085.55c	1.0000e-24	
	37087.55c	1.0000e-24	
	39089.60c	1.0000e-24	
	40090.62c	1.0000e-24	
	40091.96c	1.0000e-24	
	40092.62c	1.0000e-24	
	40093.50c	1.0000e-24	
	40094.62c	1.0000e-24	
	40096.62c	1.0000e-24	
	41095.96c	1.0000e-24	
	42095.50c	1.0000e-24	
	42096.96c	1.0000e-24	
	42097.60c	1.0000e-24	
	42098.50c	1.0000e-24	
c	42100.50c	1.0000e-24	
	43099.50c	1.0000e-24	
	44100.96c	1.0000e-24	
	44101.50c	1.0000e-24	
	44102.60c	1.0000e-24	

44103.50c 1.0000e-24  
44104.96c 1.0000e-24  
45103.50c 1.0000e-24  
46104.96c 1.0000e-24  
46105.50c 1.0000e-24  
46106.96c 1.0000e-24  
46108.50c 1.0000e-24  
46110.96c 1.0000e-24  
47109.60c 1.0000e-24  
48110.62c 1.0000e-24  
48111.62c 1.0000e-24  
48112.62c 1.0000e-24  
48113.60c 1.0000e-24  
48114.62c 1.0000e-24  
49115.60c 1.0000e-24  
50117.96c 1.0000e-24  
51121.96c 1.0000e-24  
51123.96c 1.0000e-24  
52125.96c 1.0000e-24  
52128.96c 1.0000e-24  
52130.96c 1.0000e-24  
53127.60c 1.0000e-24  
53129.60c 1.0000e-24  
54128.62c 1.0000e-24  
54130.62c 1.0000e-24  
54131.50c 1.0000e-24  
54132.62c 1.0000e-24  
54134.62c 1.0000e-24  
54136.62c 1.0000e-24  
55133.60c 1.0000e-24  
55134.60c 1.0000e-24  
55135.60c 1.0000e-24  
55137.60c 1.0000e-24  
56132.96c 1.0000E-24  
56135.96c 1.0000e-24  
56136.96c 1.0000e-24  
56134.62c 1.0000e-24  
56137.62c 1.0000e-24  
56138.60c 1.0000e-24  
57139.60c 1.0000e-24  
58140.96c 1.0000e-24  
58142.96c 1.0000e-24  
59141.50c 1.0000e-24  
60142.96c 1.0000e-24  
60143.50c 1.0000e-24  
60144.96c 1.0000e-24  
60145.50c 1.0000e-24  
60146.96c 1.0000e-24  
60148.50c 1.0000e-24  
60150.96c 1.0000e-24  
61147.50c 1.0000e-24  
61148.60c 1.0000e-24  
62147.50c 1.0000e-24  
62148.96c 1.0000e-24  
62149.50c 1.0000e-24  
62150.50c 1.0000e-24  
62151.50c 1.0000e-24  
62152.50c 1.0000e-24  
62154.96c 1.0000e-24  
63151.60c 1.0000e-24  
63152.50c 1.0000e-24  
63153.60c 1.0000e-24  
63154.50c 1.0000e-24  
64154.60c 1.0000e-24

```

64155.60c 1.0000e-24
64156.60c 1.0000e-24
64157.60c 1.0000e-24
64158.60c 1.0000e-24
65159.96c 1.0000e-24
66160.96c 1.0000e-24
66161.96c 1.0000e-24
66162.96c 1.0000e-24 $ end_mcode_FP
90232.86c 1.0000e-24 $ begin_mcode_ACT
90233.35c 1.0000e-24
91231.60c 1.0000e-24
91233.50c 1.0000e-24
92232.60c 1.0000e-24
92233.86c 1.0000e-24
92234.86c 1.0000e-24
92235.86c .3108452941e-2
92236.86c 1.0000e-24
92237.50c 1.0000e-24
92238.86c .2797607647e-1
92239.35c 1.0000e-24
93235.35c 1.0000e-24
93236.35c 1.0000e-24
93237.82c 1.0000e-24
93238.35c 1.0000e-24
94237.86c 1.0000e-24
94238.86c 1.0000e-24
94239.86c 1.0000e-24
94240.86c 1.0000e-24
94241.86c 1.0000e-24
94242.86c 1.0000e-24
95241.82c 1.0000e-24
95242.82c 1.0000e-24
95243.10c 1.0000e-24
96242.82c 1.0000e-24
96243.10c 1.0000e-24
96244.82c 1.0000e-24
96245.60c 1.0000e-24 $ end_mcode_ACT
m16 007015.60c 0.031084529 $ N15
35081.55c 1.0000e-24 $ begin_mcode_FP
36083.50c 1.0000e-24
36084.50c 1.0000e-24
37085.55c 1.0000e-24
37087.55c 1.0000e-24
39089.60c 1.0000e-24
40090.62c 1.0000e-24
40091.96c 1.0000e-24
40092.62c 1.0000e-24
40093.50c 1.0000e-24
40094.62c 1.0000e-24
40096.62c 1.0000e-24
41095.96c 1.0000e-24
42095.50c 1.0000e-24
42096.96c 1.0000e-24
42097.60c 1.0000e-24
42098.50c 1.0000e-24
c 42100.50c 1.0000e-24
43099.50c 1.0000e-24
44100.96c 1.0000e-24
44101.50c 1.0000e-24
44102.60c 1.0000e-24
44103.50c 1.0000e-24
44104.96c 1.0000e-24
45103.50c 1.0000e-24
46104.96c 1.0000e-24

```

46105.50c 1.0000e-24  
46106.96c 1.0000e-24  
46108.50c 1.0000e-24  
46110.96c 1.0000e-24  
47109.60c 1.0000e-24  
48110.62c 1.0000e-24  
48111.62c 1.0000e-24  
48112.62c 1.0000e-24  
48113.60c 1.0000e-24  
48114.62c 1.0000e-24  
49115.60c 1.0000e-24  
50117.96c 1.0000e-24  
51121.96c 1.0000e-24  
51123.96c 1.0000e-24  
52125.96c 1.0000e-24  
52128.96c 1.0000e-24  
52130.96c 1.0000e-24  
53127.60c 1.0000e-24  
53129.60c 1.0000e-24  
54128.62c 1.0000e-24  
54130.62c 1.0000e-24  
54131.50c 1.0000e-24  
54132.62c 1.0000e-24  
54134.62c 1.0000e-24  
54136.62c 1.0000e-24  
55133.60c 1.0000e-24  
55134.60c 1.0000e-24  
55135.60c 1.0000e-24  
55137.60c 1.0000e-24  
56132.96c 1.0000E-24  
56135.96c 1.0000e-24  
56136.96c 1.0000e-24  
56134.62c 1.0000e-24  
56137.62c 1.0000e-24  
56138.60c 1.0000e-24  
57139.60c 1.0000e-24  
58140.96c 1.0000e-24  
58142.96c 1.0000e-24  
59141.50c 1.0000e-24  
60142.96c 1.0000e-24  
60143.50c 1.0000e-24  
60144.96c 1.0000e-24  
60145.50c 1.0000e-24  
60146.96c 1.0000e-24  
60148.50c 1.0000e-24  
60150.96c 1.0000e-24  
61147.50c 1.0000e-24  
61148.60c 1.0000e-24  
62147.50c 1.0000e-24  
62148.96c 1.0000e-24  
62149.50c 1.0000e-24  
62150.50c 1.0000e-24  
62151.50c 1.0000e-24  
62152.50c 1.0000e-24  
62154.96c 1.0000e-24  
63151.60c 1.0000e-24  
63152.50c 1.0000e-24  
63153.60c 1.0000e-24  
63154.50c 1.0000e-24  
64154.60c 1.0000e-24  
64155.60c 1.0000e-24  
64156.60c 1.0000e-24  
64157.60c 1.0000e-24  
64158.60c 1.0000e-24

```

65159.96c 1.0000e-24
66160.96c 1.0000e-24
66161.96c 1.0000e-24
66162.96c 1.0000e-24 $ end_mcode_FP
90232.86c 1.0000e-24 $ begin_mcode_ACT
90233.35c 1.0000e-24
91231.60c 1.0000e-24
91233.50c 1.0000e-24
92232.60c 1.0000e-24
92233.86c 1.0000e-24
92234.86c 1.0000e-24
92235.86c .3108452941e-2
92236.86c 1.0000e-24
92237.50c 1.0000e-24
92238.86c .2797607647e-1
92239.35c 1.0000e-24
93235.35c 1.0000e-24
93236.35c 1.0000e-24
93237.82c 1.0000e-24
93238.35c 1.0000e-24
94237.86c 1.0000e-24
94238.86c 1.0000e-24
94239.86c 1.0000e-24
94240.86c 1.0000e-24
94241.86c 1.0000e-24
94242.86c 1.0000e-24
95241.82c 1.0000e-24
95242.82c 1.0000e-24
95243.10c 1.0000e-24
96242.82c 1.0000e-24
96243.10c 1.0000e-24
96244.82c 1.0000e-24
96245.60c 1.0000e-24 $ end_mcode_ACT
c
c COOLANT
c
m2 002004.50c 1.0 $Helium Coolant
c
c ODS steel cladding
c
m3 26000.50c -0.745 $ Fe
    24000.50c -0.200 $ Cr
    13027.60c -0.045 $ Al
    22000.60c -0.005 $ Ti
    06000.50c -0.0005 $ C
    39089.60c -0.00394 $ Y
    08016.50c -0.00106 $ O
m4 40000.60c 3.00
    14000.60c 2.00 $ Zr3Si2 reflector
m6 73181.60c 50
    50010.10c 90
    50011.10c 10
m9 40000.60c 1.00
    01001.50c 2.00 $ ZrH2 moderator
c
c
c
c PROBLEM SPECIFICATION
c
c dbcn 1 0 1 2 1e5 0 1 73
ksrc 8.5 4.9 0
mode n
kcode 12000 1.0 25 75
prdnr 75 75 75

```

print



## Appendix F Demonstration Core MCODEv1 Input File

```
$ MCODE input file for B&B GFR
$ ODS Hex pin$ defines title
$ CTRL command initial-inp
MCD 0 mcrp.exe n151.i $ MCNP files def. 0=start from ksrc source
$ ORIGEN-COMMAND ORIGEN-LIBRARIES
ORG /usr/local/bin/origen22/origen22 /usr/local/bin/origen22/LIBS DECAY.LIB
GXUO2BRM.LIB
$ total# ID TYPE IHM(g) VOL(cm3)
CEL 6 11 1 17454423 1421370 FFTFC.LIB
21 1 17454423 1421370 FFTFC.LIB
31 1 17454423 1421370 FFTFC.LIB
41 1 17454423 1421370 FFTFC.LIB
51 1 17454423 1421370 FFTFC.LIB
61 1 17454423 1421370 FFTFC.LIB
$ total volume of fuel (cm3)
VOL 8528220
$ normalization method, 1=flux, 2=power
NOR 1
$ predictor-corrector option, 1=P-C on, 0=P-C off
COR 0
$ core power density per liter of core volume, opt: WGU=W/gIHM, KWL=kW/(liter fuel)
PDE 340 KWL
$points 0 1 2 3 4 5 6
DEP E 0 0.1 5 10 20 25 27
NMD 40 40 40 40 40 40
STA 0 $ starting point !!If first time, must start with 0
END 5 $ ending point
```

## Appendix G Advanced B&B GFR MCNP Model and MCODEv2 Input

```
B&B GFR TID UC Core,
c Peter Yarsky
c 4.12.05
c
c PURPOSE:
c The purpose of this MCNP model is to do burnup calculations on a full
c core model of a Breed and Burn reactor.
c TEST FOR MCODE2
c
c PRECONDITIONS:
c The geometry is a tube-in-duct configuration ~ 60 v/o UC fuel
c There are 91 coolant channels per assembly, the pitch is 1.45 cm
c
c Hot case, coolant pressure is 11.5 MPa
c coolant temperature is 370oC (8.76 kg/m3)
c 5 a/o enriched UC reload fuel (BOC)
c Fuel is taken at 91% Theoretical Density (VIPAC)
c
c GRADED ENRICHMENT BOL
c 01: 5 a/o
c 02: 6 a/o
c 03: 8 a/o
c 04: 10a/o
c 05: 10a/o
c 06: 10a/o
c
c The initial assumption is 6 batch reloading of assemblies,
c The initial startup core is purely uranium fuel.
c
c startup core uses uranium enrichment gradient to simulate equilibrium
c
c A Zirconium Silicide reflector is included at the
c top and bottom of the core.
c
c assuming interstitials ~ duct / cladding (put into model as such)
c
c spacing between assemblies is 0.6 cm (delta/2)
c
c volume fuel = 91 x 96 x 200 cm x (sqrt(3)/2 x pitch^2 - pi (cladOR)^2)
c volume fraction fuel = 6 volume fuel / total volume
c = (6 vf)/(FIF^2 sqrt(3)/2 576 200cm) = 54.5%
c
c
c
c FUEL CELLS
c
c mt density
11 11 5.987e-02
   +2 u=11 imp:n=1 vol = 2118665 $ fuel
12 3 -7.2 +1 -2 u=11 imp:n=1 $ ODS cladding
13 2 -0.00876 -1 u=11 imp:n=1 $ He coolant
21 12 5.987e-02
   +2 u=22 imp:n=1 vol = 2118665 $ fuel
22 3 -7.2 +1 -2 u=22 imp:n=1 $ ODS cladding
23 2 -0.00876 -1 u=22 imp:n=1 $ He coolant
31 13 5.987e-02
   +2 u=33 imp:n=1 vol = 2118665 $ fuel
32 3 -7.2 +1 -2 u=33 imp:n=1 $ ODS cladding
33 2 -0.00876 -1 u=33 imp:n=1 $ He coolant
41 14 5.987e-02
   +2 u=44 imp:n=1 vol = 2118665 $ fuel
42 3 -7.2 +1 -2 u=44 imp:n=1 $ ODS cladding
```

```

43 2 -0.00876 -1      u=44 imp:n=1  $ He coolant
51 15 5.987e-02
+2      u=55 imp:n=1  vol = 2118665 $ fuel
52 3 -7.2      +1 -2   u=55 imp:n=1  $ ODS cladding
53 2 -0.00876 -1      u=55 imp:n=1  $ He coolant
61 16 5.987e-02
+2      u=66 imp:n=1  vol = 2118665 $ fuel
62 3 -7.2      +1 -2   u=66 imp:n=1  $ ODS cladding
63 2 -0.00876 -1      u=66 imp:n=1  $ He coolant
c
c CONTROL
c
71 5 -2.50     +2 +6    u=77 imp:n=1  $ poison
72 3 -7.2      +1 -2 +6  u=77 imp:n=1  $ ODS cladding
73 2 -0.00876 -1 +6    u=77 imp:n=1  $ He coolant
74 2 -0.00876 -6      u=77 imp:n=1  $ He fill
c
c REFLECTOR
c
c
c AXIAL
c
81 4 0.08918  +2      u=88 imp:n=1  $ axial reflector
82 3 -7.2      +1 -2   u=88 imp:n=1  $ ODS cladding
83 2 -0.00876 -1      u=88 imp:n=1  $ He coolant
c
c RADIAL
c
99 4 0.07134 +501 -601 63 -64 61 62 imp:n=1 $ radial reflector
c
c Assembly Definitions
c
101 3 -7.2 -21      $ batch 01
      imp:n=1 u=91 lat=2 fill=-6:6 -6:6 0:0
      00 00 00 00 00 00 91 91 91 91 91 91 91
      00 00 00 00 00 91 11 11 11 11 11 11 91
      00 00 00 00 91 11 11 11 11 11 11 11 91
      00 00 00 91 11 11 11 11 11 11 11 11 91
      00 00 91 11 11 11 11 11 11 11 11 11 91
      00 91 11 11 11 11 11 11 11 11 11 11 91
      91 11 11 11 11 11 11 11 11 11 11 11 91
      91 11 11 11 11 11 11 11 11 11 11 91 00
      91 11 11 11 11 11 11 11 11 11 91 00 00
      91 11 11 11 11 11 11 11 11 91 00 00 00
      91 11 11 11 11 11 11 11 91 00 00 00 00
      91 91 91 91 91 91 91 91 00 00 00 00 00
102 3 -7.2 -21      $ batch 02
      imp:n=1 u=92 lat=2 fill=-6:6 -6:6 0:0
      00 00 00 00 00 00 92 92 92 92 92 92 92
      00 00 00 00 00 92 22 22 22 22 22 22 92
      00 00 00 00 92 22 22 22 22 22 22 22 92
      00 00 00 92 22 22 22 22 22 22 22 22 92
      00 00 92 22 22 22 22 22 22 22 22 22 92
      00 92 22 22 22 22 22 22 22 22 22 22 92
      92 22 22 22 22 22 22 22 22 22 22 22 92
      92 22 22 22 22 22 22 22 22 22 22 92 00
      92 22 22 22 22 22 22 22 22 22 92 00 00
      92 22 22 22 22 22 22 22 22 92 00 00 00
      92 22 22 22 22 22 22 22 92 00 00 00 00
      92 92 92 92 92 92 92 92 00 00 00 00 00
103 3 -7.2 -21      $ batch 03
      imp:n=1 u=93 lat=2 fill=-6:6 -6:6 0:0

```

```

00 00 00 00 00 00 93 93 93 93 93 93 93
00 00 00 00 00 93 33 33 33 33 33 33 93
00 00 00 00 93 33 33 33 33 33 33 33 93
00 00 00 93 33 33 33 33 33 33 33 33 93
00 00 93 33 33 33 33 33 33 33 33 33 93
00 93 33 33 33 33 33 33 33 33 33 33 93
93 33 33 33 33 33 33 33 33 33 33 33 93
93 33 33 33 33 33 33 33 33 33 33 93 00
93 33 33 33 33 33 33 33 33 33 93 00 00
93 33 33 33 33 33 33 33 33 93 00 00 00
93 33 33 33 33 33 33 93 00 00 00 00
93 93 93 93 93 93 93 00 00 00 00 00
104 3 -7.2 -21      $ batch 04
    imp:n=1 u=94 lat=2 fill=-6:6 -6:6 0:0
    00 00 00 00 00 00 94 94 94 94 94 94 94
    00 00 00 00 00 94 44 44 44 44 44 44 94
    00 00 00 00 94 44 44 44 44 44 44 44 94
    00 00 00 94 44 44 44 44 44 44 44 44 94
    00 00 94 44 44 44 44 44 44 44 44 44 94
    00 94 44 44 44 44 44 44 44 44 44 44 94
    94 44 44 44 44 44 44 44 44 44 44 44 94
    94 44 44 44 44 44 44 44 44 44 44 94 00
    94 44 44 44 44 44 44 44 44 94 00 00 00
    94 44 44 44 44 44 44 44 94 00 00 00 00
    94 94 94 94 94 94 94 00 00 00 00 00
105 3 -7.2 -21      $ batch 05
    imp:n=1 u=95 lat=2 fill=-6:6 -6:6 0:0
    00 00 00 00 00 00 95 95 95 95 95 95 95
    00 00 00 00 00 95 55 55 55 55 55 55 95
    00 00 00 00 95 55 55 55 55 55 55 55 95
    00 00 00 95 55 55 55 55 55 55 55 55 95
    00 00 95 55 55 55 55 55 55 55 55 55 95
    00 95 55 55 55 55 55 55 55 55 55 55 95
    95 55 55 55 55 55 55 55 55 55 55 55 95
    95 55 55 55 55 55 55 55 55 55 55 95 00
    95 55 55 55 55 55 55 55 55 55 95 00 00
    95 55 55 55 55 55 55 55 55 95 00 00 00
    95 95 95 95 95 95 95 00 00 00 00 00
106 3 -7.2 -21      $ batch 06
    imp:n=1 u=96 lat=2 fill=-6:6 -6:6 0:0
    00 00 00 00 00 00 96 96 96 96 96 96 96
    00 00 00 00 00 96 66 66 66 66 66 66 96
    00 00 00 00 96 66 66 66 66 66 66 66 96
    00 00 00 96 66 66 66 66 66 66 66 66 96
    00 00 96 66 66 66 66 66 66 66 66 66 96
    00 96 66 66 66 66 66 66 66 66 66 66 96
    96 66 66 66 66 66 66 66 66 66 66 66 96
    96 66 66 66 66 66 66 66 66 66 96 00 00
    96 66 66 66 66 66 66 66 66 96 00 00 00
    96 66 66 66 66 66 66 96 00 00 00 00
    96 96 96 96 96 96 96 00 00 00 00 00
c
c NON FUEL
c
107 3 -7.2 -21      $ control assembly
    imp:n=1 u=97 lat=2 fill=-6:6 -6:6 0:0
    00 00 00 00 00 00 97 97 97 97 97 97 97

```

```

00 00 00 00 00 97 77 77 77 77 77 77 97
00 00 00 00 97 77 77 77 77 77 77 77 97
00 00 00 97 77 77 77 77 77 77 77 77 97
00 00 97 77 77 77 77 77 77 77 77 77 97
00 97 77 77 77 77 77 77 77 77 77 77 97
97 77 77 77 77 77 77 77 77 77 77 77 97
97 77 77 77 77 77 77 77 77 77 77 97 00
97 77 77 77 77 77 77 77 77 77 97 00 00
97 77 77 77 77 77 77 77 77 97 00 00 00
97 77 77 77 77 77 77 77 97 00 00 00 00
97 97 97 97 97 97 97 00 00 00 00 00 00
108 3 -7.2 -21 $ axial reflector
    imp:n=1 u=98 lat=2 fill=-6:6 -6:6 0:0
00 00 00 00 00 00 98 98 98 98 98 98 98
00 00 00 00 00 98 88 88 88 88 88 88 98
00 00 00 00 98 88 88 88 88 88 88 88 98
00 00 00 98 88 88 88 88 88 88 88 88 98
00 00 98 88 88 88 88 88 88 88 88 88 98
00 98 88 88 88 88 88 88 88 88 88 88 98
98 88 88 88 88 88 88 88 88 88 88 88 98
98 88 88 88 88 88 88 88 88 88 88 98 00
98 88 88 88 88 88 88 88 88 88 98 00 00
98 88 88 88 88 88 88 88 98 00 00 00 00
98 88 88 88 88 88 88 98 00 00 00 00 00
98 98 98 98 98 98 98 00 00 00 00 00 00

```

C  
C  
C

```

111 0 -22 u=01 fill=91 imp:n=1
121 2 -0.00876 +22 -31 u=01 imp:n=1
112 0 -22 u=02 fill=92 imp:n=1
122 2 -0.00876 +22 -31 u=02 imp:n=1
113 0 -22 u=03 fill=93 imp:n=1
123 2 -0.00876 +22 -31 u=03 imp:n=1
114 0 -22 u=04 fill=94 imp:n=1
124 2 -0.00876 +22 -31 u=04 imp:n=1
115 0 -22 u=05 fill=95 imp:n=1
125 2 -0.00876 +22 -31 u=05 imp:n=1
116 0 -22 u=06 fill=96 imp:n=1
126 2 -0.00876 +22 -31 u=06 imp:n=1
117 0 -22 u=07 fill=97 imp:n=1
127 2 -0.00876 +22 -31 u=07 imp:n=1
118 0 -22 u=08 fill=98 imp:n=1
128 2 -0.00876 +22 -31 u=08 imp:n=1

```

C  
C Core Definition  
C

```

209 2 -0.00876 -31 u=14 lat=2
    imp:n=1 fill=0:19 -10:10 0:0
00 00 00 00 00 00 00 00 00 00 00 00 00 00 14 14 14 14
00 00 00 00 00 00 00 00 00 00 00 00 00 00 14 14 14 14
00 00 00 00 00 00 00 00 00 00 00 00 00 00 14 14 14 14
00 00 00 00 00 00 00 00 00 00 00 00 08 14 14 14 14 14
00 00 00 00 00 00 00 00 00 00 08 08 08 14 14 14 14 14
00 00 00 00 00 00 00 00 08 08 08 08 08 14 14 14 14 14
00 00 00 00 08 08 08 08 08 08 08 08 08 14 14 14 14 14
00 00 08 08 08 08 08 08 08 08 08 08 08 14 14 14 14 14
07 08 08 08 08 08 08 08 08 08 08 08 14 14 14 14 14 14
00 08 08 08 08 08 08 08 08 08 08 08 14 14 14 14 14 14
00 00 08 08 08 08 08 08 08 08 08 14 14 14 14 14 14 14

```

```

00 00 00 08 08 08 08 08 08 08 08 14 14 14 14 14 14 14 14
00 00 00 00 08 08 08 08 08 08 08 14 14 14 14 14 14 14 14
00 00 00 00 00 08 08 08 08 08 14 14 14 14 14 14 14 14
00 00 00 00 00 00 08 08 08 14 14 14 14 14 14 14 14 14
00 00 00 00 00 00 00 08 14 14 14 14 14 14 14 14 14 14
00 00 00 00 00 00 00 00 14 14 14 14 14 14 14 14 14 14
00 00 00 00 00 00 00 00 14 14 14 14 14 14 14 14 14 14
00 00 00 00 00 00 00 00 14 14 14 14 14 14 14 14 14 14
210 2 -0.00876 -31 u=12 lat=2
      imp:n=1 fill=0:19 -10:10 0:0
00 00 00 00 00 00 00 00 00 00 00 00 00 00 00 12 12 12 12
00 00 00 00 00 00 00 00 00 00 00 00 00 00 00 12 12 12 12
00 00 00 00 00 00 00 00 00 00 00 00 00 00 00 12 12 12 12
00 00 00 00 00 00 00 00 00 00 00 00 00 00 01 12 12 12 12
00 00 00 00 00 00 00 00 00 00 00 00 00 07 02 01 12 12 12 12
00 00 00 00 00 00 00 00 00 00 05 06 02 02 01 12 12 12 12
00 00 00 00 00 00 00 00 07 05 05 06 06 02 01 12 12 12 12
00 00 00 00 00 00 04 03 03 05 05 06 06 02 01 12 12 12 12
00 00 00 04 04 04 03 03 03 05 06 06 02 01 01 12 12 12 12
07 04 04 04 07 04 04 03 07 05 07 02 07 12 12 12 12 12 12
00 04 04 04 04 03 03 03 05 06 06 02 01 01 12 12 12 12 12
00 00 04 04 03 03 03 05 05 06 02 02 01 12 12 12 12 12 12
00 00 00 04 03 03 05 06 06 02 01 12 12 12 12 12 12 12 12
00 00 00 00 07 05 05 06 06 02 01 12 12 12 12 12 12 12 12
00 00 00 00 00 05 06 02 02 01 12 12 12 12 12 12 12 12 12
00 00 00 00 00 00 07 02 01 12 12 12 12 12 12 12 12 12 12
00 00 00 00 00 00 00 01 12 12 12 12 12 12 12 12 12 12 12
00 00 00 00 00 00 00 00 12 12 12 12 12 12 12 12 12 12 12
00 00 00 00 00 00 00 00 12 12 12 12 12 12 12 12 12 12 12
130 0          +61 +62 -501 63 -65 fill=12 imp:n=1 $ core
132 0          +61 +62 -501 65 -64 fill=14 imp:n=1 $ top-reflector
c
c REST OF MODEL
c
c
c 1000 0          -61:-62:601:-63:64  imp:n=0 $ outside
c end of cell specification

c
c surface specification
c
c FUEL PIN GEOMETRY
c
1 cz          +0.40          $ cladding inner R
2 cz          +0.44          $ cladding inner R
c
c CONTROL RODS
c
6 pz          +124          $ Poison Bank (in =
0)
c
c FUEL ASSEMBLY GEOMETRY
c
c bottom      vector to top  facet vector
c                                pitch/2,0,0
21 hex 0 0 -500          0 0 1000          0.725 0 0
c                                [(D+1/3) 3/8 pitch] [(D+1/3)sqrt(3)/8 pitch]
22 hex 0 0 -500          0 0 1000          6.162500003 3.557921035 0
c
c
c CORE GEOMETRY
c

```

```

c assembly area = sqrt(3)/2 FTF^2
c
c          bottom      vector to top  angle = 30 degrees
c          D = number of pins across assembly diagonal
c          n = (D-1)/2
c          N = total number of pins = n(n+1)/2 + 1
c          FTF = (D+1/3) sqrt(3)/2 pitch + delta
c          sqrt(3) FTF/4 , FTF/4 , 0
c
31      hex  0 0 -500      0 0 1000      6.422307625 3.707921035 0
c
c BOUNDARY CONDITIONS
c
c          -sqrt(3)
c
*61  p  1 -1.732051 0 0      $ symmetry
*62  py 1E-5                $ symmetry
*63  pz 0                    $ symmetry
601  cz 245                  $ model limit radial reflector out
c
c axial planes
c
64  pz +125                  $ upper extreme
65  pz +100                  $ core top
c
c REST OF MODEL GEOMETRY
c
501  px +188.5              $ radial reflector in
c
c end of surface specification
c
c data specification
c
c MATERIALS
c fuel
c
m11  6000.60c 0.0294850      $ C
      92235.86c 0.00141425
      92238.86c 0.02801075
m12  6000.60c 0.0294850      $ C
      92235.86c 0.0017655
      92238.86c 0.0276595
m13  6000.60c 0.0294850      $ C
      92235.86c 0.0022628
      92238.86c 0.0271262
m14  6000.60c 0.0294850      $ C
      92235.86c 0.0028285
      92238.86c 0.0265365
m15  6000.60c 0.0294850      $ C
      92235.86c 0.0028285
      92238.86c 0.0265365
m16  6000.60c 0.0294850      $ C
      92235.86c 0.0028285
      92238.86c 0.0265365
c
c coolant
c
m2      002004.50c 1.0      $Helium Coolant
c
c ODS steel cladding
c
m3      26000.50c -0.745      $ Fe
      24000.50c -0.200      $ Cr

```

```

13027.60c  -0.045  $ Al
22000.60c  -0.005  $ Ti
06000.50c  -0.0005  $ C
39089.60c  -0.00394  $ Y
08016.50c  -0.00106  $ O
m4  40000.60c  3.00
14000.60c  2.00  $ Zr3Si2 reflector
m5  05010.60c  198
05011.60c  2
06000.60c  50  $ B4C poison
c
c
c
c PROBLEM SPECIFICATION
c
ksrc  8.5 4.9 50
mode  n
kcode 50000 1.0 25 75
prtmp 75 75 75
print

c executable (optional)
mce /home/yarsky/bin/mcnp.exe
c mcnp xs summary
mcxs /home/yarsky/bin/mcode2/mcnpxs.sum.endf
c opt (0=no source, 1=source every mcnp, 2=source all through)
mcs 1
c executable
orge /usr/local/bin/origen22/origen22
c org-library-path decay gamma
orgl /usr/local/bin/origen22/LIBS DECAF.LIB GXUO2BRM.LIB
c
c m# vol(cc) org-xs-lib imp temp mcnp-xs-opt ntal
c (K) optional optional
c 1=original (default), 2=new
11 2118665 FFTFC.LIB 0.999 900 2 10 $ batch1
12 2118665 FFTFC.LIB 0.999 900 2 10 $ batch2
13 2118665 FFTFC.LIB 0.999 900 2 10 $ batch3
14 2118665 FFTFC.LIB 0.999 900 2 10 $ batch4
15 2118665 FFTFC.LIB 0.999 900 2 10 $ batch5
16 2118665 FFTFC.LIB 0.999 900 2 10 $ batch6
c optional tally specification
c tal
c
pow 2400000000 $ watts
c
nor 1 $ 1=flux(iterated) 2=flux(once)
c
cor 1 $ predictor-corrector, 0=OFF, 1=ON (1 mcnp) default, 2=ON (2 mcnp)
c
c depletion description
c opt days/BU rel-pow-level NMD
c D/E (absolute) (default 1, negative means decay only) (default 20)
dep D 0 1 40
7 1 40
300 1 40
500 1 40
700 1 40
900 1 40
1100 1 40
1350 1 40
1720 1 40
sta $ start pint, default 0
end $ end point, default max

```



## References

1. Advanced Gas Cooled Reactor. Hacettepe University: Nuclear Engineering Department 2003. < <http://www.nuke.hun.edu.tr/english/links/agr.html>>
2. Arai, Y., Suzuki, Y., Iwai, T., Ohmichi, T., "Dependence of the thermal conductivity of (U, Pu) N on porosity and plutonium content," *J. Nucl. Mater.*, 195 (1992) p.37
3. Atefi, B., M.J. Driscoll and D.D. Lanning, "An Evaluation of the Breed/Burn Fast Reactor Concept," MITNE-229, Dec. 1979.
4. Ballinger, R., Personal Communication Regarding UCO Properties. MIT 2003.
5. Bretsher, M.M., Deen, J.R., Hana, N.A., and Matos, J.E. *Neutronic Feasibility Studies using U-Mo Dispersion Fuel (9 Wt% Mo, 5.0 gU/cc) for LEU Conversion of the Maria (Poland), IR-8 (Russia), and WWR-SM (Uzbekistan) Research Reactors*. International Meeting on RERT, Las Vegas, Nevada, USA (2000).
6. Buongiorno, J. "Temperature Limits for the Fuel and Cladding of Heavy-Liquid-Metal-Cooled Reactors" Proc. Global '01, Paris, France, Sept. 9-13, 2001.
7. Carpenter: Alloy Data Carpenter Stainless Type 310. Carpenter Technology. 2003 < <http://www.cartech.com/products/index.html>>
8. Chidester, K., Rubin, J., Thompson, M., *Vibrationally-Compacted (VIPAC/SPHERE-PAC) Nuclear Fuels – A Comparison with Pelletized Nuclear Fuels*, ICONE9, Nice, France (2001).
9. Choi, H., Ko, W.I., Yang, M.S., "Economic Analysis on Direct Use of Spent Pressurized Water Reactor Fuel in CANDU Reactors – IV: DUPIC Fuel Cycle Cost," *Nucl. Tech.* 134, (2001) 167-186.
10. Choi, H., Ko, W.I., Roh, G., Yang, M.S., "Economic Analysis on Direct Use of Spent Pressurized Water Reactor Fuel in CANDU Reactors – III: Spent DUPIC Fuel Disposal Cost," *Nucl. Tech.* 134, (2001) 149-166.
11. Choi, H., Ko, W.I., Yang, M.S., "Economic Analysis on Direct Use of Spent Pressurized Water Reactor Fuel in CANDU Reactors – I: DUPIC Fuel Fabrication Cost," *Nucl. Tech.* 134, (2001) 110-129.
12. Choi, H., Ko, W.I., Yang, M.S., "Economic Analysis on Direct Use of Spent Pressurized Water Reactor Fuel in CANDU Reactors – II: DUPIC Fuel-Handling Cost," *Nucl. Tech.* 134, (2001) 130-148.
13. Choi, H., Rimpault, G., Bosq, J., "A Physics Study of a 600 MWTH Gas-Cooled Fast Reactor" ANS 38-04, (March 2005).
14. Cunningham, M.E., Barner, J.O., Freshley, M.D., "In-Reactor Thermal Conductivity of UO<sub>2</sub> Sphere-pac Fuel," *Trans. Am. Nucl. Soc.*, Vol. **38**, 276-277, June, (1981).
15. De Laquil III, Pascal, "An Accident Probability Analysis and Design of the Gas-cooled Fast Breeder Reactor Demonstration Plant" MIT Nuclear Engineering PhD Thesis. January 1976.
16. Doran, D.G., "The Calculation of Displacement Rate in Stainless Steel Under Neutron and Electron Irradiations", *Nucl. Eng. Design.* 33 (1975) 63-77.
17. Dostal, V., Driscoll, M.J., Hejzlar, P. "A Super Critical Carbon Dioxide Cycle for Next Generation Nuclear Reactors" MIT-ANP-TR-100, (March 2004).
18. Dostal, V., P. Hejzlar, M.J. Driscoll, and N.E. Todreas "A Supercritical CO<sub>2</sub> Gas Turbine Power Cycle for Advanced Reactor Applications," *Trans. Am. Nucl. Soc.*, Vol. **85**, Reno, Nevada, November 11-15, (2001)
19. Driscoll, M.J., Hejzlar, P., Todreas, N.E., Veto, B. "Modern Gas-Cooled Fast Reactor Safety Assurance Considerations" MIT-ANP-TR-087 (May 2003).

20. Driscoll, M.J., Hejzlar, P., Todreas, N.E., Veto, B., "Modern Gas-Cooled Fast Reactor Safety Assurance Considerations," MIT-ANP-TR-087, May 2003.
21. Duderstadt J., Hamilton L.: Nuclear Reactor Analysis, John Wiley and Sons. Inc. New York, 1976.
22. Electrowatt-Ekono, A review of the processes contributing to radioactive waste in the UK. DETR/RAS/99.013, UK Nirex Ltd N/004 September 1999.
23. Feinberg, S.M., Discussion Comment, Rec. of Proc. Session B-10, ICP UAE, No. 2, Vol. 9, p.447, United Nations, Geneva, 1958.
24. Fischer, G.J., et al., "Physics and Feasibility Study of the Fast-Mixed-Spectrum Reactor Concept," BNL-25598, Jan. 1, 1979.
25. General Atomics "Gas-Cooled Fast Breeder Reactor Preliminary Safety Information Document Amendment 10: GCFR Residual Heat Removal System Criteria, Design, and Performance" GA-10298 September 1, 1980.
26. General Atomics "Gas-Cooled Fast Breeder Reactor Preliminary Safety Information Document Amendment 9: GCFR Fuel Cladding PC-5 Faulted Temperature Limit" GA-10298 February 1, 1980.
27. Gezelius, K., Driscoll, M.J., Hejzlar, P. "Design of Compact Intermediate Heat Exchangers for Gas Cooled Fast Reactors" MIT-ANP-TR-103, (May 2004).
28. GIF (Generation IV International Forum), "A Technology Roadmap for Generation IV Nuclear Energy Systems," GIF-002-00, issued by the US DOE Nuclear Energy Research Advisory Committee and the Generation IV International Forum, 2002.
29. Gnielinski, V., "New Equations for Heat and Mass Transfer in Turbulent Pipes and Channel Flow," *International Chemical Engineering*, Vol. 16, No. 2, pp. 359-368, 1976.
30. Handwerk, C.S., Driscoll, M.J., Todreas, N.E., McMahan, V. "Economic Analysis of Extended Operating Cycles in Existing LWRs" MIT-NFC-TR-007, (January 1998).
31. Hodgman, C. ed.: Handbook of Chemistry and Physics, Chemical Rubber Publishing Company. 44<sup>th</sup> ed. Cleveland, OH, 1962.
32. Hofman, G.L. *A Short Note on High Density Dispersion Fuel*. Argonne National Lab June 1996.
33. Hoyt, R.C., Rhee, B.W., "Review of the Literature for Dry Reprocessing Oxide, Metal, and Carbide Fuel: The AIROX, RAHYD, and CARBOX Pyrochemical Processes" Rockwell International, ESG-DOE-13277, (1979)
34. *INCOLOY alloy MA956*, Special Metals Corporation SMC-008, 1999
35. Inoue, M., Ono, K., Fujioka, T., Sato, K., Asaga, T., *Feasibility Study on Nitrogen-15 Enrichment and Recycling System for Innovative FR Cycle System with Nitride Fuel*, ICONE10-22622, Arlington, Virginia, USA, (2002).
36. JANIS: the new version of the nuclear data display software JEF-PC (ENDF Libraries). Typhoon Software. 2003. <<http://www.typhoonsoftware.com>>
37. LeSage, L.G., "An Overview of the Argonne National Laboratory Fast Critical Experiments 1963-1990," ANL-NT-175, April, 2001.
38. Lewis, H., Kerrisk, J., "Electrical and Thermal Transport Properties of Uranium and Plutonium Carbides" LA-6096-MS (1975).
39. Loh, W.T., M.J. Driscoll and D.D. Lanning, "An Evaluation of the Fast Mixed Spectrum Reactor," MITNE-232, Feb. 1980.
40. Los Alamos National Laboratory, "MCNP4C Monte Carlo N-Particle Transport Code System," CCC-700, April 2000.
41. Mayorshin, A.A., Skiba, O.V., Tsykanov, V.A., Kisly, V.A., *Russian Experience in Using UPUO2 VIBROPAC Fuel Pins in Fast Reactors* ICONE8-629, Baltimore, Maryland, USA, (April 2000).
42. McCarty, R.D., Arp, V.D., "A New Wide Range Equation of State for Helium", *Advances in Cryogenic Engineering*, Vol. 35, pp. 1465-1475, 1990.

43. Mitchell, C.H., Lo Pinto, P., Dominguez, M.T., van Heek, A., Every, D.P., Carlucci, B., *Gas-Cooled Fast Reactor Concept Review Studies (GCFR)*, ICAPP, Cordoba, Spain, (May 2003).
44. Morman, J.A., ed. "Reactor Physics Studies in the GCFR Phase III Critical Assembly," ANL-79-35, Jan. 2, 1981.
45. Oggianu, S.M., Kazimi, M.S.: "A Review of Properties of Advanced Nuclear Fuels" MIT-NFC-TR-021, 2000.
46. Online Plotter for MCNP and ENDF cross section data. KAERI. 2003. <<http://atom.kaeri.re.kr/endlplot.shtml>>
47. Osugi, T., Andoh, M., Takano, H., Ogawa, T., "Fuel Cycle Systems with Nitride Fuel for Transmutation," *Advanced Reactors with Innovative Fuels, Workshop Proceedings*, 21-23 October 1998.
48. Plaue, J., K.R. Czerwinski, "Evaluation of Uranium Carbide and Sulfide Fuels for a Gas-cooled Fast Reactor Utilizing Dry Reprocessing," MIT-GFR-007, May 2003.
49. Pope, M.A., Driscoll, M.J., Hejzlar, P. "Reactor Physics Design of Supercritical CO<sub>2</sub>-Cooled Fast Reactors," MIT-ANP-TR-104, September 2004.
50. Pope, M.A., Yarsky, P., Driscoll, M.J., Hejzlar, P., "An Advanced Vented Fuel Assembly for GFR Applications," *Trans. Am. Nucl. Soc.* Vol. **92**, San Diego, California, June, (2005).
51. *Record of Decision for the Treatment and Management of Sodium-Bonded Spent Nuclear Fuel* Federal Register: September 19, 2000 (Volume 65, Number 182) Page 56565-56570 From the Federal Register Online via GPO Access [[wais.access.gpo.gov](http://www.access.gpo.gov)] [DOCID:fr19se00-47]
52. Reynard, M.P., Czerwinski, K.R., "MIT Contribution to the LDRD AIROX Project: Examination of Waste Issues"
53. Ribeiro, Arnaldo Aloisio Telles, "Flow Orificing in Nuclear Power Reactors" SM Thesis MIT Nuclear Engineering Department. 1974.
54. Roberts, J.T.: Structural Materials in Nuclear Power Systems, Plenum Press. New York 1981.
55. Romano, A., P. Hejzlar, N.E. Todreas, "Optimization of Actinide Transmutation in Innovative Lead-Cooled Fast Reactors," MIT-NFC-TR-059, October 2003.
56. Ryu, K., H. Sekimoto, "A Possibility of Highly Efficient Uranium Utilization With a Pebble Bed Fast Reactor," *Annals of Nuclear Energy*, Vol. 27, p. 1139, 2000.
57. Shin, J.I., Driscoll, M.J., "Generalized Fissile Buildup Histories for FBR Blankets," *Trans. Am. Nucl. Soc.*, **23** (June 1976).
58. Soodak, H. ed.: Reactor Handbook, Vol 3, Part A Physics. Wiley. 2<sup>nd</sup> ed. 1962.
59. Stacey, W.: Nuclear Reactor Physics, John Wiley and Sons, Inc. New York, 2001.
60. Suzuki, Y., Ogawa, T., Arai, Y., Mukaiyama, T. "Recent Progress on Nitride Fuel Cycle in JAERI" Fifth OECD/NEA Information Exchange Meeting on Actinide and Fission Product Partitioning and Transmutation, 25-27 November 1998.
61. Technical Presentation, *Integral Fast Reactor Core Design Safety Strategy: Impact of Fuel and Core on Inherent Safety*. Course Notes 22.211 Fall 2002.
62. Thon, S.: "Selection of Materials for a Supercritical CO<sub>2</sub> Cooled GCFR" MIT-GCFR-001, 2002
63. Todreas, N., Kazimi, M.: Nuclear Systems I Thermal Hydraulic Fundamentals, Taylor and Francis. New York, 1993.
64. Toshinsky, G.I., "LMFBR Operation in the Nuclear Cycle Without Fuel Reprocessing." Proc. ARC'97, Orlando, June, 1997.
65. Toshinsky, V., Toshinsky, G., Hiroshi, S. "Fuel Management Optimization for the SFBR Using a Multiobjective Genetic Algorithm." *Trans. Am. Nucl. Soc.*, **81**, 296-298, (November 1999).

66. Wade, D.C., Chang, Y.I., "The Integral Fast Reactor Concept: Physics of Operation and Safety", *Nucl. Sci. Eng.* 100, (1988) 507-524.
67. Waltar, Alan E. and Albert B. Reynolds. Fast Breeder Reactors, Pergamon Press, New York, NY, 1981.
68. Winterton, R.H.S.: Thermal Design of Nuclear Reactors, Pergamon Press. New York, 1981.
69. Xu, Z. "Systems Analysis of the Nuclear Fuel Cycle: CASMO-4" (February 2003).
70. Xu, Z. "Systems Analysis of the Nuclear Fuel Cycle: ORIGEN2.1" (February 2003).
71. Xu, Z., Driscoll, M.J., Kazimi, M.S. "Design Strategies for Optimizing High Burnup Fuel in Pressurized Water Reactors" MIT-NFC-TR-053, (July 2003).
72. Xu, Z., P. Hejzlar, M.J. Driscoll, M.S. Kazimi, "An Improved MCNP-ORIGEN Depletion Program (MCODE) and its Verification for High-Burnup Applications," *International Conference on the New Frontiers of Nuclear Technology: Reactor Physics, Safety and High-Performance Computing (PHYSOR 2002)*, Seoul, Korea, October 7-10, 2002.
73. Yarsky, P., Pope, M.A., Driscoll, M.J., Hejzlar, P. "Reactor Physics Analysis of a Tube-in-Duct Fuel Design for GFR Service," *Trans. Am. Nucl. Soc.* Vol. **92**, San Diego, California, June, (2005).
74. Yu, K., Driscoll, M.J., Hejzlar, P. "Neutronic Evaluation of GCFR Core Diluents," MIT-ANP-TR-086, (May 2003).